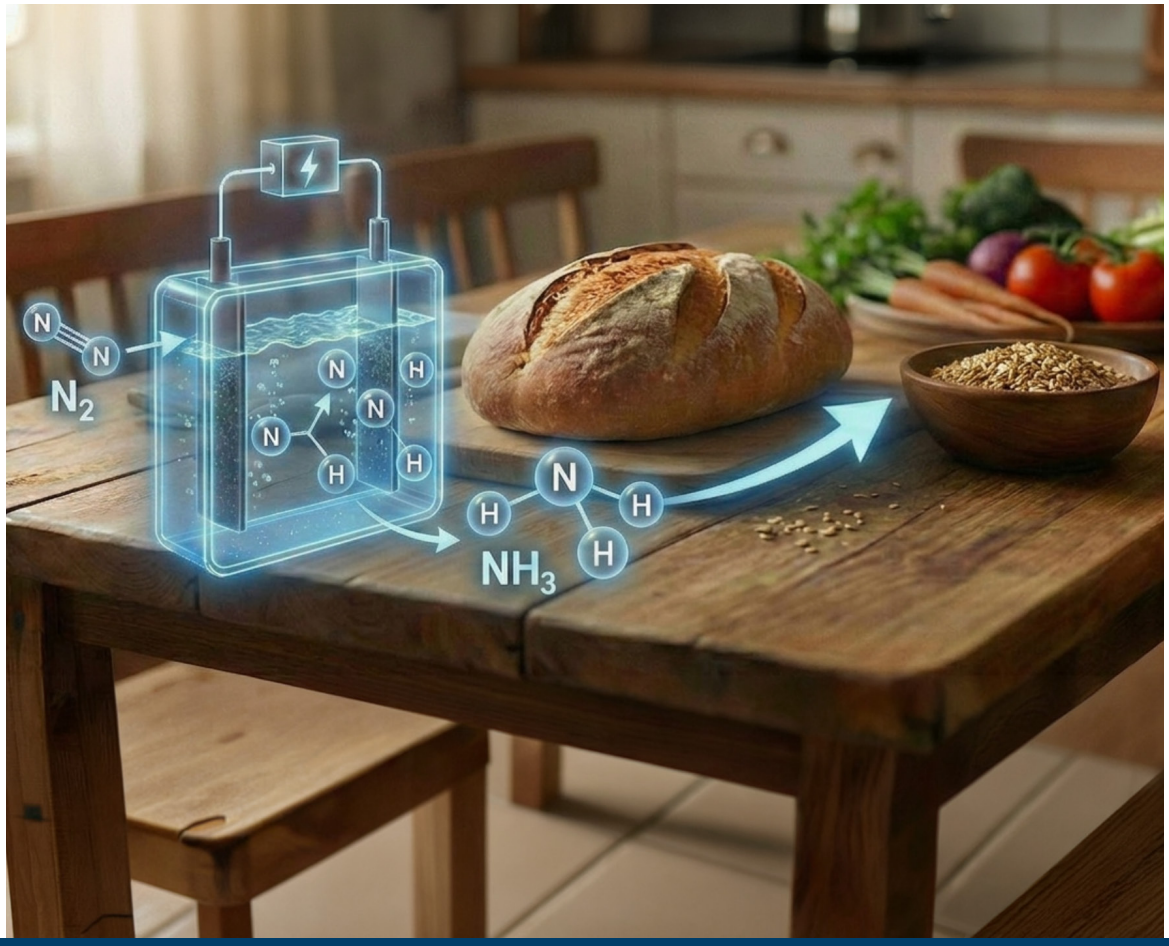


Characterization of Nitrogen Reduction Reaction Catalysts for the electrochemical Ammonia Synthesis

Dominik Sachse

Energie & Umwelt / Energy & Environment
Band / Volume 706
ISBN 978-3-95806-907-7

Mitglied der Helmholtz-Gemeinschaft

JÜLICH
Forschungszentrum

Characterization of Nitrogen Reduction Reaction Catalysts for the electrochemical Ammonia Synthesis

Von der Fakultät für Elektrotechnik und Informationstechnik der Rheinisch-Westfälischen Technischen Hochschule Aachen zur Erlangung des akademischen Grades eines Doktors der Naturwissenschaften genehmigte Dissertation

vorgelegt von

Dominik Sachse, M. Sc.

aus Rhede, Deutschland

Berichter: Univ.-Prof. Dr. rer. nat. Uwe Rau

Univ.-Prof. Dr.-Ing. Ralf Peters

Tag der mündlichen Prüfung: 06.02.2026

Diese Dissertation ist auf den Internetseiten der Universitätsbibliothek online verfügbar.

Forschungszentrum Jülich GmbH
Institute of Energy Technologies (IET)
Elektrochemische Verfahrenstechnik (IET-4)

Characterization of Nitrogen Reduction Reaction Catalysts for the electrochemical Ammonia Synthesis

Dominik Sachse

Schriften des Forschungszentrums Jülich
Reihe Energie & Umwelt / Energy & Environment Band / Volume 706

ISSN 1866-1793 ISBN 978-3-95806-907-7

Bibliografische Information der Deutschen Nationalbibliothek.
Die Deutsche Nationalbibliothek verzeichnet diese Publikation in der
Deutschen Nationalbibliografie; detaillierte Bibliografische Daten
sind im Internet über http://dnb.d-nb.de abrufbar.

Herausgeber und Vertrieb:	Forschungszentrum Jülich GmbH Zentralbibliothek, Verlag 52425 Jülich Tel.: +49 2461 61-5368 Fax: +49 2461 61-6103 zb-publikation@fz-juelich.de www.fz-juelich.de/zb
Umschlaggestaltung:	Grafische Medien, Forschungszentrum Jülich GmbH
Titelbild:	wurde mit KI generiert
Druck:	Grafische Medien, Forschungszentrum Jülich GmbH
Copyright:	Forschungszentrum Jülich 2026

Schriften des Forschungszentrums Jülich
Reihe Energie & Umwelt / Energy & Environment, Band / Volume 706

D 82 (Diss. RWTH Aachen University, 2026)

ISSN 1866-1793
ISBN 978-3-95806-907-7

Vollständig frei verfügbar über das Publikationsportal des Forschungszentrums Jülich (JuSER)
unter www.fz-juelich.de/zb/openaccess.



This is an Open Access publication distributed under the terms of the Creative Commons Attribution License 4.0,
which permits unrestricted use, distribution, and reproduction in any medium, provided the original work is properly cited.

Zusammenfassung

"Brot aus Luft". Mit diesem Leitmotiv wurde zu Beginn des 20. Jahrhunderts intensiv an der industriellen Herstellung von Ammoniak (NH_3) geforscht. Die Entwicklung des Haber-Bosch Verfahrens ermöglichte schließlich die industrielle NH_3 Produktion. Mit 170 Millionen Tonnen jährlich ist NH_3 eine der meist produzierten Chemikalien weltweit. Von diesen produzierten Mengen werden etwa 80 % als Düngemittel verwendet, um die Weltbevölkerung zu ernähren. Schätzungen zur Folge könnten nur zwei bis drei Milliarden Menschen ernährt werden, ohne Einsatz von Kunstdünger. Allerdings ist das Haber-Bosch Verfahren sehr energieintensiv. Von der global erzeugten Energie wird ca. 1 % für die Produktion von NH_3 verbraucht, wobei dies zu 1 - 2 % der jährlichen CO_2 Emissionen führt.
Aufgrund der ökologischen und klimatischen Bedeutung ist es daher von entscheidender Notwendigkeit, NH_3 und dessen Bestandteile Wasserstoff (H_2) und Stickstoff (N_2) aus regenerativen Energiequellen effizient zu gewinnen. Diese Arbeit zielt darauf ab, die kontinuierliche elektrochemische Ammoniaksynthese in einer elektrochemischen Membranelektrodeneinheit (MEA)-Zelle zu untersuchen.
Dazu wurde zunächst ein Teststand entwickelt und konstruiert. Das Verfahren zur Anreicherung von N_2 durch elektrochemische Sauerstoffreduktion wurde hinsichtlich der Zell- und Prozessparameter analysiert und optimiert. Der Restsauerstoffgehalt konnte auf unter 1 % gesenkt werden. Die elektrochemische Stickstoffreduktionsreaktion (eNRR) wurde mit einer Vielzahl vielversprechender Katalysatoren unter unterschiedlichen Zellkonfigurationen und Prozessbedingungen erforscht. Jedoch lagen die gemessen Produktionsraten im Fehlerbereich der spektroskopischen Nachweismethode. Deshalb ist unter den getesteten Bedingungen eine verlässliche Ammoniaksynthese nicht möglich. Unter Prozessbedingungen, die aufgrund von theoretischen Berechnungen keine Ammoniaksynthese aus N_2 erlauben, wurde NH_3 detektiert. Daraufhin erfolgte eine umfassende Untersuchung des Adsorptions- und Desoprtionsverhalten von NH_3 in der elektrochemischen Zelle. Besonders der Membran wurde detailliert untersucht. Es wurde festgestellt, dass geringe Mengen an NH_3 die Eigenschaften der Membran nicht beeinflussen. Dies hat zur Folge, dass die Synthese und deren Prozessbedingungen unerkannt bleiben. Die Desorption von NH_3 erfolgt bei Bedingungen, bei denen keine Synthese möglich ist. Abschließend wurde ein neuartiges elektrochemisches NH_3 Recyclingverfahren entwickelt und analysiert. Das Verfahren nutzt die Adsorptions und Desorptionseigenschaften der Membran in der Zelle, um NH_3 aus wässrigen Lösungen zu gewinnen. Mit dem Verfahren wird ein Prozess aufgezeigt, mit dem NH_3 aus Abwasser recycelt und wiederverwendet werden kann, wobei H_2 als Nebenprodukt entsteht.

Abstract

"Bread from Air". Was the guiding principle behind intensive research into the industrial production of ammonia (NH_3) at the beginning of the 20th century. The development of the Haber-Bosch process finally enabled the industrial production of NH_3. NH_3 with an annual production of 170 millions tons, is one of the most produced chemicals worldwide. Around 80 % of the produced NH_3 quantity is utilized as fertilizer to sustain the world population with food. According to estimates, only two to three billion people could be fed if there were no artificial fertilizers. However, the Haber-Bosch process is highly energy-intensive. Approximately 1 % of the globally generated energy is consumed for ammonia production, contributing to 1 - 2 % of annual CO_2 emissions.

Due to the ecological and climatic significance, it is imperative to gain NH_3 and its components, hydrogen (H_2) and nitrogen (N_2), efficiently from renewable energy sources. The objective of the present thesis is the continuous electrochemical synthesis of ammonia in an electrochemical membrane electrode assembly (MEA) cell and its in-depth analysis.

A test-rig was developed and constructed for the experiments. The process of electrochemical oxygen (O_2) depletion and N_2 enrichment by an oxygen-depolarized cathode was analyzed and optimized with regard to the cell and process parameters. The residual oxygen content could be reduced to less than 1 %. The electrochemical nitrogen reduction reaction (eNRR) was explored and characterized using a variety of promising catalysts under different cell configurations and process conditions. Nevertheless, the measured production rates were within the error range of the spectroscopic detection method. Therefore, it is not possible to synthesize NH_3 under the tested conditions. NH_3 was detected under process conditions that, based on theoretical calculations, do not allow NH_3 synthesis from N_2. Subsequently, a comprehensive examination of the adsorption and desorption behavior NH_3 in the electrochemical cell was conducted. Especially the membrane was examined in detail. It was found that small amounts of NH_3 do not affect the properties of the membrane. As a result, the synthesis and its process conditions remain unknown. The desorption of NH_3 from the cell occurred under conditions where synthesis is not possible. Finally an novel electrochemical NH_3 recycling process was developed and analyzed. This process utilizes the adsorption and desorption properties of the membrane in order to recycle NH_3 from aqueous solutions. This process demonstrates a method for recycling and reusing NH_3 from wastewater, while producing H_2 as a by-product.

Contents

1 Introduction **1**

1.1 The essential Importance of Ammonia 1
1.2 Objective and Tasks of the Work 5
1.3 Ammonia Synthesis Pathways 7
1.3.1 Haber-Bosch Process 7
1.3.2 Alternative Ammonia Synthesis Routes 10
1.4 Electrochemical Ammonia Synthesis Systems 13
1.4.1 Liquid Electrolytes 14
1.4.2 Molten Salts 16
1.4.3 Composite Membranes 16
1.4.4 Solid State Electrolytes 17

2 Electrochemical Ammonia Synthesis based on Aqueous Electrolytes **21**

2.1 Introduction 21
2.2 Challenges and Strategies 22
2.3 Reaction Mechanism of the Ammonia Synthesis 23
2.4 Catalyst Choice and Development 26
2.5 Electrochemical Reactor Design 31
2.6 Electrodes 32
2.7 Electrolytes 33
2.8 Ammonia Detection Methods 34
2.9 Contaminations in Electrochemical Ammonia Synthesis 35
2.9.1 Sources of Contaminations 35
2.9.2 State of the Art Elimination of Contaminations 37
2.9.3 Synthesis Protocol 38

3 Methods **39**

3.1 Test Benches 39
3.1.1 Construction 39
3.1.2 Measurement Accuracy 42
3.2 Electrochemical Cell 43

3.3 Ammonia Detection Methods . . . 45
3.3.1 Infrared Spectroscopy . . . 45
3.3.2 Indophenol Blue Method . . . 46
3.3.3 Determination of Ammonia . . . 51
3.4 Catalyst and Electrode Production Processes . . . 52
3.4.1 Decal Process . . . 52
3.4.2 Spray Coating . . . 52
3.4.3 Galvanic Displacement Deposition . . . 53
3.5 Electrochemical Measurement Methods . . . 55
3.5.1 Overpotential . . . 55
3.5.2 Electrochemical Impedance Spectroscopy . . . 58

4 Thermodynamic Evaluation of Ammonia Synthesis Processes 61
4.1 Introduction . . . 61
4.1.1 Thermodynamic Values . . . 62
4.2 Haber-Bosch Process . . . 64
4.3 Electrified Haber-Bosch Process . . . 69
4.4 Li mediated Synthesis . . . 71
4.5 Direct Electrochemical Ammonia Synthesis . . . 72
4.5.1 pH Dependency . . . 74
4.6 Summary and Conclusion . . . 76

5 Eletrochemical Reactants Synthesis 79
5.1 Introduction . . . 79
5.2 Water Electrolysis . . . 79
5.3 Oxygen Depletion . . . 83
5.3.1 Introduction . . . 83
5.3.2 Oxygen Separation Techniques . . . 83
5.3.3 Experimental . . . 88
5.3.4 Results and Discussion . . . 90
5.3.5 Summary and Conclusion . . . 107

6 Ammonia Synthesis 109
6.1 Introduction . . . 109
6.2 Gold Nanoparticle Catalyst . . . 113
6.2.1 Experimental . . . 113
6.2.2 Results and Discussion . . . 115
6.3 High Entropy Alloys . . . 128
6.3.1 Experimental . . . 128
6.3.2 Results and Discussion . . . 130

6.4 Summary and Conclusion 133

7 Ammonia Adsorption and Desorption of the Membrane 135
7.1 Introduction 135
7.2 Ion exchange 136
7.2.1 Experimental 136
7.2.2 Results and Discussion 139
7.3 Discharge of the electrochemical Cell 144
7.3.1 Experimental 144
7.3.2 Results and Discussion 147
7.4 Summary and Conclusion 161

8 Ammonia Recycling 163
8.1 Introduction 163
8.2 Experimental 165
8.3 Results and Discussion 170
8.3.1 Catalyst on PTL 170
8.3.2 Catalyst on Membrane 182
8.4 Summary and Conclusion 190

9 Conclusion & Outlook 191
9.1 Summary and Conclusion 191
9.2 Outlook and Future Perspectives 193

Bibliography 195

List of Figures 215

List of Tables 227

Glossary 229

Symbols 231

List of Publication 233

Curriculum Vitae 234

A Tested Catalyst 1

B Impedance Spectra and Fits 3

Danksagung

Für die Unterstützung und die Hilfestellung zum Erstellen dieser Arbeit möchte ich mich ganz herzlich bei allen Unterstützern bedanken.

Ich möchte mich bei meinem Doktorvater Prof. Uwe Rau herzlich bedanken, dass Sie mich nach dem Ausscheiden von Prof. Lehnert als Doktorand übernommen und betreut haben.

Bei Prof. Ralf Peters für die Betreuung am IEK-14 und die anregenden Diskussionen.

Ein ganz besonderer Dank gilt Dr. Andreas Glüsen, für die hervorragende fachliche Betreuung der Arbeit, für den stetigen Austausch. Ohne die Diskussionen mit Dir, wären viele Ideen und die anschließende Erkenntnisse nicht möglich gewesen.

Dr. Martin Müller und Prof. Lehnert, Danke ich dafür, dass Sie mir die Promotion am IEK-14 und diesem spannenden Thema ermöglicht haben.

Bei Dr. Klaus Wippermann für das Wissen und die Hilfe zur Impedanzspektroskopie, von der ich sehr profitiert habe. Einen besonderer Dank gilt Norbert Commerscheidt für die vielen technischen und innovativen Realisierungen im Labor. Dr. Florian Seidler, für den elektrischen Aufbau der Teststände und von Deinem Wissen, von dem ich sehr profitieren durfte. Denise Günther danke ich für die Hilfe und Unterstützung im Labor. Ebenfalls möchte ich mich bei Walter , Daniel Holtz, Sina und Andreas Everwand für Ihre Arbeit bedanken für Ihre Arbeit.

Ich möchte mich herzlich bei meinen Bürokollegen Dr. Eugen Hoppe und Sarah Zerressen für die Zeit und die tolle Atmosphäre bedanken. Johannes Häusler, Dir danke ich für den fachlichen und persönlichen Gespräche während der Promotion. Auch bei den anderen Doktoranden und Mitgliedern des "Kuchen Dienstags" möchte ich mich für die tolle Gemeinschaft und die Zeit bedanken.

Meinen Masteranden Marquise Akame und Basil Chelachottil Danke ich für ihre Arbeit.

Abschließend möchte ich mich aus ganzem Herzen bei meinen Eltern Dirk und Hildegard und meiner Schwester Annika bedanken, für den Rückhalt, die Unterstützung, das Aufbauen besonders in den schwierigen Zeiten. Ich kann nicht glücklicher sein, solch eine Familie wie Euch zu haben.

1 Introduction

1.1 The essential Importance of Ammonia

Ammonia (NH_3) is with more than 170 million tons produced annually one of the most widely produced chemical in the world [1, 2]. The market value is approximately 70 billion US $ [3]. Ammonia is the source of any other nitrogen compounds in further synthetic processes. Hydrazine (N_2H_4), hydrocyanic acid (HCN), aniline ($C_6H_5N_2$), nitric acid (HNO_3) and urea (CH_4N_2O) are mentioned as examples [4, 5]. NH_3 and and the obtained nitrogen compounds play a crucial role in the agricultural, dyes, pharmaceutical and textile industries. Fig. 1.1 illustrates different compounds, which are produced from NH_3 and their field of application. More than 80 % of the produced NH_3 are used for fertilizer production [6]. Without the industrial production of NH_3 the present world population would not exist and could not be fed [7, 8]. However, the conventional production method, known as the Haber-Bosch process, is extremely energy-intensive. About 1 % of the global energy is consumed [9] and the process is responsible for 1 - 2 % of annual CO_2 emissions [10–12]. For each ton of NH_3 produced approximately 2 t of CO_2 are produced [13].

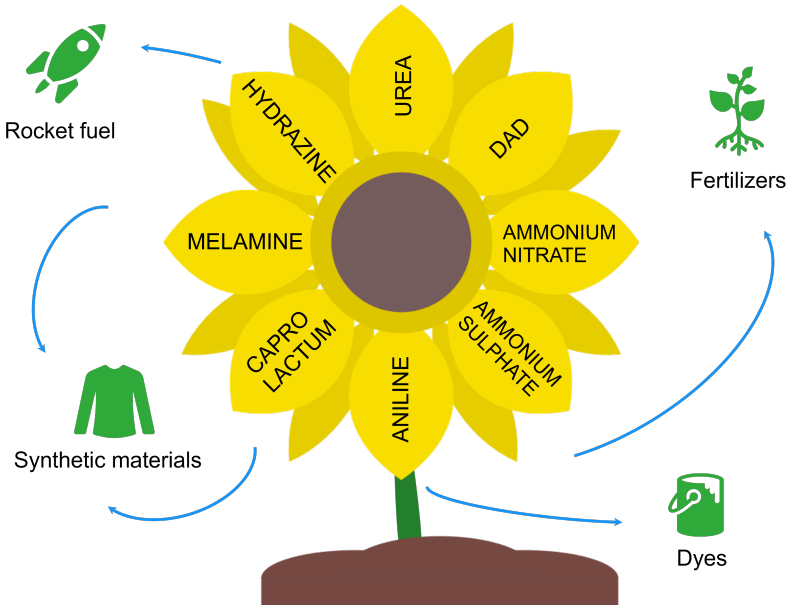


Fig. 1.1. Schematic illustration of nitrogen compounds synthesized from NH_3 and their respective field of application involving, fertilizers, rocket fuel, dyes and synthetic materials.

At the same time to the above mentioned factors, NH_3 gains more and more attention of the energy industry, as energy carrier. The energy density of liquid NH_3 is 15.6 MJ L^{-1}. The energy density is 70 % higher than the energy density of liquid hydrogen (H_2) 9.1 MJ L^{-1} at cryogenic temperature and almost three times higher compared to compressed H_2 5.6 MJ L^{-1} at 70 MPa [14]. The weight fraction of the H_2 content in NH_3 is high with 17.8 wt%. Due to this it can be used as carbon neutral energy carrier [15]. In addition NH_3 can be used as a fuel in a direct ammonia fuel cell or indirect in a hydrogen fuel cell [16]. Indirect means that the NH_3 is converted into H_2 and the H_2 is burned as a fuel. Thus, it can be utilized as fuel in gas turbines or generators [4], too. The resulting byproducts are N_2 and water (H_2O).

An additional merit associated with NH_3 in comparison to H_2 lies in its facilitation of transportation and storage. NH_3 can be liquefied and transported at moderate conditions of 20 °C and an excess pressure of 8.6 bar [4]. Fig. illustrates the conventional and new field of NH_3 application. As previously outlined, NH_3 is used as a energy carrier, with ease of transport in this form and it can be used as fuel, for power generation and heat production.

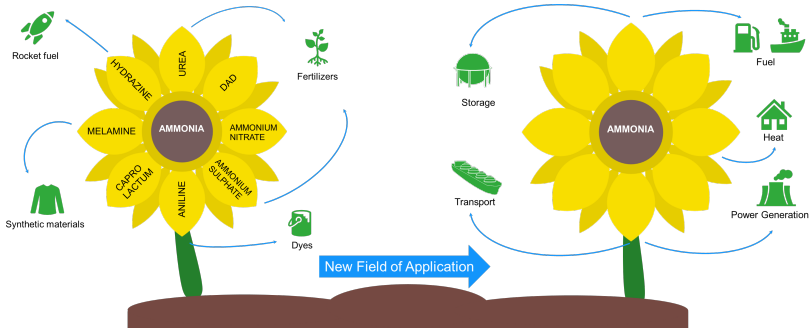


Fig. 1.2. Schematic illustration of the conventional and new NH_3 field of application.

The advantage of energy transportation in form of NH_3 in comparison to liquid H_2, and compressed H_2 at 350 bar is underscored in Fig. 1.3. This corresponds to the pressure of 35 MPa in Fig. 1.3. The cost of transportation for 1 t of the product and a distance of 1 km for the transport facilities cargo ships, railway and road trailers are the cheapest in case of NH_3 transportation as displayed in Fig. 1.3 [17]. The transport of compressed H_2 leads to the highest cost for all transport facilities. Transportation by cargo ships is the cheapest and the transport by road trailers the most expensive. The cost-effectiveness of NH_3 transportation presents a compelling prospect for the electrochemical conversion of H_2 generated via water electrolysis into NH_3. Followed by the transport as NH_3. Upon reaching the point of utilization, NH_3 can be electrochemically converted back into H_2.

The above mentioned reasons of the growing world population, thus the need for increasing fertilizer production, as well as the possibilities of NH_3 in the energy sector lead to the fact that the demand for NH_3 will sharply increase. Therefore and with respect to climate change, it is necessary to develop environmentally beneficial NH_3 synthesis routes. In consequence it will lead to a reduced energy consumption and carbon dioxide (CO_2) pollution.

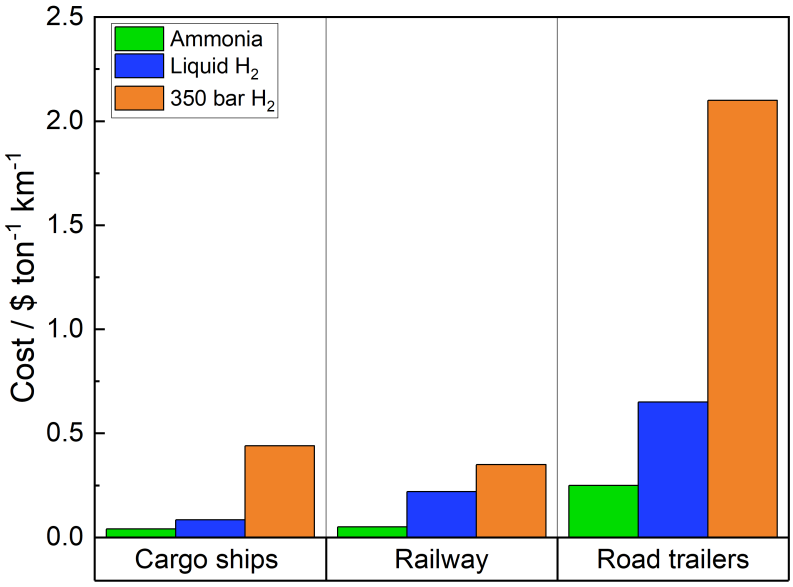


Fig. 1.3. Transportation cost of the energy carriers NH_3, liquid H_2, and compressed H_2 for a distance of 1 km and a weight of 1 t. The different transportation possibilities cargo ships, railway, road trailers are compared. Adapted and based on [18]. Found in [17].

1.2 Objective and Tasks of the Work

As outlined in the previous section, the demand for NH_3 is enormous and will grow strongly due to additional areas of applications. Due to climate change and the need for reducing CO_2 emissions, more environmentally friendly and energy-efficient processes for NH_3 synthesis must be developed and established. These technologies should replace the Haber-Bosch process. Various processes for NH_3 synthesis are currently under development. Electrochemical NH_3 synthesis is a promising process for synthesising NH_3 utilizing electrocatalysis. If the electricity is generated from renewable sources, the synthesis is completely climate-neutral. This thesis analyses and optimises the system and components from the synthesis of the reactants to the synthesis of NH_3. With the aim of production NH_3 electrochemically. The following structure and fields of work are derived from this.

- The different NH_3 synthesis pathways, Haber-Bosch, biological, photocatalysis and electrocatalysis are presented in the introduction. In particular, the various electrochemical systens are presented and explained.
- Subsequent the reaction mechanism, catalyst, cell components, reactors as well as the contaminations in the electrochemical NH_3 synthesis based on aqueous electrolyte are described and discussed in more detail.
- In the following chapter the test-rig, which was designed and constructed to carry out the experiments is described. The chapter elucidates the electrochemical cell and its constituent elements devised for the NH_3 synthesis. It delineates the employed detection methods and expounds upon the synthesis of catalysts. Finally, electrochemical principles are explained, which are important for understanding the work.
- In chapter 4 thermodynamic evaluations of NH_3 synthesis processes are carried out. The energetic efficiency of these different NH_3 production pathways are calculated and their pros and cons are discussed and compared. Moreover, a Pourbaix-diagram is created, which illustrates the impact of the pH on the thermodynamic of the NH_3 synthesis. From this diagram inferential insights are derived.
- Chapter 5 deals with reactant synthesis. Although water electrolysis is not part of this research work, the principle and processes are briefly presented. It then examines how N_2 can be electrochemically enriched from air and how the O_2 content can be reduced. Various parameters are studied and their influences are then evaluated and assessed regarding O_2 depletion.

- Chapter 6 exhibits the achieved electrochemically NH_3 synthesis results, which are gained utilizing the different catalysts under the influence of different cell and process parameters. The achieved results are placed in relation to literature. Additionally, the detection limits of the employed analytical methods are discussed in relation to the observed NH_3 production rates, enabling the determination of the minimum production rate required for reliable electrochemical NH_3 synthesis. An overview of other catalysts and process conditions investigated during this thesis can be found in the appendix.

- The adsorption, desorption behavior and the transport process of NH_3 in the membrane, which strongly influences the properties of NH_3 synthesis are analyzed in chapter 7. The detected discharge rates are set in relation to the detection limit of the used detection method, to underscore the reliability of these measured rates. With these obtained insights of this interaction the understanding is expended, aiming to the attainment of reliable and reproducible electrochemical NH_3 production.

- Chapter 8 explores the feasibility of electrochemical recycling of NH_3 from NH_4^+ containing solutions. The idea is to apply this methodology in agriculture, such as extracting NH_3 from liquid manure for subsequent reuse as fertilizer. For this purpose, a novel electrochemical recycling process has been devised that is markedly better scalable than the conventional processed described in the literature and also enables the production of H_2 as byproduct. In this respect diverse process parameters are investigated. The rates attained through this process significantly exceed the documented rates in literature.

1.3 Ammonia Synthesis Pathways

1.3.1 Haber-Bosch Process

The Haber-Bosch process is named after the the chemists Fritz Haber and Carl Bosch. In 1904 Fritz Haber started the first experimental investigations concerning the equilibrium between N_2, H_2 and NH_3 [19]. The proportion of NH_3

$$3\,H_2(g) + N_2(g) \rightleftharpoons 2\,NH_3(g) \tag{1.1}$$

at equilibrium state is less than 1 %. On the 2nd July 1909 Haber succeed to synthesizes NH_3 in his laboratory for the first time. The major difficulty was that the conversion rates at low temperatures (about 100 °C) were very low. However, due to the thermodynamics of this reaction, an increase in temperature leads to a shift in the equilibrium to the reactant side. Therefore, with regard to Le Chatelier's principle, the pressure was increased to shift the thermodynamic equilibrium towards the products. To protect the steel of the pressure pipe from embrittlement the inside of the tube was lined with a carbon-free iron (Fe) tube [19]. On September 19th 1913, the NH_3 synthesis was carried out on an industrial scale for the first time in the in Oppau near Ludwigshafen at BASF [7, 19].
In 1918 Fritz Haber was honored with Noble price in chemistry for the development of synthetic ammonia production. Carl Bosch was honored also with the Noble price in chemistry for the industrial scale up in 1931 [8].

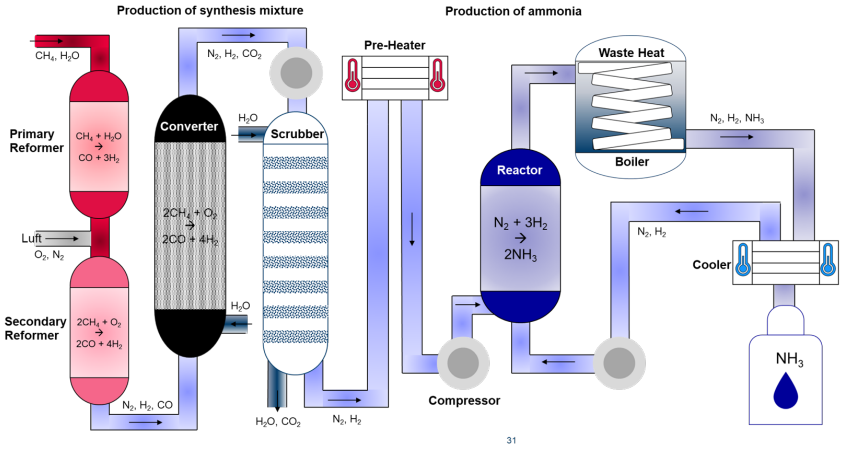


Fig. 1.4. Illustration of the process steps of the Haber-Bosch process, the industrial synthetic NH_3 production. Starting with the production of the synthesis mixture until the production of NH_3 in the blue reactor.

The Haber-Bosch process with the resulting process steps is shown in Fig. 1.4. Depending on the source of H_2 (water electrolysis, coal, natural gas), the energy input of the NH_3 is strongly influenced. This thermodynamic consideration will be carried out in chapter 4. At present, natural gas is mainly used as the primary source for H_2 production. Depending on the origin of the natural gas, it contains impurities like hydrogen sulfide (H_2S) or organic sulphur compounds. These impurities act as catalyst poison. Therefore, they have to be removed [20].

At first the natural gas, containing methane (CH_4) and water steam are introduced into the primary reformer. The gas mixture is converted by means of steam reforming

$$CH_4 + H_2O \longrightarrow CO + 3\,H_2 \tag{1.2}$$

using nickel catalyst [21]. In the second process step compressed air (N_2, O_2) is introduced. In the secondary reformer the remaining CH_4 is converted with oxygen (O_2)

$$2\,CH_4 + O_2 \longrightarrow 2\,CO + 4\,H_2O \tag{1.3}$$

into H_2 and carbon monoxide (CO). Subsequently carbon needs to be removed. Therefore, CO is catalytically converted to CO_2 with water vapor

$$CO + H_2O \rightleftharpoons CO_2 + H_2 \tag{1.4}$$

by using iron oxide and chrome oxide catalyst [21]. CO_2 is removed with a CO_2-scrubber. The CO_2 is recovered and can be used for urea production. Traces of CO and CO_2,

$$CO + 3\,H_2 \rightleftharpoons CH_4 + H_2O \tag{1.5}$$

$$CO_2 + 4\,H_2 \rightleftharpoons CH_4 + 2\,H_2 \tag{1.6}$$

which are still in the synthetic gas are removed by means of methanation [21]. This gained CH_4 can be introduced then into the steam reformer, producing H_2 (Eq. 1.2). The gas mixture is compressed to the required operating pressure 150 - 300 bar [8, 22] utilizing turbo compressors. The main component of the catalyst is α-Fe. The starting material of the catalyst is a mixture of magnetite (Fe_3O_4) and promoters. Promoters (for example Al_2O_3) are substances that have an activating effect and increase the life time of the catalyst [21]. The resulting compression heat is dissipated with heat exchangers. The heat is used to preheat raw gases. The reaction products are continuously removed for maximum yield. In dependency of the reaction conditions a conversion up to 20 % is possible. The gas mixture is cooled down from 450 °C and hence the produced NH_3 condenses. Unreacted N_2 and H_2 are reintroduced into the reactor and added into the fresh gas stream (Eq. 1.1) [21].

1.3.2 Alternative Ammonia Synthesis Routes

Due to the energy-intensive and strongly CO_2 emitting Haber-Bosch process, it is important to execute the NH_3 synthesis more efficient, sustainable, environmental friendly and less CO_2 emitting [11]. Especially the decentralisation of the NH_3 production plays an important role in the present time. Based on these reasons, three NH_3 synthesis strategies biocatalysis, photocatalysis and electrocatalysis have attracted increasing research interest in recent years [11].

Biological N_2 Fixation

Only microorganisms which contains the enzyme nitrogenases are able to fixate N_2 and convert atmospheric N_2 into NH_3 under atmospheric conditions [23, 24]. The enzyme consists of two compounds. The enzymes are distinguished by their metal-centred cofactors (the cofactor is necessary for the catalytic activity of the enzyme), which are molybdenum-iron protein (FeMo), iron-iron and vanadium-iron (VFe). FeMo is the most active and abundant enzyme to reduce N_2 [25]. The Fe protein delivers the necessary electrons to the second protein, FeMo protein. This proteins binds N_2 and convert it into NH_3 [23, 26]. The nitrogenase is susceptible to deactivation by O_2 [27]. Another major shortcoming of the biological process is the large-scale application. As a result of the low conversion rate, the complexity of the reaction and the stability of the catalyst, the realization of a large-scale application is challenging [28].

Photocatalysis

The photocatalytic nitrogen reduction reaction (NRR) under atmospheric conditions have been intensively studied in recent years [29]. The first experiments of N_2 photo reducution by means of water splitting were published by Schrauzer and Guth in 1977 [30].

In general, photocatalysis can be divided into two types of photoconversion. The types are the photochemical cell and the photoelectrochemical cell. In the following, each mode of operation will be briefly explained. In the photochemical cell system, semiconductor nanoparticles are placed in an aqueous solution saturated with N_2 (Fig. 1.5a). In this system, photoreduction and photooxidation occur simultaneously on one side of the same nanoparticle. Unfortunately, this can lead to a back reaction or reoxidation of the product [29]. In Fig. 1.5b, there are four different types of photoelectrochemical cells. The types are a photoanode coupled with a metal counter (i), a photocathode with a metal counter electrode (ii), a photoanode connected with a photocathode (iii) and a photoanode directly connected with the photocathode in a back-to-back configuration (iv).

The photoelectrodes collect light to generate photoinduced electrons and holes and it favors the separation of the charge carriers. On the surface of the photocathode the NRR occurs and the corresponding oxidation reaction takes place on the surface of the counter electrode. It is proposed that the overall process of photo-driven NRR involves three essential steps in the photochemical and photoelectrochemical cell systems [29, 31]. First, the electrons and holes are generated in the valence band and conduction band of the semiconductor nanoparticles. The next step is the charge separation and migration of the photoinduced charge carriers. Subsequently, electrons flow, so that on the cathode side N_2 reacts to NH_3. At the same time H_2O is oxidized using the holes on the cathode side [29]. The disadvantage of this method is the high negative potential of at least $-3.2\,V$ vs. NHE (normal hyodrogen electrode), which is a problem for conventional semiconductors [32]. In most experiments TiO_2 is used as semiconductor material. It is modified by hetero atom dopin [33, 34] or by surface plasmon modification [35]. However, the NH_3 production rates are still very low under this mild conditions. Thus, the key task is to develop special nano catalysts based on semiconductors with high efficiency and stability to run the photocatalytic synthesis [29].

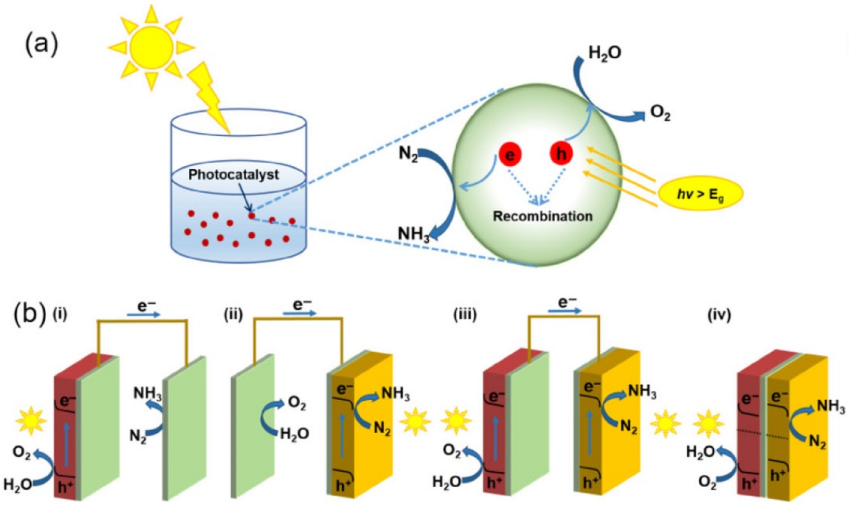


Fig. 1.5. Illustration of photo-driven ammonia production systems, (a) the photochemical system is based on semiconductor nanoparticle catalysts dispersed in aqueous solution, (b) different types of photoelectrochemical nitrogen fixation systems. Adapted with permission from [29], Springer Nature.

Electrochemical NH_3 Synthesis

The electrochemical nitrogen redcution reaction (eNRR) is considered to be a promising, environmentally friendly method to convert nitrogen into ammonia at mild conditions (below 100 °C) by adsorption, activation and desorption processes [36]. The production can be CO_2 neutral if renewable energy is utilized as energy supply and air and water as reactants.

In general the synthesis is carried out in three main reaction steps. Initially N_2 must reach the catalyst surface for activating the nitrogen molecule. Several intermediates occur through the protons (H^+) and electrons (e^-) transfers. In the end NH_3 desorbs from the surface of the catalyst [36]. The individual reaction mechanisms and the thermodynamic evaluation are discussed in chapter 4. It can be stated that the electrochemical NH_3 synthesis benefits from 20 % higher energy efficiency than the Haber-Bosch process [37]. The modularity and scalability are further advantages of electrochemical systems, such as water electrolysis. This knowledge can be applied to the NH_3 production [37].

Compared to photocatalysis, electrocatalysis has the advantage that this process is more tunable and scalable [38]. Nevertheless, production rates are still very low.

1.4 Electrochemical Ammonia Synthesis Systems

The electrolysis offers the advantage for decentralization as noted previously. Therefore the production of fertilizers would be possible everywhere in the world in a small scale. This in turn has the effect of eliminating the transportation and storage of NH_3 because it is consumed where it is produced [39].
For the evaluation of the electrochemical ammonia synthesis two parameters are mostly used in literature. The NH_3 production rate is considered either regarding time and active catalyst surface area or regarding time and used catalyst mass. The second parameter is the Faraday efficiency (FE). The FE indicates what percentage of the supplied electrical charge is actually used for the desired electrochemical reaction. The NH_3 synthesis can be distinguish in four different synthesis systems. These systems are categorized concerning their electrolytes and operation parameters [40]. The systems are presented in Fig. 1.6 and a brief explanation of the systems and the literary results are the subject of the following section.

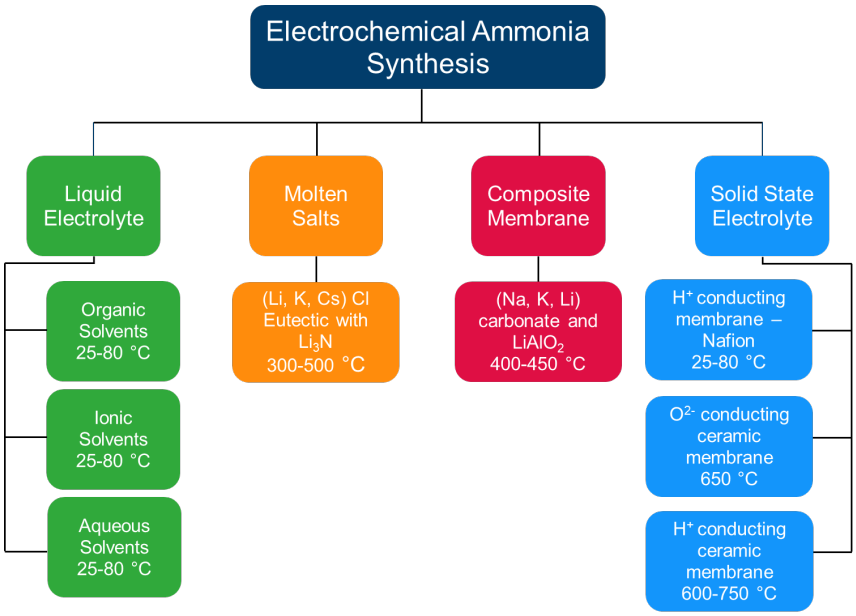


Fig. 1.6. Different electrochemical NH_3 synthesis systems with respect to different electrolytes and temperature ranges. Adapted with permission from [40], Elsevier.

1.4.1 Liquid Electrolytes

N_2 reduction based on liquid electrolytes is done at low temperature (25 - 80 °C. Liquid electrolytes include aqueous solvents, organic solvents, and ionic solvents [41, 42]. These liquids are characterized by their liquid ionic conducting phase. It is important that N_2 dissolves in the electrolyte to maximize the adsorption of N_2 on the catalyst. For this reason, much research is being done on electrolytes, which have high nitrogen solubility capacity. Ionic liquids offer the possibility of excellent non-aqueous electrolytes due to their hydrophobic property. This characteristic facilitates the regulation of the H_2O content. As a consequence it enables the promotion of NH_3 synthesis and the suppression of H_2 production [41, 43]. The solubility of N_2 in ionic liquids is 20 times greater than in aqueous solutions [44]. With roughly 0.000 61 M (M is defined as mol/L) at 25 °C and 1 bar is the solubility of N_2 in H_2O extremely low. In the work of Kim et al. [45], 2-propanol was used as an electrolyte. Its N_2 solubility is more than 30 times higher than the solubility of N_2 in H_2O. Furthermore, 2-propanol suppressed the H_2 formation better than water [45].

Lithium mediated NH_3 synthesis belongs to the liquid electrolytes methods as well. Li binds N_2 strongly and the dissociation barrier is low [46]. In the beginning, the FE of the Li mediated synthesis was 5 to 20 %. In the work of Suryanto et al [47], they reached a FE up to 69 % and a NH_3 production rate of 53 nmol cm^{-2} s^{-1} under a N_2 pressure of 20 bar [10, 47]. Li et al. [48] were able to increase the FE to 78 % by adding 0.6 to 0.8 mol% O_2 at 20 bar N_2. It was assumed that the solid electrolyte interface was modified by the addition of O_2.

The Li mediated electrocatalysis is shown in Fig. 1.7. Initially, the lithium ions are dissociated in the electrolyte. Metallic Lithium is deposited on the electrode under a reduction potential of −3.04 V. The metallic Li dissociates N_2 to produce lithium nitride Li_3N. Finally, after transfer processes of protons and electrons between Li_3N and a proton source NH_3 is produced [49]. However, currently the process is not fully understood. Until now, the most common lithium salt is a combination of lithium perchlorate $LiClO_4$ and lithium tetrafluoroborate $LiBF_4$ solved in ethanol, which is the proton donor and shuttle [50]. H_2 can be used as proton source as well and it would avoid the decomposition of the electrolyte [51]. Though, H_2 oxidation rate in non-aqueous solvents at flooded electrodes is limited by the solubility of H_2 [52] and the solubility is too low for practical application [53].

The solid electrolyte interface (SEI) is formed from the decomposition products of an organic electrolyte during Li depositon on the cathode. The SEI is ion conducting but not electronically conductive [10] and it improves the stability of the system by avoiding excess electrolyte decomposition and lithium dendrite formation [48].

The major drawback of the lithium mediated method is the required large negative potential of −3.04 V vs. SHE (standard hydrogen electrode) [10]. This corresponds to more than 3 V overpotential and results in a low energy efficiency [54]. In addition this strongly reducing potential leads to electrode degradation and instability over time [55]. The thermodynamic properties of electrochemical nitrogen reduction reaction (eNRR) via a Lithium mediated system are discussed in chapter 4.

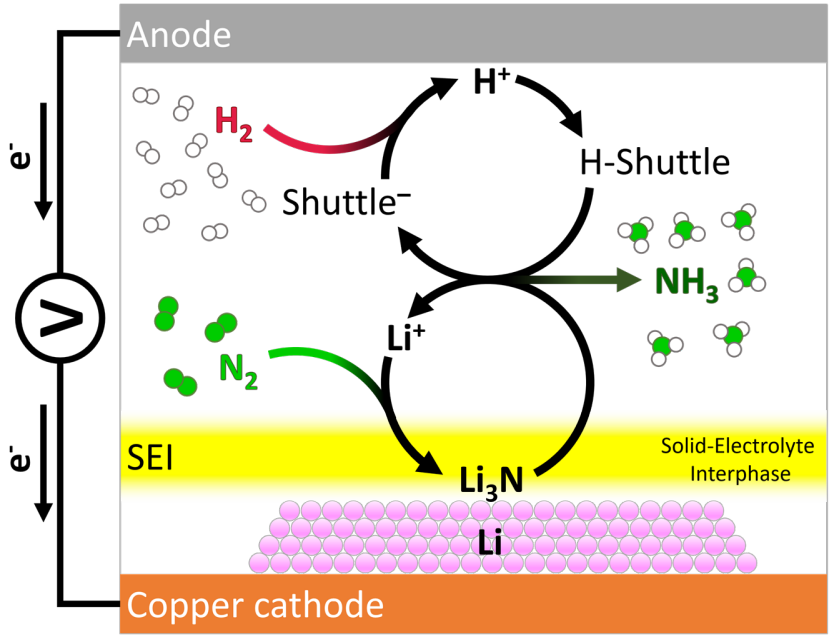


Fig. 1.7. Illustration of the necessary steps of the Li mediated eNRR. Li^+ are dissociated in the electrolyte. Under an electrical potential Li is deposited. Li dissociates N_2 to produce Li_3N. Under supply of a H^+-source and e^--transport NH_3 is formed. Own illustration based on the illustration of [47].

1.4.2 Molten Salts

Electrolysis cells based on liquid salts for electrochemical NH_3 synthesis operate at temperatures between 300 and 500 °C [40]. Liquid salt cells are based on two systems, alkali metal chloride cells and liquid hydroxide salts. Murakami et al. [56] used a eutectic of LiCl, KCl, and CsCl as the electrolyte and 0.5 mol% Li_3N, which served as the source for of nitride (N^{3-}), was dissolved in this electrolyte. Using porous nickel as working and counter electrodes the supplied N_2 was reduced to N^{3-} at the cathode. N^{3-} was reduced to NH_3

$$NH^{3-} + H_2 \rightleftharpoons NH_3 + 3\,e^- \tag{1.7}$$

caused by the supply of H_2 at the anode. A production rate of $3.33\times10^{-9}\,mol\,cm^{-2}\,s^{-1}$ with a FE of 72 % was achieved [56]. Electroreducution of N_2 compounds and ionic forms like N^{3-} are thermodynamically and kinetically more favourable pathways of NH_3 production than NRR from molecular N_2 [57]. But, it needs to be considered that NH_3 is unstable at high operating temperatures [58].

1.4.3 Composite Membranes

Composite electrolytes, as the name implies, consist of a composite of several ionic conductive phases. By adding a second or third ionic phase to the parent phase, the electrical, thermal or mechanical property can be modified [40]. Wang et al. [59] were the first to synthesis NH_3 electrochemically using compound electrolytes. They used an yttrium doped cerium oxide (YDC)-$Ca_3(PO_4)_2$-K_3PO_4 with two Ag-Pd electrodes. Natural gas was fed as reactant at the anode and N_2 at the cathode. The process ran at atmospheric pressure and a temperature of 650 °C. Applying a potential of 1 V, a maximum production rate of $7\times10^{-9}\,mol\,cm^{-2}\,s^{-1}$ was obtained [59]. Amar et al. [60] studied different oxide-carbonates compounds materials to generat NH_3. They achieved an ammonia production rate of $5.39\times10^{-9}\,mol\,cm^{-2}\,s^{-1}$ at 0.8 V and 450 °C. They mentioned that the synthesis rate of NH_3 increases with a temperature increase from 400 to 450 °C due to the enhanced proton conductivity of the composite electrolyte. However, a further temperature increase leads to NH_3 decomposition [60].

1.4.4 Solid State Electrolytes

Depending on the material and material structure solid state electrolytes can be applied in a wide temperature range from 25 to 750 °C. Either ceramics or polymers are used as solid electrolytes.

Polymer Electrolytes

There are several types of polymeric ion exchange membranes that can be used as electrolytes for electrochemical ammonia synthesis, fuel cells, or water electrolysis. The best known ion conducting membrane is Nafion® from Chemours™. Nafion is a perfluorinated membrane and the ionic sulfonic group (R-SO_2-OH) (Fig. 1.8) enables ion conductivity. The sulphit ions are firmly incorporated into the chemical structure of Nafion. The attached H^+ ensure charge neutrality in the membrane. The mobility of these protons is pivotal in facilitating ionic conductivity. The protons can be exchanged with other cations within the membrane. The microstructure of Nafion is schematically illustrated in Fig. **??**. Furthermore, there are polyetheretherketone (PEEK) and polybenzimidazoles (PBI), which are also proton conducting [40]. Anion conducting (OH^-) membranes are still under development and so far cannot match the ionic conductivity and stability of Nafion.
Kordali et al. [61] were the first, who demonstrated electrochemical ammonia synthesis at temperatures below 100 °C and atmospheric pressure. The cell consisted of a Nafion membrane, ruthenium-coated (Ru) carbon flux served as the cathode, and platinum (Pt) served as the anode catalyst. A potassium hydroxide solution (KOH) was used as the electrolyte. The maximum ammonia production rate was $2.12 \times 10^{-11}\,\mathrm{mol\,cm^{-2}\,s^{-1}}$ at a cathode potential of 0.81 V and 90 °C. The FE was extremely low at 0.24 % [61].

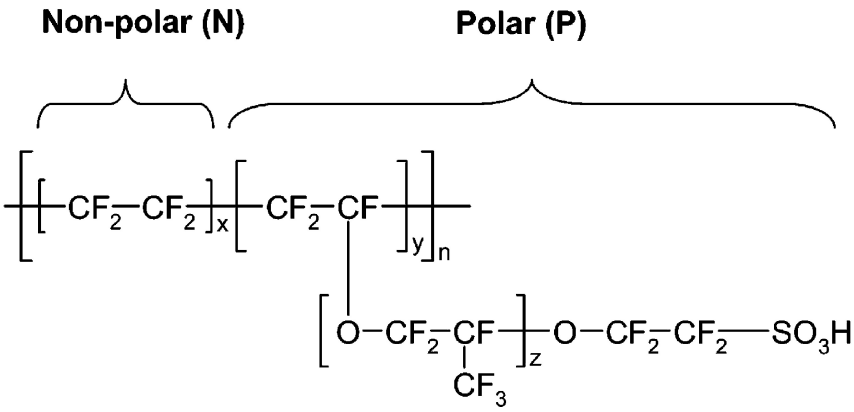


Fig. 1.8. Nafion structural formula. Nafion consist of a non-polar and polar part. The sulphit ion is incorporated into the chemical structure of Nafion. The attached H^+ ensure charge neutrality in the membrane. Adapted with permission from [62], American Chemical Society.

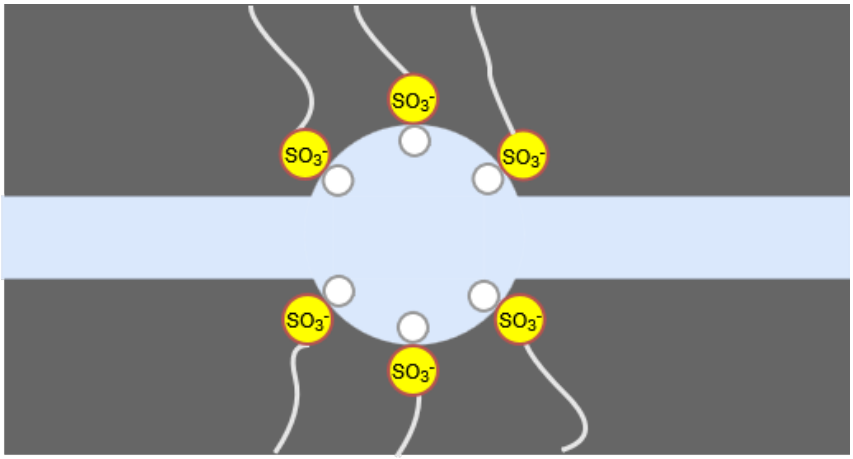


Fig. 1.9. Schematic illustration of the microstructure of Nafion. The sulphit ions (SO_4^{2-}) are bound to $[CF_2]_n$, resulting in SO_3^-. SO_3^- is firmly bound within the membrane. The protons (white circles) are mobile and can be exchanged with other cations within the membrane.

Ceramic Electrolytes

Marnellos and Stoukides [63] were the first, who used ceramics as electrolyte to synthesize electrochemical NH_3. A strontia-ceria-ytterbia pervoskite of the form $SrCe0.95Yb0.05O_3$ with two porous paladium (Pd) electrodes were used. While introducing N_2 and H_2 at 570 °C and atmospheric pressure, a maximum NH_3 production of $3.1 \times 10^{-9}\,\mathrm{mol\,cm^{-2}\,s^{-1}}$ was achieved [63]. In majority the electrolyte material has a pervoskite structure. However, materials with fluorite or pyrochlore structure are used also [64]. Amar et al. [65] found out that water vapor increases the proton conductivity of perovskite electrolytes [65]. Liu et al. [66] used a lanthanum-doped cerium oxide as proton conducting electrolyte with Ag-Pd electrodes. They obtained the highest production rate of $8.2\,\mathrm{mol\,cm^{-2}\,s^{-1}}$ so far. Also, O^{2-} conducting ceramics can be used as electrolytes to produce NH_3 according to the following anode and cathode reaction

$$\text{Anode:} \qquad 3\,O_2^- \longrightarrow 1.5\,O_2 + 6\,e^- \,, \tag{1.8}$$

$$\text{Cathode:} \qquad N_2 + 3\,H_2O + 6\,e^- \longrightarrow 2\,NH_3 + 3\,O_2^- \,. \tag{1.9}$$

O^{2-} conducting ceramics have one to three orders of magnitude lower production rates than H^+ conducting ceramics due to the presence of oxygen containing compounds like H_2O. Kyriakou et al. [64] give an overview of ceramic electrolytes and their resulting NH_3 production rates.

2 Electrochemical Ammonia Synthesis based on Aqueous Electrolytes

2.1 Introduction

The research on the electrochemical ammonia synthesis based on NRR at atmospheric conditions has been intensified in the last years. Depending on the literature, the process must achieve a production rate of $1 \times 10^{-7}\,\mathrm{mol\,cm^{-2}\,s^{-1}}$ with an efficiency of 50 % [40] or a production rate of $1 \times 10^{-6}\,\mathrm{mol\,cm^{-2}\,s^{-1}}$ with an efficiency of 90 % and an operating electrical current density of $300\,\mathrm{mA\,cm^{-2}}$ [6] in order to be economically and commercially viable. In any case, the current results achieved are still far from the desired values in terms of economical use. The most intense research is done in the field of direct NRR using aqueous electrolytes. The aqueous eNRR have several advantages. High temperature resulting in an energy intensive process and possible decomposition of NH_3 and flammable and toxic solvents are avoided [57, 67].

2.2 Challenges and Strategies

The catalysis of nitrogen is extremely difficult due to several properties of N_2 and thus the kinetic is very sluggish. The properties are the enormous strength of the triple bond of a N_2 molecule with a bond dissociation energy of 9.8 eV per bond at 298 K [68] (compared to O_2) 5.16 eV [69], the high ionisation potential 15.84 eV, the low electron affinity −1.9 eV, the non polarity of N_2, and the high energy gap 10.82 eV between the highest occupied and lowest unoccupied molecular orbital [4, 16, 70]. The selectivity of the reaction is a big issue as well. The competing hydrogen evolution reaction (HER) is favored, because only two electrons are necessary to generate hydrogen. This results in a faster kinetic and a lower overpotential [71]. In addition the solubility of H_2 in H_2O is at least 3 orders of magnitude higher than the solubility of N_2 in H_2O (0.65 mmol L^{-1} are dissolved at 298 K and atmospheric pressure [72]) and the binding energy of H_2 is greater on most catalyst, which promotes the HER [73].

One possible solution to increase the selectivity and suppress the HER is to use non-aqueous solutions that limit the activity of protons at the cathode surface [39, 41, 74]. For example the lithium mediated method as mentioned in 1.4.1 [75]. If liquid aqueous electrolytes are used, in many cases a H-cell was used, the solubility of N_2 in H_2O is low as written previously. The synthesis in an H-Cell is discontinuous and therefore a continuous production of NH_3 is not possible. In addition it is necessary to pump continuously N_2 into the cell to maintain a N_2 saturated environment. A discontinuous production is not beneficial for industrial applications [76]. Therefore, a continuous production can be realised by using a membrane system and separation. The membrane electrode assembly (MEA) offers the possibility of a continuous supply of water at the anode side and N_2 at the cathode side. The aqueous NH_3 electrolysis operates at lower temperature and it offers advantages and disadvantages at the same time. The requirement of the system and materials are reduced drastically, which leads to cost reduction. However, the low temperature hinders the catalytic activation and binding of N_2, because the molecule is thermodynamically very stable and kinetically inert [11]. Another draw back of membranes, like the Nafion membrane, is that the membranes are not completely inert. They can absorb and desorb NH_3 during the NRR. This causes significant errors of the measurement of NH_3 production [75, 77]. Another strategy is to lower the accessibility of protons and electrons. This will slow down the HER [74].

2.3 Reaction Mechanism of the Ammonia Synthesis

The catalytic NRR includes three general process steps. The first step is the adsorption of N_2 molecules on the heterogeneous catalyst surface. The second step is the dissociative or associative breaking of the N_2 bond and hydrogenation (addition of H* to N_2). The last step is the desorption of the formed NH_3 [9, 12]. The different reaction pathways are shown in Fig. 2.1. The dissociative mechanism, where the triple bond of nitrogen is broken before hydrogenation, only proceeds at high temperature as in the Haber-Bosch process, because the initially very high energy barrier of the N_2 bond can be broken. The dissociative mechanism is illustrated in Fig. 2.1(a) [11].

Since the eNRR takes place at mild temperatures, the associative mechanism is usually the assumed mechanism in the literature as written in the work of Wu et al. [12]. At mild temperatures, it is not possible to overcome the high energy barrier of N_2 fixation. The N_2 binding therefore breaks down gradually, which is referred as associative mechanism. In the same time as the N_2 breaks, hydrogenation occurs. The associative mechanism can be divided into an alternating, distal and enzymatic reaction pathway. In the alternating reaction pathway, N_2 is first adsorbed on the surface of the catalyst in an end-on mode, and then the N atoms of N_2 are alternately hydrogenated (Fig. 2.1(b)). The distal pathway is also characterized by end-on mode adsorption of the N_2. The N atom removed from the adsorption site is first sequentially hydrogenated. Afterwards the hydrogenation of the other nitrogen atom occurs (Fig. 2.1(c)) [9, 78]. During the enzymatic pathway, the N atoms are also alternately hydrogenated. However, the adsorption of N_2 onto the surface of the catalyst results in a side-on mode (Fig. 2.1(d)) [79, 80]. Since the adsorption configurations of N_2 are difficult to determine experimentally, they are studied by simulation. In this case, the possible intermediate steps during the reduction process are investigated by estimating the free energy change [79].

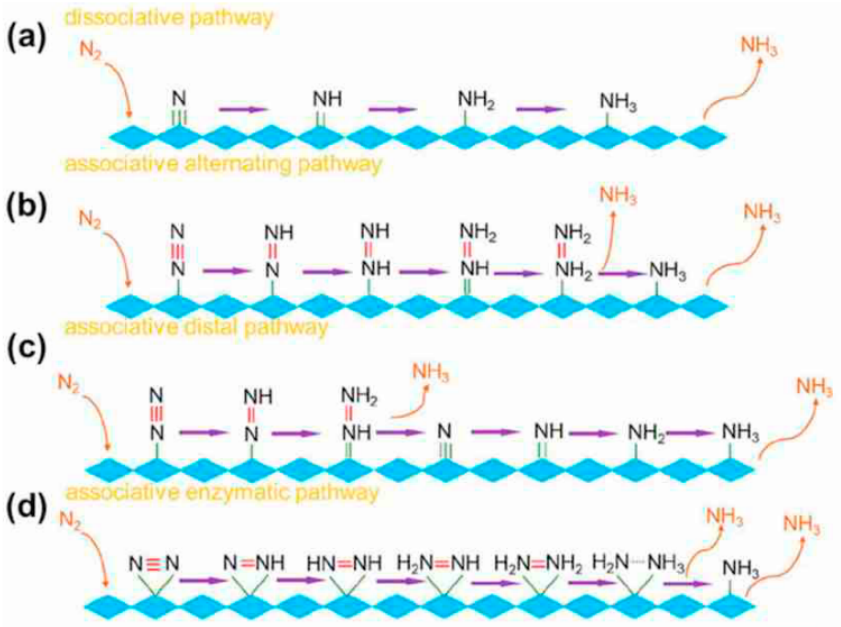


Fig. 2.1. The different reaction mechanisms on heterogeneous catalysts of the NH_3 synthesis. (a) Dissociative mechanism, where the triple bond of nitrogen is broken before hydrogenation. (b) Alternating mechanism, the N atoms of N_2 are alternately hydrogenated. (c) Distal pathway, the N atom removed from the adsorption site is first sequentially hydrogenated. (d) Enzymatic pathway, the adsorption of N_2 onto the surface of the catalyst results in a side-on mode instead of the end-on mode. Adapted with permission from [79], American Chemical Society.

The Mars-van-Krevelen (MvK) mechanism does not rely on the adsorption of N_2 on the catalyst surface. In transition metal nitrides, such as vanadium nitride, eNRR occurs by the MvK mechanism, where an N atom from the nitride lattice is hydrogenated to form NH_3. The vacancy in the lattice is occupied by an atom from the nitrogen stream (Fig. 2.2) [58, 81]. The deactivation of the catalyst is also displayed (Fig. 2.2). It is assumed that only surface N atoms adjacent to a surface O atom are active for the reaction. The catalyst surface can be accompanied by the accumulation of the vanadium nitride phase due to the reducing environment for the NRR reaction. The reducing (negative) potential leads to a fast removal of surface oxygen atoms. The generated surface vacancies are filled with N atoms, because the binding energy of N_2 on a vacancy is much higher than that of O_2. Hence, the catalyst becomes inactive [58]. Using quantitative isotope (^{15}N) experiments combined with density functional theory (DFT) calculations, show that vanadium nitride reduces N_2 to NH_3 via the MvK mechanism [58].

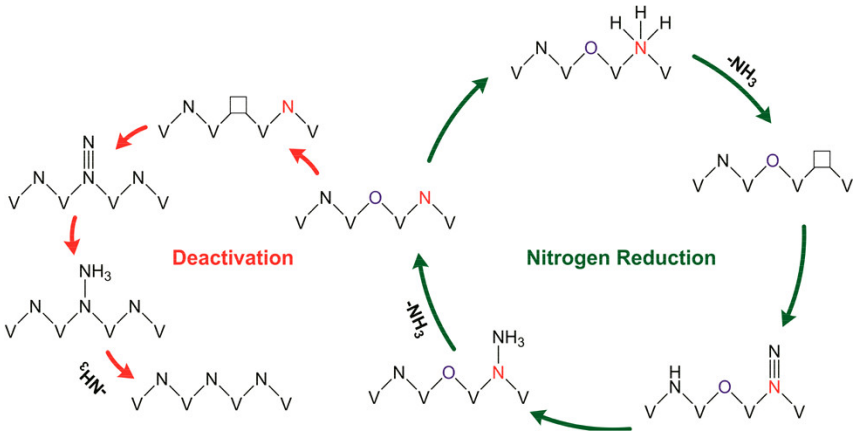


Fig. 2.2. Illustration of the activation and deactivation of the catalytic reaction pathway for the NRR via Mars-van Krevelen mechanism. Adapted with permission from [58], American Chemical Society.

2.4 Catalyst Choice and Development

In recent years, research on synthesis has been greatly intensified. With the goal of improving the NH_3 production rate and increase of the FE. Fig. 2.3 from 2019 shows the huge increase in publications from 2016 to 2019 [6]. The electrocatalyst is the critical component in the electrochemical nitrogen reduction process. However, since around 2020, numerous publications have been published showing that impurities that enter the process of electrochemical NH_3 synthesis have an extrem influence on NH_3 production. NH_3 is therefore not synthesised from molecular N_2, but from the impurities. Therefore, many older publications that did not take these impurities into account are not reliable. The respective impurities that can occur are discussed in section 2.9.

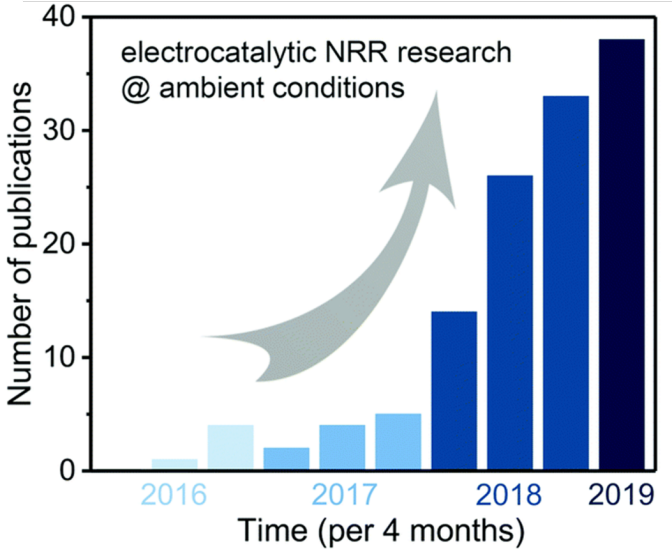


Fig. 2.3. The number of publications based on ambient eNRR during 2016 and 2019. Adapted with permission from [6], Royal Society of Chemistry.

A primary screening of catalysts is necessary and three properties are crucial for a catalyst. The first property is that the catalyst surface needs to have enough activation energy to bind N_2. In addition the catalyst must stabilizes N_2H^* intermediates and destabilzes NH^*_2 to guarantee a reduction of overpotentials [16]. The second parameter is the design of the electrocatalyst. The design is very important, because the morphology / crystal structure, electronic structure and effective active sites are the main factors for the electrocatalytic activity [2, 76, 82, 83]. In case of a

porous structured catalyst the surface area is increased and thereby more active sites are exposed [84]. Doping or defects in the catalyst layer can adjust the electronic structure [76, 82]. The last property that the catalyst must have is low hydrogen activity and low *H coverage, so that $*N_2$ coverage and NRR is feasible [73].
Theoretical studies like DFT plays an important role in the choice of the catalyst. DFT helps to understand the eNRR mechanism. The calculation enables the determination of the reaction pathway by determining the Gibbs reaction energies and the influence of other factors. There are a wide range of catalysts, which were used to syntheses NH_3 electrochemically.
In Fig. 2.4 a volcano diagram of noble metals and transition metals for the reduction of N_2 are shown. The applied potential (U) is plotted against the energy of binding N-adatoms (ΔE_{N*}). It is distinguished between the associative reaction pathways (dashed lines) and the dissociative pathways (solid lines). Moreover, the effect of flat (blue) and stepped (red) surfaces are shown. The step surfaces are more active than the flat surfaces, because of the possible stable configuration of N_2H at a step. Due to this the first hydrogenation at a step is less endothermic than on the flat surface [67]. In addition the green shaded area indicates the area where the adsorption of $*N_2$ on the metal surface showed to be dominant and the white area indicates the surface dominated by *H. However, the metals which bind N_2 more strongly than H_2 have a limited eNRR activity, because their binding to N_2 species is too strong and the desorption of certain intermediates would be very slow [67, 85].

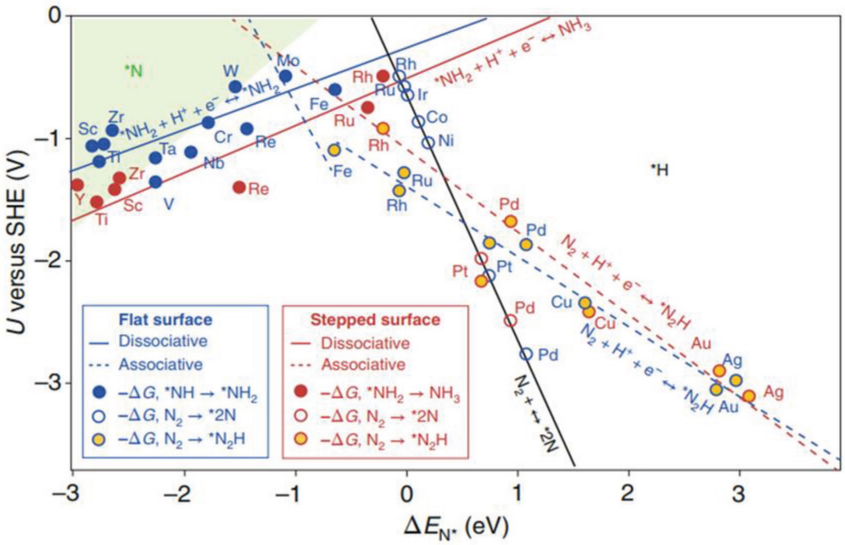


Fig. 2.4. Volcano diagrams evaluating the onset potential (U) on metal surfaces for the reduction of N_2. The solid lines illustrates the dissociative mechanisms, and the dashed lines the associative. A catalyst reaction on a flat surface area is indicated in blue and a stepped surface area in red. An overlap of the red and blue lines is indicated by the black line. The surfaces of catalysts, which are likely covered by adsorbed nitrogen are in the green shaded area and the ones covered by hydrogen are in the white area [67, 76]. Adapted with permission from [76], John Wiley and Sons.

Fig. 2.4 shows that noble metal based materials are not recommended, because they bind H_2 better than N_2. Nevertheless, they are used due to the conductivity, stability and the active surface area. The advantage of gold (Au) is that it has various active sites for N_2 adsorption and reduction and owes a low HER activity. But, as shown in Fig. 2.4, the DFT calculation, the catalytic activity of Au is poor. It has been proven that the eNRR on Au follows the associative mechanism in which the breaking of the N_2 triple bond and the hydrogenation of N atoms occurs simultaneously [71]. Nazemi et al. [86] found that the morphology of the Au nanoparticles are crucial. The produced nanocages exhibit a two times higher production rate than nanotubes. Additionally the crystallinity of Au plays an important role [86]. Li et al. [87] achieved with amorphous Au nanoparticles higher catalytic activity than with crystalline ones [87]. Ruthenium is used in the Haber-Bosch process and is promising for eNRR likewise [88]. It has the highest catalytic activity compared to other metals and a low free Gibbs energy, which makes it an very efficient electrocatalyst for eNRR [76].

Bimetallic catalysts enhances the electrocatlytic performance due to the synergetic effect of the combination of two metals [79]. The bimetallic alloy AuRu achieved a maximum NH_3 yield rate of 101.4 $\mu mol/g_{cath}$ in eNRR [89]. Another example is a bimetallic catalyst of Pd and Cu. Due to the introduction of Cu the desorption of H_2 is accelerated and the NRR activity is increased [90]. Hence, the doping or alloying of these noble metals enables a structure adjustment and a better NRR activity [76].

The main disadvantage of noble metals are their high cost. Therefore, transition metal have been studied as NRR catalyst as well [76]. As written in chapter 1 Fe is the active catalyst in the Haber-Bosch process. Thus, Fe shows NRR activity. It is predicted that Fe and Mo adsorbs N_2 and form metal-nitrogen bond on the basis of the interaction between metals and the N 2p states [91]. Like it is written in chapter 1.3.2 nitrogenase utilizes Mo to produce NH_3. Ti as catalyst is also interesting, because it binds stronger towards N-adatoms than H-adatom (see 2.4) [92]. Other possible transition metals based materials are combinations of transition metals with carbides, sulfides, phosphides, nitrides or with oxides [76]. The transition metal nitrides such as ZrN or VN are supposed to reduce N_2 via the MvN mechanism [58, 81]. Metal free catalysts were studied as well like carbon based materials or boron based materials. A summary of representative reports can be found in Liu et al. [76].

Two more classes of materials which should be mentioned in this work are single atom catalysts (SAC) and high entropy alloys (HEA). SACs are catalyst which contain atomically dispersed metal atoms in support materials. The SAC has the highest specific activity per metal atom, because the catalytic performance increases with downsizing of the metal particle. Moreover, SAC can suppress HER, so SAC can be promising [11, 93]. HEAs are synthesized by five or more metal elements and have distinctive properties like corrosion resistance under difficult conditions and adjustable properties [94]. Fig. 2.5 illustrates a schematic HEA.

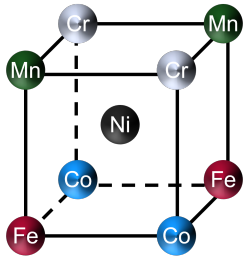


Fig. 2.5. Schematic illustration of a HEA catalyst that consists at least out of five metals. In this case, the catalyst consist of Ni, Cr, Co, Mn, Fe.

Furthermore, the catalysts provide unprecedented compositional diversity, which potentially leads to tune reaction pathways, selectivity, rates alongside entropic stabilization of the material [95]. Fe is a good catalyst regarding N_2 adsorption and activation as noted previously. Co-Cu and Ni-Ru couples offer a remarkable hydrogenation ability at low overpotential [94]. In summary, HEAs are possible candidates for utilizing as a NRR catalyst. Tables and graphics of catalyst and the resulting NH_3 production rates and FE can be found in the literature [11, 70, 76, 96].

2.5 Electrochemical Reactor Design

The back-to-back cell illustrated in Fig. 2.6 (a) is based on a solid electrolyte separating the anode and cathode compartments. The membrane electrode assembly (MEA) cell, which is used in this work, is also based on this reactor design. The configuration can be used in a wide temperature range (25 - 800 °C) [78] as explained in chapter 1.4.4.
Liu et al. [97] reached a maximum production rate of $1.05 \times 10^{-8}\,\mathrm{mol\,cm^{-2}\,s^{-1}}$ at 80 °C using this kind of cell configuration. At higher temperatures the NH_3 production rate decreases due to the decrease of H_2O content, which leads to a reduced proton conductivity of the Nafion membrane [78, 97]. Lan et al. [98] used H_2O as H^+ source, air as N_2 source and using Pt/C catalyst as both anode and cathode electrode. They reached a maximum production rate of $1.14 \times 10^{-9}\,\mathrm{mol\,cm^{-2}\,s^{-1}}$ at 1.6 V and ambient temperature and pressure [78, 98]. The PEM-Type cell reactor configuration (Fig. 2.6 (b)) has an anode chamber, which is filled with an electrolyte. The liquid electrolyte in the chamber has two advantages. A reference electrode (RE) can be added, that enables the measurement of the potential at the working electrode (WE). Furthermore, the membrane is better moistened [78]. Using this type of cell configuration Kordali et al. [61] carried out eNRR. They reached an ammonia production rate of $1.3\,\mathrm{\mu g\,cm^{-2}\,h^{-1}}$ supplying N_2 and 2 M KOH as electrolyte in the anode chamber separated by a Nafion membrane. Ru deposited on carbon felt was used as catalyst at −1.02 V vs. Ag/AgCl at 90 °C. The H-type cell (Fig. 2.6 (c)) is the reactor configuration that has been used in most studies [96]. The cell also consists of two chambers separated by a membrane. Both chambers are filled with a liquid electrolyte. The gaseous N_2 is bubbled into the cathode chamber. The WE and RE are placed in the cathode chamber, which allows a more accurate measurement of the applied potentials. In general, also regarding the other cell configurations (see. Fig. 2.6 (a) and (b) crossover effects of NH_3 / NH_4^+ can occur and need to be considered [78]. Liu et al. [99] reached a production rate of 23.88 $\mu g/mg_{cat}h$ with an ultra thin Rh nanosheet as catalyst at −0.2 V. Fig .2.6 (d) illustrates the single chamber cell. The oxidation and reduction reaction takes place in the same chamber. This cell has the disadvantage that gaseous products can be oxidized at the anode. Wessling et al. [100] produced NH_3 with a single chamber cell filled with 0.5 M H_2SO_4. The production rate was $1.2 \times 10^{-10}\,\mathrm{mol\,cm^{-2}\,s^{-1}}$ with Ru structured on Ti felt as electrocatalyst. Nevertheless, it has to be mentioned that with these reactor configurations H_2 is produced as side product.

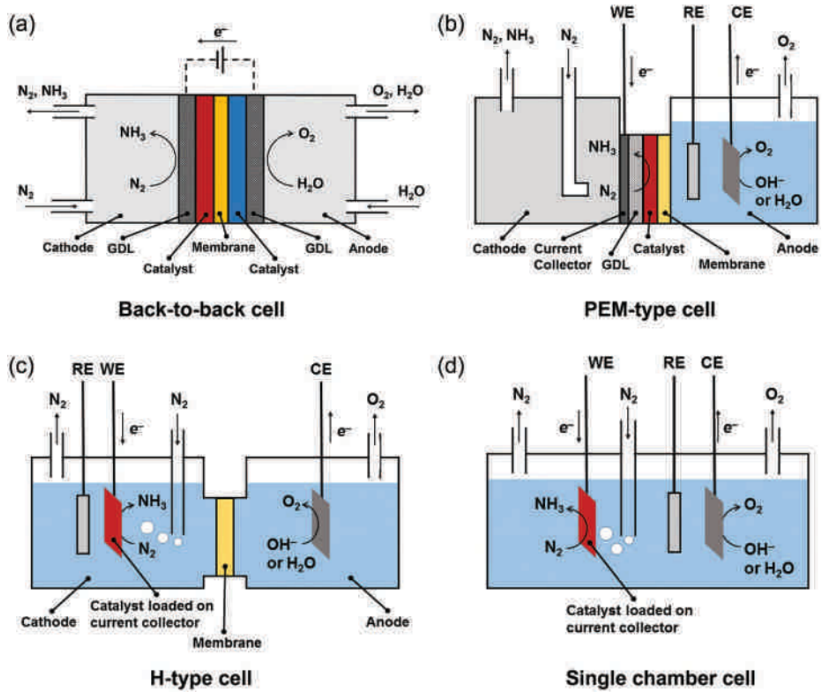


Fig. 2.6. Schematic illustration of the different reactor configuration for electrochemical NRR, (a) back-to-back cell, (b) PEM-type cell, (c) H-type cell, and (d) single chamber cell. Adapted with permission from [78], John Wiley and Sons.

2.6 Electrodes

Various working electrodes are used in the literature for electrochemical NH_3 synthesis: glassy carbon rotating disc electrode, glassy carbon plates, carbon electrodes (paper, felt, cloth), porous metal electrodes (titanium felt, nickel felt, nickel foam) [6]. These electrodes are used as the anode and cathode in the MEA cell. Carbon paper is the most commonly used electrode substrate because it is inexpensive and the surface of the electrode can be modified. It can be hydrophilic or hydrophobic. This property will affect the electrocatalytic reaction [6]. In the case of the other reactors, the Ag/AgCl electrode is mostly used as the reference electrode. Pt or graphite are employed as the counter electrode (CE). It is important that the CE is electrochemical inert, so that it will not react with NH_3 [6].

2.7 Electrolytes

Aqueous electrolytes have a strong influence on HER activity and thus on NRR performance [74]. Here, the limitation of proton supply plays a crucial role [74, 101]. NRR research is conducted over a wide pH range. In the literature, acids like hydrochloric acid (HCl), H_2SO_4, neutral solutions H_2O, sodium sulfate (Na_2SO_4) or bases KOH are used in different concentrations as electrolytes [6]. Mukherjee et al. [102] demonstrated that catalysis with 0.1 M KOH as electrolyte performed better than 0.1 M HCl over a temperature range of 25 to 60 °C. The KOH concentration of 0.1 M performs better than 0.5 M [102]. In comparison, Hao et al. [85] found out that no significant electrocatalytic pH dependence is shown from acidic to alkaline. This difference possibly results from the different cell configurations, intrinsic properties of the catalysts, impurities in the electrolytes, and reaction-induced local pH gradients [103]. The local pH gradient can occur due to the H^+ consumption by the reduction reaction at the electrode. Therefore, the pH near the electrodes can deviate strongly from the bulk concentration. Thus, the HER and NRR activitiy and selectivity can be influenced significantly [103]. More recently, lithium ion (Li^+) compounds have been used as electrolytes (0.5 M Li_2SO_4, $LiClO_4$) because lithium ions effectively suppress HER and improve NRR. This is due to the property of Li, it interacts with N_2 and activates N_2 [104] (see. section 1.4.1).

In most cases for aqueous electrolytes, depending of the reactor design, a separation medium is needed. In an acid or neutral environment Nafion is used, due to its good proton conductivity and chemical and mechanical stability. Due to the excellent properties of Nafion it is used as default material [105].

2.8 Ammonia Detection Methods

In literature several NH_3 detection methods are used with various detection limits. The detection methods operate continuous or discontinuous. NH_3 can be detected optically with wet-chemical methods using UV-Vis spectroscopy. These include the two classical methods indophenol blue or Nessler's reagent or physically using ion chromatography, infrared spectroscopy (IR), and nuclear magnetic resonance spectroscopy (NMR) [4, 106]. It can be detected electrochemically using ion-selective or gas-selctive electrodes also [107]. Combination of detection methods are done as well [4]. Due to the low NH_3 production rate and the strong influence of contaminations (see section 2.9) the detection of produced NH_3 out of molecular N_2 is quite challenging. NMR offers the possibility, that it can differentiate the isotopes $^{14}NH_3$ and $^{15}NH_3$. If $^{15}N_2$ is the source whose concentration is known, NMR can determine how much $^{15}NH_3$ is formed from $^{15}N_2$ [4, 75]. But, it should be considered that the $^{15}N_2$ gas contains impurities as well. This can lead to false results [57, 75].
In this work IR spectroscopy as a continuous and the indophenol blue as discontinuous methods are used to detect and determine NH_3. A detailed description of these both detection methods is done in section 3.3.

2.9 Contaminations in Electrochemical Ammonia Synthesis

2.9.1 Sources of Contaminations

On the basis of the difficulty of the eNRR the amount of produced NH_3 is in the range of 1×10^{-12} to $1 \times 10^{-11}\,\mathrm{mol\,cm^{-2}\,s^{-1}}$. These small production rates are hardly confirmed from the contribution of eNRR, because different non-negligble contaminations affect the detection and result in false detected amount of NH_3. There are several sources of contamination [75, 76].

Contamination from Environment

Ammonia is ubiquitous in the atmosphere and is primarily emitted from animal production facilities and the resulting manure. NH_3 is the only naturally occurring alkaline gas in the atmosphere [108]. Chen et al. [101] detected $0.05\,\mathrm{mg\,L^{-1}}$ dissolved NH_3 in a beaker after leaving it open with 50 mL of 0.01 M HCl solution for 12 h in the laboratory. Human breath was also measured as NH_3 source [109] and nitrile gloves can be a factor of contamination as well [75].

Gas Supply

The feed gas of N_2 can contain contaminations, which can lead to false positive results. Dabundo et al. [110] analyzed different commercial $^{15}N_2$ gas stocks and they found that substantial levels of nitrate (NO_3^-) / nitrite (NO_2^-), ammonium (NH_4^+) and nitrous oxide (N_2O) were detected [110]. These contaminations can be electrochemically reduced to NH_3. Choi et al. [111] demonstrated in their study that neither nanoparticulate carbon-supported Au, nor bismuth powder were active catalysts for the electrochemical N_2 reduction. But, both can efficiently catalyze the reduction of NO_2^-, NO_3^-, NO and NO_2. If the purity of the N_2 is 99.999 % then 0.001 % of the gas stream are contaminations. The amount of contaminations must be considered and their mass must be calculated based on the flow rate and duration of the experiment [4].
To demonstrate the impact and scale of these impurities, an illustrative calculation is presented. The typical N_2 flow rate employed in this work is 10 mL/min. Based on the assumption that 0.001 % of the gas stream are impurities, which are converted to NH_3, the volume of these impurities is 1×10^{-4} mL/min. The average density of NO

($\rho = 1.25\,\mathrm{g\,L^{-1}}$, $\mathrm{M} = 30.01\,\mathrm{g\,mol^{-1}}$) and NO_2 ($\rho = 3.66\,\mathrm{g\,L^{-1}}$, $\mathrm{M} = 46.01\,\mathrm{g\,mol^{-1}}$) is $\rho = 2.44\,\mathrm{g\,L^{-1}}$ and the average molar mass is $38.01\,\mathrm{g\,mol^{-1}}$. This corresponds to a conversion rate of 6.42×10^{-9} mol/min from impurities to NH_3. If the conversion rate is related to the standard electrode surface area of the cells utilized in this work ($6.25\,\mathrm{cm^2}$) and per second, then the conversion rate is $1.71 \times 10^{-11}\,\mathrm{mol\,cm^{-2}\,s^{-1}}$ ($1.71 \times 10^{-5}\,\mu\mathrm{mol\,cm^{-2}\,s^{-1}}$).
It can be concluded that this rate represents the absolute minimum NH_3 production rate that must be achieved to ensure synthesis of NH_3 solely based on gas purity. The error of the detection method has not been considered in this assessment.

Impurities in the Electrochemical Cell

Catalysts, conducting layers, which contain N_2 compounds such as nitrogen oxides, metal nitrides are sources of false positive results [112–114]. The resulting nitrogen surface atoms can be removed and subsequently reduced to NH_3 [114]. In addition during the catalyst synthesis N traces can be added to the structure, when either solvents or surfactants contains nitrogen and leads to erroneous conclusions [114]. The electrolyte, which is considered to be part of the electrochemical cell, influences the detection of NH_3 also. The pH value of the electrolyte needs to be constant, otherwise a change will result in a miscalculation of the electrode potential. Hence, it will lead to unrepeatability [114]. Moreover, Li et al. [115] showed that Li salts, which are commonly used in the preparation of the electrolyte contain traces of NO_3^- and NO_2^-. These traces were electrochemically reduced to NH_3 and hence, false results occurred.

Uptake and Release from the Membrane

In several experiments it was found that Nafion as a separating membrane or as an electrolyte accumulates and releases NH_4^+ through ion exchange with acid groups [75, 77, 114, 116, 117]. During the pre-cleaning of Nafion, the membrane can become a source of NH_3 contaminations and this can lead to a release of NH_3 afterwards [75]. Furthermore, the membrane can soak up the produced NH_3 from the electrolyte in am H-cell, which will lead to a "negative" concentration relative to the blank electrolyte [75]. Nafion is as the separating medium and / or the electrolyte are crucial part of the electrochemical cell. However, due to theses mentioned facts, there is still a lack of understanding the adsorption and discharge behavior of Nafion. The interaction of Nafion with NH_4^+-ions is researched and described in more detail in chapter 7.

2.9.2 State of the Art Elimination of Contaminations

A lot of research is done to research the elimination of contamination, so that the determination of NH_3 is more accurate. Several different procedures are needed to remove the various impurities. Atmospheric contamination cannot be avoided and they are from laboratory to laboratory dependent. For example, agricultural land near the research facility has a different influence than urban research facilities on the concentration of NH_3 in the air [108]. Assuming that the air contamination is constant, the amount of contamination can also be determined in a control experiment using Ar. This measured value can simply be subtracted from the measured amount of NH_3 during the N_2 trial. Glasswares and tubes should be cleaned by boiling in ultra pure water. NH_3 in the feed gas can be removed by introducing the feed gas through H_2SO_4 and N and O compounds can be removed by reduction with a Cu catalyst. Otherwise commercial gas purifier are an option [4]. Impurities inside the electrochemical cell can be removed by purging the cell. In addition repeating the experiment utilizing Ar as the cathode gas are helpful to determine whether the contamination may originate from the electrochemical cell. Liu et al. [118] described a way to remove impurities in the catalyst via pre-reduction.

The easiest way to prevent the uptake and discharge of NH_3 in the membrane like Nafion, which shows a strong accumulation of NH_3, is to use a membrane, which has not the properties of adsorption and desorption. The membrane Celgard 3501 is a possible solution [118].

2.9.3 Synthesis Protocol

Due to the low NH_3 production rate and the large number of affecting impurities it is essential to have a strict synthesis protocol. Many research groups have defined their own synthesis protocol. They are most often quite similar. The following sources have created such protocols [2, 4, 6, 11, 75, 76, 101].

The general idea of this protocol is that in the beginning of each experiment, possible contaminations of the catalyst production and other impurities, e.g. from the cell components have to be considered. If NH_3 is measured two control experiment should be done. The experiment should be carried out with Ar instead of N_2 and N_2 without an applied driving force. If significantly less NH_3 is detected in the control tests than in the original experiment, the original test should be repeated with identical set-up using a new, independent batch for ensuring reproducibility. In addition different NH_3 determination methods can be used and a combination of the methods leads to a more trustful result. As mentioned earlier, NMR spectroscopy can differentiate between isotopes. This allows the comparison of the quantities produced by $^{14}N_2$ and $^{15}N_2$. If the NH_3 values match, it can be assumed that the NH_3 production process is reliable. It is important to note that the $^{15}N_2$ may contains impurities as well [57, 75].

Choi et al. [57] critically evaluated NRR reports and derived three key criteria from the reports. The first criteria is that the NH_3 production rate has to be sufficiently high enough. As second criteria $^{15}N_2$ (isotope nitrogen) should be used to confirm the results and the last criteria is that the oxidised forms of N_2 which may be present are determined in the experiment. They set up a traffic light system as a rating system for the three criteria with the colors red, yellow and green. The evaluating system is shown in Tab. 2.1. This rating system is applied to evaluate and asses the respective publications in terms of their measured NH_3 production capacity. Not a single publication completely fulfils the requirements to prove NH_3 beyond doubt. More information can be found in their publication and the supplementary [57].

Tab. 2.1.: Criteria for reliable NH_3 detection. The three criteria are a sufficient NH_3 production rate, the quantitative analysis of NH_3 via isotope determination and the control of oxidised forms of N_2.

Rating	Sufficient NH_3 Production Rate	Quantitative $^{15}NH_3$ Analysis	Control of NOx
■	$R(NH_3) < 0.1\,nmol\,cm^{-2}\,s^{-1}$	Unreliable	Insufficient control
■	$0.1 \leq R(NH_3) < 10\,nmol\,cm^{-2}\,s^{-1}$	Inconclusive	N_2 and NO_x reduction might occur
■	$R(NH_3) \geq 10\,nmol\,cm^{-2}\,s^{-1}$	Reliable	NOx reduction is negligible

3 Methods

3.1 Test Benches

3.1.1 Construction

Two test benches were developed and set up to synthesize NH_3 electrochemically. Nitrogen and hydrogen are required for producing NH_3. H_2 can be utilized as the source of H (see Eq. 1.1). Figure 3.1 displays the test rig utilizing H_2 as H^+ source. H_2 is supplied at the anode side via a mass flow controller. The used mass flow controller "GF40" for controlling the gas fluxes are from Brooks Instruments. On the cathode side N_2 and Ar are supplied into the electrochemical cell. Ar is used to clean the cell from impurities in the beginning and to verify the results of the experiments. If Ar is supplied instead of N_2, the detected NH_3 is caused by reacting impurities in the system. In the case that N_2 is supplied and the detected quantity of NH_3 is in the same range as with Ar, the underlying production rate is too low to verify electrochemical NH_3 synthesis. The detected amount of NH_3 falls within the error range of the detection method. On anode and cathode side a humidifier cell is integrated. Nafion must be humidified. Therefore, the humidifier cells are necessary. Otherwise the ion conductivity of the membrane would be very poor. Before the gas stream is introduced into the cell at the cathode side, the gas flows through a wash bottle containing a solution composed of 50 mL of 0.45 mol L^{-1} (mol L^{-1} = M) H_2SO_4. This cleaning trap is used to remove nitrogenous impurities from the gas flow. NH_3 and H_2 are produced at the cathode, with H_2 being a by-product. The produced NH_3 is detected with the fourier-transform infrared spectrometer (FTIR) "DX4000N" from GASMET and the H_2 is measured with the sensor "FTC 300" from Messkonzept. This sensor is a thermal conductivity detector. The indophenol method is another used detection method (see section 3.3.2) for determining NH_3. For this method, the gas stream on the cathode side is introduced into a wash bottle filled with 25 mL of a 0.45 M H_2SO_4 solution. This bottle acts as a trap for NH_3. NH_3 reacts with H_2SO_4 and forms NH_4^+. Unlike gaseous NH_3, $NH_4{}^+$ is non-volatile. After adding further reactants for performing the indophenol method, the amount of NH_3 is determined with the visible light spectrometer "PV4" from VWR International®.

The priniciple of the indophenol method and the reactants are elucidated in section 3.3.2. Measurements can be carried out from room temperature (25 °C) to 80 °C with the test rig and the pressure of the cathode is adjustable from atmospheric pressure (1 bar) to 5 bar overpressure.

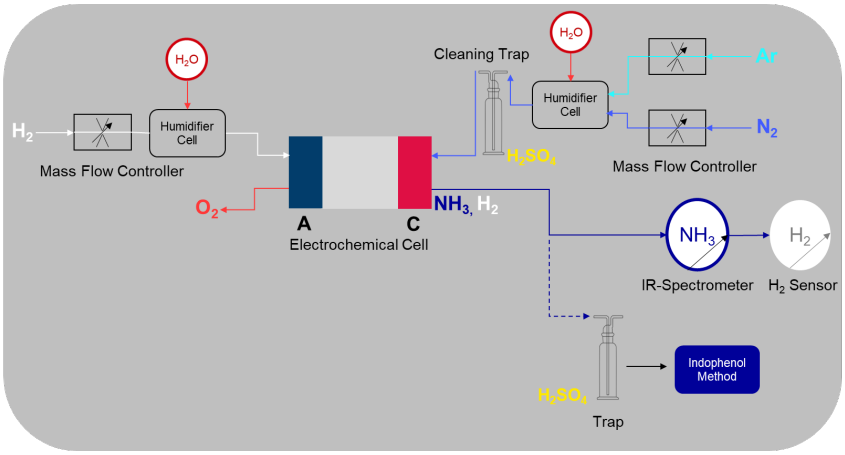


Fig. 3.1. Illustration of the test bench utilizing H_2 as reactant. H_2 is supplied via a mass flow controller on the anode side. The gas is humidified with a humidifier cell. Due to the chemical reaction O_2 is produced at the anode. On the cathode side either N_2 or Ar are supplied via mass flow controllers. The gases are also humidified. The humidification is needed for the membrane. The gas streams through a cleaning trap before entering the cell. The synthesized NH_3 is determined with the indophenol method or with an IR-spectrometer. H_2 is determined with a hydrogen sensor.

H_2O can be utilized as H^+ source as well

$$3\,H_2O(l) + N_2(g) \rightleftharpoons 2\,NH_3(g) + 1.5\,O_2(g)\,. \tag{3.1}$$

Fig. 3.2 illustrates the corresponding test bench. H_2O, or other aqueous solution such as Na_2SO_4, and KOH are pumped with an circulation pump into the anode of the electrochemical cell. These various solutions serve as H^+ source. Due to the various aqueous solutions, the pH value in the electrochemical cell is adjustable, thereby the influence of the pH value on the NH_3 synthesis can be investigated. The flow rate of the pump is adjustable as well. During the electrochemical reaction, O_2 is produced at the anode (Eq. 3.1). The produced O_2 can escape into the atmosphere through the opening of the solution container. The H_2O supply humidifies the membrane, hence additional humidification cells are not needed on anode and cathode side. It is assumed that the membrane is not dried out by the N_2 gas stream due to the H_2O supply. Besides from the humidification cell at the cathode side, the set up is the same as in Fig. 3.1. It has to be mentioned that H_2O can move trough the membrane to the cathode side via diffusion and the electroosmotic drag. The operation conditions are the same as for the H_2 test rig (Fig. 3.1).

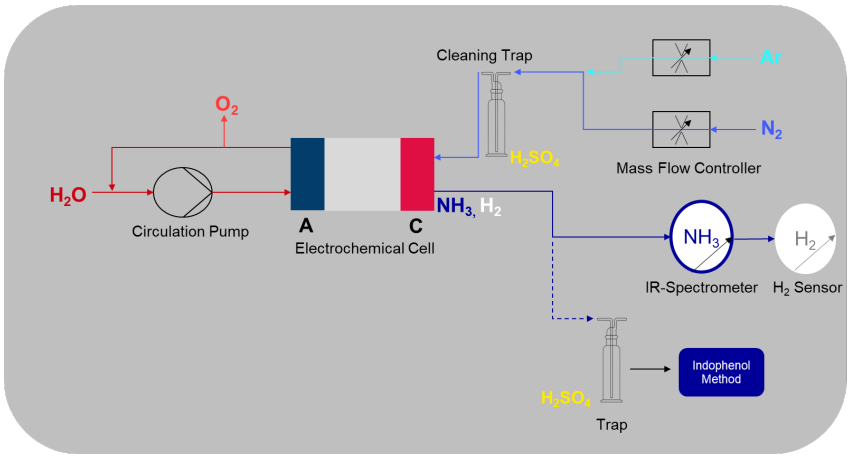


Fig. 3.2. Illustration of the test bench utilizing H_2O as reactant. H_2O is introduced on the anode side via a circulation pump. Due to the supply of H_2O humidifier cells are not required. At the anode O_2 is as well produced. On the cathode side either N_2 or Ar are supplied via mass flow controllers. The gas streams through a cleaning trap before entering the cell. The synthesized NH_3 is determined with the indophenol method or with an IR-spectrometer. H_2 is determined with a hydrogen sensor.

3.1.2 Measurement Accuracy

As noted in the literature review discussed and shown in the following chapters, the achieved NH_3 production rates are very low and not fully reliable. That is why the resolution limits of the devices in test benches could play an important role. Therefore, these resolutions limits are discussed in the following.

The resolution limit of the potentiostat depends on the mode, the galvanstatic (current driven) or potentiostatic (potential driven) operation mode. In the case of an applied current, the accuracy of the potential measurement is $\pm$ 0.2 % or 2 mV of the measured value. For potentistatic operation, the current measuring accuracy is 20 pA plus 0.025 % of the selected current range ($\pm$ 100 pA to $\pm$ 10 A). As depicted in chapter 6, the measured current flow is sufficient to synthesize NH_3. Consequently, it can be inferred that the accuracy of the potentiostat does not impact on the accuracy of the NH_3 detection. The mass flow controller from Brooks Instrument are specified with an accuracy of 1 % of the flow rate. Due to a internal temperature sensor the flow rate is adjusted so that at the specific measured temperature, the employed flow rate is carried out. Therefore, an additional error regarding the accuracy of the sensor does not occur. The accuracy of the circulation pump SIMDOS® 10 from KNF Group™ is specified with $\pm$ 2 % of the pump capacity. The default pump capacity of this thesis is 10 mL/min. Experiments showed that the pump rate, did not influence the outcomes of the experiment and thus it was not further investigated. It is assumed that the applied temperature is constant, because it is not feasible to control the temperature in the laboratory and the test bench precious at room temperature.

The crucial impact on the measurement accuracy has the detection devices (sensors, spectrometer) of each element. As described in section 2.9 the purity of the gas supply has also an significant influence on the reliability of the determined NH_3 rates. Furthermore, the repeatability and the resulting scattering of the trials has a remarkable influence as shown in the presented results of this thesis.

3.2 Electrochemical Cell

The configuration of the membrane electrode assembly (MEA) cell employed for synthesising NH_3 is illustrated in Fig. 3.3. The anode and cathode side consist of identical components. The end plates are made of stainless steel and are connected to the potentiostat. The end plates ensure electrical contact of the cell components and transfer mechanical compression to the cell in to order to keep the components in close contact and dense. The potentiostat "Ocotostat 500" is from Ivium® and is employed consistently throughout all experiments. It has a maximum current supply of 5 A. The anodic and cathodic bipolar plates are made of stainless steel and are coated with platinum and gold respectively. The flow field of the bipolar plates feature a meander structure. The bipolar plate channels the reactants into the cell and discharge the products. The cell is sealed by Polytetrafluoroethylene (PTFE) layers, which are adapted to the thickness of the porous transport layers (PTL). The properties of PTFE as sealing layers are the chemical inertness, the non electrical conductivity, temperature stability and the good flexibility and sealability. The PTL distributes the gases and liquids to the membrane, removes the produced products and is an electrical conductor. Therefore, the electrical conductivity and contact resistance of the PTL are important. The core of the electrochemical cell is located in the center of the MEA cell. The catalyst layers are coated on either the PTL or directly on the membrane. Either Pt or Ir are used as the anode catalyst. As cathode catalyst various catalyst were tested in terms of NRR. These catalyst are presented in chapter 6 and in the appendix A. Nafion 115 is used as default membrane for the acid and neutral environment. While Zirfon from Agfa™ is used for the alkaline environment. The active surface cell area utilized for the NH_3 synthesis is 6.25 cm^2 (25 mm x 25 mm).

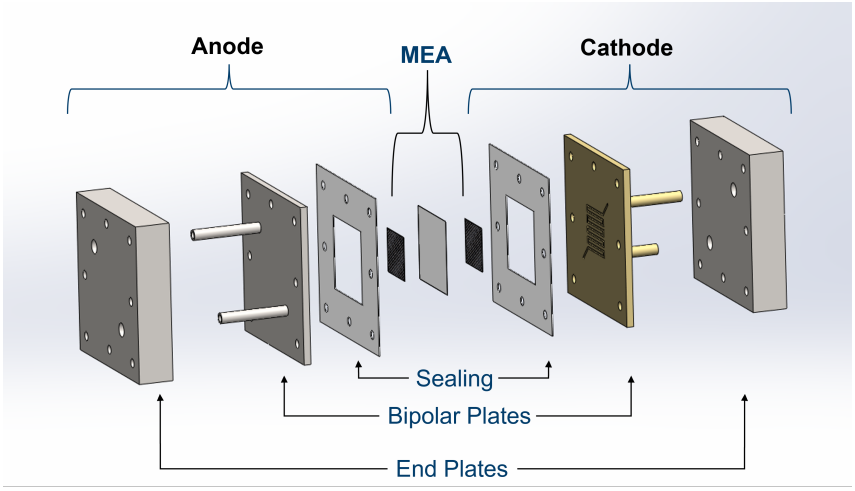


Fig. 3.3. The end plate, which are made of stainless steel enables the electrical contact of the cell components and applies mechanical compression to the cell. The flow fields in the bipolar plates channels the reactants into the cell and exports the products out of the cell. The anode bipolar plate is coated in platinium and the cathode one in gold. The flat sheet sealing is PTFE, which is adapted to the thickness of the porous transport layers of the MEA. In the center of the cell is the MEA, which consist of PTLs on anode and cathode side, catalyst layers and the membrane. The catalyst layers can be coated on either the PTLs or the membrane.

3.3 Ammonia Detection Methods

3.3.1 Infrared Spectroscopy

The infrared spectroscopy measures the absorbance of a sample material in the gas phase. Absorbance is the attenuation of radiation caused by all sources and it is the dominant quantity measured in IR spectroscopy. The absorbance is caused by the excitation of vibrational modes at molecular level. This requires an IR active sample material. Materials without dipoles like N_2 or O_2 can not be measured. Each substance has a characteristic molecular structures and these structures result in characteristic absorption bands in dependency of the wavenumber. Based on the absorbances, the substances can be distinguish. The intensity of the radiation before *(I_0)* and after *(I)* passing the sample at a specific wavenumber in relation with the concentration of the substance is described by the Lambert-Berr´s law [119, 120]

$$A = -\log \frac{I}{I_0} = \epsilon \, c \, l \, . \tag{3.2}$$

The absorbance *(A)* is a linear function of the concentration *(c)* of the substance and the path length *(l)* of the radiation through the medium. The absorption coefficient *(ϵ)* is material and wavelength dependent. Assuming a constant path length, the Lambert-Berr's law allows the quantification of substance concentration by measuring the absorbance. Instead of the originial IR spectroscopy, which requires a variation of the wavelength in order to generate spectra, the FTIR spectroscopy is usually used today. The emitted light is modulated in an interferometer and after passing the sample, the detected interferogram is converted with fourier-transformation in a measurement spectra. Comparing both methods, FTIR offers a much better signal-to-noise ratio [120, 121].
The detection limit of the FTIR "DX4000N" Gasmet™ from Gasmet Technologies® is specified with 0.2 to 2 ppm in dependency of the gas composition, which is specified in the manual. If a detection limit of 2 ppm is assumed and the flow rate of N_2 is 50 mL/min the detection limit volume flow of NH_3 is $1.67 \times 10^{-12}\,m^3\,s^{-1}$. At room temperature, atmospheric pressure, and an active cell area of $6.25\,cm^2$ the resolution limit of an NH_3 production rate is approximately $1.1 \times 10^{-11}\,mol\,cm^{-2}\,s^{-1}$. The volume of the heating tube, the distance from the cell to the FTIR spectrometer is $5.65 \times 10^{-5}\,m^3$ and the dead volume of the spectrometer is 0.45 L. Thus a flow rate of 50 mL/min is the absolute minimum as a supplied flow rate, because otherwise the determined H_3 is very imprecisely.

3.3.2 Indophenol Blue Method

The indophenol blue method is a typical determination technique of NH_3 [6]. The method is done through colorimetric reactions and the blue colour is formed by the reaction of NH_3 with hypochlorite and phenol in an alkaline solution. Berthelot was the first who achieved it [122].

The indophenol method used in this thesis is based on the method reported by Li et al. [123] and Zhao et al. [106]. Gaseous NH_3 is introduced into a 0.45 M H_2SO_4 solution. 2 mL of this solution are introduced into a sample vessel. As the reaction takes place in an in an alkaline environment, the pH value needs to be increased [124]. Hence, 2 mL of a 1 M sodium hydroxide (NaOH) solution, including sodium salicylate and potassium sodium tartrate, is then added. Sodium salicylate is the source of phenol and potassium sodium tartrate acts as a buffer. The solution consist of 5 g sodium salicylate and of 5 g potassium sodium tartrate in a 100 mL of 1 M NaOH. Subsequently, 0.2 mL of a nitroprusside solution is added. It serves as catalyst [122]. Then, 0.2 g of nitroprusside was dissolved in 20 mL of deionized water. In the end, 1 mL of a sodium hypochlorite solution containing 0.005 % sodium hypochlorite is added to the solution. Between each addition, the solution is mixed using a vortex mixer. In the following, the reaction steps are shown.

NH_3 reacts with hypochlorite (OCl^-) to monochloramine (NH_2Cl)

$$NH_3 + H_2O \rightleftharpoons NH_4^+ + OH^- \,, \tag{3.3}$$

$$NH_3 + OCl^- \rightleftharpoons NH_2Cl + OH^- \,. \tag{3.4}$$

The monochloramine reacts with the phenol from the salicylate to 4-(chloroimino)cyclohexa-2,5-dien-1-one (Fig 3.4). The reaction is catalyzed by nitroprusside.

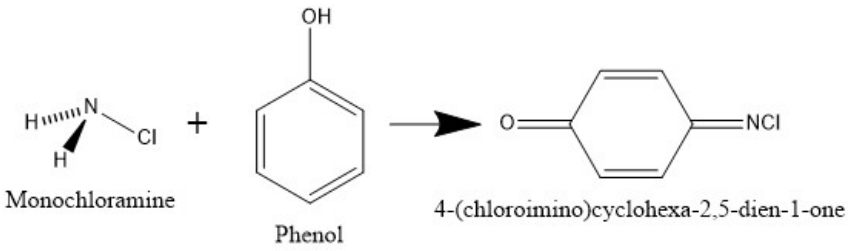


Fig. 3.4. The reaction of monochloramine with phenol.

The last reaction step is the reaction of 4-(chloroimino)cyclohexa-2,5-dien-1-one with another phenol molecule to indophenol blue (Fig. 3.5).

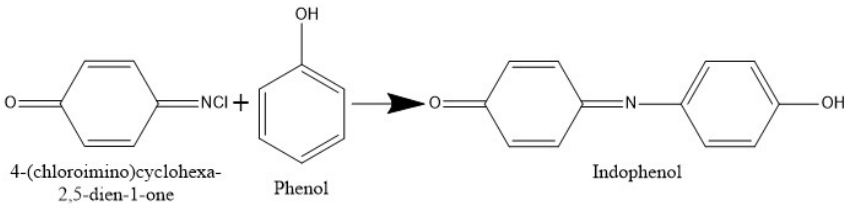


Fig. 3.5. The reaction to indophenol blue.

The samples are then stored for 30 min and analyzed using the VIS-spectrometer at a wavelength of 655 nm like Zhao et al. [106]. Fig. 3.6 displays the spectra of the calibration samples from 0.2 to 6 mg L^{-1}. The absorbance of these spectra are calculated as well with Lambert-Beer´s law (Eq. 3.2), because the spectra are dependent of the intensity of the light. The calibration samples shown in Fig. 3.7, are samples with known concentration. 970 mg of dried ammonium sulfate ($(NH_4)_2SO_4$) is utilized as the source for NH_3 and it is diluted in H_2O for producing a 1000 mg L^{-1} NH_3 solution. The needed mass of $(NH_4)_2SO_4$ is calculated with

$$m((NH_4)_2SO_4) = \frac{c(NH_3)\ V\ M((NH_4)_2SO_4)}{2\ M(NH_3)}\ . \tag{3.5}$$

Where V is the volume, $c(NH_3)$ the concentration of NH_3 and M the molar mass of the corresponding chemical.

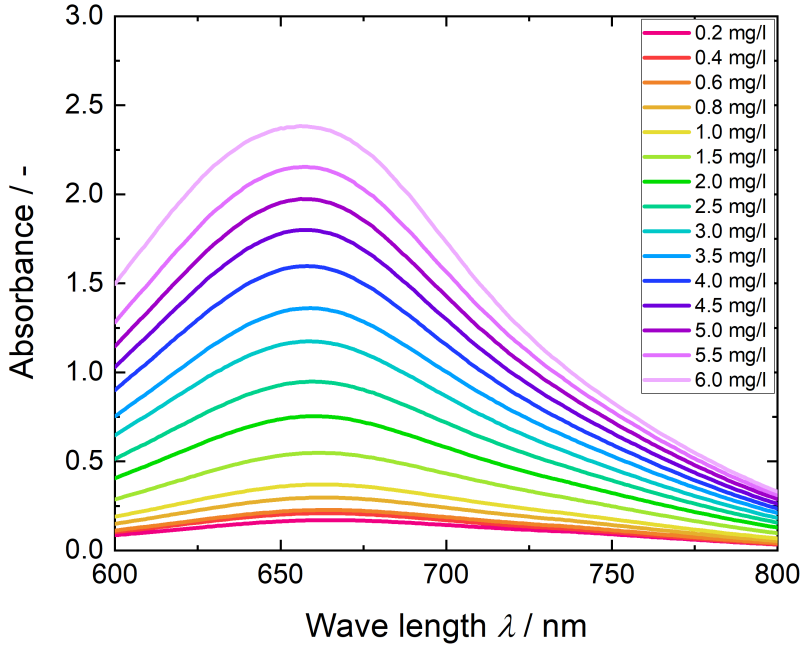


Fig. 3.6. Indophenol blue absorbance spectrum of the calibration samples from 0.2 to 6 mg L^{-1}.

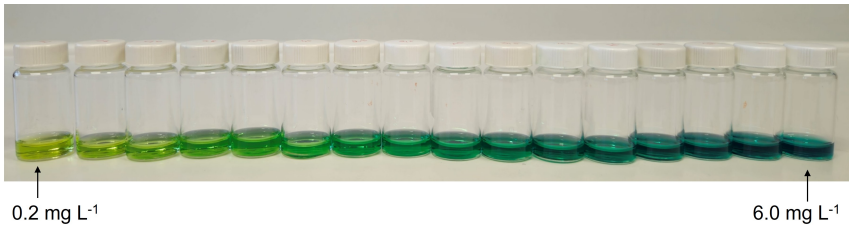


Fig. 3.7. Color change of samples. The higher the intensity of the blue color, the more NH_3 the sample contains.

By diluting 2 mL of the primary stock solution in H_2O, a second stock solution is prepared containing 20 mg L^{-1} NH_3. From this stock solution samples of known concentration in the range of 0 to 6 mg L^{-1} NH_3 are prepared. The higher the intensity of the blue color, the more NH_3 the samples contains (see Fig. 3.7).
The calibration curve resulting from the concentration is displayed in Fig. 3.8. Utilizing the linear equation of the trend line of the calibration curve the NH_3 concentration is calculated from the measured UV/VIS absorption values. The VIS-spectrometer exhibits an inaccuracy of ± 0.004 in absorbance values. Additionally an error of ± 0.05 is added to the absorbance error due to the measurement uncertainties during the sample preparation. Therefore, the total error on the absorbance value of the spectrometer is ± 0.054. The impact of this error increases as the measured absorbance decreases. For instance, the calibration sample with the lowest concentration of 0.2 mg L^{-1} yielded an absorbance of 0.167 at a wavelength of 655 nm. Consequently, the spectrometer error translates to a significant relative deviation of ± 32 %.
As illustrated in Fig. 3.6, the calibration spectra for sample concentrations of 0.2 mg L^{-1} and 0.4 mg L^{-1} are relatively close to that of the 0.6 mg L^{-1} sample. Their absorbance values at 655 nm are excessive / over-concentrated, because both values exceed the expected calibration curve in Fig. 3.8.
Nevertheless, the coefficient of determination is very close to 1 ($R^2 = 0.998$), indicating a very good calibration curve. The giving slope equation is $y = 0.391x$, this results in an error / resolution limit of the spectrometer of 0.14 mg L^{-1} of NH_3.

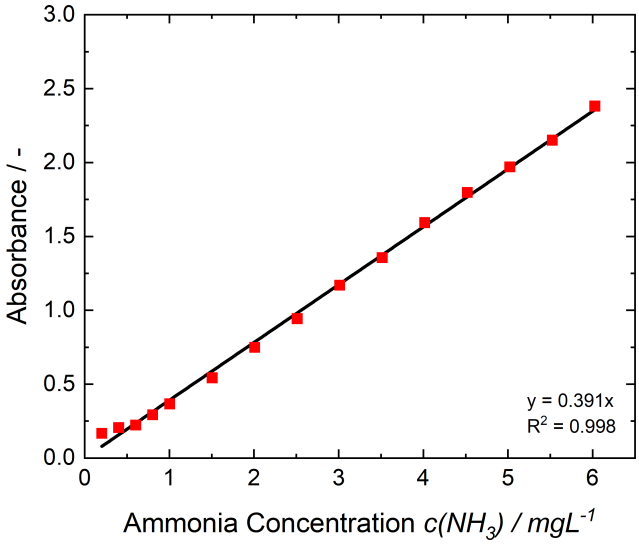


Fig. 3.8. Calibration line of the NH_3 samples of the known concentration in range from 0 to $6\,\mathrm{mg\,L^{-1}}$. The red dots are the measured absorbance of the calibration samples.

3.3.3 Determination of Ammonia

The two main parameters, which are of interest for evaluating the results are the NH_3 production rate *(R(NH$_3$))* and FE as noted in chapter 1.4. The production rate is defined as the amount of produced NH_3 per experimental time and catalyst area perpendicular to the ionic flux. The slope equation converts the absorbance value in a concentration value. The volume of the added sampled into the vessel is 2 mL. The total volume of the sample is the volume of the H_2SO_4 solution trap. This volume is 25 mL. The molar mass of NH_3 is $17.03\,\mathrm{g\,mol^{-1}}$. This leads to the following equation for *R(NH$_3$)*,

$$R(\mathrm{NH_3}) = \frac{c(\mathrm{NH_3})\ 25V}{2M(\mathrm{NH_3})}\ \frac{1}{t}\ \frac{1}{A}\ . \tag{3.6}$$

Where t is the time and A the active cell area of the cell.

The FE *(η)* gives the ratio of the charge *(Q(NH$_3$))* required for NH_3 synthesis in dependency of the total charge (Q_{tot}). The total charge is the sum of the charge required for NH_3 plus the required charge for the resulting H_2. The FE is calculated with

$$\eta(\mathrm{NH_3}) = \frac{Q(\mathrm{NH_3})}{Q_{tot}}\ . \tag{3.7}$$

Faraday's law delivers the value of the charge

$$Q = n\ z\ F\ , \tag{3.8}$$

where F is the Faraday constant $F = 96\,485\,\mathrm{C\,mol^{-1}}$, and z the number of electrons which are required for the reaction and n the amount of substance. Three electrons are needed for the NRR resulting in NH_3.

3.4 Catalyst and Electrode Production Processes

Three different catalyst production processes were used to synthesize catalysts. The catalyst layer needs to satisfy three criteria to be used in an electrochemical reaction. The criteria are protons access, reactant access and electronic conductivity [125].

3.4.1 Decal Process

For the ink production, the catalyst powder is initially humidified with H_2O and then shaken for homogenisation. Subsequently a Nafion solution "D1021" from Chemours™ is added, so that the Nafion content is 25 w% of the powder and the dispersion is mixed for homogenisation again. In the end an organic solution is added and the dispersion is shaked over again. After the ink solution is prepared, it is coated on a PTFE coated fiberglass substrate and dried.
The catalyst layer coated on the PTFE coated fiberglass is either hot pressed with the polymer membrane directly or on a PTL. In the case of Nafion, the hot pressing is done at its glass transition temperature of 130 °C. Additionally or in a second process step, the counter electrode with its catalyst layer is pressed on the membrane. After cooling, the MEA can be assembled into the cell.

3.4.2 Spray Coating

The spray coating is done with the "ExactaCoat" from Sonotek™. For spray coating the catalyst is also diluted with H_2O, an organic solvent and with the Nafion solution "D1021". The solution is filled in a syringe. The spray coater sprays the solution evenly either onto the membrane or on the PTL, which is placed on a plate. The spray coating occurs at 80 °C. The solvent evaporates at this temperature.

3.4.3 Galvanic Displacement Deposition

The galvanic displacement deposition is used for producing nanoparticle (NP) catalyst. As it is written previously, based on their size and shape NP has different properties than a bulk material. The small size enables quantum effects, change of optical properties, and changes in the electronic band structure [126]. In the case of galvanic deposition an electrical potential is applied. By adjusting the potential, the rate and extent of the deposition can be controlled. Spontaneous galvanic displacement deposition occurs without the need of a potential. Spontaneous galvanic displacement deposition is simple compared to other deposition methods, by just dipping the substrate in a plating solution made of metal salt [126]. Particles can grow directly on a conductive substrate. Carbon or Ni are used as PTLs, because the cost are low. In addition, the 3D structure and the high specific surface area result in macro pores in the PTL. These properties are beneficial for electrolyte penetration and gas diffusion within the PTL [127]. The shape and size of the deposited NP can be changed by the selection of the metal precursors, concentration, and deposition time [126].
The galvanic displacement deposition is a process where a less noble metal (in this case Ni) is exposed to a more noble metal (in this case Au). A spontaneous electrochemical reaction, a redox reaction occurs wherein the more noble metal is reduced by the electrons generated from the less noble metal [128]. The anodic and cathodic reaction can be written as

$$\mathrm{Ni} \longrightarrow \mathrm{Ni}^{n+} + \mathrm{ne}^{-} \,, \tag{3.9}$$

$$\mathrm{Au}^{n+} + \mathrm{ne}^{-} \longrightarrow \mathrm{Au} \,. \tag{3.10}$$

In this work Au is deposited on Ni electrodes via this deposition technique. Potassium tetrachloroaurate ($[KAuCl_4]$) is utilized as Au source, which is dissolved in distilled H_2O. The substrate is dipped in the solution for various amount of time, for studying the deposition time. Fig. 3.9 illustrates the schematic reaction. The upper graphic exhibits the initial conditions, a pure Ni substrate and dissolved $K[AuCl_4]$ molecules. Over time, Ni ions oxidize, dissolve and release electrons releases electrons. Au absorbs the electrons and is deposited on the substrate as pure metal.

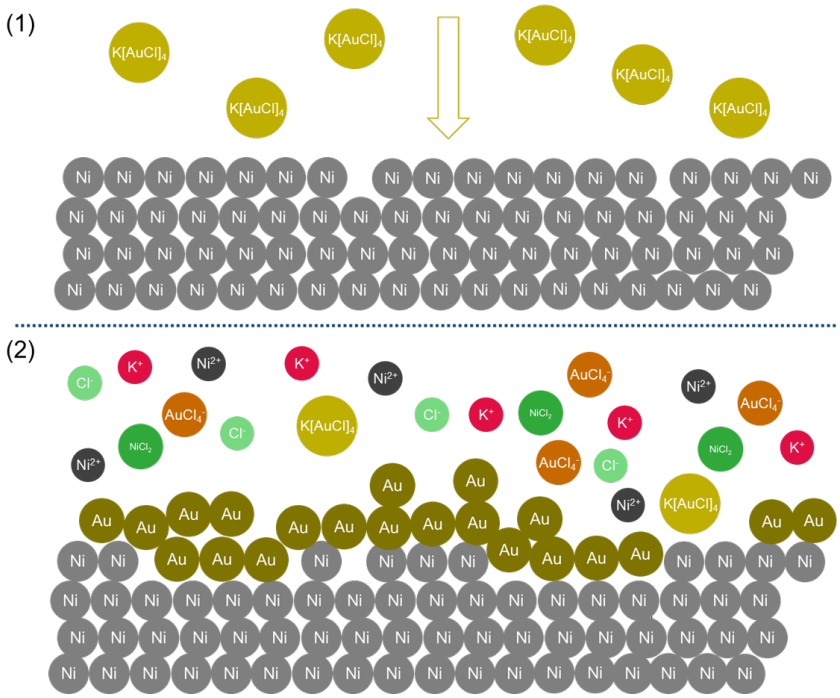


Fig. 3.9. Schematic illustration of the spontaneous galvanic displacement deposition process. Nickel is displaced with gold particles.

3.5 Electrochemical Measurement Methods

3.5.1 Overpotential

The reversible cell potential also called equilibrium potential *(U^0)* denotes the potential at which the electrochemical reactions forward and reverse processes occur without energy loss. This parameter is characterized by the difference between the electrode potentials (U_{cat} and U_{an}) (Eq. 3.11) in the unloaded state of the cell [129]

$$U^0 = U_{cat} - U_{an} \tag{3.11}$$

and no current results in this state. In the case of H_2O electrolysis the equilibrium potential is $U^0 = -1.23\,V$ ($U_{cat} = 0\,V$ $U_{an} = 1.23\,V$) at 1 bar and 25 °C. Under these conditions, the equilibrium potential is called standard potential. The electrode potential can be calculated from thermodynamic in dependency of the Gibbs free energy also known as Gibbs energy *(ΔG)*

$$\Delta G = -z\ F\ U\ . \tag{3.12}$$

Where z is the number of electrons and F the Faraday constant. If $\Delta G < 0$ the reaction occurs spontaneous, exothermic ($U > 0$) and if $\Delta G > 0$, energy in form of heat (endothermic) is required ($U < 0$). In the case of H_2O electrolysis the standard Gibbs energy is $\Delta G^0 = 237.35\,kJ\,mol^{-1}$, thus energy is required for the H_2O electrolysis.
However, the needed cell potential to run electrochemical reactions are always higher than the equilibrium potential, due to losses. The losses are referred to as overpotentials (η)

$$\eta_B = \Delta U - U^0\ . \tag{3.13}$$

Where η_B is the breakthrough potential, the difference between the potential at which the reaction takes place and the equilibrium potential. The efficiency of an electrolysis depends strongly from overpotentials, which are caused by several mechanism, inside the electrochemical cell. Thus, η is a sum of various overpotentials. Fig. 3.10 display polarisation curves of H_2O electrolysis at different temperatures.

The polarisation curves exhibit the reaction kinetic at 25 and 80 °C. The different overpotentials are shown in the graphic as well and are briefly explained.

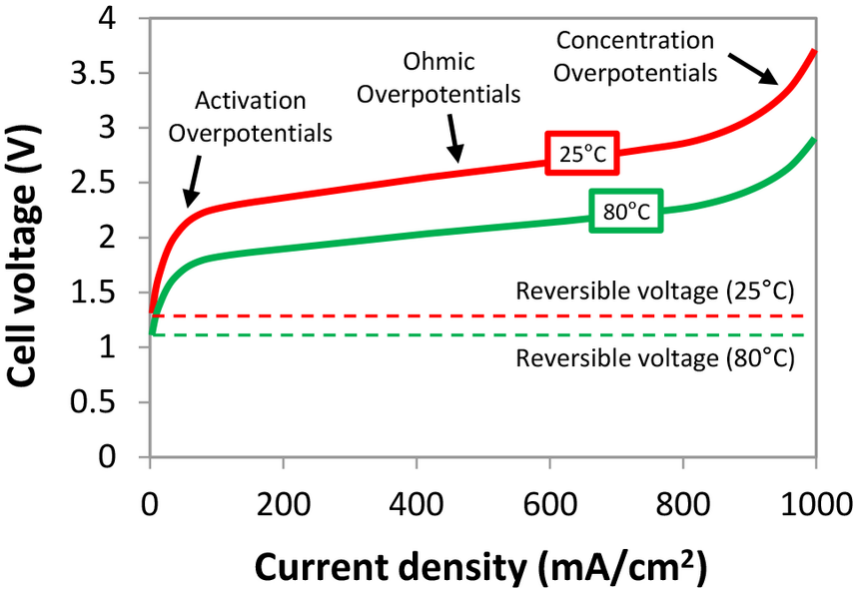


Fig. 3.10. Polarisation curves of H_2O electrolysis at 25 (red line) and 80 °C (green line). The resulting overpotentials actionvation, ohmic, and concentration are marked. The reversible cell potential of both temperatures are drawn as dashed lines with the respective color [130].

Charge Transfer Overpotential $\eta_{An/Ca}$

The charge transfer overpotential results due to the inhibited charge transfer between the electrolyte and the corresponding electrode. This overpotential is the required activation energy for starting the reaction, therefore it is referred as activation overpotential. The catalyst strongly affects the charge transfer overpotential. Furthermore, the charge transfer is influenced by the reactants, concentration of the electrolyte, and the temperature [131].

Ohmic Overpotential η_{Ω}

The ohmic losses which lead to this overpotential include the contact resistances of the PTL, bipolar plates, the catalyst layer, and interfacial resistance between different layers. A particularly large factor is the ionic conductivity of the membrane / electrolyte [132]. In terms of membranes, it is important that the membrane is sufficiently moistened. In addition, there should be no corrosion of the cell components, as this also leads to an increase in ohmic resistance.

Diffusion Overpotential η_{Diff}

Diffusion overpotential is also called concentration overpotential. The gas bubbles formation at the electrodes reduce the access of H_2O to the catalyst surface. In the beginning, the gas, which is formed is present in the dissolved form at the electrode surface [133]. Gas bubbles form when dissolved gases at the phase boundary reach a certain supersaturation [134]. The removal of dissolved gas occurs through diffusion. With escalating current densities and correspondingly increased gas production rates, the duration of diffusion becomes inadequate, resulting in gas accumulation within the cell. Consequently, this accumulation leads to an elevation in the in the resistance of the electrochemical cell. Gas bubble formation and gas bubble size depend on multitude of factors. These include the electrode material, electrode geometry, current density, temperature, operating pressure, and the flow rate of the reactants [135].

3.5.2 Electrochemical Impedance Spectroscopy

The resistance of an electrochemical cell is the result of many individual resistances of various cell components. The electrchemical double layer, a charged layer in between the catalyst layer of the electrode and the electrolyte, exhibits capacitive behavior. Diffusion processes exhibit a time or a frequency dependent resistance [136]. The superposition of these individual processes results in a frequency dependent cell impedance. Through the utilization of electrochemical impedance spectroscopy (EIS), detailed insights can be obtained regarding fundamental electrochenmical processes occuring within the electrochemical cell.

The measurement is carried out with an alternating voltage via varying the frequency applied to the electrochemical cell. The alternating voltage can be added to a base voltage so that the system can be measured in defined operating states [137]. The oscillating excitation voltage which is applied to the cell induces an alternating current response of the cell. The time shift between the voltage and the current is indicated by a phase angle (ϕ). The cell impedance *(Z)* is represented by a complex number which includes both the magnitude (amplitude) and the phase angle. The cell impedance is determined out of the current and the voltage. The impedance, the complex number consists out of a real part Re(Z) and an imaginary part Im(Z) [136, 138]. The EIS measurement can be done current controlled likewise.

Because, impedance spectra do not show the individual effects of each resistance, equivalent circuits are used for evaluating the impedance. Tab 3.1 presents elements of equivalent circuits for describing impedance spectra. The ohmic resistance is frequency independent and hence the phase displacement is for a pure ohmic resistance 0°. The current response of a capacitor is shifted by 90° due to the charging and discharging of the electrochemical double layer. The capacitor is completely permeable at high frequency and hence at these frequencies the ohmic resistance can be measured. The lower the frequency the more dominant the capacitor becomes [136, 138].

Tab. 3.1.: Impedance elements for EIS and their physical meaning.

Impedance element	Description	Physical meaning
R	Resistance	Electrolyte and permeation resistance
C	Capacity	Double layer capacity
L	Inductance	Cable inductance
W	Warburg	Diffusion influence
CPE	Constant phase element	Similar to capacity

The elements in the circuit can be arranged in parallel or in series. Fig. 3.11 shows a Randles circuit, which is one of the simplest and most common cell models for describing electrochemical systems. It includes an ohmic resistance (R_Ω) caused by the electroylte resistance, a parallel combination of a double layer capacitor (C_{DL}) and a charge transfer resistance (R_{CT}) [139]. The elements of a suitable equivalent circuit describe the physical quantities within the tested cell.

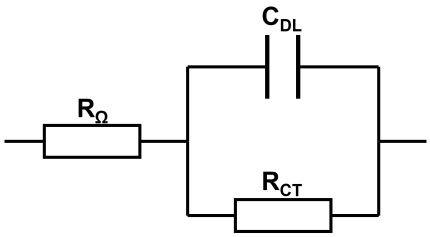


Fig. 3.11. Randle circuit for describing electrochemical systems. The randle cell consist of an ohmic resistance (R_Ω), which is in serial connection with a capacitor, which is connected in parallel with a resistor. The capacitor (C_{DL}) describes the electrochemical double layer and the resistance (R_{CT}) the charge transfer resistance.

Impedances can be illustrated by plotting the two impedance components in a so called Nyquist plot [140] (left graphic in Fig. 3.12). The imaginary ratio is plotted against the real ratio. In a Bode diagram the phase angle and real ratio and the logarithmic amplitude are plotted against the logarithmic value of the frequency [141]. The Bode plot is the right graphic in Fig. 3.12. The plots can be converted into each other.

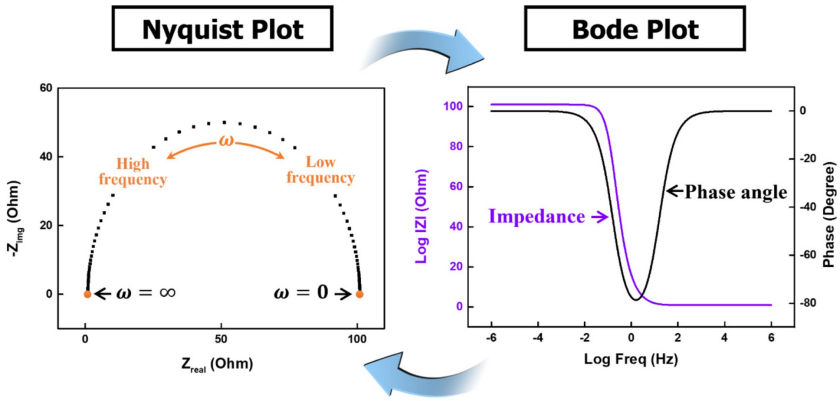


Fig. 3.12. The Nquist plot is shown on the left side and the Bode plot on the right side. They can be converted into each other [142].

4 Thermodynamic Evaluation of Ammonia Synthesis Processes

4.1 Introduction

In the preceding chapters, multiple techniques for NH_3 synthesis have been described, each with its unique pros and cons. The present chapter will highlight the thermodynamic and energetic aspects of these techniques. Three synthesis pathways are compared with each other and with the Haber-Bosch process.

4.1.1 Thermodynamic Values

Eq. 4.1 is the reaction equation of producing NH_3 out of N_2 and H_2

$$N_2 + 3\,H_2 \rightleftharpoons 2\,NH_3\ . \tag{4.1}$$

The reaction enthalpy $\Delta H_R(NH_3)$ and the reaction entropy $\Delta S_R(NH_3)$ of NH_3 refer to 298 K are [143]

$$\Delta H_R(NH_3) = -46.2\,\mathrm{kJ\,mol^{-1}}\ , \tag{4.2}$$
$$\Delta S_R(NH_3) = -99.06\,\mathrm{J\,mol^{-1}\,K^{-1}}\ . \tag{4.3}$$

The Gibbs energy (see. Eq. 3.12), can be calculated using the Gibbs-Helmholtz equation

$$\Delta G = \Delta H - T\ \Delta S\ . \tag{4.4}$$

The Gibbs energy is the work of a system at constant pressure ($\Delta p = 0\,Pa$). Where H is the enthalpy and S the entropy.
Hence, the Gibbs energy of NH_3 is $\Delta G(NH_3) = -16.68\,\mathrm{kJ\,mol^{-1}} = 931\,\mathrm{MJ\,t_{NH_3}{}^{-1}}$ at 298 K. The Gibbs energy of an electrochemical system is described with Eq. 3.12. Inserting the values in the equation, the standard potential of the reaction equation Eq. 4.1 is $\Delta U^0(NH_3) = 0.057\,V$. From the thermodynamic perspective, the reaction would occur spontaneously under this conditions. As the temperature increases, the Gibbs energy increases and the thermodynamic equilibrium is shifted towards the reactants and thus energy is required. However, due to the sluggish reaction kinetic, energy is required also at $\Delta G < 0$.
If H_2O is the reactant for producing H^+ instead of H_2, it leads to the NH_3 synthesis equation

$$3\,H_2O + N_2 \rightleftharpoons 2\,NH_3 + 1.5\,O_2\ . \tag{4.5}$$

More energy and thus a higher electrical potential is required $\Delta U^0(NH_3) = -1.17\,\mathrm{V}$. This results in a Gibbs energy of $\Delta G(NH_3) = 19.9\,\mathrm{GJ\,t_{NH_3}}^{-1}$.
Thermodynamic systems are described by heating values. The higher heating value (HHV), which correspond to the reaction enthalpy [129] and the lower heating value (LHV). LHV is the subtraction of the HHV with the heat of vaporisation. In the case of NH_3 the values are $HHV = 22.5\,\mathrm{GJ\,t_{NH_3}}^{-1}$ and $LHV = 18.6\,\mathrm{GJ\,t_{NH_3}}^{-1}$.

4.2 Haber-Bosch Process

As mentioned previously the Haber-Bosch process is strongly energy intensive [9]. In the middle of 1950s H_2 was gained from coal and therefore, the required energy consumption was 60 GJ $t_{NH_3}{}^{-1}$ [144]. Due to the methane reforming process and continuously optimisation of the process the energy requirement was reduced to 27.4 - 31.8 GJ $t_{NH_3}{}^{-1}$ [144]. Nevertheless, the energy waste is between 32 - 42 %, which respect to the LHV value of NH_3 (18.6 GJ $t_{NH_3}{}^{-1}$). A modern Haber-Bosch process emits roughly 1 - 2 % of the global CO_2 emissions [10–12]. Fig. 4.1 shows a schematic illustration of the Haber-Bosch process using fossil fuels as H_2 source. The N_2 is enriched with pressure swing adsorption (PSA), which is used for O_2 depletion.

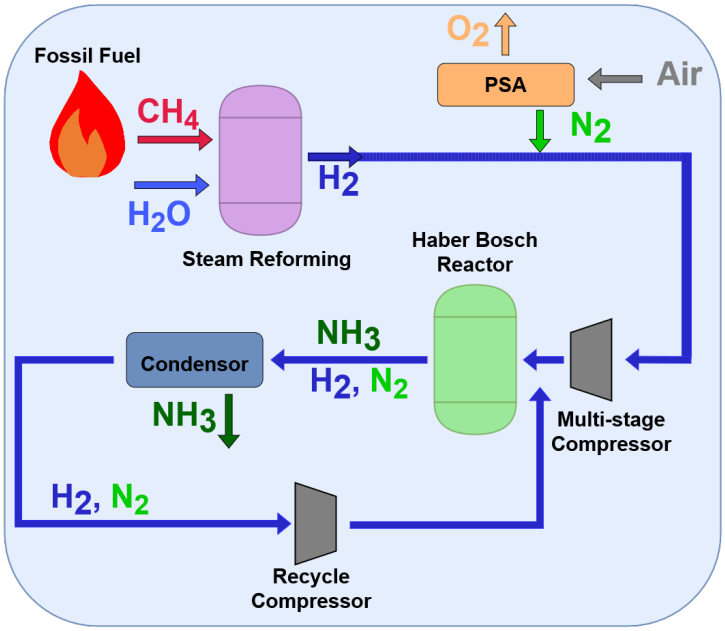


Fig. 4.1. Simplified illustration of the Haber-Bosch process. Fossil fuels and water are used to generate H_2 in the the steam reformer. N_2 from air is enriched with PSA. The reactants, H_2 and N_2 are then introduced into the Haber-Bosch reactor. NH_3 is synthesized in the Haber-Bosch reactor. NH_3 is condensed and the reactant gases that do not react are fed back into teh reactor. Own illustration based on the illustration of [144].

As written previously the Haber-Bosch process runs at high temperature to increase the reaction kinetic and the catalyst activity, but this shifts the equilibrium of the redox reaction to the reactant side. According to the Le Chatelier principle elevated pressure shifts the equilibrium of the NH_3 reaction to product side. While using Eq. 4.4 the Gibbs energy (red line) and the potential (blue line), that are required for the reaction Eq. 4.1 are plotted in Fig. 4.2 in dependency of the temperature. The temperature range where the eNRR (green area) and the Haber-Bosch process (orange area) operate are highlighted. From the thermodynamic point of view, the reaction is exothermic up to approximately 450 K. textitΔG 0 J mol^{-1} is marked as the black dashed line. ΔG is negative and thus U positive. The reaction would therefore take place voluntarily. But energy is required for the temperature region of the Haber-Bosch process.

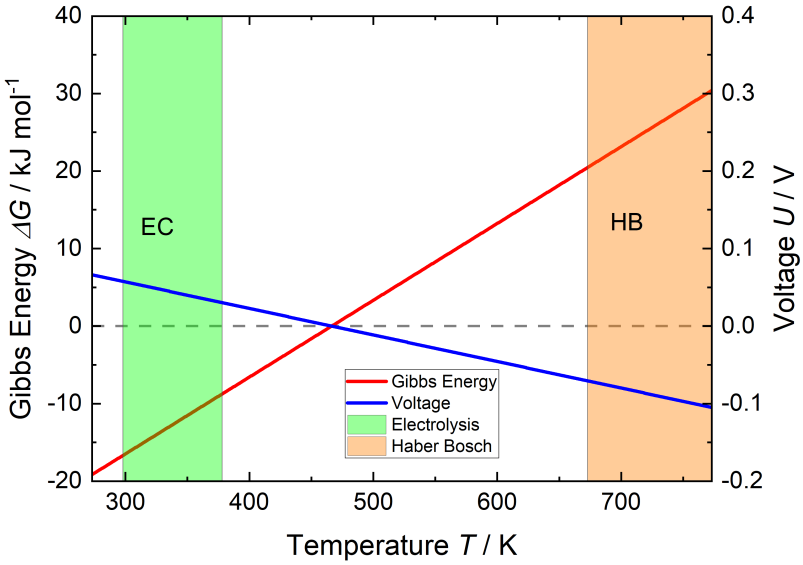


Fig. 4.2. Gibbs energy (red line, left y-axis) and voltage (blue line, right y-axis) considering constant enthalpy and entropy in dependency of temperature. The temperature ranges in which the electrochemical NH_3 synthesis (green area) and the Haber-Bosch process (orange area) operate are highlighted. The dashed grey line indicates the change from an exothermic to an endothermic process.

The chemical equilibrium constant (K) is determined as a function of the Gibbs energy and the temperature

$$K = e^{-\frac{\Delta G}{RT}} \,. \tag{4.6}$$

If K = 1 then the system is in equilibrium. In the case of K < 1, the thermodynamic system is on the side of the reactants and for K > 1, the thermodynamic system is on the side of the products. Therefore, Fig. 4.2 shows that the chemical equilibrium in the temperature range of the Haber-Bosch process favors the reactants, making NH_3 synthesis difficult. To overcome this, the pressure is increased during synthesis, even though the equilibrium constant remains independent of pressure, because the Gibbs energy is defined for a certain pressure and hence it does not change with pressure change [145] and thus K is also pressure independent

$$\left(\frac{\partial K}{\partial p}\right)_T = 0 \,. \tag{4.7}$$

The fact that the equilibrium constant is independent of pressure does not necessarily mean that the equilibrium composition is independent of the pressure, the composition depends on the partial pressures (p_x) and the concentrations of the elements [145]. The equilibrium constant can be written as follow,

$$K = \left(\frac{p_A}{p^\Theta}\right)^{\nu_A} \left(\frac{p_B}{p^\Theta}\right)^{\nu_B} \left(\frac{p_C}{p^\Theta}\right)^{\nu_C} \tag{4.8}$$

where ν_x is the stoichiometric factor and Θ the default pressure. Due to Dalton's law it applies

$$K = x_A^{\nu_A} \, x_B^{\nu_B} \, x_C^{\nu_C} \left(\frac{p}{p^\Theta}\right)^{\nu_A+\nu_B+\nu_C} \,. \tag{4.9}$$

Where x_x is the mol fraction of the element. K_x is introduced

$$K = \left(\frac{p}{p^\Theta}\right) K_x \tag{4.10}$$

and is declared as the part of the equilibrium constant expression, which contains the equilibrium mole fractions of the reactants and products.
In the case of the reaction equation of NH_3 synthesis (Eq. 4.1) it leads to

$$K = \frac{\left(\frac{p(\mathrm{NH_3})}{p^{\ominus}}\right)^2}{\left(\frac{p(\mathrm{H_2})}{p^{\ominus}}\right)^3 \left(\frac{p_{N_2}}{p^{\ominus}}\right)} , \tag{4.11}$$

and

$$K_x = \frac{K}{\left(\frac{p}{p^{\ominus}}\right)^{2-3-1}} . \tag{4.12}$$

Fig. 4.3 exhibits K_x in dependency of the pressure and temperature. The red characteristic curve on the left-hand y-axis shows the K_x values at a constant pressure of 1 bar against the temperature. In blue on the right-hand y-axis, K_x is shown for a pressure of 200 bar. It can be seen that K_x at 1 bar is initially greater than 1 and therefore the chemical equilibrium is on the product side. However, from approximately 450 K the equilibrium shifts to the reactant side ($K_x < 1$) and thus the equilibrium in the Haber-Bosch process is shifted to the reactant side. Through, due to the strong increase in pressure (blue curve), $K_x > 1$ in the temperature region of the Haber-Bosch process.

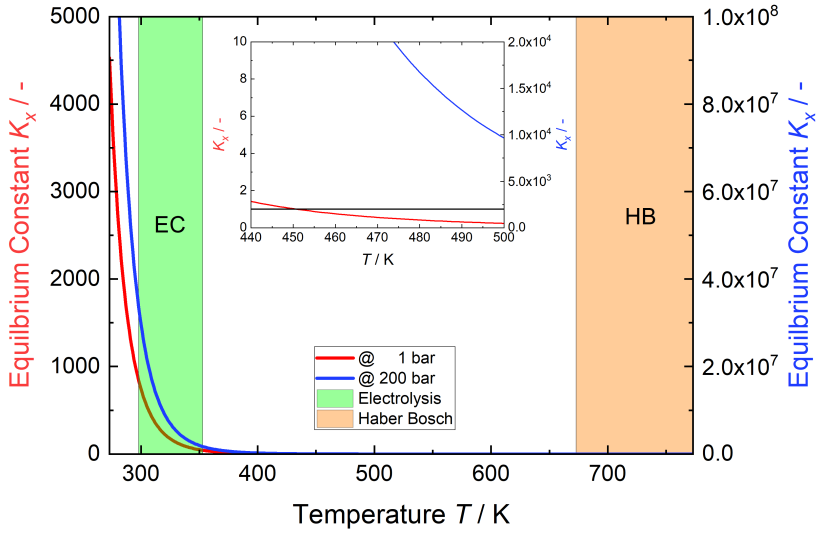


Fig. 4.3. The equilibrium constant K_x at 1 bar (red line) and 200 bar (blue line) depends on the temperature. The small graphic in this figure shows the trend of the K_x in the temperature region from 440 to 500 °C. In case of a constant pressure at 1 bar, K_x falls below 1, thus the Haber-Bosch process shifts to the reactant side The temperature ranges in which the electrochemical NH_3 synthesis (green area) and the Haber-Bosch process (orange area) operate are highlighted.

4.3 Electrified Haber-Bosch Process

Fig. 4.4 illustrates the electrified Haber-Bosch process. In this case H_2 is produced via water electrolysis and without steam reforming. N_2 is enriched and O_2 depleted as well with PSA. The produced H_2 and N_2 are introduced into the Haber-Bosch reactor like it is done in the traditional Haber-Bosch process.

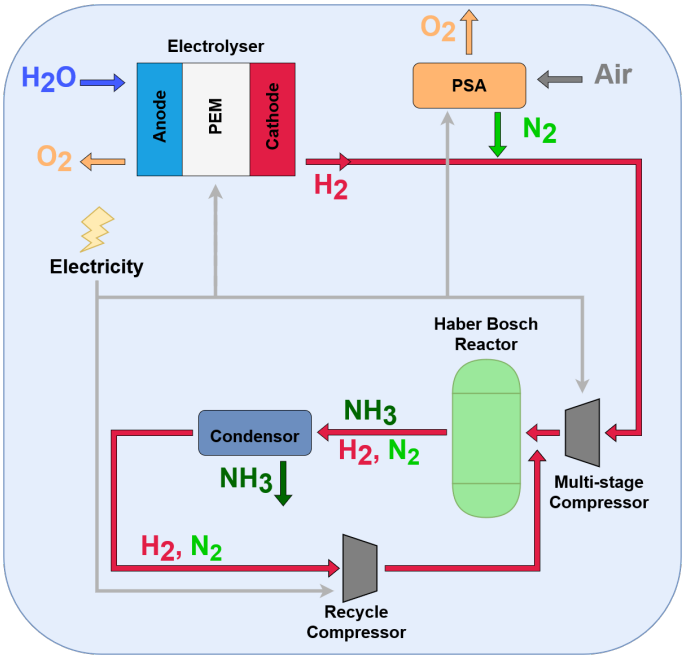


Fig. 4.4. Schematic illustration of the electrified Haber-Bosch process. A water electrolyzer is utilized to produce H_2 from H_2O. The further part of the process is the same as the process of the Haber-Bosch process. Own illustration based on the illustration of [144].

The LHV of H_2 is $120\,\mathrm{GJ\,t^{-1}}$ and the HHV is $142\,\mathrm{GJ\,t^{-1}}$. The difference between these values is the molar enthalpy of water vaporization, which is $44.01\,\mathrm{kJ\,mol^{-1}}$, $22\,\mathrm{GJ\,t^{-1}}$ [146]. In the context of technical H_2O electrolysis, the heat necessary for the reaction has conventionally originated directly electrical energy input. Therefore, the HHV serves as the fundamental parameter for energy calculations. It is assumed that the maximum achievable useful energy is the Gibbs energy, as it is the maximum electrical energy that can be obtained during combustion of H_2. For the NH_3 synthesis three H-atoms are needed. The molar mass fraction of H ($M(H) = 1.01\,\mathrm{g\,mol^{-1}}$) in NH_3 ($M(NH_3) = 17.03\,\mathrm{g\,mol^{-1}}$) is

$$\chi M = \frac{3.03}{17.03} \tag{4.13}$$

χM = 0.178. Regarding the production of 1 t of NH_3, then 177.92 kg H_2 are required. Considering the Gibbs energy of H_2O electrolysis to produce 1 mol of H_2 $\Delta G^0(H_2)$ = 273.35 kJ mol^{-1}, 20.93 GJ are required for producing 177.92 kg of H_2.

In the idealistic case, the energy value of HHV is sufficient to drive the electrochemical reaction and to provide the heat to maintain constant temperature. In terms of 177.92 kg of H_2, HHV = 25.26 GJ. This lead to an efficiency of 83 % (20.93 / 25.26). As a consequence 4.33 GJ $t_{NH_3}{}^{-1}$ are present as residual heat. Smith et al. [144] assumed that further 3.76 GJ $t_{NH_3}{}^{-1}$ are lost due to the production of N_2 and the steam turbine compressors, because in the idealistic case the H_2O electrolysis operates at atmospheric pressure. Thus, with the respect to the NH_3 production the efficiency is 81 % (19.9/24.69). Therefore, the total efficiency of the electrified Haber-Bosch process is 67 %.

In general, shifting from the steam reforming to H_2O electrolysis leads to increase of energy loss for the H_2 production due to the lower energy efficiency of the current H_2O electrolysis. The efficiency of H_2O electrolysis is between 62 - 74 % at present [146]. But, the energy loss in the synthesis loop decreases due to several reasons. The H_2O electrolysis can be operated under pressure and this offsets the gas compression energy. Purging is not necessary anymore, due to the purity of H_2 and N_2. Also, the compressors are powered from more efficient electric motors instead of steam turbines [144]. In principle, this process can be completely CO_2-neutral. However, under current conditions, a reduction of 78 % is achieved [144]. Thus, the technology is much more environmentally beneficial. Another advantage of the electrically driven Haber-Bosch process is that the facility is smaller and decentralized production is feasible. The outcome of this process development is that the NH_3 can be produced at the location where H_2 is gained.

Compared to the other NH_3 synthesis processes mentioned (Li mediated and direct electrochemical), the Haber-Bosch process and H_2O electrolysis are two processes that are technically understood and established. Therefore, the electrified Haber-Bosch process is the process with the highest technological readiness level. This process has an acceptable energy efficiency. The disadvantages are that still the high pressures 300 - 400 bar and high temperatures 400 - 500 °C are required to run the process. Additionally, several process steps have to be executed, which leads to a quite complex and big facility.

4.4 Li mediated Synthesis

The principle of the Lithium mediated synthesis is explained in chapter 1.4.1. The solution contains Li^+-ions which are reduced to Li by the electrical potential. Li reacts with N_2 to form Li_3N, which leads to the formation of NH_3 in further steps. This synthesis pathway provides a high NH_3 production rate of $53 \times 10^{-9}\,\mathrm{mol\,cm^{-2}\,s^{-1}}$ and a high FE of 69 % at a relative low pressure of 20 bar and room temperature. The advantage of this synthesis system is that the reaction has a very high selectivity, as no H_2O is present and therefore no competing H_2 formation can take place, resulting in a high FE for the NH_3 synthesis. On the other hand the H_2O-free electrolyte complicates the H^+ generation. Furthermore, the investment costs are low and small facilities are construable and the small facilities enable a decentralized production. However, the limiting maximum energy efficiency due to the high required reduction potential of (Li/Li^+) $U^0 = -3.04\,V$ is the biggest drawback of this synthesis pathway. This electrode potential results in a minimum Gibbs energy of $\Delta G(NH_3) = 879\,946.3\,J\,mol^{-1}$, which corresponds to $\Delta G(NH_3) = 51.67\,GJ\,{t_{NH_3}}^{-1}$.
From this values follows the efficiency regarding the $HHV(NH_3)$. The efficiency is approximately 44 % (22.5 / 51.67). Regarding the Gibbs energy of NH_3 the efficiency is 39 % (19.9 / 51.67). In addition to the high energy loss, the high potential leads to electrode degradation and instability over time.

4.5 Direct Electrochemical Ammonia Synthesis

The electrochemical NH_3 synthesis can operate from the acid to alkaline environment as noted previously in chapter 2. In both environments if liquid H_2O and N_2 are used as reactants the reaction Eq. 4.5 results. The standard anode potential is $U_A^0 = 1.23\,V$ vs. NHE and the standard cathode potential is $U_C^0 = 0.057$ V vs. NHE resulting in a standard electrode potential of $U^0 = -1.17\,V$.

Fig. 4.5 displays the synthesis of NH_3 in an alkaline MEA cell. H_2O or mostly KOH are introduced into the anode PTL. KOH is normally used, because as a strong base it dissolves in H_2O, resulting in a high concentration of freely mobile OH^-. Due to the applied potential, OH^- oxidizes into H_2O and O_2 in the catalyst layer. H_2O diffuses through the membrane or diaphragm to cathode side

$$\text{Anode:} \qquad 4\,OH^- \longrightarrow O_2 + 2\,H_2O + 4\,e^- \tag{4.14}$$

$$\text{Cathode:} \qquad N_2 + 6\,H_2O + 6\,e^- \longrightarrow 2\,NH_3 + 6\,OH^- \tag{4.15}$$

and is reduced to OH^-. Subsequently N_2 is reduced to NH_3.

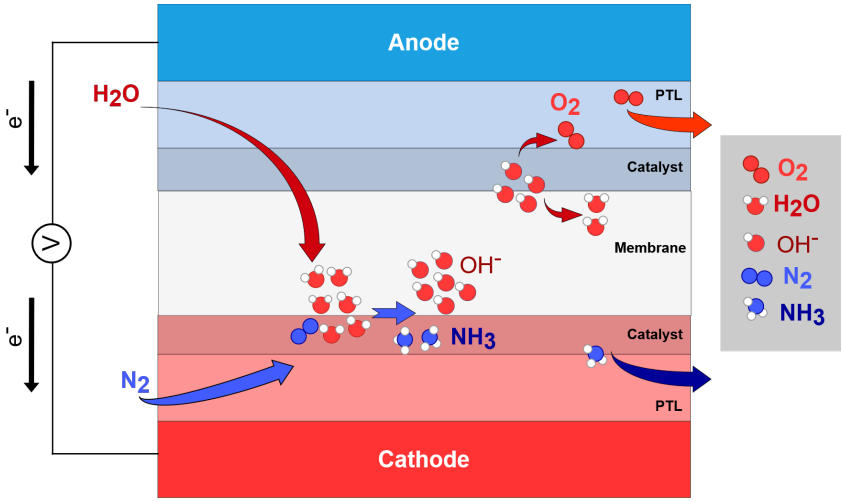


Fig. 4.5. Schematic illustration of the direct electrochemical NH_3 synthesis and the movement of molecules and ions in an alkaline cell. H_2O is introduced into the PTL of the anode, where it diffuses through the membrane. N_2, which is supplied at the cathode, reacts with H_2O and the electrons to NH_3 and OH^- in the catalyst layer. This process is facilitated by the applied electrical energy. The resulting NH_3 exits the cell on the cathode side. Concurrently. OH^- diffuses through the membrane and oxidizes to O_2 and H_2O. The produced O_2 exits the cell on the anode side. The coloring of the atoms is done according to the CPK color model.

The Gibbs energy of the reaction equation is $\Delta G(NH_3) = 339\,322\,\mathrm{J\,mol^{-1}}$ and it results in an energy requirement of $19.9\,\mathrm{GJ\,t_{NH_3}{}^{-1}}$ at 1 bar and 298 K for executing this equation. However the energy which is sufficient not only to drive the cell reaction, but to also provide the heat necessary to maintain a constant temperature is $HHV(NH_3) = 22.5\,\mathrm{GJ\,t_{NH_3}{}^{-1}}$. Therefore, in this case, the energy loss is only the evaporation enthalpy. This leads to energy loss of 11.5 % (19.9 / 22.5). Hence, the energy loss is much less compared to the other pathways. However, the NH_3 production rate is very low and so the electrochemcical synthesis is far away from commercial utilization.

4.5.1 pH Dependency

As written previously the activity and selectivity of the NRR is quite challenging. Due to these reasons, it is necessary to minimize the HER. It is known that the electrolyte pH-value affects the binding energy of H_2 [73] and the solubility of N_2 [147]. In acidic electrolytes HER is favored while alkaline electrolytes suppress H^+ supply and transfer. To study the influence of the pH on the thermodynamic stability of chemical compounds, the pH-value is set in relation to the potential and this is shown in a Pourbaix-diagram.

Fig 4.6 presents the Pourbaix-diagram for N_2 and regions of thermodynamic stability are graphically displayed in case of introducing N_2 into H_2O. The red solid line displays the equilibrium potential, which is required to reduce N_2 at the specific pH-value in H_2O. The blue solid line depicts the equilibrium potential of the N_2 oxidation reaction. The black dotted lines represents the values for the competing H_2O reduction and oxidation reaction. The reduction line of N_2 results out of the reduction from N_2 to $NH_4{}^+$

$$N_2(g) + 8\,H^+(aq) + 6\,e^- \rightleftharpoons 2\,NH_4{}^+(aq)\ . \tag{4.16}$$

in the pH range from 0 to 9.2 (the vertical red line), because the reaction equation of $NH_4{}^+$ formation is dominant. The Gibbs energy of $NH_4{}^+$ is $\Delta G^0(NH_4{}^+ = -79.31\,kJ\,mol^{-1}$, resulting in a potential of $U^0 = 0.274\,V$ vs. SHE. Then, from pH 9.2 to 14 the NH_3 formation is dominant. Resulting in the reaction equation

$$N_2(g) + 2\,H_2O(l) + 6\,H^+(aq) + 6\,e^- \rightleftharpoons 2\,NH_3 \cdot H_2O(aq)\ . \tag{4.17}$$

The Gibbs energy at pH 0 is $\Delta G^0(NH_3 = -26.50\,kJ\,mol^{-1}$, resulting in a potential of $U^0 = 0.092\,V$ vs. SHE.
Hence, at a pH-value of 0, both equilibrium potentials are positive, which lead to exothermic reactions from the thermodynamic point of view. However, From 0 to a pH-value of 9.2 the formation of $NH_4{}^+$ is dominant. Therefore, it is expected that $NH_4{}^+$ is formed below pH 9.2 instead of NH_3. Due to this, there is only a narrow potential range in the alkaline environment, where NRR can proceed without being disturbed by the HER.

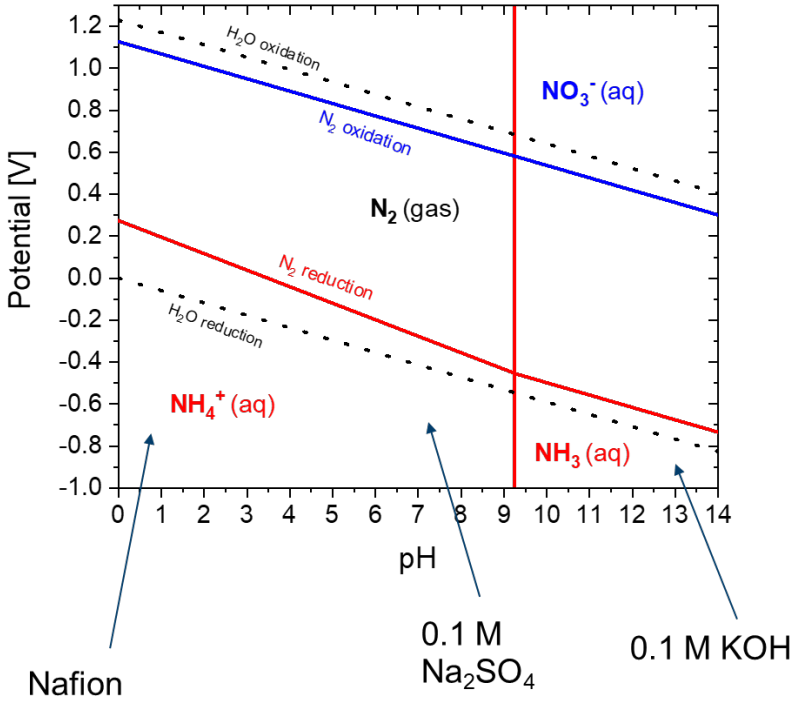


Fig. 4.6. Pourbaix diagram for N_2 and H_2O. The red solid line represents the NRR to NH_4^+ or NH_3. The blue solid line represents the N_2 oxidation to NO_3^-. The black dotted lines denote the H_2O reduction and oxidation.

The potential window where only eNRR can occur under ideal thermodynamic conditions is quite small. However, overpotentials which result in realistic systems are not considered in Fig. 4.6. As a result of these overpotentials the potential required for the NRR is from absolute value greater than the theoretical equilibrium potential (pH 14: $U^0 = -0.734\,\mathrm{V}$). This means that the HER cannot be avoided. Moreover, it was found that the impact of the electrolytes and the pH is not universal [11]. For this reason, the NH_3 synthesis was carried out at different pH-values with different electrolytes for researching the pH influence. The pH-values of the used electrolytes, Nafion as the polymer electrolyte and aqueous solutions of Na_2SO_4 and KOH are shown in Fig. 4.6 as well.

4.6 Summary and Conclusion

In this section, the results of this chapter are summarized and the thermodynamic energy efficiency limits of the three ammonia synthesis pathways electrified Haber-Bosch process, Li mediated electrosynthesis and direct electrochemical synthesis are evaluated. As presented, each pathway has advantages and disadvantages. The main advantage and the thermodynamic energy efficiency of these pathways are presented in Tab. 4.1. Considering the research focus of this thesis, which concentrates on direct electrochemical NH_3 synthesis, an efficiency of 89 % is feasible, representing the highest thermodynamic energy efficiency of compared pathways. In conclusion, the losses of the three synthesis pathways that occur during the electrochemical conversion of electrical energy into NH_3 and the thermodynamic efficiency are graphically presented in Fig. **??**.

Tab. 4.1.: Thermodynamic energy efficiency of the three synthesis pathways and their specific advantage.

Pathway	Efficiency	Advantage
Electrified Haber-Bosch	67 %	Known technology
Lithium mediated electrosynthesis	39 %	High rates
Direct electrosynthesis	89 %	High efficiency

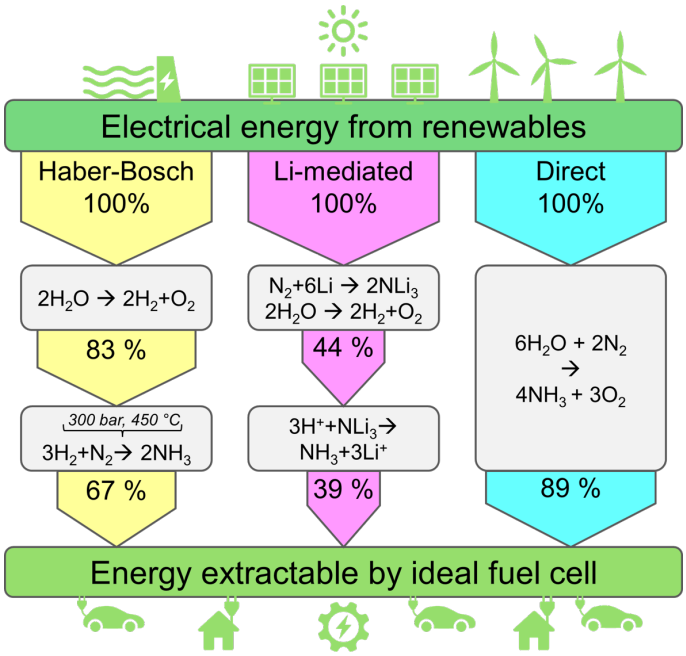


Fig. 4.7. Graphical illustration of the energy losses that occur during the electrochemical conversion of electrical energy into NH_3 and the thermodynamic efficiency of the three NH_3 synthesis pathways.

5 Eletrochemical Reactants Synthesis

5.1 Introduction

In this chapter the electrochemical reactants synthesis are described. As noted previously NH_3 is a molecule that consists out of hydrogen and nitrogen. By means of water electrolysis H_2 is produced electrochemically out of H_2O by the HER. The study of water electrolysis is not part of this thesis. Therefore, the process is just explained briefly. The process of N_2 enrichment from air and the associated reduction of O_2 is carried out and studied electrochemically. This process is described in section 5.3.

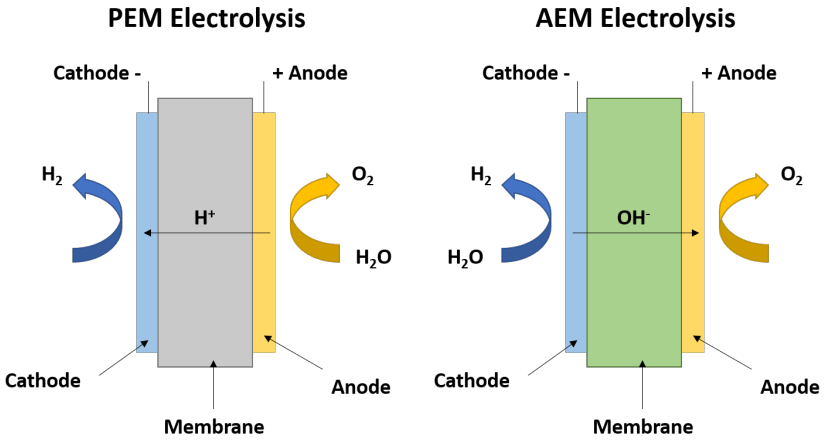
5.2 Water Electrolysis

Water electrolysis is a technology, which allows the splitting of water in H_2 and O_2

$$2\,H_2O(l) \rightleftharpoons 2\,H_2(g) + O_2(g) \tag{5.1}$$

when an electrical current is applied. This technology allows the generation of "green" H_2 without producing climate-damaging CO_2 or other climate-damaging products [148].

In principle, water electrolysis is divided into four technical variants. These are the high-temperature electrolysis (SOEC), alkaline electrolysis (AEL), proton exchange membrane electrolysis (PEM) and anion exchange membrane electrolysis (AEM). The PEM and AEM are briefly explained and are illustrated in Fig. 5.1.



(a) PEM electrolysis cell with reactants and products.

(b) AEM electrolysis cell with reactants and products.

Fig. 5.1. Water electrolysis cells in acid and alkaline environment [149].

PEM water electrolysis works in the acid or neutral environment. The membrane consist of a proton conducting polymer, which separates the reaction products H_2 and O_2, otherwise H_2 and O_2 react with an enormous release of energy. The membrane is the ionic contact between anode and cathode, which allows the transport of protons and it is electrically insulating [148]. The proton conductivity is due to the sulfonic acid groups bound into a perfluorinated polymer [150]. The temperature and the relative humidity influences strongly the ion conductivity of the membrane [151]. A distinction is made between two different transport processes inside the membrane the Grotthuss (hopping) mechanism and the vehicle (diffusion) mechanism. H^+ is transferred from hydronium ions (H_3O^+) to H_2O molecules. H_2O becomes ionized and passed H^+ to the next H_2O molecules. Hence, the protons are hopping from one H_2O molecule to the next. The Grotthuss mechanism plays the major role at high H_2O content of the membrane. Thus, a decreasing water content leads to decreasing H^+ conductivity [152]. In the vehicle mechanism H^+ connects with H_2O molecules to form H_3O^+ ions. These ions act as vehicles for the protons. Above 85 °C this mechanism becomes predominant. Furthermore the water transport needs to be balanced, because H^+ carries H_2O molecules through electro-osmosis.

As written Nafion is used as a polymer membrane by default [105]. Usually the electrodes and catalyst layers are hot pressed with the membrane. This leads to a better ionic conductivity, a larger current and thus to an improved H_2 production [153, 154]. The redox reaction of PEM is

$$\text{Anode:} \qquad 2\,H_2O \longrightarrow 4\,H^+ + 4\,e^- + O_2 \tag{5.2}$$

$$\text{Cathode:} \qquad 4\,H^+ + 4\,e^- \longrightarrow 2\,H_2\,. \tag{5.3}$$

H_2O is split into O_2 and four H^+ at the anode (Eq. 5.2). H^+ diffuses through the membrane and is reduced to H_2 at the cathode (Eq. 5.3).

Anode and cathode in an AEM electrolysis are separated with an anion conducting polymer. The membrane is anion conducting, electric isolating and separates the gases H_2 and O_2 [155]. Right now, an AEM membrane has not been synthesized, which has an ion conductivity comparable with Nafion as the standard PEM membrane. Moreover, the AEM membrane lacks in the combination of chemical and mechanical stability regarding high pH and high temperature environments [156]. The redox reaction of the AEM is

$$\text{Anode:} \qquad 4\,OH^- \longrightarrow 2\,H_2O + O_2 + 4\,e^- \tag{5.4}$$

$$\text{Cathode:} \qquad 4\,H_2O + 4\,e^- \longrightarrow 2\,H_2 + 4\,OH^-\,. \tag{5.5}$$

H_2O is split into H_2 and OH^- at the cathode. H_2 rises as a gas and can be stored or used in a fuel cell. OH^- diffuse through the membrane to the anode (see. Fig. 5.1b) and at the anode the OH^- ions are oxidized to H_2O and O_2.
The most common electrolysis process that is still used today is alkaline electrolysis (AEL). Instead of an membrane a diaphragm is used and concentrated KOH is needed as electrolyte. Due to the diaphragm the ion conductivity is poor and the ohmic resistance is high. For this reason, intensive research is being carried out on the AEM.

Both electrolysis methods offer advantages and disadvantages. The PEM electrolysis reaches current densities above $3\,A\,cm^{-2}$ at $2\,V$ and $80\,°C$ [157]. The high current densities are possible due to the ion conducting membrane. In AEL these current densities are not possible, because the the ion conductivity is poor. Furthermore, a polymer electrolyte membrane leads to a lower ohmic resistance, because it can be up to 20 times thinner compared to a diaphragm [148] and which reduced the ohmic resistance. However, the investment costs are higher. They are at least 1000€ per kilo watt power. Moreover, as a result of the acidic environment the materials have to be very robust. This means, that expensive materials like platinum or iridium are needed as a catalyst material and for the cell components titanium is

used.

The AEM combines the positive aspect of AEL and PEM. The investment costs are low due to the reason that relatively cheap materials like nickel, cobalt or iron can be used as catalyst. An ion conducting membrane is used as separating medium, which enables better ion conductivity. Thus, a high and effective H_2 production is feasible [158]. But nevertheless as mentioned before, the biggest challenge, drawback right now is the low ion conductivity, which is 3 - 10 times lower than the ion conductivity of Nafion [159]. Additionally, the mechanical and chemical stability of AEMs is not comparable with Nafion [156]. Therefore, the AEM cannot compete technological and economical with PEM and AEL at the current state.

5.3 Oxygen Depletion

5.3.1 Introduction

Electrochemical oxygen depletion using an oxygen-depolarized cathode offers the possibility of a green, carbon dioxide neutral, separation of N_2 and O_2 from air. The gained N_2 can be used as a source for electrochemical NH_3 synthesis. During the electrochemical reaction using O_2 depolarized cells, H_2O is oxidized at the anode, where H^+ and O_2 are also produced. The pure O_2 can be used in different fields such as in medicine, including in the treatment of patients suffering from heart or lung diseases [160]. The oxygen can also be used as an oxidant in fuel cells, instead of air. The partial pressure is higher and the needed volume is less. Fuel cells enable a CO_2 neutral energy supply [161].
Argon (Ar), CO_2 and other noble gases are still present in the gas. The noble gases do not influence the process. CO_2 can be removed by means of liquid or solid adsorbents [162]. Currently, for the large-scale separation of N_2 and O_2 cryogenic air separation and pressure swing adsorption (PSA) are the most utilized technologies [160].

5.3.2 Oxygen Separation Techniques

Cryogenic Air Separation

Cryogenic air separation is currently the most efficient and cost-effective technology for producing large quantities of O_2, N_2, and Ar as gases or liquids [163]. In the first step the air is compressed and then the air is cooled and purified. Thus dust particles, CO_2, water vapor and hydrocarbons are removed [163, 164]. By means of low temperature heat exchange the process is cooled down to nearly liquefaction temperature, cryogenic temperatures (below $-150\,°C$). The air is distilled into N_2, O_2 and optionally Ar. The product stream is warmed against the incoming air feed to conserve refrigeration. Via configuration of heat exchange and distillation equipment the air is separated into the required product streams [163, 164]. It enables a very pure production of N_2 ($> 99\,\%$), but it is an energy intensive process [165]. Cryogenic N_2 takes about $0.7\,kWh$ per norm cubic meter (Nm^3) of N_2 resulting in $0.89\,kWh$ for $1\,kg$ N_2 ($\rho(N_2) = 1.25\,kg\,m^{-3}$) [166].

Pressure Swing Adsorption

PSA is based on physical adsorption. In dependency of the produced gas N_2 or O_2 different adsorbent are used. In the case of N_2 production carbon molecular sieves (CMS) adsorbents are used. Due to the fact that O_2 is adsorbed much faster than N_2, a separation is possible. In terms of O_2 production Zeolites are used [166].
PSA systems consist out of two towers filled with CMS. The driving force of this diffusion controlled process is the partial pressure. Therefore, the adsorption is done at higher pressure (8 bar). While the desorption is carried out at atmospheric pressure [166]. O_2 is adsorbed in the tower and N_2 (and the other air components) leave the tower. The gas flow velocity through the CMS filled tower determines the remaining O_2 content. At the same time, in the other vessel the desorption of the previously captured O_2 takes place by reducing the pressure to ambient pressure. Thus, continuous production is possible through the two towers. The adsorption time is between 60 to 120 s [166]. This technology offers purity's in the range of 95 - 99.9 % N_2 at flow rates up to 3000 N m^3 h^{-1}. The necessary energy, electrical power for reducing the O_2 content depends on the desired purity of N_2. The electrical power for PSA is 0.31 kWh per Nm^3 of N_2 resulting in 0.39 kWh for the production of 1 kg of N_2, assuming a residual O_2 concentration of 1 %. When the residual O_2 concentration decreases to 0.1 %, the corresponding required electrical power demand escalates to 0.58 kWh per 1 kg of N_2 [166].

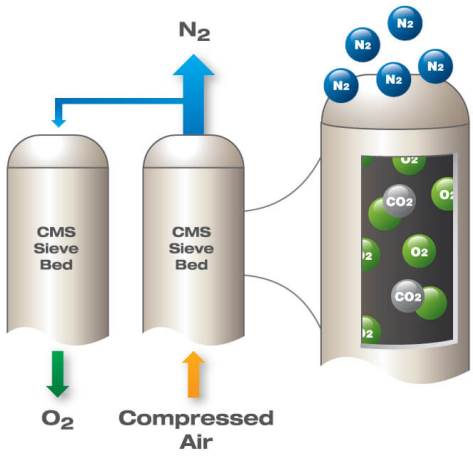


Fig. 5.2. Illustration of the pressure swing adsorption method, which is based on physical adsorption. The carbon molecular sieves adsorb O_2 at high pressure, leading to the separation of O_2 and N_2. At the same time, in the other tower vessel the previous captured O_2 desorbs by reducing the pressure to ambient pressure. The figure is taken from [167].

Electrochemical Oxygen Depletion Cell

This separation technique uses a polymer electrolyte membrane as separation medium. The membrane can be a PEM or an AEM. The membrane is chosen with respect to the environment, catalysts and electrodes. In the case of an acidic environment, Nafion can be used [168]. Fig. 5.3 displays schematically the cell and the flow of the reactants and products.

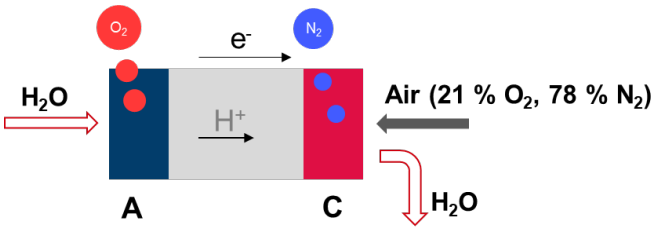


Fig. 5.3. Illustration of the oxygen depletion cell with the incoming H_2O and air. Resulting in O_2 production on anode side and N_2 accumulation and O_2 depletion on cathode side.

In this particular application, during the electrochemical process in an acid or neutral environment, H_2O is introduced on the anode side, while air is supplied at the cathode. An electrical potential is applied across the cell, resulting in the redox reaction

$$\text{Anode:} \qquad 2\,H_2O(l) \longrightarrow 4\,H^+ + 4\,e^- + O_2(g) \tag{5.6}$$

$$\text{Cathode:} \qquad O_2(g) + 4\,H^+ + 4\,e^- \longrightarrow 2H_2O(l)\,. \tag{5.7}$$

The H_2O molecules oxidize at the anode, resulting in the generation of H^+ and O_2 (Eq. 5.6). These H^+ subsequently diffuse through the membrane and react with O_2 from the incoming air to form H_2O molecules at the cathode (Eq. 5.7).
The relative content of N_2 in the air increases at the outlet of the cell. Within the gas flow remains N_2 , CO_2, and Ar as well as other noble gases. From the thermodynamic viewpoint, this reaction is possible at $U^0 = 0\,V$, if the concentration gradient from the anode to the cathode side is not considered. Due to over potentials and the concentration gradient, an applied potential is necessary. The increase of potential resulting from the Nernst potential is

$$U = U^0 + \frac{RT}{zF} \ln \frac{C_{Ox}}{C_{Re}} . \tag{5.8}$$

Where C are the concentrations of O_2 on the anode (C_{Ox}) and cathode (C_{Re}) side. R is the ideal gas constant $R = 8.314\,J\,K^{-1}\,mol^{-1}$ and T the temperature. The dependency of the O_2 concentration on the cathode side is displayed in Fig. 5.4. To achieve 1 % of remaining O_2 in the gas stream, a Nernst potential of 30 mV is required. For 0.1 % of O_2, the required potential is 44 mV.

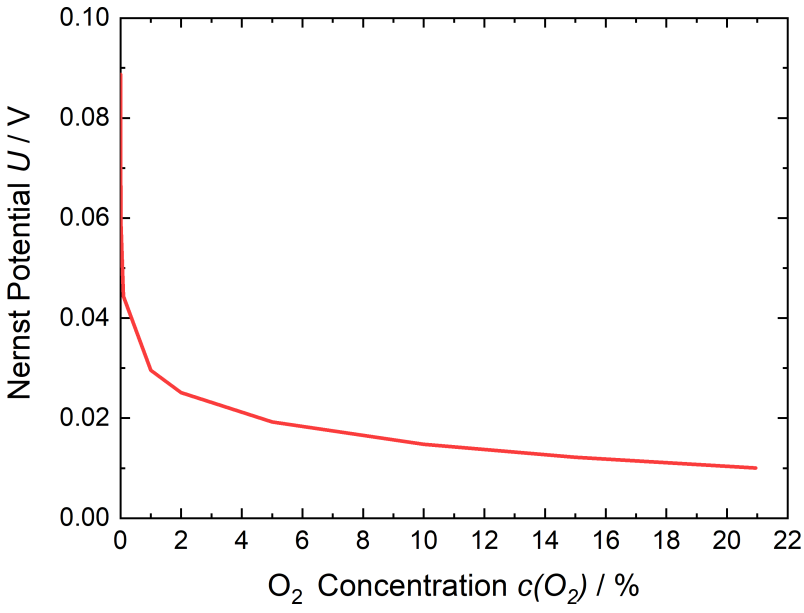


Fig. 5.4. The Nernst potential is plotted as a function of the O_2 concentration of the gas mixture at the cathode.

H_2 can be produced at the cathode at a potential of 1.23 V as well (Eq. 5.3). Under this condition, it must be assured that operation is always outside the explosion limits of the ternary mixture of H_2, O_2, and N_2. An explosive mixture is formed when H_2 and O_2 contents are higher than 4 % in the gas mixture [169]. The produced H_2 can be used as an energy source [170] or a recombination with the remaining O_2 is possible to reduce the O_2 content even further [171].
Different operating parameters are outlined, such as: temperature, the flow rate of air and H_2O, potential, hot pressing of the membrane with catalyst layers, the size of the active cell area and the membrane thickness regarding their influence on O_2 reduction using a depolarized cathode. In addition, the FE is studied with respect to the production of pure N_2.
This oxygen depletion technique offers several advantages over the convential methods crogenic air separation and PSA. If the required electricity is sourced from renewable energy, the N_2 enrichment process is CO_2-neutral. In the summer months in Germany the excess of the produced electrical power by solar causes considerable cost (23 billion €) for the network operator and thus for the state [172]. Converting the excess of solar energy into a valuable products like N_2, H_2, NH_3 would be very beneficial, because these products can either store the produced energy or the energy is used in a different way. As outlined in the report, storing 10 GW of energy in batteries is not a practically feasible solution [172]. Due to the system's simple design, scalability and low investment costs, the electrochemical oxygen depletion cell provides consumers with the opportunity to produce pure N_2 independently, rather than relying on large-scale producers.

5.3.3 Experimental

The cell is a combination of a fuel cell cathode with a loading of 1.3 - 1.4 $\mathrm{mg\,cm^{-2}}$, 60 % Pt/C HiSpec 9100 supported on carbon felt H2315 CX312 from Freudenberg and a PEM electrolysis anode with a loading of IrO_x 2 $\mathrm{mg\,cm^{-2}}$ from Alfa Aesar / Thermo Fisher Scientific™ supported on carbon paper from Toray, TGP-H120®. The Pt/C cathode cathode is produced by means of the decal method and the IrO_x layer via spray coating directly onto the membrane. Both electrodes were produced in-house. These electrodes have high active surface areas and are fairly common materials [173, 174]. Alternative materials were not considered, because these catalysts consistently yielded the most favorable outcomes, as asserted by Giddey et al [160]. As PEM, Nafion with different thicknesses were used. The active cell area was 6.25 $\mathrm{cm^2}$ and 17.64 $\mathrm{cm^2}$ in the smaller and large cell, respectively. A hot-pressing process was studied with regard to O_2 depletion and cell performance. During hot pressing, the cathode electrode and anode gas diffusion layer are pressed together with the membrane (the anode catalyst was sprayed on the membrane directly), which leads to better ionic conductivity, and so a higher current density [154]. This technique is used by default in water electrolysis [153]. Hot pressing is performed at 130 °C the glass transition temperature of Nafion and 0.5 $\mathrm{kN\,cm^{-2}}$. The cell components are the same as described in section 3.2. The quantification of the O_2 content is measured using the oxygen sensor “OMD-507 Oxygen Analyzer” from Southland Sensing, while the H_2 content is measured with the sensor “FTC 300” from Messkonzept. It is noteworthy that both sensors have a specified error of 1 % of their selected measuring range. The used mass flow controller for air flux is from Brooks Instruments MultiFlo™ "GF40". The mass flows were calibrated to 0 °C by Brooks Instrument and are given in norm milliliter. The air flow rates employed in this study conform to the prescribed standard flow rates as established in the literature, specifically 10, 50, and 100 mL/min. At the same time, the H_2O flow rate was maintained at a constant level of 10 mL/min. The maximum possible consumption of O_2 is limited through the current supply provided by the potentiostat (5 A). If Faraday’s law (Eq. 3.8) is considered and the ideal gas equation

$$p\,V = n\,R\,T\,. \tag{5.9}$$

The resulting pressure of the experiments is atmospheric pressure $p = 101\,325$ Pa. Four electrons are needed for the O_2 reduction reaction. The calculation is based on a temperature of 273.15 K, because the mass flow controller were calibrated to 0 °C. If a current of 5 A is supplied for 1 min, it result in the amount of substance

of 7.77×10^{-4} mol and hence, an O_2 volume of 17.42 mL/min. The O_2 content 20.94 % [175] of an air flow rate of 100 mL/min (20.94 mL O_2) is a little above the maximum content of O_2, which can be reduced. Nevertheless, the flow rates of 10, 50, and 100 mL/min are used as standard flow rates. In terms of the active cell area 17.64 cm^2, these are these are 0.57 ≈ 0.6 mL/min/cm^2, 2.83 ≈ 3 mL/min/cm^2 and 5.67 ≈ 6 mL/min/cm^2.

The test set-up, illustrated schematically in Fig. 5.5, was constructed to realize the experiments. H_2O was pumped with a circulation pump into the anode to provide the protons. The mass flow controller delivers the specific air flow rates to the cathode. Based on the reaction equation, Eq. 5.7, H_2O is produced on the cathode side. In addition H_2O from the anode side can move through the membrane via diffusion and electroosmotic drag. H_2O is emitted on the cathode side with N_2, remaining O_2 (also noble gases and CO_2), and possible produced H_2. Hence, the H_2O influences the total volume flux and so the values of the O_2 and H_2 sensors. As a function of the temperature, the partial pressure of H_2O is influenced [176], as is the gaseous volume. Therefore, a condenser is integrated into the into the system to remove H_2O from the gas stream. Thus, the gaseous volume of H_2O is reduced. The water condenser cools the gas down to 3 °C. Hence, the H_2O volume content of the gas is 0.75 % (758.05 / 101325) of the gas stream. In comparison, the H_2O content is 3.13 % (3179 / 101325) of the gas stream at room temperature. The O_2 and H_2 contents are measured with their corresponding sensors. The O_2 sensor was calibrated specifically with mixtures of O_2 and N_2, while the H_2 sensor was calibrated with mixtures of H_2 and N_2.

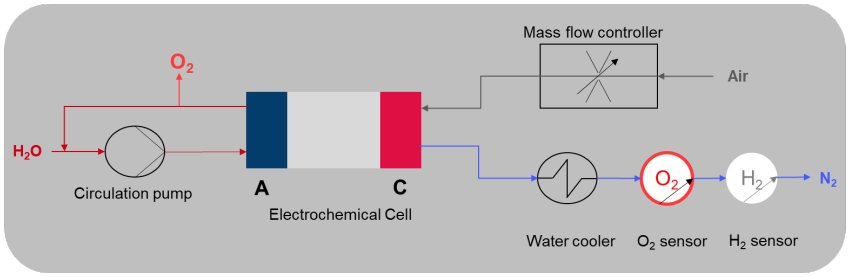


Fig. 5.5. Illustration of the O_2 depletion test set-up. H_2O is introduced with a circulation pump on the anode side. Due to the applied electrical potential O_2 is produced and H^+ are generated. At the cathode the H^+ reacts with the incoming O_2 from air to H_2O. The produced H_2O is condensed with a water cooler and the remaining O_2 in the gas stream is measured with the O_2 sensor. Additionally, if H_2 is generated, it can be determined with the H_2 sensor.

5.3.4 Results and Discussion

Hot Pressing

During hot pressing, the cathode electrode and anode gas diffusion layer are pressed together with the membrane (the anode catalyst was sprayed on the membrane directly), which leads to a better ionic conductivity, thus a higher current density [154]. This technique is used by default in water electrolysis [153] as written before. The hot pressing is done at 130 °C, close to the glass transition temperature of Nafion 123 °C [177]. A schematic sketch of the hot pressing process is shown in Fig. 5.6.

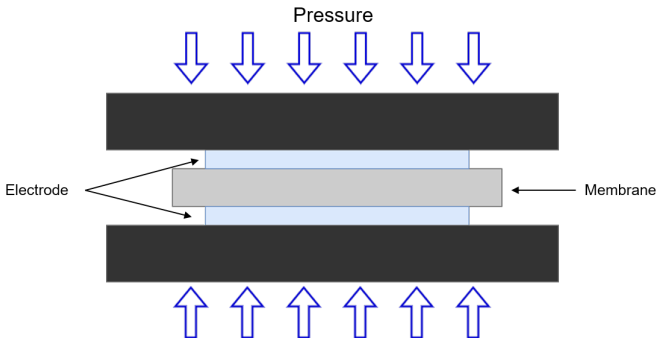
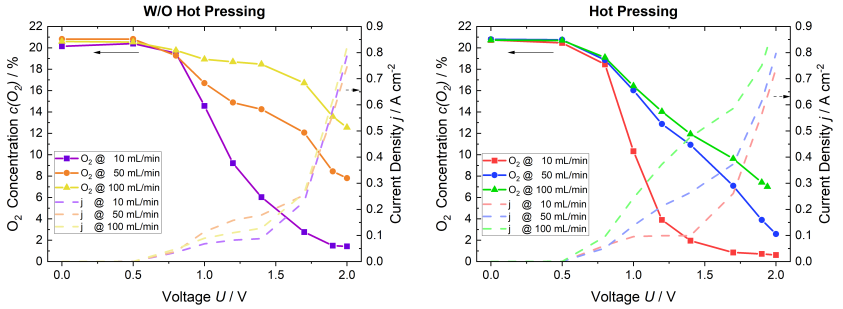


Fig. 5.6. Sketch of the hot pressing process. An applied pressure presses the catalyst layer onto the membrane, leading to a reduction of ohmic resistance, thus better ion conductivity.

After hot pressing, a cell with an active cell area of 6.25 cm^2 was used to analyze the impact of hot pressing at RT. The employed air flow rates were, as previously mentioned, 10, 50, and 100 mL/min. The H_2O flow rate was maintained at a constant rate of 10 mL/min. The H_2O flow rate was also changed and studied. However, the experimental outcomes indicated that alteration in the H_2O flow rate does not influence the extent of the O_2 reduction. The effect of hot pressing on the O_2 reduction was studied by measuring the O_2 ratio in the gas at the respective potentials. These O_2 values were then compared with the results of a cell that was not hot pressed.

For all flow rates, the remaining O_2 decreased comparing Fig. 5.7a, results without hot pressing with Fig. 5.7b, results with hot pressing. In the circumstance of 100 mL/min, the O_2 content decreases roughly from 13 to 7 %. For the applied air flow rate of 50 mL/min, the decline is from 8 to 3 %, and for the last flow rate of 10 mL/min, it is from 1.5 to 0.5 % at a potential of 2 V, with a comparable

concentration also being obtained at lower voltages. Furthermore, as is written in [154], the current densities increase due to hot pressing. Thus, it has a positive effect on the electrochemical cell's performance. Therefore, this method was used for the subsequent cell assemblies.



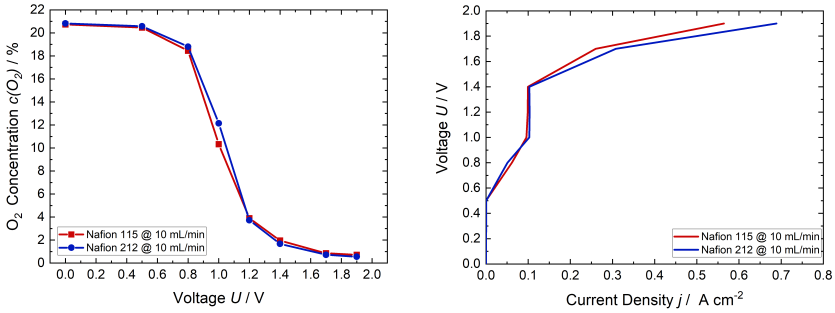
(a) O_2 depletion (solid line) without hot pressing and the resulting current density (dashed line).

(b) O_2 depletion (solid line) with hot pressing and the resulting current density (dashed line).

Fig. 5.7. (a) Remaining O_2 content (as line with dots) at the cathode outlet and current density results (as dashed line), without hot pressing the MEA, (b) remaining oxygen content and current density, with hot pressing the MEA.

Membrane Thicknesses

In Fig. 5.8a the thickness of the membrane is analyzed comparing Nafion 115 (127 µm thick, red) and Nafion 212 (51 µm thick, blue). The results are only studied for an air flow rate of 10 mL/min. Both membranes exhibit the same reduction in O_2 while applying a flow rate of 10 mL/min (Fig. 5.8a). In the case where only O_2 reduction occurs below 1.23 V, the current densities of both membranes are equal. Starting from approximately 1.4 V, the current densities of Nafion 212 increase more strongly than in the case of Nafion 115. Nafion 212 is thinner than Nafion 115 therefore the ohmic resistance is lower. This leads to higher current flow at the same applied potential.



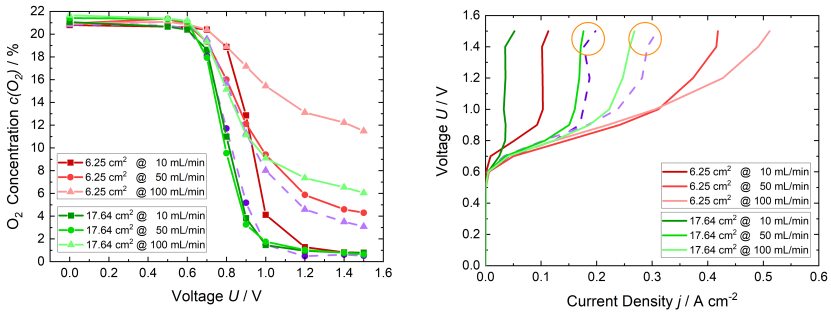
(a) O_2 depletion of Nafion 115 (red) and Nafion 212 (blue).

(b) Current density of Nafion 115 (red) and Nafion 212 (blue).

Fig. 5.8. (a) Comparison of the oxygen content of different membrane thicknesses (127 µm, red and 51 µm, blue). (b) The respective voltage-current characteristic showing that there is no clear trend.

Influence of Active Cell Area

The results of the comparison of different active cell areas are displayed in Fig. 5.9. Fig. 5.9a shows in red the O_2 depletion of the active cell area of 6.25 cm^2, with air flow rates of 10, 50, and 100 mL/min. In violet the results of the flow rates are marked, which are referred on an area of 1 cm^2, resulting in flow rates of roughly 3 and 6 mL/min/cm^2, which are the same flow rates referred on 1 cm^2 as for the cell area of 17.64 cm^2 with flow rates 50, and 100 mL/min to enable an area-related comparison of both cells. The O_2 reduction regarding 3 mL/min/cm^2 are similar. The O_2 reduction content is lower for the smaller cell area with respect to 6 mL/min/cm^2 (see Fig. 5.9a). However, due to the potentiostat it must be said that a complete depletion of an air flow rate of 100 mL/min is not possible. Thus, regarding 3 mL/min/cm^2 there is no difference in the cells.
In Fig. 5.9b the polarization curves of the data shown in Fig. 5.9a are plotted. If the area-related flux rate is considered again, it can be seen that the current density, with the larger cell area (17.64 cm^2), being a bit lower. This means that the current, energy, which is required for O_2 depletion is lower for the same specific conditions. As a result, not only is the quantitative amount of O_2 depletion with the larger cell area higher, but is also more efficient in terms of energy. In conclusion, it can be said that a larger cell area is beneficial for the O_2 depletion and N_2 enrichment process.



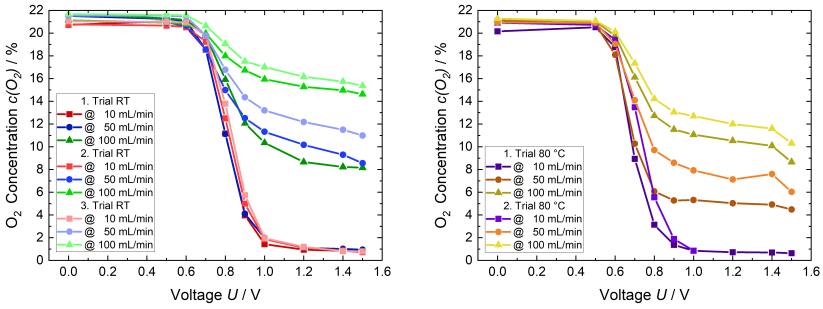
(a) O_2 depletion of active cell areas of 6.25 cm^2 and 17.64 cm^2. **(b)** Current density of active cell areas of 6.25 cm^2 and 17.64 cm^2.

Fig. 5.9. (a) Comparison of the O_2 content of different active cell areas with respect to different air flow rates. (b) The respective voltage-current characteristic. The violet characteristic curves are the results of the green characteristic curves in relation to an active cell area of 6.25 cm^2, to enable an area-related comparison of both cells.

Temperature Effect on O_2 Depletion and H_2 Production

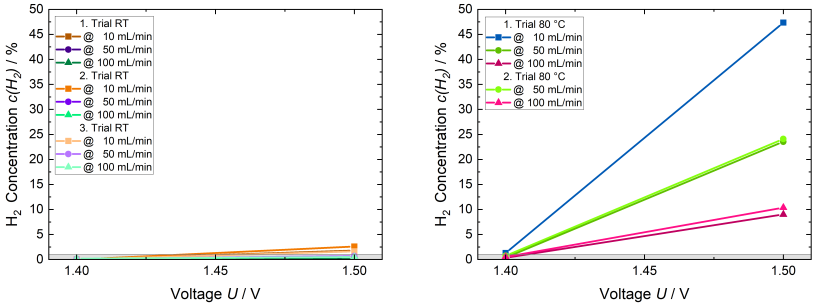
Fig, 5.10a and Fig. 5.10b show the temperature influence, which was studied with respect to extent of the O_2 reduction and H_2 formation. In addition, the degradation effect was investigated, and takes place through the temperature change and repeated measurements. Fig. 5.10a displays the result the respective trends of three trials at room temperature. The measurements at 80 °C are illustrated in Fig. 5.10b. Fig. 5.10c and Fig. 5.10d exhibit the corresponding H_2 results. In between the room temperature trials, the trials at 80 °C were measured. For the lowest flow rate, 10 mL/min, the changing temperature and experiments had no influence on the performance of O_2 depletion (see Fig. 5.10a and Fig. 5.10b). The O_2 content was roughly reduced to 1 % from 1 V. In the case of 50, and 100 mL/min, the O_2 content in the gas increased strongly from the first to the second and third run at room temperature (Fig. 5.10a). At a potential of 1.2 V, the amount of O_2 increased from roughly 1 to 10 % at 50 mL/min. The increase was from approximately 8 to 16 % for 100 mL/min. It is assumed that caused by the temperature stress the O_2 reduction reaction was not so efficient anymore at room temperature. The results applying 10 mL/min were approximately the same at 80 °C as noted previously. There is a degradation from the first trial to the second in the case of the other flow rates at 80 °C, the O_2 quantity for both trials was lower compared to the second and third trials at room temperature due to the better kinetic at elevated temperatures. However, as written previously, if the results of the first and second trial of Fig. 5.10a are considered, it seems that the degradation is strengthened due to the temperature stress. The assumption is that the catalyst layer becomes ever more catalytic-inactive concerning the O_2 reduction reaction, but the kinetic becomes faster due to the temperature increase resulting in a higher O_2 reduction at 80 °C in comparison to the second and third trials at RT. H_2O condensation resulting in flooding the PTL and an impairment of the O_2 transfer to the cathode catalyst layer is a huge challenge in a fuel cell system [178]. This is not a difficulty in this system and not the reason for the lower O_2 reduction, as the higher the air flow rate the better the removal of the H_2O should be. Fig. 5.10c and Fig. 5.10d present the H_2 ratio, which is measured. The H_2 production at 1.5 V strongly increases from room temperature to 80 °C. At RT, the H_2 amount is below 5 % for all flow rates. The grey colored area displays the error margin of the H_2 sensor, which is 1 %. The produced H_2 concentration of the flow rates 50 and 100 mL/min are in the error range. At 80 °C, it is higher than 10 % for all flow rates. The grey shaded area, the small area in Fig. 5.10c and 5.10d, is the error range of the H_2 sensor, thus most values are in the error range during the measurement at RT. Repeating the measurement at 80 °C does not degrade the HER. As expected the kinetic in

terms of H_2 production is improved through the temperature increase. Furthermore, the lower the flow rate, the higher the amount of H_2. The reason for this is that in terms of 10 mL/min most O_2 is already reduced at the higher potential, and hence the current can be used for HER. The increase of the relative H_2 extent from 1.4 to 1.5 V is huge, from 1.3 to 47.3 % at 80 °C. Nevertheless, an overpotential is necessary to produce H_2. The increases production of H_2 at elevated temperature is in this case, the competing reaction and reduces O_2 reduction.



(a) O_2 depletion at room temperature.

(b) O_2 depletion at 80 °C.



(c) H_2 evolution at room temperature.

(d) H_2 evolution at 80 °C.

Fig. 5.10. (a) Measured O_2 content of all trials at room temperature, (b) measured O_2 content for all trials at 80 °C, (c) measured H_2 content for all trials at room temperature, and (d) measured H_2 content for all trials at 80 °C.

The results of temperature influence, degradation effects on the voltage-current characteristic, and subsequent determination of FE, are shown for the air flow rate 50 mL/min in Fig. 5.11. There are two distinct regions for both temperatures. The first region is the current density increase (Eq. 5.11) from approximately 0.6 to 0.9 V. The reactions according to Eq. 5.7 occur, when the O_2 out of the air gas stream is reduced to H_2O and O_2 is produced at the anode. From 0.9 to 1.4 V the current remains almost constant. At the temperature of 80 °C, there is no current increase from 0.9 to 1.4 V. Starting from 1.4 V the second region occurs, a second electrochemical reaction is carried out. H_2 evolution then starts to occur. This leads to an increase in current density. H_2 and current density increase sharply at 80 °C and 1.5 V, which is due to the better catalytic kinetic that results in enhanced H_2 production at 80 °C.

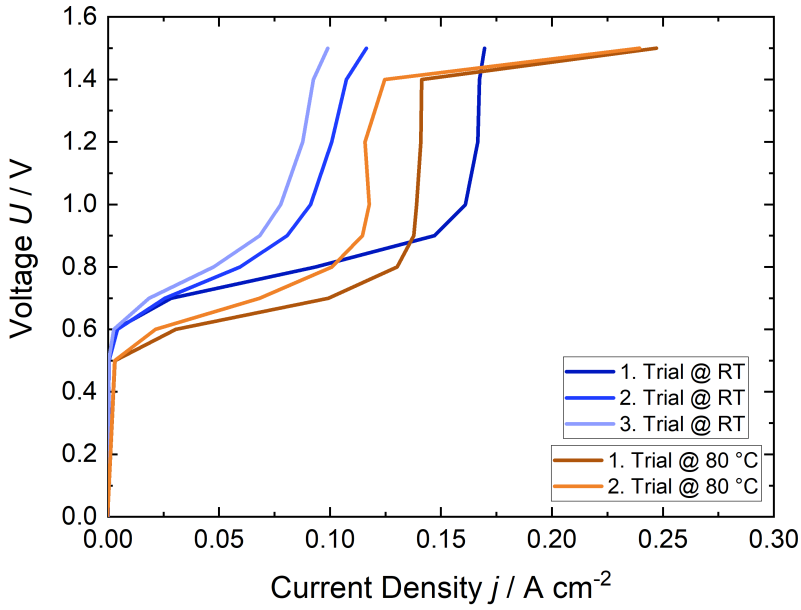


Fig. 5.11. Polarisation curves showing the effect of temperature increase and the resulting influence of degradation while applying an air flow rate of 50 mL/min at RT (blue lines) and 80 °C (orange lines).

This corresponds to the increasing H_2 content in Fig. 5.10d compared to Fig. 5.10c. The current density decreases at RT, after applying 80 °C. This correlates with the effect of the increased measured O_2 content at room temperature. As is shown in Fig. 5.10 the air flow rate impacts the O_2 reduction and H_2 production, and hence the current density. The higher the air flow rate, the higher the current density, which leads to higher absolute reductions of O_2, but not relative ones. The FE of O_2 reduction $\eta(O_2)$ was close to 100 % for the first and second trials at RT in the voltage range of 0.8 - 1.5 V with respect to the error (Fig. 5.12). At 80 °C, the FE was close to 100 % as well, but drops sharply at 1.5 V because H_2 formation significantly increases. Nevertheless, the FE is quite high over the temperature range and voltage range.

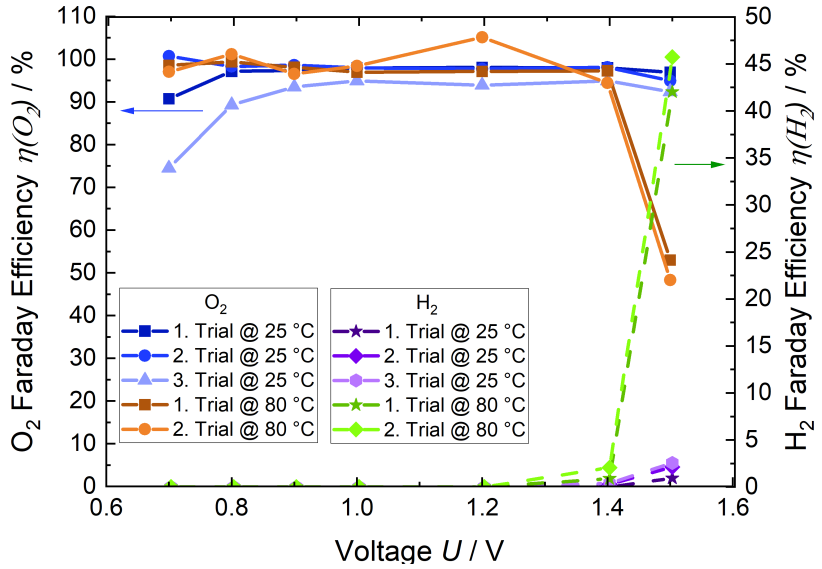


Fig. 5.12. FE of O_2 depletion (solid line) and H_2 evolution (dashed line) for all measurements while applying an air flow rate of 50 mL/min.

Electrochemical Impedance Spectroscopy

Fig. 5.13 presents the polarisation curves of a MEA cell at the three air flow rates and RT like Fig. 5.9b. It is presented here for discussing the selected potentials of the impedance spectra. The charge transfer losses, which occurred up to 0.6 V are similar for the three different flow rates. From 0.8 V, the current density reached a limiting current density and the resistance of the electrochemical cell increased due to the mass transport inhibition at a flow rate of 10 mL/min. The resistance increase led to an almost vertical increase in voltage. HER occurs and thus the current density increases starting from 1.4 V. Due to higher air flow rates, the produced H_2O was better removed out off the cell. Therefore, the diffusion overpotentials were lower that resulted in higher current densities. The limit current density starts at 0.9 V at the air flow rate of 50 mL/min. In the case of 100 mL/min this behavior occurred roughly at 1 V. The error result from the selected current range ± 10 A, resulting in ± 0.14 mA cm^{-2}.

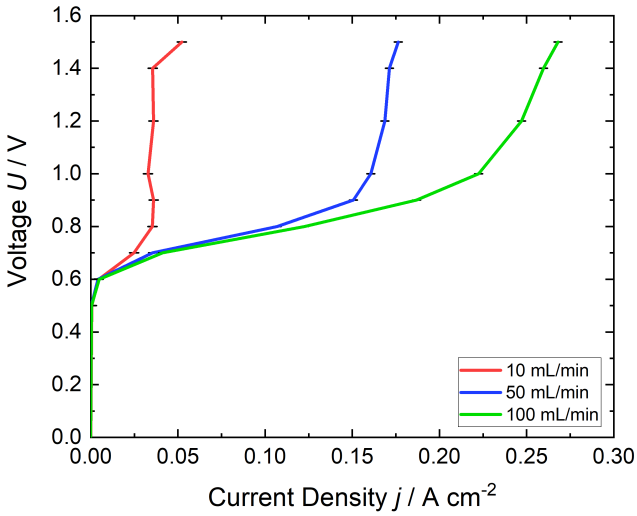


Fig. 5.13. Polarisation curves of the MEA at different air flow rates.

To evaluate the results of the MEA cell the electrochemical changes are investigated in more detail. Therefore, EIS were recorded and fitted by means of the equivalent circuits shown in Fig. 5.16. Figs. 5.14 and 5.15 exhibit the spectra (points) for the respective air flow rates and fits (solid line) of the spectra at the potentials of 0.6, 0.8, and 1.5 V. The results at the applied potential of 0.6 V are fitted with the equivalent circuit in Fig. 5.16a and of the other potentials with Fig. 5.16b. The

spectra of the applied potentials were fitted over the whole frequency range from 100 kHz to 1 Hz.

The high frequency part of the spectra contains an inductance (L) that is an measurement artefact caused probably by the potentiotstat or the test facility and an ohmic resistance (R_Ω) that is mainly caused by the electrolyte resistance. Each spectrum consists of a high high frequency (h.f.) semicircle and a low frequency (l.f.) semicircle. The increase in potential and air flow rate leads to a diminution of the h.f. semicircle. The charge transfer at the catalyst / ionomer interface (electrochemical double layer) is described by the charge transfer resistance (R_{CT}) parallel to the double layer capacitance. Due to the depressed semicircle the capacitance is replaced by a constant phase element (CPE_{CT}). At 1.5 V for all flow rates and at 0.8 V for 50 and 100 mL/min the h.f semicircle is not very distinct. The l.f. semicircle is incomplete due to the frequency limit and it is described by a resistance (R_2) and a constant phase element (CPE_2).

L is almost constant for all spectra. As noted previously, it is an artefact and should be independent on the measuring conditions. R_Ω is also almost constant. This is expected, because R_Ω is current independent and thus the air flow rate does not have an influence. R_{CT} and R_2 and hence their respective time constant decrease due to the faster kinetic and lower charge transfer resistance caused by the increased potential. The small increase of the resistance from 0.6 V to 0.8 V should not occur, this probably due to the ideal resolution of the spectra and the corresponding fit error. The exponent of CPE_P of the CPE elements is set to one in some cases for CPE_{CT} and in most of the cases for CPE_2. This corresponds to a capacitance. At a potential of 0.6 V the current is largely independent of the flow rate and therefore the charge transfer resistance is independent as well. Diffusion overpotentials do not occur. At 0.8 V and a flow rate of 10 mL/min, the system is already in the limiting current regime. In the cases of the other flow rates, the current is in a mixed area of charge transfer and diffusion control. Therefore, is in their cases the diffusion resistance (W_R) lower. This is probably caused because the produced $\mathrm{H_2O}$ is removed faster at the higher air flow rates. At 1.5 V the current is limited by the diffusion for all flow rates and W_R increases. W_R decreases in the case for 10 mL/min, this may be due to the fact that the limiting current regime was already reached at 0.8 V. Additionally, W_R increases with the flow rate, possibly because HER starts to occur at the lower flow rates as shwon in Fig. 5.10.

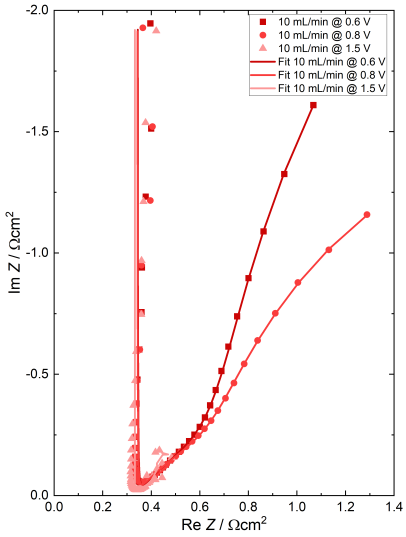
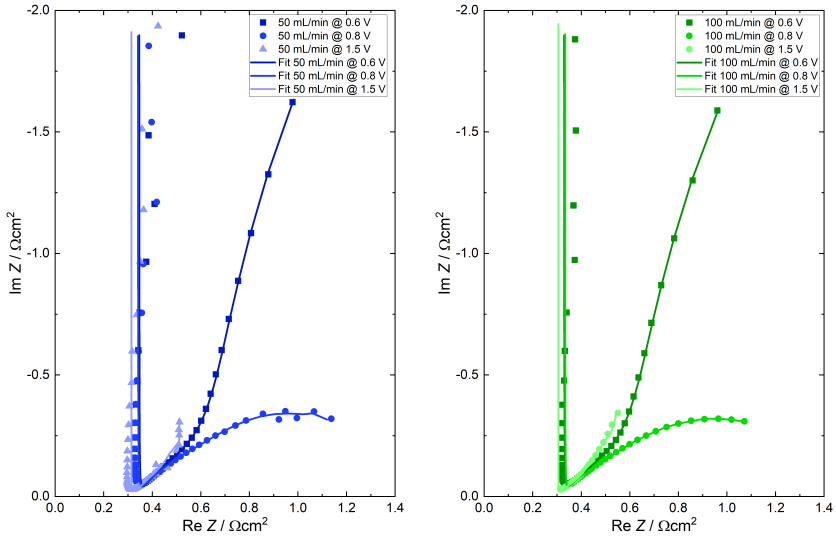


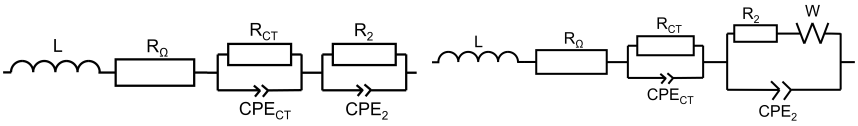
Fig. 5.14. EIS of an air flow rate of 10 mL/min and their respective fits.



(a) EIS of an air flow rate of 50 mL/min and their respective fits.

(b) EIS of an air flow rate of 100 mL/min and their respective fits.

Fig. 5.15. Electrochemical impedance spectra (dotted lines) and their respective fits (solid lines) for both air flow rates.



(a) 1. Equivalent circuit for describing the EIS. **(b)** 2. Equivalent circuit for describing the EIS.

Fig. 5.16. Equivalent circuits for the O_2 depletion process. Both circuits contain artefacts, which are represented through inductance. Ohmic resistances are present due to electrolyte resistance and the eletrochemical double layer in the circuits are described with the charge transfer resistance parallel to the constant phase element. Constant phase element are chosen as the semicircles are depressed. In addition, a resistor connected in parallel with a constant phase element are added to describe the incomplete low frequency semicircle. In (b) a diffusion resistance is added, because the current of the flow rates 50 and 100 mL/min is also controlled by diffusion.

Flow Rate	Potential [V]	L [H]	R_Ω [Ωcm^2]	R_{CT} [Ωcm^2]	CPE_T [Ω^{-1} s^{-1} cm^{-2}]	CPE_P	R_2 [Ωcm^2]	W_R [Ωcm^2]	W_T [s]	W_P	CPE_T [Ω^{-1} s^{-1} cm^{-2}]	CPE_P
10 mL min^{-1}	0.6	$-1.73 \times 10^{-7} \pm 1 \times 10^{-9}$	0.344 ± 0.003	0.46 ± 0.03	0.15 ± 0.02	0.61 ± 0.02	7.8 ± 0.3				0.098 ± 0.001	1 ± 0
	0.8	$-1.72 \times 10^{-7} \pm 1 \times 10^{-9}$	0.342 ± 0.003	0.47 ± 0.05	0.12 ± 0.02	0.63 ± 0.03	2.4 ± 0.5	2.3 ± 1.6	1.3 ± 1.9	0.6 ± 0.5	0.107 ± 0.005	1 ± 0
	1.5	$-1.73 \times 10^{-7} \pm 1 \times 10^{-9}$	0.333 ± 0.003	0.03 ± 0.01	0.04 ± 0.02	1 ± 0	0.08 ± 0.03	0.88 ± 0.09	0.66 ± 0.07	0.8 ± 0.03	0.17 ± 0.08	1 ± 0
50 mL min^{-1}	0.6	$-1.71 \times 10^{-7} \pm 1 \times 10^{-9}$	0.346 ± 0.005	0.40 ± 0.04	0.12 ± 0.03	0.66 ± 0.05	9.3 ± 0.9				0.097 ± 0.002	1 ± 0
	0.8	$-1.71 \times 10^{-7} \pm 1 \times 10^{-9}$	0.340 ± 0.004	0.48 ± 0.1	0.12 ± 0.04	0.64 ± 0.05	0.50 ± 0.07	0.9 ± 0.2	1.3 ± 0.2	0.89 ± 0.04	0.15 ± 0.04	1 ± 0
	1.5	$-1.72 \times 10^{-7} \pm 1 \times 10^{-9}$	0.315 ± 0.004	0.04 ± 0.02	0.04 ± 0.01	1 ± 0	0.13 ± 0.05	1.1 ± 0.2	0.7 ± 0.1	0.70 ± 0.04	0.11 ± 0.05	1 ± 0
100 mL min^{-1}	0.6	$-1.71 \times 10^{-7} \pm 1 \times 10^{-9}$	0.328 ± 0.003	0.39 ± 0.02	0.14 ± 0.02	0.63 ± 0.03	8.6 ± 0.4				0.099 ± 0.001	1 ± 0
	0.8	$-1.72 \times 10^{-7} \pm 1 \times 10^{-9}$	0.333 ± 0.003	0.09 ± 0.08	0.08 ± 0.08	0.79 ± 0.2	1.1 ± 0.2	0.01 ± 0.04	0.36 ± 0.01	1.00 ± 0.01	0.20 ± 0.02	0.07 ± 0.1
	1.5	$-1.75 \times 10^{-7} \pm 1 \times 10^{-9}$	0.30 ± 0.01	0.03 ± 0.02	0.03 ± 0.01	1 ± 0	0.08 ± 0.03	1.4 ± 0.1	0.9 ± 0.1	0.65 ± 0.04	0.06 ± 0.04	1 ± 0

Tab. 5.1.: Oxygen depletion, values of the elements of the equivalent circuits.

Reproducibility of Oxygen Depletion

In order to verify the O_2 reduction process, the reproducibility of the experiments was assessed and the influence of the error also examined (Fig. 5.17). The exact same measurement was repeated twice with two fresh cells and MEAs. An average value and the standard deviation were then calculated. The error of the oxygen sensor as written before was specified with 1 % of the selected measuring range. Concerning the measuring range of 0 - 25 % of the sensor, which was used, resulted in an error of 0.25 %. The total error is shown for each air flow rate of 10, 50 and 100 mL/min as the colored area in Fig. 5.17. The error was bigger for smaller potentials in case of 10 mL/min whereas for 50 mL/min, it was the other way around. However, the scatterings of 10 and 50 mL/min were fairly small. Applying 100 mL/min leads to an increase in errors if the applied voltage becomes greater than 1.0 V. An applied voltage greater than or equal to 1.2 V will cause the residual O_2 to drop below 1 % while using 10 or 50 mL/min as flow rates. It is possible to strongly enrich N_2. The parameters should be selected on the basis of the desired result. Already at a potential of 1 V, the remaining O_2 quantity is only slightly larger than at 1.5 V. This means that one third of the energy can be saved. Furthermore, it must be considered which quantity of O_2 should be reduced and at which time. In dependency of the amount of N_2, which is needed, a flow rate of 10 mL/min allows much lower power consumption than the flow rate of 50 mL/min. As mentioned previously, a total depletion of an air flow rate of 100 mL/min is not possible within the current limit of the potentiostat. This leads to a higher remaining O_2 content.

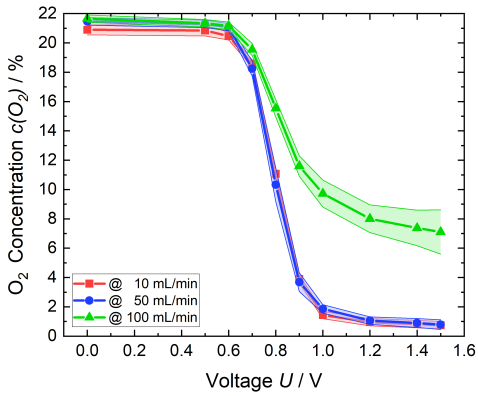


Fig. 5.17. Remaining O_2 content (line) and the resulting error (colored area) of each air flow rate.

The affirmation of favorable outcomes for the air flow rate of 100 mL/min is substantiated by the empirical results displayed in Fig. 5.18. The mean value of the FE of 100 mL/min is approximately 97 %, considering the error a FE of 100 % is reached. The efficiency of 50 mL/min is similar. Over the voltage range from 0.8 to 1.5 V the FE remains stable, and close to 100 %. The FE while applying 10 mL/min exhibits a lower profile across the potential range, expect at the applied potential of 1.4 V. Görlín et al. [179] found in a study on O_2 evolution that oxidation of metal surfaces can significantly reduce the FE. It is assumed that a similar reaction may be the competing reaction here at the anode.

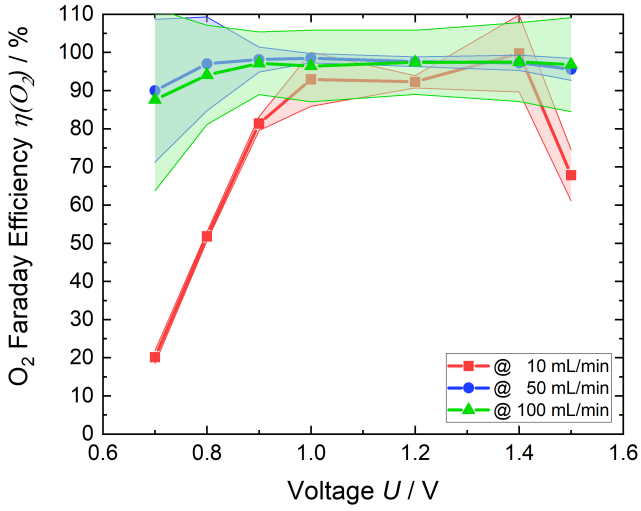


Fig. 5.18. Faraday efficiency of O_2 (lines with dotes) and respective error (colored area) of each air flow rate.

Drawing on results of this work, a calculation was performed, to study how much energy is needed to produce 1 kg of N_2 using the electrochemical oxygen depletion method. 1 kg of N_2 corresponds to 0.79 Nm^3 of N_2. If the traces of CO_2 and noble gases are neglected in air, the amount of N_2 is 79 % and O_2 is 21 % in the air. This leads to an inlet air gas stream of 1.0 m^3. Hence, 0.21 Nm^3 / 0.3 kg O_2 ($\rho(O_2)$) = 1.43 kg m^{-3}) needs to be reduced to generate 1 kg N_2. The molar mass of oxygen is $M(O_2) = 32\,g\,mol^{-1}$. The equation used to calculate the amount of substance (n) is

$$n = \frac{m}{M}\,. \tag{5.10}$$

If Eq. 5.10 is inserted into Eq. 3.8, the charge can be calculated that is necessary to reduce 0.3 kg O_2, which is 9.375 mol O_2, resulting in a charge of 3618 kC. The following equation

$$E = Q\ U \tag{5.11}$$

is used to calculate the theoretical energy, which is required to reduce the amount of O_2 and producing 1 kg of N_2. Where E is the energy, Q the charge and U the applied potential. 2.95 A are measured (Fig. 5.11, 1. Trial) at the applied potential of 1.2 V of the air flow rate of 50 mL min^{-1}, leading to less than 1 % O_2. Therefore, the calculation is based on 1.2 V and the required energy is $U(1.2\,V) = 1.18$ kWh. The theoretical value is quite similar, because almost a FE of 100 % is reached. Considering Fig. 5.8 and Eq. 5.7 and 5.8 to reach 1 % of remaining O_2 in the gas, the absolute minimum required energy is $U(0.03\,V) = 0.03$ kWh. If the actual energy requirement can be brought close to this value due to optimization of parameters like higher catalyst loading, larger active cell area, which lead to reducing overpotentials, the process will be much more energetic efficient. If it is assumed that due to these mentioned factors, the O_2 content is decreased to less than 1 % at a potential of 0.8 V, the required energy would be $U(0.8\,V) = 0.79\,kW\,h\,kg^{-1}$ for producing 1 kg of N_2. Thus, the electrochemical technique would be more energetic efficient than the cryogenic distillation (0.89 kW h kg^{-1}). Nevertheless, for all methods the energy consumption increases in dependency of the desired purity of N_2. However, the needed energy increase of these methods is not equal.

5.3.5 Summary and Conclusion

This chapter presents the electrochemical generation of the reactants (N_2 and H_2), which are needed for the electrochemical NH_3 synthesis.

An oxygen-depolarized cathode was studied for the reduction of O_2 and enrichment of N_2 for the electrochemical ammonia synthesis. Through optimization of the cell and process parameters, the O_2 content in an air gas stream can be reduced to less than 1 % of O_2 in the gas stream. These parameters are the air flow rates, hot pressing, active cell area, membrane thickness, potentials, and temperature. A lower air flow rate, hot pressing and a higher active cell area lead to higher degrees of O_2 reduction. A low flow rate extends the residence time in the cell and therefore the reaction time. Hot pressing results in decreasing the ohmic resistance, which leads to higher current densities and due to the larger active cell area, the catalyst surface area is larger. This shows that a better MEA enables a better O_2 reduction and reduces the energy consumption. Fig. 5.19 illustrates in a table for visualisation the impact of each parameter. Higher potentials also lead to better O_2 reduction. However, depending on the air flow rate a maximum reduction is reached above a certain voltage. A maximum reduction is reached for an air flow rate of 10 mL/min at 1.2 V. A further increase of voltage lead to higher losses and a less efficient system. A higher temperature leads to cell degradation and less O_2 reduction depending on the air flow rate. After the temperature increase and the respective measurement, the O_2 content in the cathode outlet gas stream increased from 1 to 10 % at an air flow rate of 50 mL/min and 1.2 V at RT. Thus, operation at room temperature achieved much better O_2 depletion. Thus, the temperature increase is poor and therefore marked in red. No influence of membrane thickness could be detected in the experiments, so it is marked in yellow. The small single cell with an active cell area of 17.64 cm^2 reduces the O_2 content below 1 % in an air gas stream of 50 mL/min. The FE remains high and close to 100 %, and stable across a wide potential range. These achieved results are illustrated in the cell illustration in Fig. 5.19 below the table.

With respect to the extent of remaining O_2, air flow rate and energy consumption conditions can be chosen, which are suitable for their specific applications. The energy consumption calculation shows that the required energy needed to provide 1 kg of N_2 by electrochemical O_2 depletion, at an applied potential of 1.2 V, is with a consumption of 1.18 kW h kg^{-1} is a little bit larger than cryogenic distillation (0.89 kW h kg^{-1}) and PSA (0.39 kW h kg^{-1}). It is expected that by reducing the overpotentials, due to the mentioned parameters, the electrochemical O_2 depletion can be more efficient than the current technologies. Using renewable energy, the electrochemical O_2 reduction offers a very good possibility to extract green N_2 from

air and the production of pure O_2 at the anode. Especially a surplus of existing electrical energy caused by strong sunshine, can be converted into these products. In addition, due to the easy cell setup, an up scaling is feasible and it facilitates a distributed N_2 all over the world. In particular, a production by the consumer is economically beneficial.

Parameter	O_2 Content
Lower air flow rate	Relative O_2 content decreases
Potential increase	The O_2 content decreases
Hot pressing	The O_2 content decreases
Membrane thickness	No influence
Increase of active cell area	The O_2 content decreases
Temperature increase	Degradation of cell and increase of O_2 content

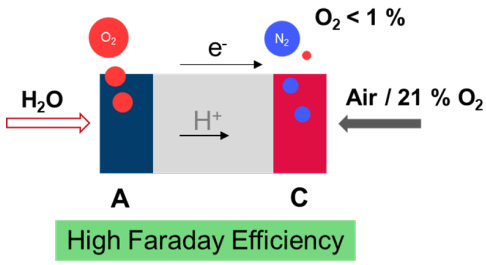


Fig. 5.19. Parameters that lead to a relative O_2 depletion and N_2 enrichment on the cathode side are marked in green, those that have no influence on the O_2 content are marked in yellow and the parameter that leads to a relative increase in the O_2 content on the cathode side is marked in red in the table. The illustration of the cell shows, that the O_2 content of an air gas stream can be reduced to less than 1 % of remaining O_2, while achieving a high FE close to 100 %.

6 Ammonia Synthesis

6.1 Introduction

As outlined in chapter 2, the NH_3 synthesis is a challenging process, particularly due to the triple bond of the N_2 molecule and the energetically favored HER, as opposed to NRR. Additionally, the electrochemical NH_3 synthesis process should occur at low temperature, which hinders the catalytic activation of the reaction. As shown in section 2.4, a variety of tested catalysts for the eNRR, which were tested in the literature, are presented. The presented rating system from Choi et al. [57] (see. section 2.9.3) exhibits that there are no catalysts in the studied literature that fulfil the three criteria (sufficient NH_3 production rate, quantitative $^{15}NH_3$ analysis, control of NO_x) for producing reliable and reproducible quantities of NH_3. This underscores that the electrochemical NH_3 synthesis is a very challenging research topic.

As mentioned in section 2.9, NH_3 can be generated from a variety sources other than its electrochemical synthesis from N_2. These sources of contaminations are illustrated in Fig. 6.1. The presence of contamination in the environment exerts an influence on the other sources of contamination, because they are themselves exposed to the environment. Catalyst production and cell assembling are given as examples. This source is shown graphically as the cloud (1). The further sources are the anode supply presented as the blue drop (2), the gaseous N_2 supply on the cathode (3), the anode components (4), cathode components, (5) and the membrane (6). It is essential to differentiate between NH_3 resulting from reduced N_2 (NH_3 molecule in Fig. 6.1, blue line) and NH_3 resulting from impurities (black lines). Given the doubtful NH_3 production rate in the literature, it is imperative to ascertain whether the measured NH_3 production rates are reliable and do not originate from impurities. Otherwise, the results are not reliable.

To this end, the aforementioned sources are discussed in the following with regard to their contaminating capacity. If the findings reported by Chen et al. [101] (section 2.9. $c(NH_3) = 0.05\,mg\,L^{-1}$) are considered as a reference point, it can be estimated that 147 nmol of NH_3 accumulate within 12 h. In relation to the used active cell area of $6.25\,cm^2$, an NH_3 production rate of $5.44 \times 10^{-7}\,\mu mol\,cm^{-2}\,s^{-1}$ is expected, resulting from the contamination of the environment.

Given the very low value in question, contamination from environment is not considered in the following.

H_2 and H_2O in form of aqueous solutions of H_2SO_4, Na_2SO_4, and KOH were used as H^+ source on the anode side. The data sheets of the respective solids, which were dissolved in H_2O do not list any impurities that could potentially lead to NH_3 formation. During the preparation of the aqueous solutions, the solutions may absorb NH_3 from the environment. However, as previously described, this effect is negligible and therefore it is assumed that the anode supply is clean and does not need to be considered as source of contamination. Conversely, the presence of impurities in the N_2 supply on the cathode results in the overlap of the signals, NH_3 formation from N_2 and the impurities. The contamination in the N_2 gas stream under the assumption outlined and elucidated in section 2.9, leads to a conversion rate of $1.71 \times 10^{-5}\,\mu mol\,cm^{-2}\,s^{-1}$. These impurities are reduced by the wash bottle filled with H_2SO_4 as shown in Fig. 3.2, but nevertheless they are considered in determination of the error margin.

Apart from the electrodes, the components of the anode and cathode are identical. Upon subjecting these components to a H_2SO_4 solution in order to expel NH_3, no NH_3 was found in the solution. The utilized electrodes with the respective tested catalyst layers do not contain any nitrogen compounds, and no nitrogen compounds were employed in their manufacture. Consequently, it can be posited with a high degree of probability that no impurities in the compounds are present that could facilitate NH_3 synthesis. Preliminary testing of electrode samples revealed the absence of NH_3 as well. As outlined in section 2.9, an accumulation of NH_3 was observed in the membrane, particularly in Nafion as mentioned in the literature [75, 77, 114, 116, 117]. To address this, multiple pieces of Nafion were placed in H_2SO_4 solutions. In cases of these samples a mean absorbance of 0.016 was measured. This value is below the determined resolution limit of 0.054 of the VIS-spectrometer. The interaction of Nafion with NH_3 and the corresponding adsorption and desorption behavior of NH_3 are elucidated and discussed in depth in chapter 7.

In conclusion, it can be stated that the contamination in the N_2 supply is the sole source of contamination that significantly leads to an overlap of the signals and thus affects the detection limit of eNRR. In relation to the cell surface area ($6.25\,cm^2$), the margin of error of this source is a rate of $192\,nmol\,s^{-1}$. This value must be added to the resolution limit of the VIS-spectrometer. The resolution limit of the spectrometer is $0.14\,mg\,L^{-1}$ with respect to NH_3 (see. section 3.3.2), which corresponds to an error limit of 206 nmol in relation to the trap volume of 25 mL. Hence, in order to proof electrochemical NH_3 synthesis resulting from N_2, the production rate must exceed 206 nmol in addition to a rate of $192\,nmol\,s^{-1}$.

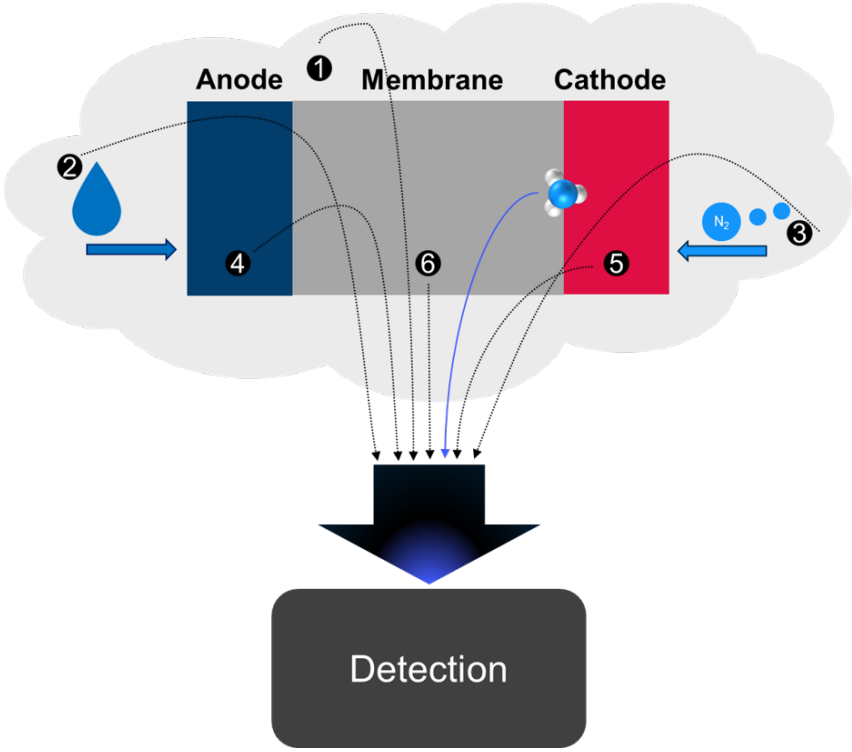


Fig. 6.1. Schematic illustration of the different sources of contaminations. These sources of impurities are (1) impurities from the environment, (2) impurities in the anode supply, (3) impurities in the cathode supply, (4) impurities in the anode components, (5) impurities in the cathode components, and (6) impurities in the membrane. The produced NH_3 from these contaminations overlap the signal of NH_3 synthesized by NRR from N_2 (NH_3 molecule, blue line).

Fig. 4.5 in chapter 4 shows a schematic illustration of the eNRR and the corresponding diffusion of the ions occurring in alkaline environment. The anode and cathode reaction are displayed in Eq. 4.14 and Eq. 4.15.
Fig. 6.2 illustrates the NH_3 synthesis and the corresponding H^+ transport in an acidic and neutral environment. H_2O is introduced in the PTL on anode side. H_2O oxidizes in the anodic catalyst layer,

$$\text{Anode:} \qquad 3\,H_2O \longrightarrow 1.5\,O_2 + 6\,e^- + 6\,H^+ \tag{6.1}$$

$$\text{Cathode:} \qquad N_2 + 6\,H^+ + 6\,e^- \longrightarrow 2\,NH_3 \tag{6.2}$$

while producing O_2 and generating H^+. Due to the applied potential and the resulting electric field, the protons diffuse through the membrane or diaphragm. N_2 is introduced into the cathode PTL. It is reduced in the catalyst layer and reacts with the incoming H^+ to NH_3. NH_3 is released at the cathode outlet.

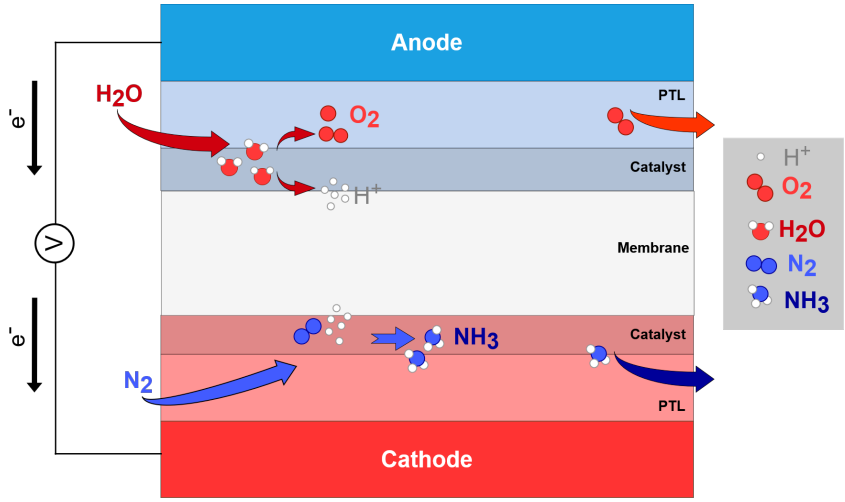


Fig. 6.2. Schematic illustration of the direct electrochemical NH_3 synthesis and the movement of molecules and ions in an acid and neutral cell. H_2O is introduced into the GDL of the anode. In the catalyst layer it oxidizes to O_2 and H^+. The produced O_2 exits the cell on the anode side and the H^+ diffuses through the membrane. N_2 is reduced at cathode and reacts with the incoming H^+ to NH_3 in the catalyst layer. This process is facilitated by the electrical energy. The resulting NH_3 exits the cell on the cathode side. The coloring of the atoms is done according to the CPK color model.

The obtained results in this chapters are structured as follows, firstly the outcome of the NH_3 production using Au nanoparticles as catalyst are presented, followed by the results using HEA catalysts, which were provided by the project partner Department of Materials Science and Engineering, Solid State Physics, Uppsala University (UU) Additional catalysts, the MEA and their respective parameters, as well as further process parameters, which were studied are listed in the appendix (9.2). Finally, a summary and discussion follows.

6.2 Gold Nanoparticle Catalyst

6.2.1 Experimental

Catalyst Preparation

The Au catalyst particles were deposited on porous Ni electrodes with an electrode size of 25 x 25 mm^2 (see. 3.4.3). Prior to the deposition of the Au catalyst, the Ni substrate underwent a cleaning process. At first the substrate was introduced into acetone for 10 min at 60 °C and then, in a solution of 10 mM HCl for 30 min at 60 °C also. Afterwards it was shortly washed in DI water. A 1 mM $K[AuCl_4]$ solution was used as the precursor and 10 mM HCl was added for enhancing the deposition. The electrode was immersed in the precursor solution for either 20 or 60 s to produce Au NPs. After the deposition the electrodes were cleaned with DI water. It was assumed that a shorter deposition time leads to a smaller particle size. However, no difference was found between the deposition times. Fig. 6.3 shows the images of scanning electrode microscopy (SEM) of the deposited Au particles. As the images show, the particles were several hundred nanometers in size. Though, the Ni electrodes were fully covered with Au.

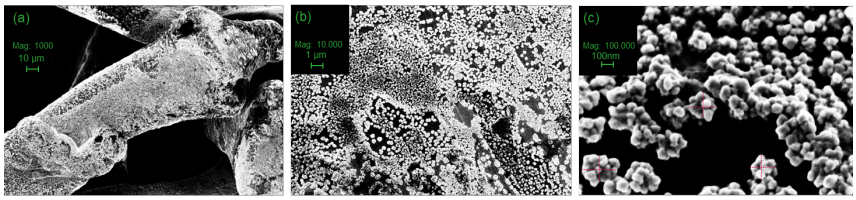


Fig. 6.3. SEM images of the Au particles. (a) Magnification of 1000, (b) magnification of 10.000 and (c) magnification of 100.000.

Ion exchanged Nafion membrane

Due to the fact that the Nafion membrane is strongly acidic on grounds of the sulfonic acid group (Fig. 1.9), metals like Ni, which were used as electrode were oxidized. Thus, they dissolved and the catalysis was not possible anymore. A fast deactivation of the catalyst occurred.
To prevent the oxidation of metals, the acidity needs to be reduced. Nafion can be neutralized by introducing ions like sodium (Na^+) ions, which are depicted as violet circles (referable CPK model) in Fig. 6.4. So, the membrane was introduced into a sodium hydroxide solution (NaOH) at 80 °C for 4 h. The concentration of the NaOH solution must be high enough so that every sulfonic acid group can react with a Na^+-ion. During the ion exchange H^+ are exchanged with Na^+, leading to a decrease in acidity. This is a suitable method for protecting catalysts from potentially corrosive acidic conditions.

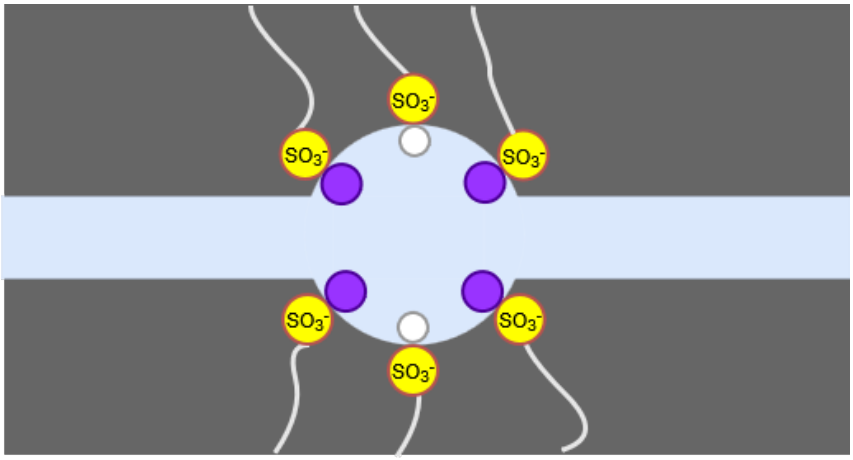


Fig. 6.4. Illustration of the ion exchanged Nafion membrane. The H^+, which are bounded to SO_3^- are exchanged with Na^+ during the immersion of the Nafion membrane into a NaOH solution. Nafio is transferred into its Na^+-form.

Cell Assembling

The produced AuNi electrode was used as the cathode in the cell configuration. Using the decal, 60 % Pt/C HiSpec 9100 from Johnson Matthey was deposited onto carbon felt H2315 CX312 from Freudenberg to serve as the anode. The loading of the catalyst was 1.3 - 1.4 mg cm^{-2}. The utilized test benches are shown in section 3.1

(Fig. 3.1, 3.2) the cell components are delineated in section 3.2 also and illustrated in Fig. 3.3. Several parameters were studied during the experiments.

6.2.2 Results and Discussion

Hydrogen as Reactant

The first tests were done with Nafion 115 in its initial form (H^+-form). But, no NH_3 was produced. The Na^+-form of Nafion was used, for protecting the catalyst layer in order to produce NH_3. The supplied H_2 flow rate was 20 mL/min on the anode. N_2 and Ar were supplied to the cathode with flow rates of 50 mL/min. Ar was used for verification of the measured NH_3. Measurements were carried out at cell temperatures ranging from room temperature (RT) to 80 °C. The following experiment was carried out at RT.

The initial idea was to determine NH_3 with FTIR spectroscopy. The advantage of the FTIR in comparison to the indophenol method, lies in the capacity for continuous NH_3 detection. Consequently, variations in the detected NH_3 quantity can be directly attributed to changes in the operating conditions. Fig. 6.5 presents the FTIR results elucidating the quantification of NH_3 (solid lines). The detected quantity of NH_3 remained equal during the supply of N_2 and Ar. The amount of NH_3 did not increase while increasing the applied potential. This observation established that NH_3 was not synthesized under these specified electrochemical conditions. Additionally, it can be deduced from Fig. 6.5 that the ratio of H_2O (dashed lines) entering the MEA cell from the humidifier cells remained constant over time. This ratio was unaffected by variations in applied voltages, underscoring the stability of H_2O flux into the MEA cell amidst changing electrochemical conditions. Nevertheless, it was not feasible to detect reliable NH_3 via IR in this experiment. In further experiments changing operation properties like cell temperature, humidifier temperature, flow rate, potential, and the usage of different catalyst material led to the same outcome of no NH_3 production. The alleged measured value of NH_3 via IR is 0.2 ppm. As noted previously in chapter 3.3.1 the concentration should be at least 2 ppm. Consequently, the recorded values fall below the resolution limit of the spectrometer, thereby categorizing these values as errors.

Moreover, it is noted in the manual of the FTIR that the flow rate should be flushed at an optimal flow rate of 500 mL/min. This prompts the question from the obtained results: Either the production rates were too low to be detected via FTIR, or alternatively, the catalysts been used may lack in catalytic activity.

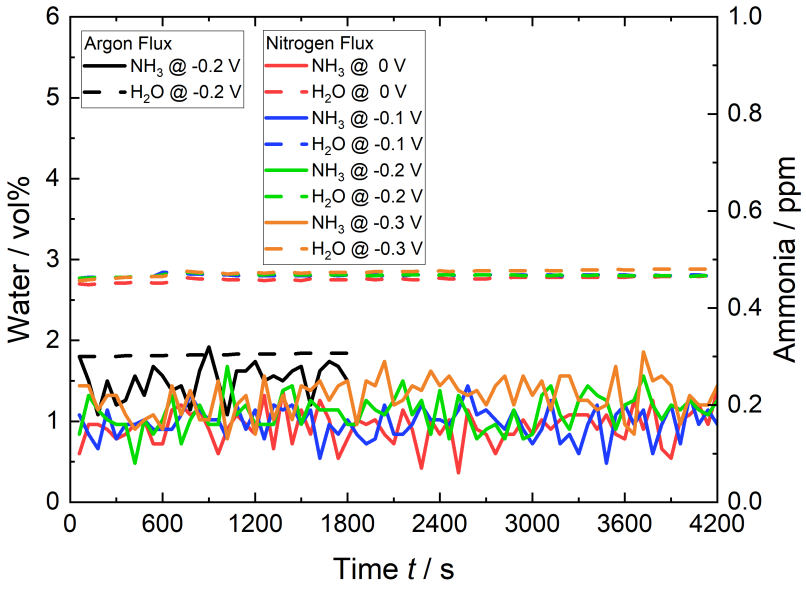


Fig. 6.5. Detected NH_3 (solid lines) and H_2O (dashed lines) in their corresponding concentration with the FTIR spectrometer. The black lines are measured during the Ar supply and the colored ones during N_2 supply.

For this reason the indophenol method was introduced. This method confers the advantage of cumulative quantification of the detected NH_3. However, it is characterised by a protracted temporal demand, and the discernment of the repercussions of parameter adjustment can only be determined during post-analysis. Fig. 6.6 shows the corresponding VIS spectra of this method. The absorbance values of all applied voltages were below zero for the expected absorption maximum at 655 nm, and hence no NH_3 was detected. It can be concluded that it is not possible synthesizing NH_3 under these operating conditions and this catalyst.

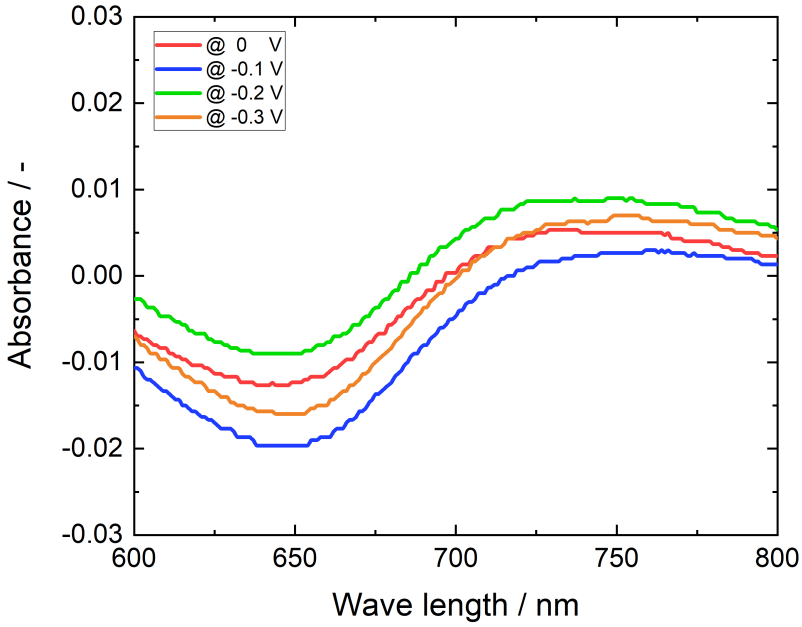


Fig. 6.6. Absorbance spectra of the VIS spectrometer for the different applied potentials while introducing H_2 at the anode.

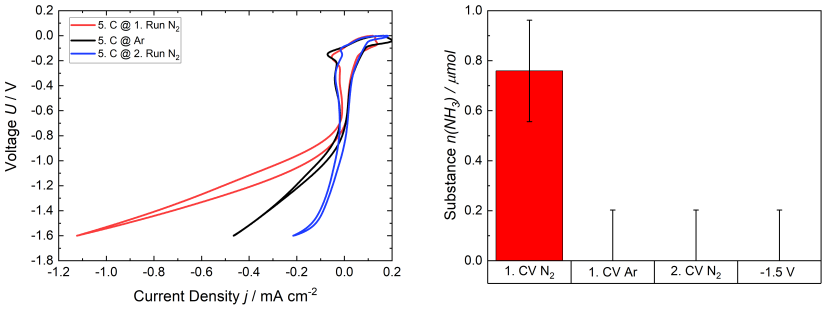
Consistent outcomes were observed across alternative catalysts when introduced to the supplemented reactants H_2 and N_2 (see appendix 9.2). Due to the fact that Nafion had to be wetted and considering H_2 non-natural availability as a reactant, the majority of measurements were conducted employing an aqueous solution as H^+ source. Higher potentials are required for the oxidation of H_2O and generation of H^+.

KOH as Electrolyte

Instead of H_2 a 0.1 M KOH solution was utilized as electrolyte. The NH_3 synthesis in an alkaline environment is described in section 4.5. In this case, the solution was circulated with a flow rate of 10 mL/min at the anode. Zirfon was used as diaphragm and the measurement was executed at RT.

Cyclic voltammetry (CV) measurement were conducted for determination the potential range in which NH_3 synthesis takes place. It was hypothesized that the electric current would increase when N_2 was used instead of Ar due to the NRR and so that it can be identified, which voltage range is the most promising one. In addition, the respective gas was then passed into the H_2SO_4 trap of the test rig (see. Fig. 3.2), in order to determine the synthesized amount of NH_3. Fig. 6.7 presents the results. Firstly, N_2 with a flow rate of 10 mL/min was introduced into the cell, then Ar with the same flow rate and once again N_2. Five CV cycles were recorded and the last cycle of each measurement is plotted in Fig. 6.7a. During the initial run supplying an N_2 flux (dark red solid line), the current density notably increased with an increase in the applied potential in contrast to the current density recorded when Ar (black solid line) was introduced. But, in the subsequent iteration involving the reintroduction of N_2, the current density dropped strongly (red solid line).

Concomitant with the measured current density, the corresponding quantification of NH_3 is depicted in Fig. 6.7b. It shows the detection of NH_3 during the initial run while N_2 was introduced into the electrochemical cell. However, NH_3 was no longer detected in subsequent runs. Also, in the case where a potential of -1.5 V was applied for 30 min. This prompts the question, did the cell undergo deactivation after a brief operational duration, or alternatively, did the ascertained NH_3 emanate from sources other than molecular nitrogen (N_2). Therefore, the experiment was repeated with a second cell and a new MEA.

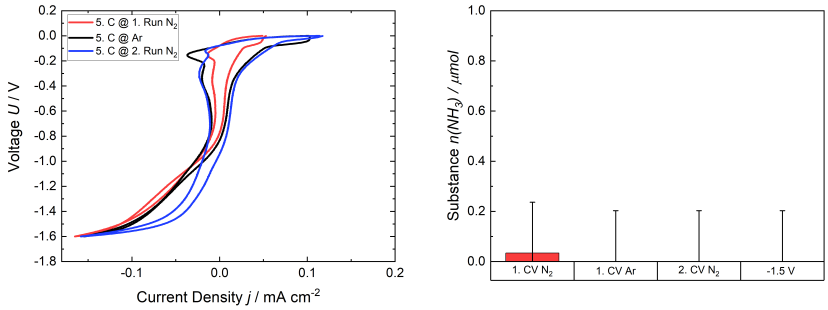


(a) Last CV cycles of the trials.

(b) Determined amount of NH_3 and error.

Fig. 6.7. (a) CV results of the experiments. In red and blue the results during N_2 supply and in black during Ar supply. (b) The corresponding detected NH_3 and the error bars of the first MEA cell employing KOH as electrolyte.

Fig. 6.8 depicts the outcomes optained from repeating the trial presented in Fig. 6.7, employing a new MEA. There was no increase in current density observed supplying N_2 compared to Ar (Fig. 6.8a). Furthermore, the current densities at each applied potential step were much lower than the equivalent current densities in Fig. 6.7a where NH_3 was ascertained. During the measurement with the second cell, no NH_3 was detected properly under any conditions, because the error bars are clearly larger as the measured values of NH_3 shown in Fig. 6.8b. The absorbance is associated with an error of 0.054 (see. 3.3.2), this leads to an error of 206 nmol. These positive and false results occurred several times and no specific parameter could be found, which is responsible for the detection of NH_3. This leads to the assumption that the detected NH_3 in the first experiment was caused by impurities. Another reason that underscores the assumption is that the detected NH_3 was always found in the beginning of the experiments.



(a) Last CV cycles of the trials.

(b) Determined amount of NH_3 and error.

Fig. 6.8. (a) CV results of the experiments. In red and blue the results during N_2 supply and in black during Ar supply. (b) The corresponding detected NH_3 and the error bars of the second MEA cell employing KOH as electrolyte.

For this reason, a new cleaning process was introduced. In the beginning of each experiment, Ar was supplied without applying a current for 30 min. The quantity of NH_3 was still determined via the indophenol method. In addition defined potentials were applied or CV cycles were recorded during the supply of Ar and the found impurities of NH_3 were measured. If no NH_3 was found or if the quantified amount falls within the margin of error, the experimental protocol initiates with the introduction of N_2.

Three MEA cells equipped with identical materials and operating under equivalent conditions, were studied. Fig. 6.9 shows the results for the Ar flux. For the first sample, a nominal quantity of NH_3 was detected. Nonetheless, This value remained within the established error range. Hence, the electrochemical cells were confirmed to be free from impurities, and the system exhibited a state of cleanliness. N_2 can be supplied for the execution of the experiment.

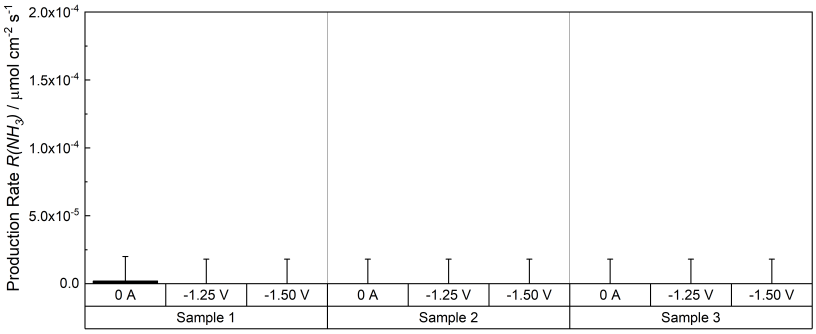


Fig. 6.9. Calculated rates of NH_3 production and the corresponding error bars that are determined while Ar is supplied at the specific conditions.

Potentials of -1.25 V, -1.5 V, and -1.6 V were applied for 20 min each and a constant N_2 flow rate of 10 mL/min. The potential -1.25 V was applied twice. The same trap solution was used for the individual samples for all three potentials. Therefore, in the case of NH_3 production, the amount of NH_3 should be added up.
The resultant quantification of NH_3 is graphically depicted as the NH_3 production rate in Fig. 6.10. Throughout all measurements, the calculated production rate was consistently within the ascertained error range and the quantity was not increasing. Hence, it implies that under this specific conditions NH_3 synthesis is not feasible. The variation of the parameters, temperature, pressure, and the concentration of the KOH solution did not lead to NH_3 synthesis. Due to the fact that changing these parameters did not lead to any change, the results are not presented graphically.

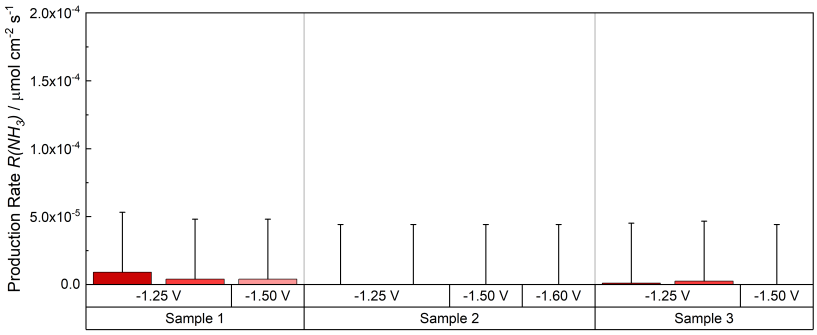


Fig. 6.10. Calculated rates of NH_3 production and the corresponding error bars that are determined while N_2 was supplied at the specific conditions.

The polarisation curves of the measurements are shown in Fig. 6.11. The current density was stable over time, therefore it is not presented. The error of the potentiostat is 0.025 % of the applied current range. The applied current range was 10 mA, which resulted in an error of 400 nA cm^{-2}. The error resolution is outside the significance range, therefore it is neglected. As the applied potential increased, the current density elevated. But, at the second measurement at -1.25 V the current density decreased, it could be that there was a degradation regarding H_2 evolution. No NH_3 is detected (Fig. 6.10, the question arises if the resulting current was insufficient for producing NH_3. At -1.25 V the approximately measured average current density was $-0.05\,mA\,cm^{-2}$. Utilizing Faraday's law Eq. 3.8 (z is 3), it resulted in a maximum possible production rate of

$$R(NH_3) = \frac{50 \times 10^{-6}}{3\ F} \tag{6.3}$$

$1.73 \times 10^{-10}\,mol\,cm^{-2}\,s^{-1}$. Hence, the resulting current density was large enough for producing quantities of NH_3 that can be detected via indophenol method. A minimum of 206 nmol was required, that corresponds to an production rate of $2.74 \times 10^{-11}\,mol\,cm^{-2}\,s^{-1}$ concerning the active cell area of $6.25\,cm^2$ and 20 min

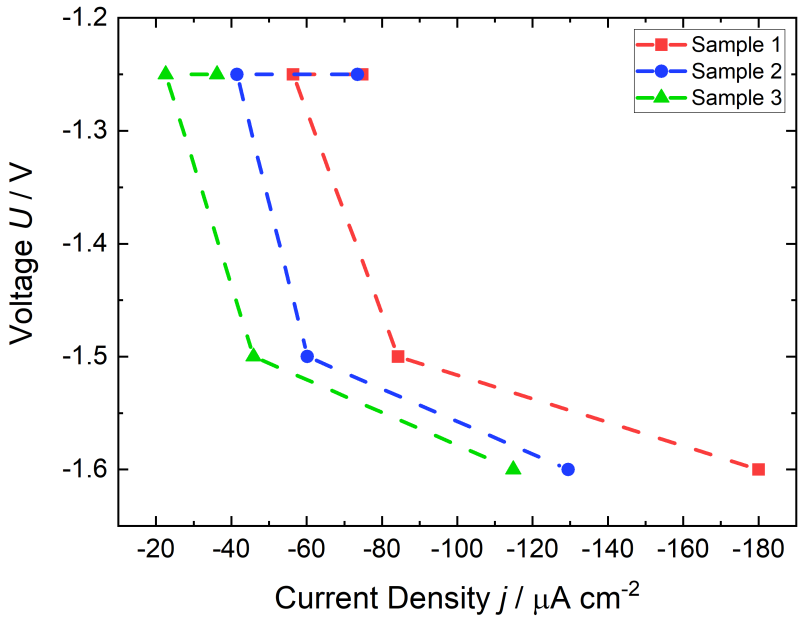
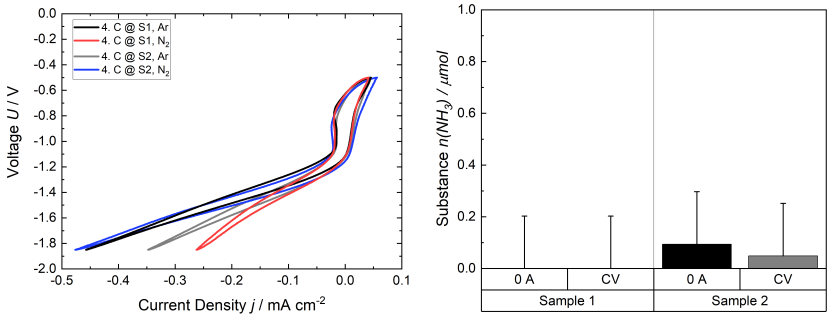


Fig. 6.11. Polarisation curves of the three samples, which were used for electrochemical NH_3 production. These three samples, three MEA cells, had identical materials and were operated under equivalent conditions.

Na_2SO_4 as Electrolyte

MEA Cell

Subsequent to adopting Na_2SO_4 as the electrolyte, the prescribed cleaning procedure was directly applied. In the iinital phase of each experiment 10 mL/min of Ar was supplied for 30 min at 0 A. Afterwards four CV cycles were recorded and the gas flux supplied alternated between Ar and N_2 (Fig. 6.12a). For the first sample, the recorded current density during the N_2 flux was less than that during the Ar flux. For the second sample, it was the reversed case. These outcomes did not indicate a possible NH_3 synthesis. No NH_3 impurities were detected in the first sample (Fig. 6.12b). The values of the second sample were within the error range. Therefore, it can be concluded that both electrochemical cell were clean. The determined quantity of NH_3 were zero during the N_2 supply.



(a) Last CV cycles of the trials.

(b) Determined amount of NH_3 and error.

Fig. 6.12. CV results and the corresponding detected NH_3 of the trials employing Na_2SO_4 as electrolyte. In red and blue the results during N_2 supply and in black and grey during Ar supply.

Potentials from −1.3 to −1.8 V were applied for 10 min after recording the CV data. The starting potential was raised from -1.25 to -1.3 V, because it was expected that the overpotential was too less. Furthermore, the range was extended. The NH_3 production rates of both samples are shown in Fig. 6.13. Similar to the experimental set up employing KOH as the electrolyte, the same trap solution was employed for each individual sample. As written previously, this implies that if NH_3 was produced, a summation of NH_3 should occur. So it must be assumed that the production rate value at −1.7 V was erroneous of the first sample as at -1.75 and −1.8 V the rate were zero. The production rates for the second sample fall within the error range for most voltages, and no rate rising was observed during the measurement. However, there was a sharp increase in the production rate at −1.75 V. Theoretical calculations indicate that NH_3 production is not feasible at these high potentials, because these high potentials result in the complete coverage of the catalyst surface area with H_2, preventing the adsorption of N_2 and thus the production of NH_3 [180]. This leads to the hypothesis that this measured value was either inaccurate or that NH_3 was produced at lower potentials, remained in the electrochemical system and was only driven out of the system at higher potentials. For this reason, the adsorption and desorption behavior of an electrochemical cell is examined in detail in chapter 7.

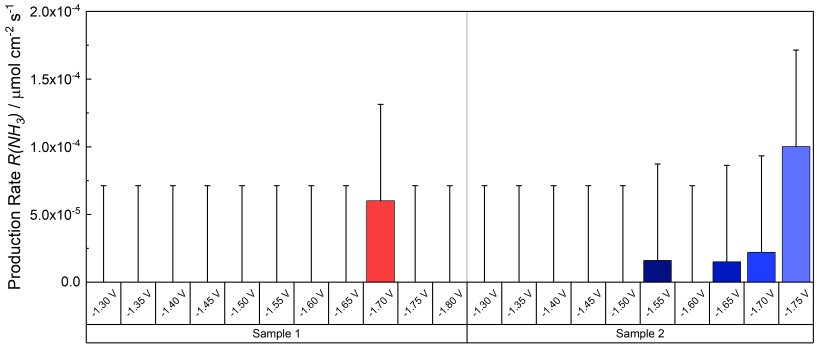


Fig. 6.13. Calculated rates of NH_3 production and the corresponding error bars that are determined while N_2 was supplied at the specific conditions.

H-Cell

The H-cell is the electrochemical cell, which is used in most of the publication (chapter 2.5). Due to the three electrode set up, the H-Cell is a simpler electrode reactor than the MEA cell. In addtion, this cell was used to compare the results with the results from project partners.
In both chambers 0.1 M Na_2SO_4 was filled and the chambers were separated by Zirfon. An Ag/AgCl electrode was used as the reference electrode. Such as the MEA cell, the H-cell was flushed with Ar in the beginning and no NH_3 was detected. Afterwards N_2 was supplied and potentials from -0.635 to -0.955 V vs. Ag/AgCl were applied for 10 min. After each applied potential a little of the solution was taken out of the cathode chamber for analyzing the concentration of NH_3 by the indophenol method. Fig. 6.14 exhibits the measured NH_3 production rates. As in the case of the other measurements, the values fell within the error range. Accordingly, it cannot be assumed that the production is feasible under this conditions in the H-cell.

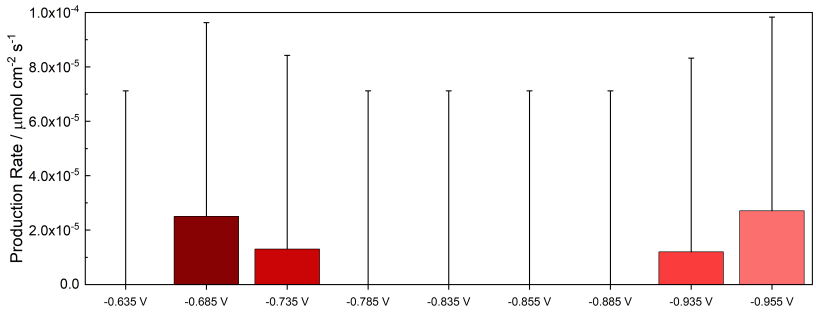


Fig. 6.14. Calculated production rates of NH_3 production and the corresponding error bars that are determined while N_2 was supplied at tje specific conditions in the H-cell.

6.3 High Entropy Alloys

6.3.1 Experimental

Catalyst Preparation

The HEA are the other class of catalysts that have been studied intensively. The HEA catalyst CoCuFeMoNi were provided from the project partner UU. The properties of these alloys are described in chapter 2.4. The HEA was deposited on carbon felt H2315 CX312 via sputtering. The sputtering led to a catalyst layer instead of individual particles. Fig. 6.15 illustrates SEM images of the electrode. Figs. 6.15 (a) and (b) show images of the "InLens" detector, this detector offers a better surface characterisation. Image (c) is recorded with an "AsB" detector, this detector offers information of the material composition due to the back scattered electrons. Image (b) and (c) are images of the same area and same resolution of the sample recorded with different detectors. Metals have a stronger back scattering than carbon and therefore they are represented brighter in the SEM image. Consequently, the darker the image area, the less or no metals were deposited on the carbon felt. Either the metals have not been deposited on these fibers or the metals have flaked off. Utilizing point measurement of Energy-dispersive X-ray spectroscopy (EDX), the amount of each element on the carbon felt can be measured. It was applied to both areas (a and b) of the sample. The average mole fractions of the sputtered metals are shown in Tab. 6.1.

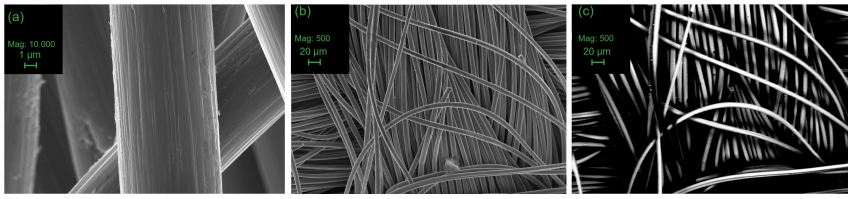


Fig. 6.15. SEM images of the sputtered HEA on carbon felt. (a) Magnification of 16000 using an "InLens" detector, (b) magnification of 500 using an "InLens" detector and (c) magnification of 500 using an "AsB" detector.

Tab. 6.1.: Average mole fraction the sputtered metals on the carbon felt of the images (a) and (b).

Metal	Image a: $\overline{\chi}$ atom [%]	Image b: $\overline{\chi}$ atom [%]
Cobalt	4.38 ± 1.05	2.28 ± 1.91
Copper	6.69 ± 1.65	4.16 ± 2.81
Iron	3.92 ± 0.94	2.51 ± 1.67
Molybdenum	3.37 ± 0.63	2.12 ± 1.46
Nickel	4.78 ± 1.17	3.03 ± 2.05

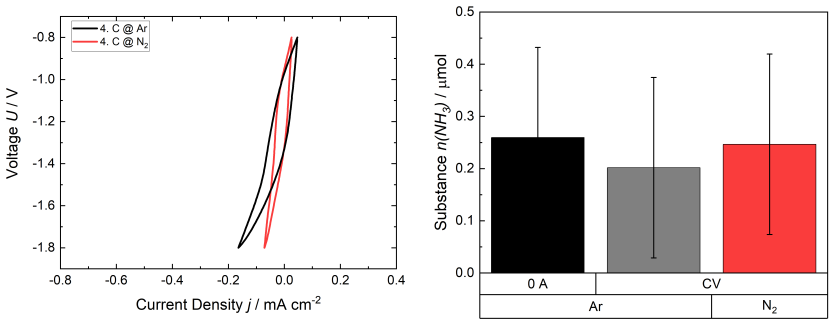
MEA Composition

The HEA was utilized as the cathode and still 1.3 - 1.4 $\mathrm{mg\,cm^{-2}}$ of the composition 60 % Pt/C HiSpec 9100 that was also deposited on carbon felt H2315 CX312 was used as the anode. The test bench was the same.

6.3.2 Results and Discussion

KOH as Electrolyte

The electrochemical properties of the HEA were studied at RT. As with the Au NP, the cell was flushed with 10 mL/min of Ar for 30 min at 0 A and afterwards CV cycles were recorded for determination the optimal potential range of NH_3 production. A 0.1 M KOH solution was used as the electrolyte. Fig. 6.16a shows the last recorded CV cycles. The measured current density during the N_2 supply was lower than during Ar supply. Therefore, no potential range could be identified and it led to the assumption that the catalyst was not active in reducing N_2. The corresponding detected amount of NH_3 is plotted in Fig. 6.16b. The detected NH_3 quantity while supplying N_2 was as low as while Ar was supplied. Thus, no NH_3 was produced during CV.



(a) Last CV cycles of the trials.

(b) Determined amount of NH_3 and error.

Fig. 6.16. CV results and the corresponding detected NH_3 employing KOH as electrolyte. In red are the results during N_2 supply and in black and grey during Ar supply.

Potentials from −1.3 to −1.8 V were applied for 10 min after recording the CV data like it was in done in the case of Au catalyst (see Fig 6.13). The NH_3 production rates are shown in Fig. 6.17. In the case of the HEA catalyst for every potential a fresh trap solution was used. The measured production rate are within the error margin. Consequently, the tested catalyst is not catalytically active under the investigated conditions.

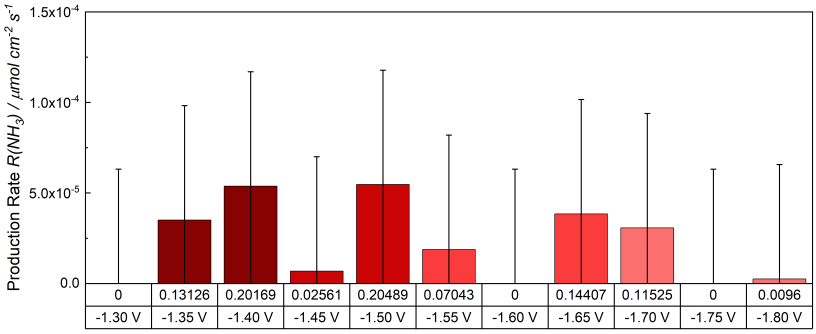
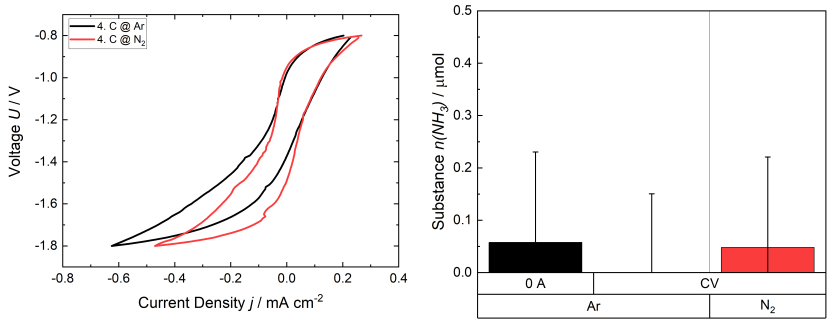


Fig. 6.17. Calculated rates of NH_3 production and the corresponding error bars that were determined while N_2 was supplied at the specific conditions.

Results Na_2SO_4 as Electrolyte

Also, in the case of the HEA catalyst, Na_2SO_4 was tested as electrolyte. The principle of this experiment was the same as with KOH. The CV cycles of the samples for the Ar and N_2 gas flux are depicted in Fig. 6.18a. Like the case with KOH, the measured current density during the N_2 supply was lower than during Ar supply. However, the resulting current density of the CV curves were larger in comparison to the results in Fig. 6.16a. This probably resulted from a better ionic conductivity of in Na_2SO_4 than in KOH.



(a) Last CV cycles of the trials.

(b) Determined amount of NH_3 and error.

Fig. 6.18. CV results and the corresponding detected NH_3 employing Na_2SO_4 as electrolyte. In red the results during N_2 supply and in black and grey during Ar supply.

The measured NH_3 production rates utilizing Na_2SO_4 as electrolyte (Fig. 6.19) are within the error margin over the entire potential. Independent from the electrolyte, eNRR is not feasible with the HEA catalyst.

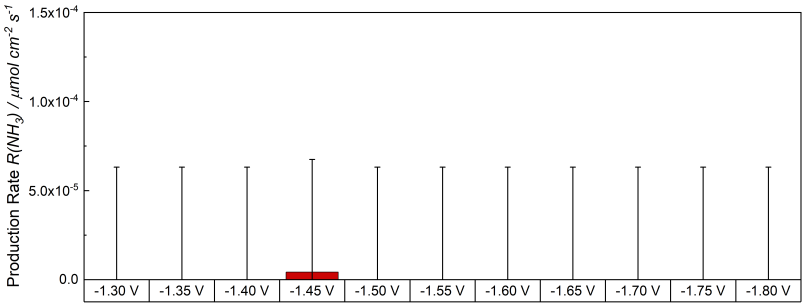


Fig. 6.19. Calculated rates of NH_3 production and the corresponding error barsthat were determined while N_2 was supplied at the specific conditions.

6.4 Summary and Conclusion

The results in this chapter and in the appendix 9.2 show clearly that NH_3 synthesis utilizing the tested catalysts is not reliable possible. Different cell parameters like form of the membrane, membrane or diaphragm were studied. The process parameters temperature, electrolyte, reactant, flow rate, energy supply were also investigated. However, the alteration in parameters did not result in eNRR. Consistent with the assertions in the introduction and the mentioned literature, the unequivocal detection of NH_3 is very challenging. This can easily result in false-positive outcomes. For this reason, the sources of impurities were examined and evaluated for their influence to interfere the determination of the electrochemical NH_3 synthesis from N_2. The subsequent developed cleaning process led to a significant reduction of the false-positive results. Though, it is shown that NH_3 was detected above the error level (Fig. 6.13). These values were observed at potentials where, according to theory, no synthesis should occur. Consequently, NH_3 was either introduced in the beginning and remained in the cell or NH_3 was synthesised under specific conditions and remained in the cell. The quantity of NH_3 that remained in the cell, most likely in the membrane, until the potential, energy was enough to discharge NH_3, as shown in Fig. 6.13.

7 Ammonia Adsorption and Desorption of the Membrane

7.1 Introduction

The electrochemical synthesis of NH_3 is conducted near the limit of detection in literature. As elucidated in the preceding chapter 6, the unambiguous demonstration of the eNRR remains not feasible with the tested catalyst in this work. Furthermore, the detected NH_3 in literature is hardly confirmed by the contribution of eNRR, as different non-negligible contamination affects the synthesis and result in false amounts of NH_3 being detected. There are several sources of contamination [75, 76]. The impact of these specific impurities on the determination of the eNRR is examined in the introduction of chapter 6. As previously stated, the membrane, especially the Nafion membrane, plays a decisive role.

In many cases for eNRR, Nafion was used as electrolyte and separator between the anode and cathode [58, 61, 98, 181, 182]. Due to the basic character of NH_3, it reacts with the protons of Nafion, forming NH_4^+ ions, i.e, the NH_4^+-form of Nafion. This in turn has a strong influence on the unequivocal determination of the NH_3 production rate, because atmospheric NH_3 pollution, impurities in the feed-gas stream like NH_3 itself, and impurities inside the electrochemical cell can persist in the form of NH_4^+ within the membrane. These resulting NH_4^+-ions from the impurities can be expelled from the membrane and subsequently dissociate into NH_3 at the cathode, leading to a falsely interpreted production of NH_3 particularly with respect to the catalyst and operating parameters. Conversely, if NH_3 is produced within the cell it may be absorbed by the membrane, thereby preventing the detection of NH_3 at the outlet of the cell. This outcome leads to a false negative result. Moreover, the NH_4^+-ions within the membrane have been demonstrated to affect significantly the ion conductivity and ohmic resistance of the electrolysis system [77, 114, 116, 117, 183]. It is not known under what conditions NH_3 is driven out of the membrane. Whether this process happens purely over time or whether a force like an electrical current or a concentration gradient is responsible for it.

To expand the understanding of the adsorption behavior of NH_3 / NH_4^+ in Nafion and to determine the specific conditions and extent to which the NH_4^+-ions introduced

into the membrane are expelled as NH_3 from the cell especially from the membrane. The adsorption and desorption behavior of Nafion is studied in-depth. Additionally, the influence of desorbed NH_3 / NH_4^+ on the properties of Nafion is studied. Subsequently, Nafion is integrated into an electrochemical cell configuration and its behavior is meticulously examined under the dynamic influence of electrochemical reactions.

7.2 Ion exchange

7.2.1 Experimental

Nafion 115, with a thickness of 127 µmol and a size of 42*42 mm^2 was used. The average weight was determined, based on five dried membrane pieces, yielding am average of 432.4 mg with an error of ± 15.3 mg. The pieces were dried in an oven at 80 °C for 1 h before the weight was measured. The equivalent weight is defined as the value of the amount of substance of the sulfonic acid groups (-SO_3H) per gram of dry polymer. For Nafion, this value is 1100 g mol^{-1} [184]. With respect to the weight of the membrane pieces, these contain 403 µmol ± 14 µmol of sulfonic acid groups.

To introduce NH_3 in the form of NH_4^+-ions into the membrane, the H^+, which are bound to the sulfonic acid groups, must be be exchanged with NH_4^+-ions. This exchange occurs in a one-to-one ratio. Thus, the maximum amount of NH_3 / NH_4^+, that can be bound inside the polymer structure is 403 µmol ± 14 µmol.
Ammonium sulfate ($(NH_4)_2SO_4$) is utilized as NH_4^+ source. By placing Nafion 115 into a 25 mL $(NH_4)_2SO_4$ solution H^+ within the membrane is exchanged with NH_4^+. The immersion time was varied in order to investigate its influence. The ion exchanged Nafion membrane in NH_4^+-form is shown in Fig. 7.1.

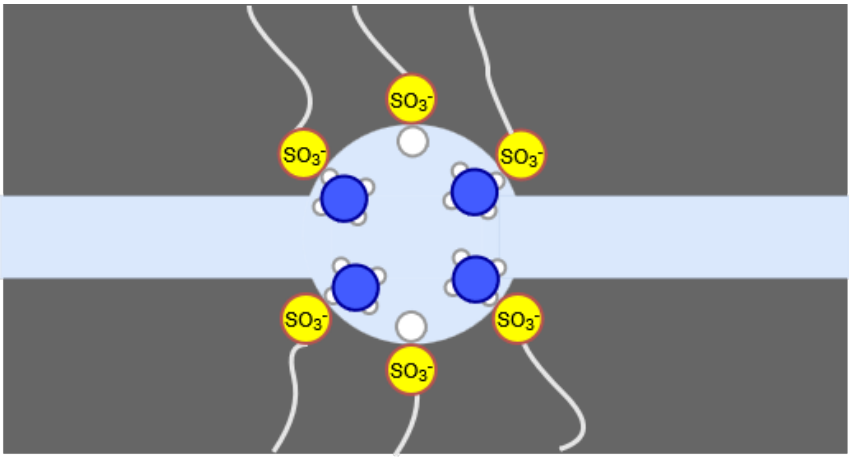


Fig. 7.1. Illustration of the ion exchanged Nafion membrane. H^+, which are bounded to SO_3^- are exchanged with NH_4^+ during the immersion of the Nafion membrane into a $(NH_4)_2SO_4$ solution. Nafion is transferred into its NH_4^+-form.

The study aims to investigate the influence of the quantity of NH_4^+ in the solution and on the ion exchange. For this reason, $(NH_4)_2SO_4$ solutions were prepared with different amounts of substance (n) of NH_4^+-ions in relation to the amount of H^+ in the membrane. The ratio 1:1 (Tab. 7.1) therefore means that the amount of NH_4^+ in the solution is the same as the amount of H^+ in the membrane. To gain the specific amount of substance of NH_4^+, the mass (m) of $(NH_4)_2SO_4$ must be calculated with the following equation

$$m((NH_4)_2SO_4) = \frac{\beta(NH_4^+)\ V\ M((NH_4)_2SO_4)}{2\ M(NH_4^+)}\ . \tag{7.1}$$

Where β is the mass concentration inside the volume (V) of 25 mL. The molar masses are $M((NH_4)_2SO_4) = 132.14\,\mathrm{g\,mol^{-1}}$ and $M(NH_4^+) = 18.04\,\mathrm{g\,mol^{-1}}$.
The corresponding quantity of NH_4^+ to the ratio, the concentration of NH_4^+ (c), the mass concentration of NH_4^+ in the prepared $(NH_4)_2SO_4$ solution, and the required mass of $(NH_4)_2SO_4$ for preparing the specific NH_4^+ concentration are shown in Tab. 7.1.

.

Tab. 7.1.: The different studied rates, the corresponding quantity and concentration of NH_4^+ are listed. Additionally the mass of $(NH_4)_2SO_4$, which is required for preparing the rates.

NH_4^+ vs. H^+	$n(NH_4^+)$	$c(NH_4^+)$	$\beta(NH_4^+)$	$m((NH_4)_2SO_4)$
0.5:1	201.5 µmol	0.008 mol L^{-1}	142 mg L^{-1}	13 mg
0.8:1	322.4 µmol	0.013 mol L^{-1}	227 mg L^{-1}	21 mg
1:1	403 µmol	0.016 mol L^{-1}	284 mg L^{-1}	26 mg
1.5:1	604.5 µmol	0.024 mol L^{-1}	425 mg L^{-1}	39 mg
2:1	806 µmol	0.032 mol L^{-1}	567 mg L^{-1}	52 mg

After the ion exchange took place, the Nafion membrane was dried and introduced into a sulfuric acid (H_2SO_4) solution to expel the NH_4^+-ions from the membrane. The H_2SO_4 solution facilitates a re-exchange of NH_4^+ with H^+. Subsequently, the amount that was exchanged is analyzed. The concentration of the H_2SO_4 solution is 0.45 mol L^{-1} and the volume is 25 mL, thus a substantial excess of H^+ os available.

7.2.2 Results and Discussion

Ammonia Adsorption

The thickness and size of the membrane was determined before and after insertion of the membrane pieces in the ammonium sulfate solution using a caliper gauge. Swelling, an increase in the size and an increase of the thickness of the membrane, was not detected. The swelling behavior of Nafion in the literature is also different [185, 186].

The ion exchange of H^+ with $NH_4{}^+$ was studied at temperatures ranging from 25 - 80 °C and for different exchange times of 30 and 60 min. The objective was to study the effects of elevated temperatures and extended exchange times. However, it has not been proven that the quantity of the ion exchange increases at higher temperatures. In addition, no difference in the quantity of ion exchange was observed when varying the exchange time while the membranes were placed in the same solution concentration at the same temperature.

Despite this, a scattering of results was observed when the experiments were repeated. Fig. 7.2 shows the amount of $NH_4{}^+$ remaining in the $(NH_4)_2SO_4$ solution with the respective mean values and error bars for the ratio of NH_4^+ vs. H^+ 1:1 (red) and 2:1 (blue) ($c(NH_4{}^+) = 0.016$ and $0.032\,\mathrm{mol\,L^{-1}}$). The ion exchange was conducted at RT for a period of 1 h for both ratios. The spread of the average value of the ratio 1:1 was ± 17 µmol and in the case of 2:1, ± 26 µmol.

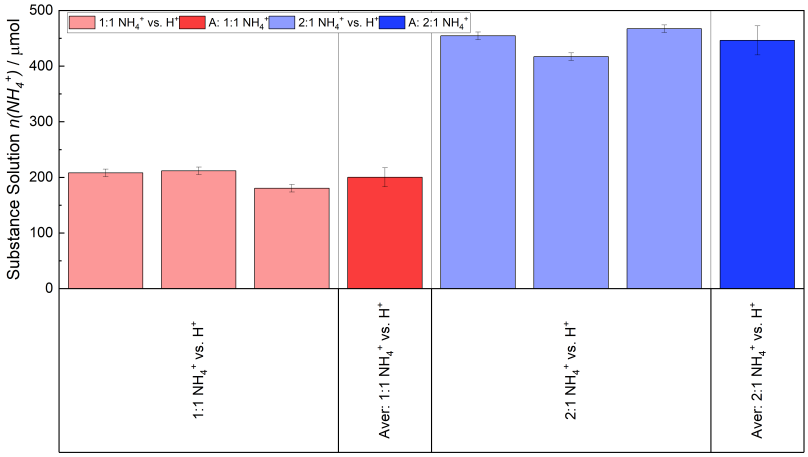


Fig. 7.2. Deviation of the ion exchange for two different ratios of $NH_4{}^+$ vs. H^+ (bright colors). The y-axis displays the quantity of $NH_4{}^+$ remaining in the solution. The average of both ratios is indicated by the red and blue bar.

The question arises as to whether there is a correlation of the provided quantity of NH_4^+-ions and the ion exchange. Tab. 7.1 exhibits the diverse proportion of NH_4^+ vs. H^+, that were prepared to analyze the ion exchange. The ion exchange process of the NH_4^+-ions and the H^+ is an equilibrium-controlled process (Eq. 7.2). In the initial stage, the NH_4^+-ions are present exclusively in the solution ($c(NH_4^+, Sol)$), while the H^+ are located within the membrane ($c(H^+, Mem)$). Over time, the process of ion exchange occurs, resulting in the exchange of H^+ within the membrane with NH_4^+. In doing so, the H^+ desorbs into the solution

$$c(NH_4^+, Sol) + c(H^+, Mem) <=> c(NH_4^+, Mem) + c(H^+, Sol)\ . \qquad (7.2)$$

The equilibrium constant (K_{eq}) is determined through the concentrations of the ions in the media (membrane and solution) after reaching the equilibrium state

$$K_{eq} = \frac{c(NH_4^+, Mem)\ c(H^+, Sol)}{c(NH_4^+, Sol)\ c(H^+, Mem)}\ . \qquad (7.3)$$

In light of the assumption that the volume of the solution and the membrane remain constant, it is reasonable to calculate the equilibrium constant using the amount of substance in place of the concentration. As previously outlined, the quantity of protons present within the membrane is 403 µmol. The quantity of NH_4^+-ions in the solution depends on the chosen ratio of NH_4^+ against H^+, as illustrated in Tab. 7.1 (NH_4^+ vs. H^+). The adsorbed NH_4^+-ions within the membrane are quantified through the indophenol method after extracting it from the membrane with an excess of sulfuric acid solution. Given that the exchange of NH_4^+-ions and H^+ occurs in one-to-one ratio, the original NH_4^+ solution contains now an equivalent quantity of H^+ to that of NH_4^+ within the membrane.

Fig. 7.3 shows the determined equilibrium constant of the tested NH_4^+ vs. H^+ ratios as red squares with their respective error bars for each tested concentration. As $K_{eq} > 1$, the equilibrium is on the product side. Consequently, the NH_4^+-ions from the solution prefer to exchange with the H^+ within the membrane. The error bars of the ratios 0.8:1 and 1.5:1 are larger in comparison to the error bars of 0.5:1 and 1:1, as the determined amount of NH_4^+ in the solutions of these ratios showed a larger scatter compared to the latter one. This scattering has a magnifying effect on the error bar of K_{eq}. Additionally, the error bars of the ratio 2:1 is very large, because the concentration of H^+ in the membrane after exchange is calculated by subtracting the concentration of the NH_4^+-ions in the membrane after exchange

from the concentration of H^+ in the membrane before exchange. For the ratio 2:1 most protons are exchanged and therefore the difference is small and in the order of magnitude of errors of the errors of minuend and subtrahend. This leads to a substantial error in K_{eq} for the ratio 2:1. The average value of K_{eq} is 2.81 ± 2.62 including the ratio of 2:1. If this ratio is not considered for this reason, K_{eq} is 2.00 ± 1.31, as depicted by the blue line in Fig 7.3.

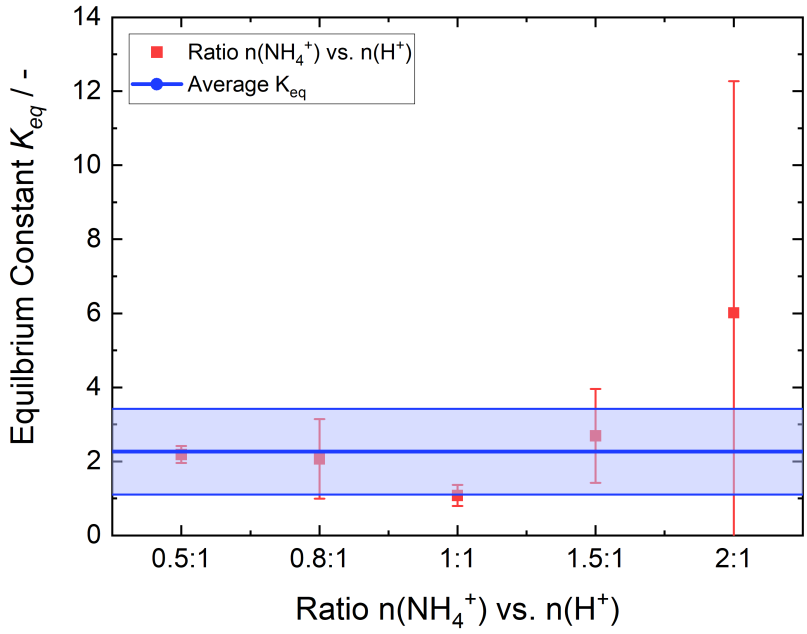


Fig. 7.3. Equilibrium constants of the different ratios of NH_4^+ vs. H^+ (red squares) and their corresponding error bars. The average value of K_{eq} is shown as the blue line. The colored area is the error of the average value. The value of the ratio 2:1 is not considered for the average value.

Ammonia Desorption

The ion exchanged Nafion membranes were immersed into the H_2SO_4 solution for evaluating the desorption kinetic of NH_3 / NH_4^+ in relation to the time and temperature. This study aimed to elucidate whether increased temperature correlates with increased NH_3 desorption. No correlation was found. The desorbed quantity of NH_3 at RT up to 80 °C was similar. Furthermore, it sought to determine the impact of immersion duration in the H_2SO_4 solution on desorption behavior. The desorption time ranged from 10 to 60 min. Similar results were obtained. The used Nafion pieces, as noted previously, had a size of 17.64 cm^2 and each one contained 403 µmol ± 14 µmol of H^+, which were bonded to sulfonic acid groups.

The red bar in Fig. 7.4, which is the same as in Fig. 7.2, depicts the average remaining quantity of NH_4^+ in the solution. 200 µmol of NH_4^+ remained in the solution. The green bar illustrates the amount of NH_4^+ that was ion-exchanged into the membrane by subtracting the red bar from the membrane's initial concentration of H^+ (403 - 200 µmol). The ion-exchanged membranes were placed in three fresh H_2SO_4 solutions, because during experiments it was found that the NH_4^+-ions were not fully removed from the membrane at first. An equilibrium was established between the membrane and the H_2SO_4 solution. By replacing the H_2SO_4 solution with a fresh one, the desorption of NH_3 continued. Approximately 85 % of the quantity was removed in the first H_2SO_4 solution (1. Drag-out NH_4^+). Nearly 15 % in the second solution (2. Drag-out NH_4^+) and less than 0.5 % in the third solution (3. Drag-out NH_4^+). The average totaled amount of NH_3 that was expelled from the membrane is displayed as the blue bar. It can be concluded that the quantity of NH_4^+ that was previously exchanged into the membrane has been recovered within the margin of error.

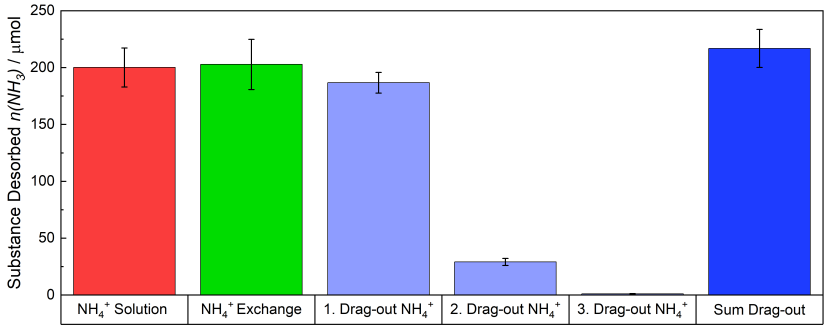


Fig. 7.4. The detected and measured quantities of NH_3 are presented. In red the quantity of NH_4^+ that remained in the solution is represented and in green the initial quantity of NH_4^+ that was exchanged into the membrane. The blue bar presents the sum NH_3 that was driven out from the membrane. In total the membrane was placed three times in a fresh $(NH_4)_2SO_4$ solution, because an equilibrium of NH_3 is established between membrane and solution, thereby preventing further desorption of NH_3. These quantities are referred as first to third drag-out, depicted as the bright blue bars.

7.3 Discharge of the electrochemical Cell

7.3.1 Experimental

For studying the NH_3 adsorption and desorption behavior of Nafion 115 in an electrochemical cell, the membrane was assembled into a membrane electrode (MEA) cell. An MEA and the cell are illustrated in Fig. 3.2. The core of this cell is the MEA. Nafion 115 was introduced into solutions with different concentrations of $(NH_4)_2SO_4$. $2\,mg\,cm^{-2}$ of the IrO_x catalyst, supplied by Alfa Aesar / Thermo Fisher Scientific was spray-coated onto titanium felt substrate from Bekeart, Bekipor® 2GLD10-0.35. Prior to the spray-coating of the catalyst, a thin Ir-layer was sputter-deposited onto the titanium felt substrate. This electrode functions as the anode. Knife-coating was employed to deposit 60 % Pt/C HiSpec 9100 from Johnson Matthey onto a carbon felt substrate from Freudenberg, H2315 CX312. This electrode functions as the cathode. The loading of the catalyst was 1.3 - $1.4\,mg\,cm^{-2}$. Both electrodes were produced in-house.
The other cell components (bipolar plate and etc.) are used as described in section 3.2. In order to avoid transfer of NH_4^+ from the membrane to the electrodes and to facilitate disassembling for analysis, a hot-pressing step was not employed. The active cell area was $6.25\,cm^2$. To investigate the electrochemical change in more detail, the impedance spectra were fitted with the software Zview from Scribner.

Fig. 7.5 displays the movement of the ions like in Fig. 6.2, including an enlargement of the membrane structure. The membrane structure is the channel-shaped structure of Nafion like Fig. **??**. The described H^+ exchange by NH_4^+ causes the binding of NH_4^+ to the SO_3^- groups within Nafion. During the experiment, H_2O is supplied into the anode PTL and is oxidized by applied electrical potential, resulting in the production of O_2. O_2 exits the cell on the anode outlet. The generated H^+ interacts with NH_4^+ within the membrane. NH_4^+ is displaced with H^+, as shown in the middle channel. Consequently, NH_4^+ desorbs from the membrane. At the cathode,

$$\text{Anode:} \qquad 2\,H_2O \longrightarrow 4\,H^+ + 4\,e^- + O_2 \tag{7.4}$$

$$\text{Cathode:} \qquad 4\,NH_4^+ + 4\,e^- \longrightarrow 4\,NH_3 + 2\,H_2 \tag{7.5}$$

NH_4^+ deprotonates, producing NH_3. The dissociated H^+ is reduced to H_2 with the supplied e^- from the cathode.

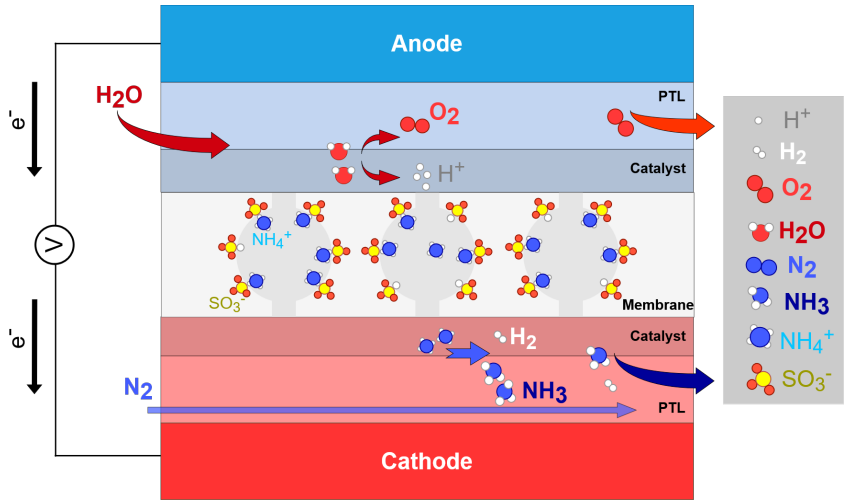


Fig. 7.5. Schematic illustration of the exchange and desorption process of NH_4^+ within the membrane. H_2O is introduced into the PTL of the anode. In the catalyst layer it oxidizes to O_2 and H^+. The produced O_2 exits the cell on the anode side. The generated H^+ interacts with NH_4^+ within the membrane. NH_4^+ is displaced with H^+. NH_4^+ desorbs from the membrane. At the cathode, NH_4^+ deprotonates, producing NH_3. The dissociated H^+ is reduced to H_2 with the supplied e^- from the cathode. N_2 is used as carrier gas to remove NH_3 and H_2 from the cell. The coloring of the atoms is done according to the CPK color model.

The corresponding test bench is illustrated in Fig. 7.6. H_2O was pumped into the anode of the electrochemical cell with a circulation. The flow rate of the pump was 10 mL/min. On the cathode side, N_2 is introduced as a carrier gas via a mass flow controller from Brooks Instruments to remove NH_3 from the cell. The cleaning trap filled with H_2SO_4 is needed to remove impurities of NH_3 out of the N_2 feed gas stream, otherwise these impurities can be detected and lead to false results. The trap collects the desorbed NH_3 for subsequent determination via the indophenol method. In the case that H^+ does not displace the $NH_4{}^+$,

$$\text{Anode:} \qquad 2\,H_2O \longrightarrow 4\,H^+ + 4\,e^- + O_2 \tag{7.6}$$

$$\text{Cathode:} \qquad 4\,H^+ + 4\,e^- \longrightarrow 2\,H_2 \tag{7.7}$$

only H_2 is produced.

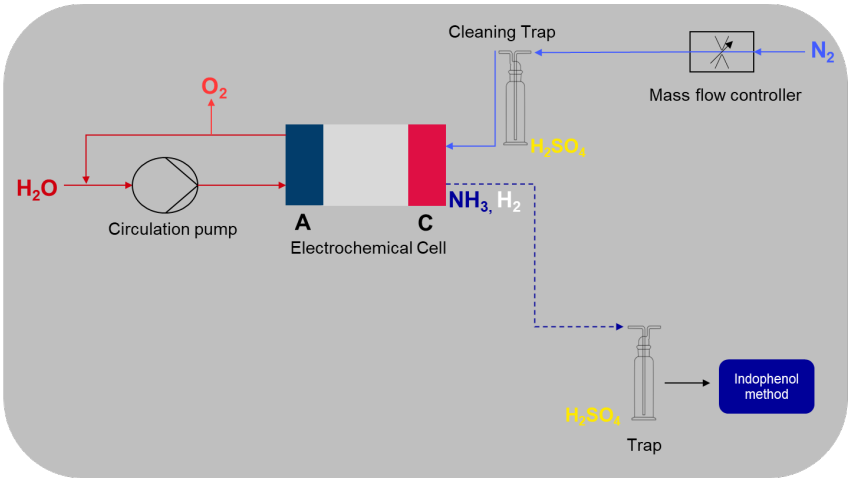


Fig. 7.6. Schematic illustration of the test bench. H_2O is supplied and O_2 is produced at the anode. NH_3 is expelled from the membrane and H_2 is produced at the cathode.

7.3.2 Results and Discussion

Ammonia Desorption

Fig. 7.7 displays the desorption of NH_3 during the trials of a ratio 2:1 NH_4^+ vs. H^+ ($c(NH_4^+) = 0.032\,mol\,L^{-1}$) at ambient temperature. The measurement protocol was repeated with a fresh cell, including a fresh MEA, to ensure reproducibility. The first bar of each measurement point is attributed to the first trial (T1), and the second bar is attributed to the second trial (T2). The measurement protocol was entirely carried out twice, with each measurement point held for a duration of 30 min. At the beginning of each run, an impedance spectrum was recorded. The impedance spectra will be discussed later. For the splitting of water and the generation of H^+, which are needed to drive out NH_4^+ from the membrane, an electrical potential is required. For this purpose the potentials 1.5, 1.75, and 2 V were applied, which are common for water electrolysis [148]. As these potentials did not lead to the desorption of NH_3, the maximum current supply of the potentiostat, 5 A, resulting in a current density of $0.8\,A\,cm^{-2}$, was applied in order to expel NH_3. After this step, a measurement run was finished and the next started with the mentioned potentials.

The values are plotted logarithmically and each run is illustrated in a different color. The graphical representation exclusively shows bars corresponding to conditions that lead to NH_3 desorbed quantities surpassing the margin of the error of 0.2 µmol. During the applications of the current densities a considerable quantity of NH_3 / NH_4^+ was expelled from the membrane in proportion to the quantity expelled while the potentials were applied. The desorption rate declines with each subsequent run when the highest current density was applied. In the case of the second run, the determined desorption is only 25 % of that determined in the first run. No desorbed NH_3 was detected above the margin of error in the initial run when the potentials were applied and in the second run applying 2 V. However, NH_3 was detected in the subsequent run after the current density was applied. That was unexpected because in the first run no NH_3 was detected at 1.5 V. Therefore, it is assumed that the NH_4^+-ions were no longer ionically bound in the membrane. They have been released by the previous current supply, converted to NH_3, remained in the cell and subsequently left the cell by diffusion. The current densities exhibited an increase from the first run to the second run, relating to the applied potentials. This increase in current density was attributed to the drive out of NH_4^+ from the membrane, leading to an enhancement in ionic conductivity and thus an increase in current density.

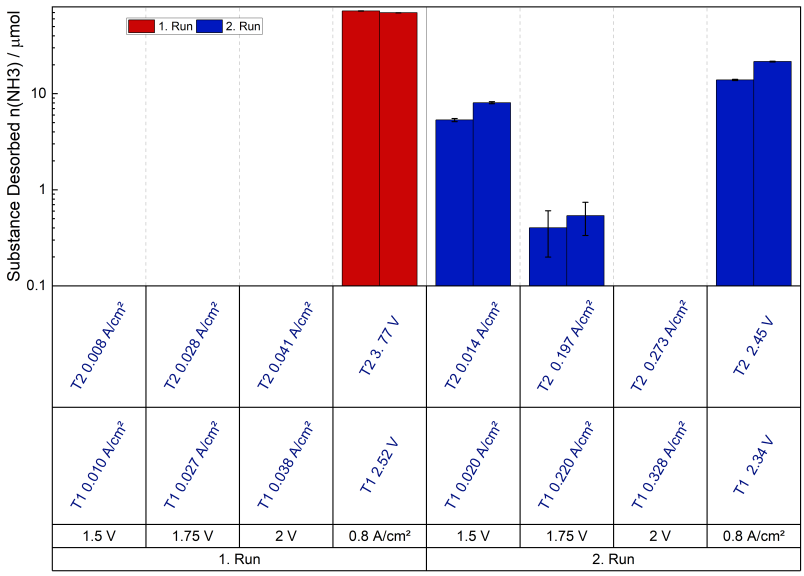


Fig. 7.7. Expelled amount of NH_3 of the 2:1 ratio, a logarithmic scale is used. The red color represents the measurement protocol of the first run and the blue of the second run. The applied potentials / current densities are written in black, while the measured potentials / current densities are written in blue.

A 1:1 ratio of NH_4^+ vs. H^+ was employed ($c(NH_4^+) = 0.016\,mol\,L^{-1}$) to study whether a different ratio has a major influence on the desorption behavior (Fig. 7.8) at ambient temperature. The absolute desorption of NH_3 was lower, yet the qualitative desorption was highly comparable and the experiment was also reproducible. Furthermore, the behavior subsequent to the initiation of the current density of $0.8\,A\,cm^{-2}$ was investigated. Therefore, the potential was set to 0 V, precluding any further electrochemical reaction that results in an NH_3 desorption. However, NH_3 was driven out at the dead-voltage state, as depicted in Fig. 7.8. The results underscore that the NH_4^+-ions were no longer ionically bound, but already in the NH_3 state and were subsequently removed by diffusion. Hence, the desorption of NH_3 was not solely contingent upon electrochemical processes driven by potential, but diffusion also plays a contributory role. Apparently, some NH_3 was removed from the membrane under the current flow and persisted in another part of the cell, from where it could be expelled by a purely diffusive process in the subsequent step with no potentials applied. Additionally, a third run was executed at $0.8\,A\,cm^{-2}$. The trend continuous that the desorbed quantity declines with successive runs.

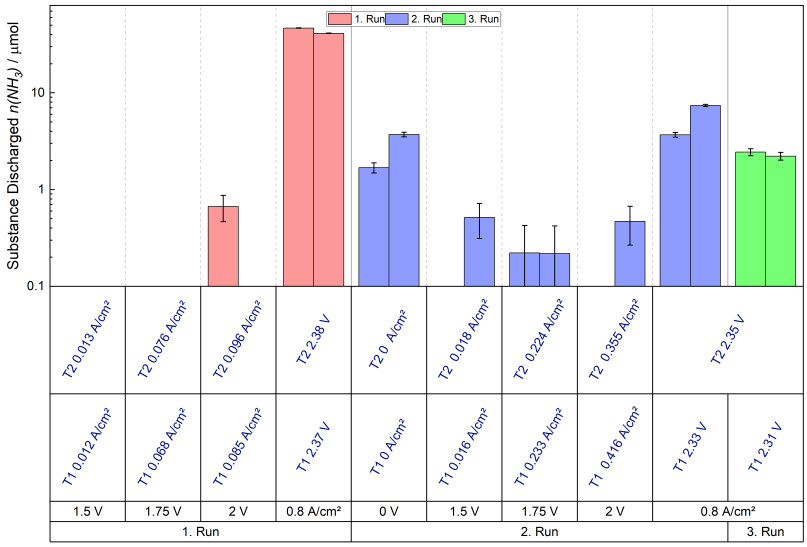
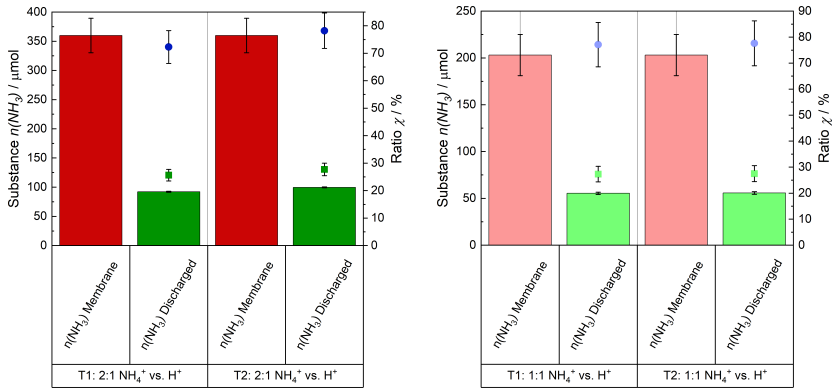


Fig. 7.8. Expelled amount of NH_3 of the 1:1 ratio, a logarithmic scale is used. The red color represents the measurement protocol of the first run, the blue the second, and the green the third run. The applied potentials / current densities are written in black, while the measured potentials / current densities are writtem in blue.

In order to demonstrate transparency and reliability of NH_3 desorption and the resulting consequences on the properties of the membrane, both trials of the respective ratios 1:2 and 1:1 of NH_4^+ vs. H^+ are shown in Fig. 7.9.

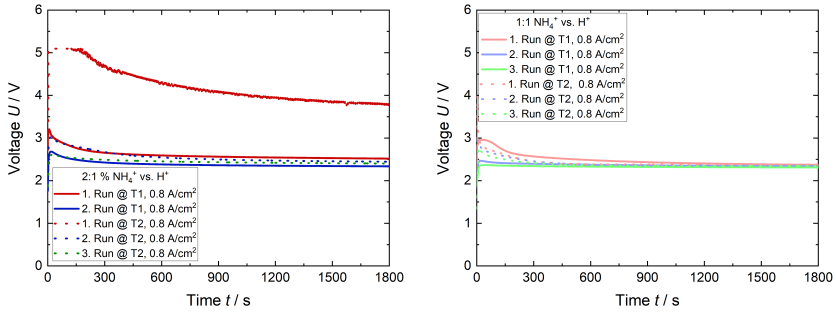
The expelled quantity of NH_3 was totaled in the respective experiments to determine whether the amount that was ion-exchanged into the membrane was expelled. This result is displayed in Fig. 7.9. Fig. 7.9a displays the outcome of the 2:1 ratio and Fig. 7.9b the outcome of the 1:1 NH_4^+ vs. H^+ ratio. The determined expelled quantities of NH_3 are shown as green bars and in red are the calculated quantities of NH_3 / NH_4^+, which were in the membrane at the start of the trials. The red bar is based on the subtraction of the average value from the initial NH_4^+ concentration of the $(NH_4)_2SO_4$ solution and the NH_4^+ concentration in the solution after the ion exchange. The ratio of the values (green bar divided by red bar) for each experiment is plotted as green square dots on the right-hand y-axis. It can be seen that only 25 - 30 % of the NH_3 present in the whole membranes were desorbed from the membranes. It must be taken into account that the active cell areas of the membranes, where the electrochemical reactions occur, were 6.25 cm^2, while their total areas of the membranes were 17.64 cm^2. The ratios of the desorbed quantities in relation to the quantities in the active cell area are shown as blue dots. A significant proportion of the NH_4^+-ions, between 70 and 80 %, in the active cell area were expelled. The remaining 20 to 30 % of the NH_4^+-ions were still chemically bounded to the sulfonic acid groups within the membrane.



(a) Ratio of 2:1 NH_4^+ vs. H^+ **(b)** Ratio of 1:1 NH_4^+ vs. H^+

Fig. 7.9. Comparison and ratio of the expelled amount of NH_3 compared to the initial amount of NH_3 in the membrane. Green dots refer to the ratio of the expelled amount to the initial amount in the entire membrane. The blue dots refer to the ratio of the expelled amount to the initial amount in the active area of the membrane only.

Galvanostatic experiments performed at the maximum current density of 0.8 A cm^{-2} are presented in Fig. 7.10. On the left-hand side are shown the results of the ratio 2:1 and on the right-hand side those of the ratio 1:1 NH_4^+ vs. H^+. The measured voltages were highest during the first run, especially during the second trial of the ratio 2:1 NH_4^+ vs. H^+ (T2). Apart from this trial, the voltages decreased up to approximately 600 - 800 s. Afterwards, they remained constant over time. Compared to the first run, the potentials decreased in the second. This decrease was particularly pronounced in T2 of the ratio 2:1 NH_4^+ vs. H^+. It is assumed, that in the case of T2 the quantity of the NH_4^+-ions within the active cell area was larger in comparison to T1. However, as the consequence of the elevated current supply during the initial run, approximately 57 % of NH_3, which was bounded as NH_4^+ to the sulfonic acid groups in the channel-shaped microstructure of Nafion in the active cell area, was expelled from the membrane. This desorption resulted in the liberation of sufficient channels from NH_4^+-ions, thereby increasing the conductivity of H^+ drastically through the membrane. As a result, a significant reduction in the potential for the second run of T2 was observed, so that the measured potential is similar to the measured potential from T1. No substantial change in measured potentials was evident from the second to the third run due to the reason that the remaining NH_4^+-ions within the active cell area of the membrane no longer interact with the incoming H^+. Therefore, the membrane resistivity decreased, leading to a reduction in the required potential for the current flow.

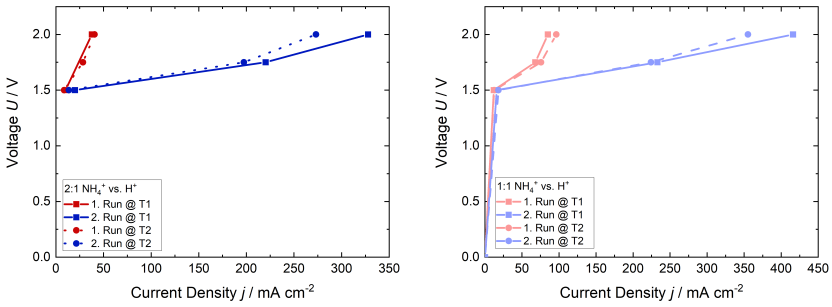


(a) Ratio of 2:1 NH_4^+ vs. H^+.

(b) Ratio of 1:1 NH_4^+ vs. H^+.

Fig. 7.10. Galvanostatic experiments for both ratios at RT. The first trials are depicted as the solid lines and the second trials as the dotted lines. The measured potentials for the first runs are shown in red, that for the second run in blue and that for the third run in green.

Fig. 7.11 shows the respective polarization curves, to which potentials were applied and the current densities measured. During the first run, the measured current densities were low at the potentials of all trials. After the first time $0.8\,\mathrm{A\,cm^{-2}}$ was applied, a significant amount of NH_3 (see Fig. 7.7 and 7.8) was expelled, resulting in a substantial decrease in the resistivity of the membrane. Thus, the current densities, which were measured during the applied potentials, increased as shown in Fig. 7.11. Notably, the current densities recorded for the ratio 1:1 were found to be higher, attributable to a lower NH_4^+ content within the membrane, leading to enhanced conductivity.



(a) Ratio of 2:1 NH_4^+ vs. H^+.

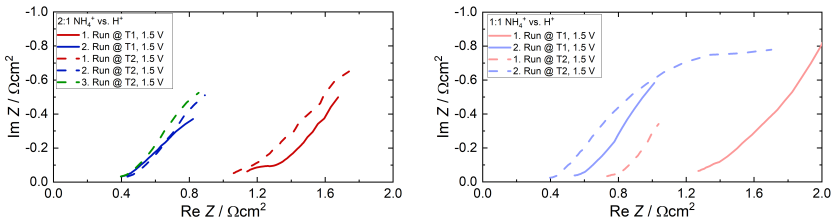
(b) Ratio of 1:1 NH_4^+ vs. H^+.

Fig. 7.11. Polarisation curves for both trials at RT. The first trials are depicted as the solid lines with square dots and the second trials as dashed lines with circular dots. The measured current densities for the first runs are shown in red, that for the second run in blue.

Fig. 7.12 depicts the corresponding impedance spectra, which were recorded in the beginning of each run at the applied voltage of 1.5 V. Each spectrum consists of a high frequency (h.f.) semicircle and display more or less linear behavior at low frequencies (l.f.) with a slope close to 45°. At the lowest frequencies down to 1 Hz, the impedance deviates from the linear slope, tending slightly to the real axis. This suggests that the l.f. impedance is dominated by a finite diffusion process that can be represented by, e.g., a finite Warburg impedance. The h.f. semicircle can be interpreted as the parallel connection of a kinetic resistance and a double layer capacitance. Together with the ohmic resistance, the overall impedance can be represented by the well-known Randles equivalent circuit shown in Fig. 7.13b. Note that due to the depressed h.f. semicircle, the double layer capacitance was replaced by a constant phase element.

The first run of T1 in Fig. 7.12a shows this most clearly, whereas the h.f. semicircle in the second and third runs is not particularly distinct. A discernible reduction in resistance is shown in both graphs. Notably, the ohmic resistances decrease

significantly from the first run to the second. The impedance spectra emphasize that NH_3 in the membrane initially has a considerable influence on the ohmic resistance and therefore on the ion conductivity. However, once a certain quantity is expelled, the remaining NH_3 / NH_4^+ in the membrane no longer has a significant influence on the ohmic resistivity.



(a) Ratio of 2:1 NH_4^+ vs. H^+.

(b) Ratio of 1:1 NH_4^+ vs. H^+.

Fig. 7.12. Recorded impedance spectra at 1.5 V and RT. The specta of the first trials are depicted as the solid lines and the second trials as dashed lines. The spectra of the first runs are shown in red, that for the second run in blue and that for the third run in green.

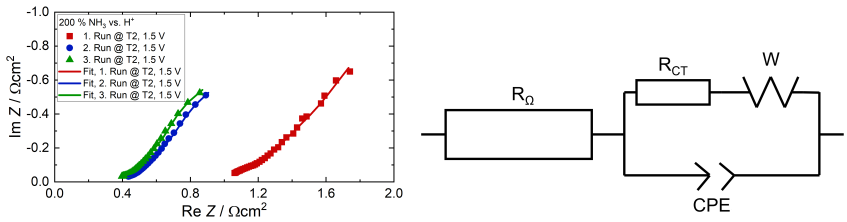
In order to investigate the electrochemical change in more detail, the spectra of T2 of the ratio 2:1 NH_4^+ vs. H^+ were fitted (Fig. 7.13a) by means of the Randles circuit shown in Fig. 7.13b. The spectrum of the first run was fitted in a frequency range from 1000 - 1 Hz and those of the second and third ones were fitted from 1200 - 1 Hz. The values of the electrical elements are shown in Tab. 7.2. The fits of the other trials and their corresponding tables can be found in the supplementary information. The ohmic resistance (R_Ω), the charge transfer resistance (R_{CT}), the diffusion resistance (W_R), and the diffusion parameter (W_T), have in common that they decrease by a factor of 2-3 from the first to the second runs. Conversely, regarding the fitting error, these parameters remain virtually constant from the second to the third runs. The Warbung exponent (W_P) also remains constant from the first to the third runs. It is close to the ideal value of 0.5 that corresponds to a 45° line in the Nyquist plot. The significant error of the constant phase element, which represents the double layer capacitance does not allow the analysis of both the CPE value (CPE_T) and exponent (CPE_P).

Although the significant decrease in the ohmic resistance from the first to the second run is clearly due to the exchange of NH_4^+ by H^+, the corresponding decrease in the other parameters needs some explanation. R_{CT} can be related to the oxygen evolution reaction (OER) at the anode, the hydrogen evolution reaction (HER), and the desorption of NH_3 at the cathode. If the OER is assumed to be less affected by the cation exchange in the membrane compared to the cathode reaction,

it might be assumed that the decrease in the charge transfer resistance from the first to the second run is caused by an increasingly dominating HER. The HER becomes dominating, because less NH_4^+ is in the membrane, leading to a better H^+ transport in the membrane. The corresponding decrease in W_R must be related to the acceleration of a diffusion process. Again, if the OER is negligible, the diffusion velocity of the H^+ increases, because the NH_4^+ in the membrane, which slows down the H^+ diffusion velocity, diminishes. W_T is related to the effective diffusion length (L) and the diffusion coefficient (D), with the equation $W_T = \frac{L^2}{D}$. If the diffusion length is assumed to be approximately constant, the higher diffusion coefficient of protons compared to NH_4^+ could explain the decrease in W_T. Alternatively, if W_T is only related to the diffusion of H^+ and considering Fick's law,

$$J = D \frac{dC}{dx} \tag{7.8}$$

the diffusion coefficient is inversely proportional to the concentration gradient ($\frac{dC}{dx}$). This means that if the concentration of H^+ increases within the membrane due to less NH_4^+ within the membrane and less resistivity, the diffusion coefficient decreases and so does the effective diffusion length. J is the flux of the diffusion species.



(a) EIS and fits (b) Equivalent Circuit

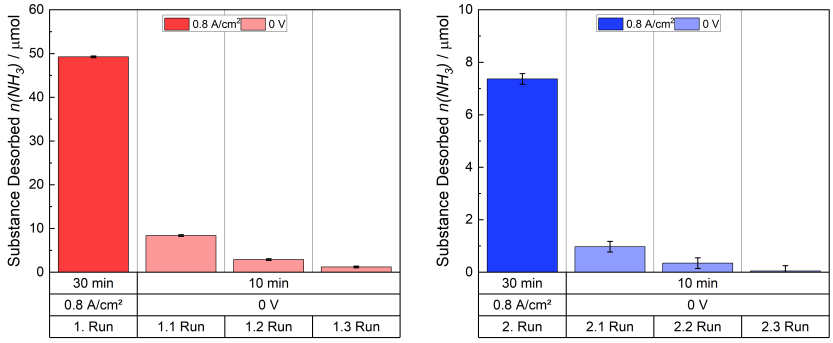
Fig. 7.13. (a) Impedance spectra of T2 of the ratio 2:1 NH_4^+ vs. H^+ with their corresponding fits at 1.5 V and (b) the Randles equivalent circuit used for fitting.

Tab. 7.2.: Elements of the impedance spectra of T2 of the ratio 2:1.

R_Ω [Ωcm²]	R_{CT} [Ωcm²]	W_R [Ωcm²]	W_T [s]	W_P	CPE_T [Ω^{-1} s^{-1} cm^{-2}]	CPE_P
0.988 ± 0.025	0.231 ± 0.063	2.81 ± 0.38	1.2 ± 0.2	0.52 ± 0.02	1.88 ± 1.88	0.6 ± 0.1
0.375 ± 0.031	0.119 ± 0.063	1.56 ± 0.25	0.67 ± 0.08	0.54 ± 0.03	3.13 ± 5	0.54 ± 0.05
0.331 ± 0.038	0.119 ± 0.056	1.44 ± 0.13	0.60 ± 0.04	0.56 ± 0.02	2.5 ± 3.1	0.6 ± 0.2

Whereabouts of Ammonia

To address the questions concerning the whereabouts of NH_3 / NH_4^+, the experiments were repeated, the cell was disassembled, and the individual MEA-components were also immersed in an H_2SO_4 solution so that the amount of NH_3 / NH_4^+ contained in them was expelled. Moreover, the time trend of the drag-out in the dead-voltage state was examined in greater detail. An MEA cell with Nafion 115, which was ion-exchanged with a solution of an NH_4^+ concentration of 0.024 M (1.5:1 NH_4^+ vs. H^+), was utilized. The concentration was chosen to determine if the desorption of NH_3 / NH_4^+ at the specific conditions was proportional to the ion exchange. Fig. 7.14 shows the detected amount of NH_3 during the runs. In the first run, 49.23 µmol was driven out at 0.8 A cm^{-2} and without an applied voltage 12.45 µmol. In the case of the second run, it was 7.37 µmol and 1.37 µmol, respectively. Table 7.3 shows the quantity and ratio of the expelled NH_3 (Σn_{tot}) during the dead-voltage state, the diffusion-driven drive-out, in comparison to the total drive-out. The corresponding drive-out during the time intervals (V1 - V3) is also shown. Approximately 20 - 25 % of the quantity of NH_3, which desorbed while supplying 0.8 A cm^{-2}, was expelled when no voltage was applied. Approximately two-thirds of this expelled quantity was driven out within the first ten minutes. In the second time interval, around 25 % was removed, whereas 3 - 10 % was removed in the last 10 min. The error of the second run increased strongly. Additionally, the ratios exhibited minor deviations in a second trial. This deviation along with the augmented error observed in the second run, can be attributed to the minimal absolute values of the measured NH_3. Such low magnitudes are significantly more susceptible to inaccuracies when expressed in percentage relation.



(a) NH_3 Desorption 1. Run

(b) NH_3 Desorption 2. Run

Fig. 7.14. Measured desorption of NH_3 while applying an electric current (red and blue bar) and the desorption of NH_3 during the dead-voltage state (bright bars).

Tab. 7.3.: Σn_{tot} is the sum of the quantity of NH_3, that was expelled during the runs in the dead-voltage states. V1 was the first 10 min time interval of 0 V, V2 the second, and V3 the third. χ is defined as the percentage of NH_3 removed without applying a potential, relative to the amount removed at a current density of $0.8\,A\,cm^{-2}$ for n_{tot}. Additionally, it represents the percentage of NH_3 removed without applying a potential for the various time intervals, in relation to the total amount of NH_3 removed without the application of a potential.

	1. Run		**2. Run**	
	n [μ**mol**]	χ [%]	**n** [μ**mol**]	χ [%]
$\Sigma\mathbf{n}_{tot}$	12.45 ± 0.60	25.30 ± 1.22	1.37 ± 0.60	18.57 ± 8.16
V1	8.38 ± 0.20	67.31 ± 3.62	0.98 ± 0.20	71.15 ± 34.46
V2	2.88 ± 0.20	23.15 ± 1.96	0.35 ± 0.20	25.27 ± 18.35
V3	1.19 ± 0.20	9.54 ± 1.67	0.05 ± 0.20	3.57 ± 15.70

After the experiment had been completed, the cell was dissembled. The active cell area of the membrane was cut out and the active cell area, the frame, the anode, and cathode were immersed in H_2SO_4 solutions for 30 min. The portion of the active cell area and the frame that is the part of the membrane, which was covered by the gasket during the experiment, were re-inserted into a fresh solution because, as previously stated, not all of the NH_4^+-ions within the membrane were expelled in the first solution. The detected quantity of NH_3 of each component is displayed logarithmically in Fig. 7.15. Most of the detected quantity, 129 µmol, was found in the frame. This is based on the fact that no electrochemical reaction took place in the frame area, only in the active cell area. In the membrane 22 µmol remained, which were detected. It is important to note that the cell remains unused, exchange processes will take place so that NH_3 becomes homogeneously distributed within membrane.

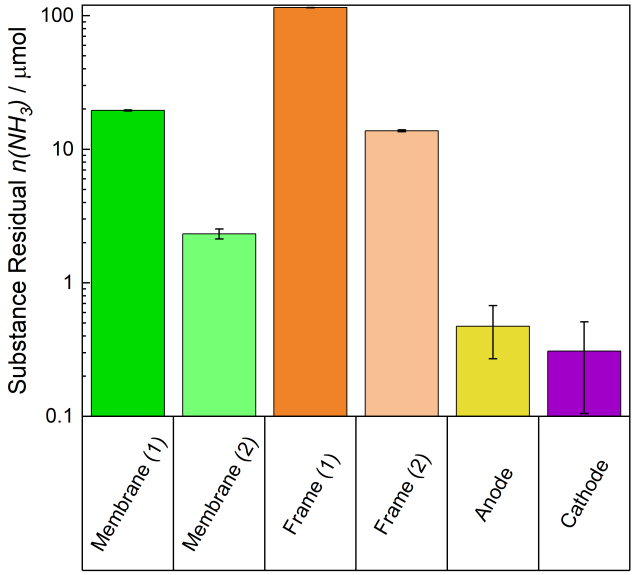


Fig. 7.15. Detected amount of NH_3 in the cell components, a logarithmic scale is chosen to show small amounts present in some components. The frame area of the membrane and the active area of the membrane were re-inserted into a fresh solution, because not all of the NH_4^+-ions within these areas were expelled in the first solution.

In the second trial, the cell was dissembled directly after applying a current density of $0.8\,\mathrm{A\,cm^{-2}}$. The NH_3 desorption during the current flow is depicted in Fig 7.16. The desorption is similar to the desorption in Fig. 7.15, if it is assumed that there is a deviation like in Fig. 7.7 and 7.8. Approximately 43 µmol of NH_3 are expelled from the membrane after dissembling the cell and introducing the components in an H_2SO_4 solution. The quantity of NH_3 is similar to the total amount of it expelled in the first test after applying $0.8\,\mathrm{A\,cm^{-2}}$ plus the remaining substance in the membrane. 122 µmol of NH_3 were detected from the frame. The difference of 7 µmol compared to the amount in Fig. 7.15 is small when considering the deviation of the ion exchange in Fig. 7.2. The determined amount of NH_3 that was found in the electrodes and tube (the connection between the trap and cell) is low. Consequently, the residual amount of substance remained within the membrane. This result highlights the fact that the drag-out of NH_3 / NH_4^+ from the membrane is an electrochemical and diffusion-driven process.

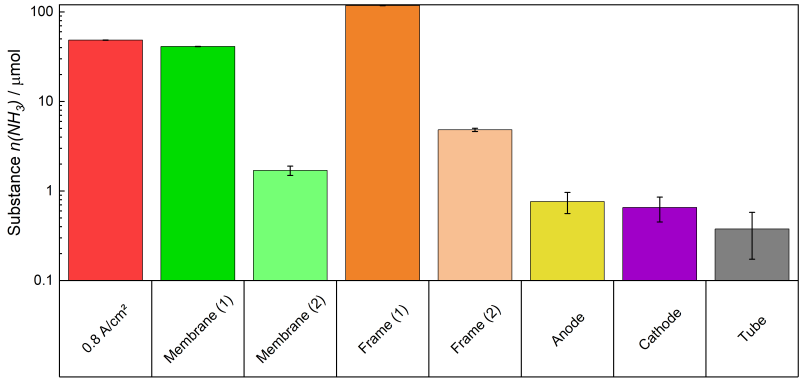


Fig. 7.16. NH_3 expelled electrochemically (red) and the detected amounts of NH_3 expelled from the cell components. A logarithmic scale is chosen to show small amounts present in some components. The frame area of the membrane and the active area of the membrane were re-inserted into a fresh solution, because not all of the NH_4^+-ions within these areas were expelled in the first solution.

Fig. 7.17 displays the ratio of the detected quantities of NH_3 in relation to the ion exchanged amount with respect to the active cell areas. T1 is the first trial where the time trend of the expelled NH_3 was investigated (Fig. 7.14 and 7.15). The red bar illustrates a ratio of 67 % ± 8 %, denoting the amount of NH_3 expelled electrochemically during the cell measurement in relation to the total ion exchanged amount. The quantity of NH_3 released from the electrode and the membrane when they were immersed into a H_2SO_4 after the electrochemical measurement is added to the electrochemical drag-out. Then a total quantity of 87 % ± 10 % of the NH_4^+-ions previously within the membrane were expelled as N_3 from the membrane (dark red bar). In the case of the second trial where the cell was dismantled directly after applying the current, 51 % ± 7 % of the initial concentration of NH_4^+ in the membrane were expelled electrochemically (blue bar). This value is lower than during the first trial, because the quantity of NH_3 that were expelled due to diffusion and when the high current density was applied for the second time, remained in the membrane. However, after disassembling and introducing the components in H_2SO_4 solutions, all of the introduced NH_4^+-ions in the beginning, were found (dark blue bar). In conclusion, it can be stated that the amount of NH_4^+ in the active cell area was almost completely recovered by electrochemical discharge and chemical extraction.

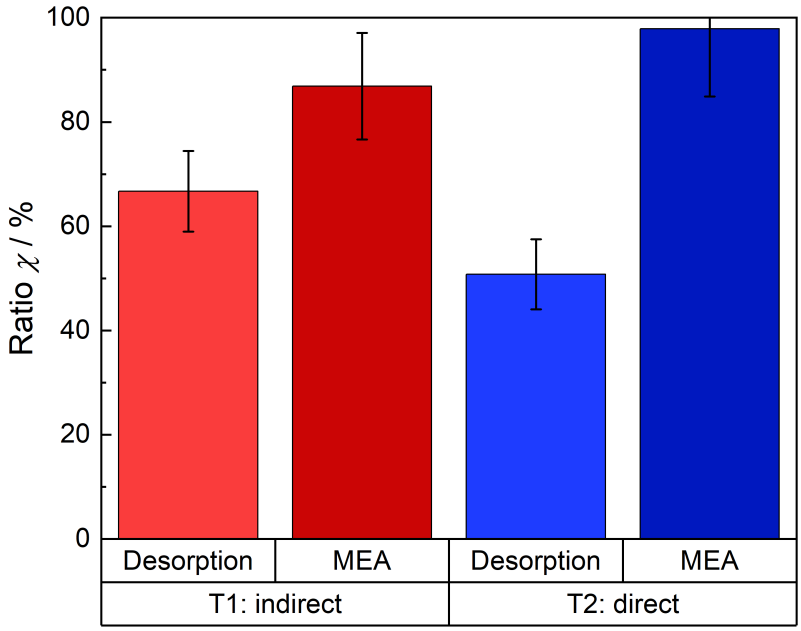


Fig. 7.17. NH_3 expelled electrochemical (red and blue bar) and the total amount of NH_3 that was found, electrochemical plus the quantity which were expelled afterwards in the H_2SO_4 solutions from the cell components (dark red and blue).

7.4 Summary and Conclusion

In this study, the interaction of NH_3 and Nafion, with the objective of enhancing understanding of the process, which will lead to more reliable analyses of electrochemical NH_3 synthesis for future work, was investigated. As expected, it was found that NH_4^+ prefers to exchange with H^+ from Nafion, K_{eq} is 2.00 ± 1.31. This results in the persistence of NH_4^+ within the membrane structure. The higher the concentration of the solution containing NH_4^+, the higher the exchange. It has been demonstrated that the quantity of NH_4^+ bound to the membrane by adsorption is detected and expelled.

In the MEA cell, the effect of NH_4^+ in the membrane and also the migration of the ions in the different components was electrochemically investigated by analyzing the current-voltage behavior and impedance spectra, and chemically by analyzing the NH_3 / NH_4^+ content in the different components by dissembling the cell at different times in the electrochemical process utilizing the indophenol method. It was found that the desorption of NH_3 is a process driven by potential and diffusion. Considering the results and errors in Table 7.3, between approximately 10 and 30 % of the amount of NH_3 that was expelled electrochemically was expelled by diffusion in the de-energized state. It was determined that a proportion (20 to 30 %) of the protons in the active cell area can be replaced by NH_4^+-ions, without affecting the ohmic resistance and ion conductivity. Consequently, if small amounts of NH_3 are synthesized electrochemically in a N_2 reduction cell, they may remain as NH_4^+ in the membrane unnoticed as the membrane itself remains unaffected. Very high potentials > 2 V are needed to expel a significant amount of NH_3. However, theoretical calculations by Araujo et al. [180] indicate that NH_3 synthesis is not feasible at these high potentials. It is shown in his publication that these potentials lead to the complete coverage of the catalyst surface area with H*. For the N_2* coverage, the potentials are small and also the potential range is very narrow. Therefore, it can be inferred that NH_3 is detected under conditions in many cases that do not enable NH_3 synthesis, leading to false conclusions. Additionally, it is shown that the majority of NH_4^+ remains chemically bound in the membrane. Only a small proportion diffuses into the electrodes. Consequently, it is recommended to critically evaluate the obtained results, especially when detecting low amounts of NH_3 and it is necessary to examine the components of the synthesis system for the presence of NH_3 before proceeding with further experiments. Otherwise, this is likely to result in subsequent experiments being influenced by the preceding one and affecting reproducibility and reliability.

8 Ammonia Recycling

8.1 Introduction

Ammonia is at the same time one of the most produced, important chemicals and a harmful substance. Therefore, recycling of NH_3 from waste solutions is an important topic.

Approximately 95 % of NH_3 emissions come from agriculture, particularly from livestock farming and the use of slurry or mineral fertilizers [187]. NH_3 is a toxic gas, it can freely diffuse across epithelial membranes of aquatic organisms and can suppress the citric acid cycle leading to progressive acidosis that decreases the O_2 carrying capacity of blood, disrupts blood vessels, and affects liver and kidney functions [188, 189]. NH_3 can be readily converted into NH_4^+, in effluent below a pH value of 9, NH_3 is present as NH_4^+. NH_4^+ is a plant nutrient and can be assimilated via the plant shoot or by the root [190, 191]. This high nutrient load can lead to stimulation of nuisance algal growth, which can contribute to hypoxia or anoxia zones, and highly undesirable changes in the ecosystem [188, 192, 193]. Microorganism can break down NH_4^+ into nitrate (NO_3^-) via the intermediate stage nitrite (NO_2^-) in effluent. During this degradation, a significant amount of O_2 is consumed from the wastewater. For the chemical transformation of 1 mg NH_4^+ to NO_3^- approximately the fourfold amount of O_2 is required [194]. Therefore, combined with the oxidized forms of N_2, the reduced forms of N_2 significantly contributes to the spread of eutrophication and acidification of ecosystems [187]. Boundary values for different section of industries are listed in Tab. 8.1. Nevertheless, the present techniques of nitrification in combination with denitrification and anammox (anaerobic ammonium oxidation) do not recover the valuable nitrogen compounds. Instead, these compounds are converted into N_2. Additionally, these techniques require a substantial energy consumption, with values of 12.5 kWh (45 MJ kg_N^{-1}) and 4.44 kWh (16 MJ kg_N^{-1}), respectively [195, 196].

For this reason, the development and implementation of a closed-loop process for recycling NH_3 can contribute to the preservation of ecosystems, energy savings, and resource conservation. The recycled NH_3 can be reused as a fertilizer, in the synthesis of further nitrogen compounds, and as an energy carrier [197, 198]. The removal of NH_3 / NH_4^+ from wastewater and other sources is achieved through a variety

of developed methods, including biological, physical, chemical, or a combination of these approaches. These methods include ion exchange with zeolites, NH_3 stripping, and chemical precipitation [198–201] . In the sewage plant NH_4^+ is predominately removed via biological methods [202]. Ion exchange possesses numerous advantageous properties when compared to alternative methods. The removal efficiency is high and the method is cost-effective, while the operational framework is simple [188, 199, 203].

On these grounds, a pure electrochemical system was developed to recycle NH_3 via a MEA cell from ammonium salt solutions through the cation exchange membrane Nafion. This system differs from the setup described in Kuntke et al. publication [204]. The utilized system in this work does not require a catholyte, does not require a secondary membrane, and produces NH_3 in a gaseous state. Additionally, H_2 is produced as a valuable byproduct, and the electrodes are directly connected to the membrane. This cell system is predominately used for water electrolysis, as described in Liu et al. work [205] and enables the possibility of a continuous recycling process by deprotonating the the introduced NH_4^+-ions and reducing H^+. To ascertain the optimal conditions for maximizing the recycling rate in this particular operating cell system, a comprehensive investigation into the influence of of various process parameters is conducted. The concentration were chosen based on limits in wastewater and low TAN (total ammonia nitrogen) ($< 0.5\,\mathrm{g\,L^{-1}}$) [206, 207]. Consequently. relatively high concentrations of NH_4^+, as found in undiluted urine ($4\,\mathrm{g\,L^{-1}}$) [208], are not included in the present study.

Tab. 8.1.: Limits of NH_4^+ in wastewater for different sections of industry [206].

Domestic and municipal wastewater	Breweries	Textile	Metal	Meat
$10\,\mathrm{mg\,L^{-1}}$	$10\,\mathrm{mg\,L^{-1}}$	$10\,\mathrm{mg\,L^{-1}}$	30 - $100\,\mathrm{mg\,L^{-1}}$	$10\,\mathrm{mg\,L^{-1}}$

8.2 Experimental

The electrochemical cell employed in the recycling process is displayed in Fig. 3.2. Nafion was utlilized due to its excellent ion conductivity resulting from its ionic sulfonic groups (R-SO_2-OH). The active cell area of the MEA cell was 6.25 cm^2, and the catalyst layer was sprayed either on the PTL or directly onto the membrane, a configuration referred to as catalyst-coated membrane (CCM). The anode catalyst, 2 mg cm^{-2} IrO_x, obtained from Alfa Aesar / Thermo Fisher Scientific, was either spray-coated onto the titanium felt substrate from Bekeart, Bekipor® 2GLD10-0.35 or onto the membrane. In order to enhance the conductivity, a thin layer of Ir was sputter-deposited onto the titanium felt substrate before spray-coating the catalytic Ir-layer. A cathode catalyst loading of 1.3 - 1.4 mg cm^{-2} of the catalyst 60 % PT/C HiSpec 9100 from Johnson Matthey, was either deposited onto a carbon felt H2315 CX312 from Freudenberg or onto the membrane. Both electrodes were produced in-house. The results of the catalyst deposited onto the substrates are presented in the section 8.3.1 and the outcome of the CCM is shown in section 8.3.2. The other cell components (bipolar plates and so on) are as described in chapter 3.2.

As illustrated schematically in Fig. 8.1, the transport of the ions and molecules in the electrochemical cell are depicted. Dissolved $(NH_4)_2SO_4$ salt in H_2O is introduced into the PTL on the anode side. The dissociation of the ions $NH_4{}^+$ and $SO_4{}^{2-}$ occurs within the aqueous medium

$$(NH_4)_2SO_4(s) \longrightarrow 2\,NH_4{}^+(aq) + SO_{42}{}^-(aq)\ . \tag{8.1}$$

The $NH_4{}^+$-ions, as graphically shown, diffuse through the membrane and deprotonates to NH_3. H^+ is reduced to H_2 by the incoming e^- from water oxidation. The e^- are generated due to the oxidation of H_2O at the anode. The corresponding generated H^+ of the oxidation,

$$\text{Anode:} \quad 2\,H_2O + NH_4{}^+ \longrightarrow 4\,H^+ + 4\,e^- + O_2 + NH_4{}^+ \tag{8.2}$$

$$\text{Cathode:} \quad 4\,NH_4{}^+ + 4\,e^- \longrightarrow 4\,NH_3 + 2\,H_2 \tag{8.3}$$

remain on the anode side. This leads to an increase of the H^+ concentration and a decrease in the pH value. O_2 is produced as a result of the oxidation process,

and subsequently exits the cell via the anode outlet. Alternatively, NH_4^+ diffuses into the membrane and interacts with H^+, that is bound to the sulfonic acid group within the membrane. This interaction facilitates an exchange of H^+ with NH_4^+. Consequently, this phenomenon also gives rise to the evolution of H_2. Due to the applied electrical potential and the resulting electric field, the generated H^+ by H_2O oxidation, can also diffuses through the membrane and either be reduced to H_2 at the cathode catalyst or interact with the NH_4^+ present in the membrane. The interacting with the NH_4^+-ions bound to the membrane leads to an re-exchange of NH_4^+ for H^+, resulting in the deprotonating of NH_4^+ and the production of NH_3 (see Fig. 7.5).

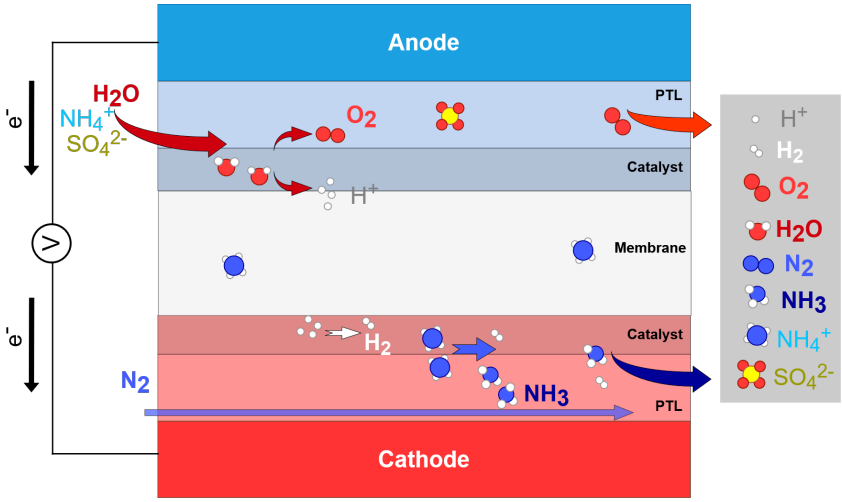


Fig. 8.1. Schmatic illustration of the NH_3 recycling process through the membrane. H_2O, which contains dissolved NH_4^+ and SO_4^{2-} is introduced into the PTL of the anode. The NH_4^+-ions can diffuse through the membrane, because Nafion is cation conductive. The SO_4^{2-} can not diffuse through the membrane, the remain on the anode side. In the catalyst layer H_2O is oxidized to O_2 and H^+. The produced O_2 exits the cell at the anode outlet. The generated H^+ either remain on the anode side, diffuses through the membrane and is reduced to H_2 or it interacts with the NH_4^+-ions, which were introduced into the membrane, within the membrane. The diffused NH_4^+-ions deprotonate at the cathode. NH_3 is produced and the resulting H^+ are reduced to H_2 with the supplied e^- from the cathode. N_2 is used as carrier gas to remove NH_3 and H_2 from the cell. The coloring of the atoms is done according to the CPK color model.

To carry out the experiments a test bench was designed, which is illustrated in Fig. 8.2. The dissolved $(NH_4)_2SO_4$ was introduced into the MEA cell on the anode side. The solution was either circulated with an circulation pump or expelled as waste via the three-way valve. The implementation of this modification was driven by the observation that the recirculation and recovery of NH_3 led to a decline in the concentration and quantity of NH_4^+ within the original solution. This in turn, exerted an influence on the pH value. The initial pH of the 0.01 M $(NH_4)_2SO_4$ solution was approximately 5.5, and decreased to ∼2. This has a significant impact on the process and efficiency as well. The concentration of NH_4^+ and the pH level of the solution remained constant if the solution was discharged after passing the cell. As mentioned, the application of electrical energy causes the oxidation of H_2O at the anode, leading to the production of O_2. N_2 was introduced into the cell on the cathode side at a constant flow rate of 10 mL/min via the mass flow controller from Brooks Instruments MultiFlo™ "GF40". The recycled quantity of gaseous NH_3 was absorbed into an H_2SO_4 trap, thereby transforming into NH_4^+. NH_4^+ is not volatile. Subsequently, the quantity was measured using the indophenol blue method (see 3.3.2). The trap, along with the ensuing transformation of NH_3, is not required in a real recycling process. In this case the trap was needed to determine the resulting recycling rate.

In addition to $(NH_4)_2SO_4$, ammonium nitrate NH_4NO_3 was selected as a salt solution, because both chemicals are used as chemical fertilizers [209] and for investigating the effect of the valence strength. NO_3^- is a monovalent anion, whereas SO_4^{2-} divalent.

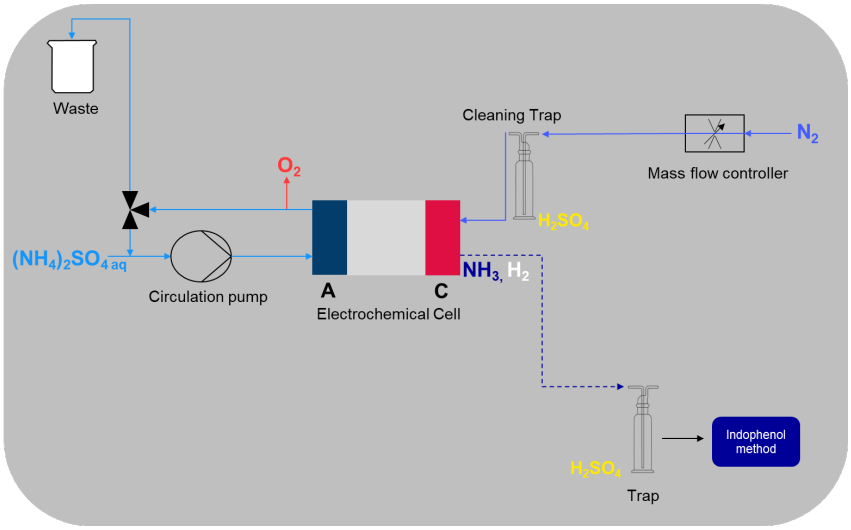


Fig. 8.2. Schematic illustration of the test setup.

Preparation of different concentrations of the initial solutions was conducted with respect to the NH_4^+ concentration in the these solutions. The concentration of NH_4^+ was in the same magnitude as found in wastewater. In the case of the recirculation experiments, In the case of the recirculation experiments, volumes of 0.1 L were prepared. Using Eq. 7.1 the required mass of $(NH_4)_2SO_4$ is calculated ($M((NH_4)_2SO_4) = 132.14\,\mathrm{g\,mol^{-1}}$). The corresponding concentration is calculated with

$$c((\mathrm{NH_4})_2\mathrm{SO_4}) = \frac{m((\mathrm{NH_4})_2\mathrm{SO_4})}{M((\mathrm{NH_4})_2\mathrm{SO_4})\ 0.1\,\mathrm{L}}\ . \tag{8.4}$$

The values are presented in Tab. 8.2. The weight measurements were rounded to milligrams due to the resolution limit of the scale "SECURA513-1S" from Sartorius Lab Instruments GmbH & Co. KG. The resolution limit is ± 1 mg. The ratio of the quantity of NH_4^+ present within the solution in comparison to the initial quantity of H^+ within the entire membrane area is also listed. NO_3^- is monovalent, leading to the equation

$$m(\mathrm{NH_4NO_3}) = \frac{\beta(\mathrm{NH_3})\ M(\mathrm{NH_4NO_3})}{M(\mathrm{NH_3})}\ . \tag{8.5}$$

The corresponding concentration can be calculated with Eq. 8.4, instead of the values for $(NH_4)_2SO_4$, the values for NH_4NO_3 must be used ($M(NH_4NO_3) = 80.04\,g\,mol^{-1}$).

Tab. 8.2.: The different concentrations of NH_4^+, the corresponding quantity and concentration of $(NH_4)_2SO_4$ and NH_4NO_3 are listed. Additionally, the ratio, the amount of NH_4^+ within the solution in comparison to the amount of H^+ within the membrane is listed.

NH_4^+ vs. H^+	c(NH_4^+)	β(NH_4^+)	m($(NH_4)_2SO_4$)	c($(NH_4)_2SO_4$)	m(NH_4NO_3)	c(NH_4NO_3)
4 mM	72 mg L^{-1}	26 mg	2 mM	31 mg	4 mM	1:1
8 mM	144 mg L^{-1}	52 mg	4 mM	63 mg	8 mM	2:1
20 mM	360 mg L^{-1}	130 mg	10 mM	157 mg	20 mM	5:1
40 mM	720 mg L^{-1}	260 mg	20 mM	315 mg	40 mM	10:1

8.3 Results and Discussion

8.3.1 Catalyst on PTL

Recycling Confirmation

To be sure that the recycling process operates in an MEA cell and the transport of the NH_4^+-ions is not caused by the concentration gradient from anode to cathode, therefore at first Nafion was ion exchanged with an $(NH_4)_2SO_4$ solution with a ratio of 1:1 NH_4^+ vs. H^+ ($NH_4^+ = 16\,mM$), to transfer Nafion into a NH_4^+-form. H_2O was supplied on the anode and due to the oxidation of it, H^+ were produced and these H^+ expel the NH_4^+-ions from the membrane. Like it was done in the previous chapter. The red bars in Fig. 8.3 depict the expelled amount of NH_3 during the H_2O supply in the beginning of this experiment. Both red colors represent one trial, utilizing fresh cells with fresh MEAs.

A maximum of 403 μmol ± 14 μmol of protons are in the membrane. Fig. 7.2 illustrates the mean quantity of NH_4^+ remaining in the solution, it is 200 μmol ± 17 μmol. Thus, 203 μmol ± 17 μmol were exchanged into the membrane. The quantities, which are discharged at the potentials, that are used in water electrolysis, are negligible and the measured current density were low in both trials. The main desorption occurred during the applied current density of $0.8\,A\,cm^{-2}$. The resulting cell potential was higher than 2 V. 2 V is often used as the maximum potential in PEM water electrolysis. The mean desorption of the trials was approximately 65 μmol, hence 138 μmol ± 17 μmol remained in the membrane. This corresponds to 68 % of the initial amount of substance.

Afterwards a $(NH_4)_2SO_4$ (blue bars) solution containing 20 mM NH_4^+ was supplied and circulated. The volume of the solution was 0.1 L. The desorption of NH_3 during the potentials 0, 1.5 and 1.75 V is in the error range of the spectrometer (Fig. 8.3). It demonstrate that the concentration gradient from anode to cathode is not sufficient for transferring NH_4^+ from anode to cathode. Thus, sufficient electrical energy is required. The released quantity of NH_3 at $0.8\,A\,cm^{-2}$ exceed 138 μmol. Furthermore, considering the detected quantity of NH_3, afterwards when H_2O was fed again (green bars), the quantity exceed the quantity which could be in the membrane in the beginning of these experiments. Based on these results, it can be concluded that NH_3 is recycled by the electrochemical process in the cell.

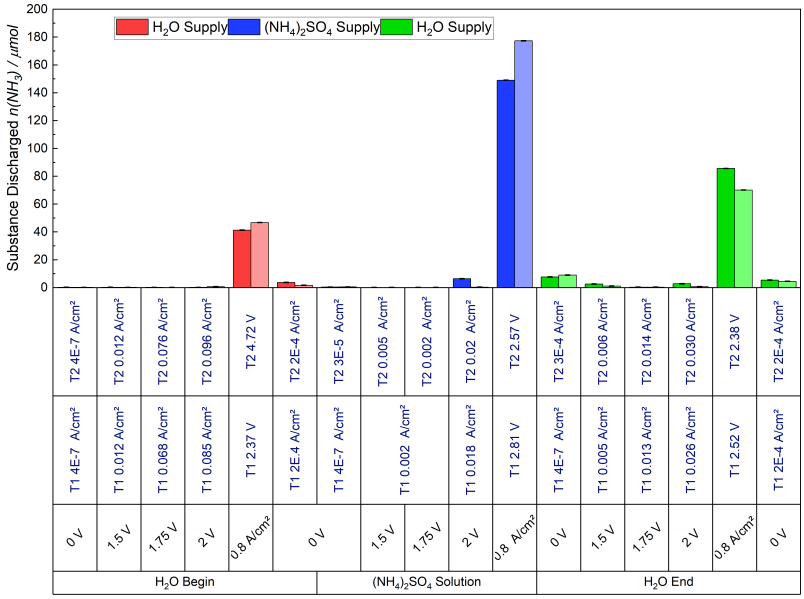


Fig. 8.3. Discharge of NH_3 during the supply of H_2O (red and green bars) and $(NH_4)_2SO_4$ solution (blue bars). Two trials were carried out, ensuring reproducibility. In black the applied potentials and current density are written and in dark blue the corresponding measured values.

Concentration Influence

For studying the concentration effect on the recycling rate shown in Fig. 8.4, two different concentrations of NH_4^+ in the initial $(NH_4)_2SO_4$ solution were prepared and introduced into the electrochemical cell with an flow rate of 10 mL/min at RT. The measured recycling rate was approximately proportional to the provided NH_4^+ concentration. The rates were 14.8 and 31.9 $nmol\,cm^{-2}\,s^{-1}$. Despite the doubled concentration, the required voltage for applying the current density was only slightly larger (2.48 and 2.59 V). In both cases during the measurement in the de-energizes state (0 V) NH_3 was discharged that was caused by diffusion. In accordance with anticipated outcomes, a higher initial NH_4^+ concentration yields elevated rates for recycling.

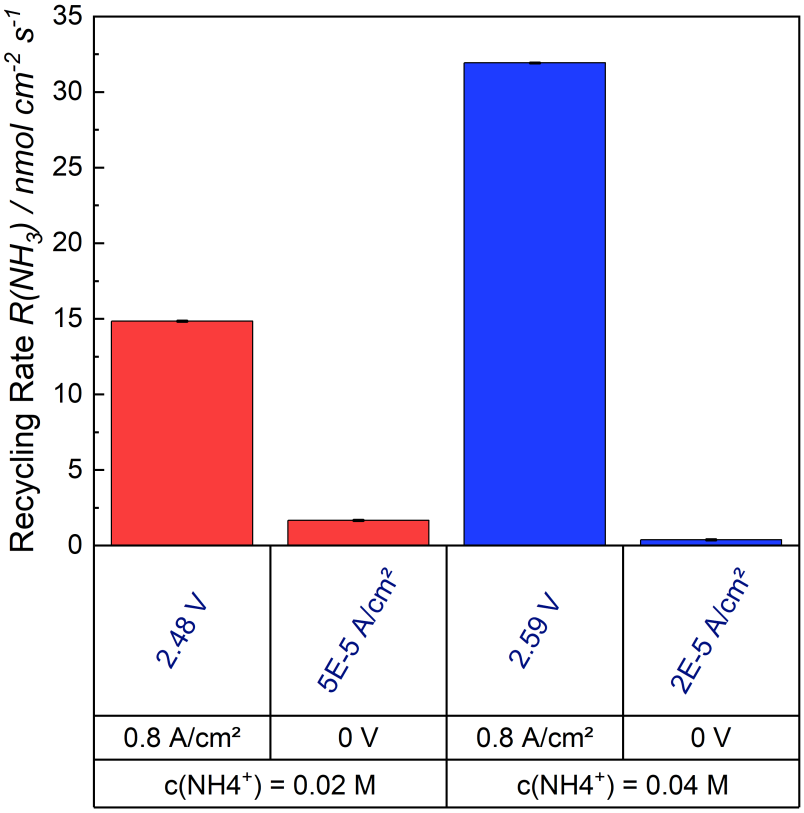


Fig. 8.4. Recycling rates of the NH_4^+ concentration of 0.02 M (red) and 0.04 M (blue) in the $(NH_4)_2SO_4$ solution. In black the applied potentials and current density are written and in dark blue the corresponding measured values.

Flow Rate Influence

Fig. 8.5 depicts the rate of recycled NH_3 in dependency of the solution flow rate at RT. The used MEA was the same for both flow rates. The prepared solution 20 mM NH_4^+ (10 mM $(NH_4)_2SO_4$) was used for both flow rates. The current density was applied twice, the first time for 15 min and the second time for 30 min. It appears that the membrane did not reach an equilibrium state within the 15 min at a flow rate of 5 mL/min, resulting in a lower recycling rate. Subsequently, the membrane reaches equilibrium, and there is no significant difference in the recycling rate of both flow rates. The measured potentials decreased during the second runs at 0.8 A cm^{-2}.

Nevertheless, these measured potentials were considerably larger than the potentials ($< 2\,\mathrm{V}$) used for water electrolysis.

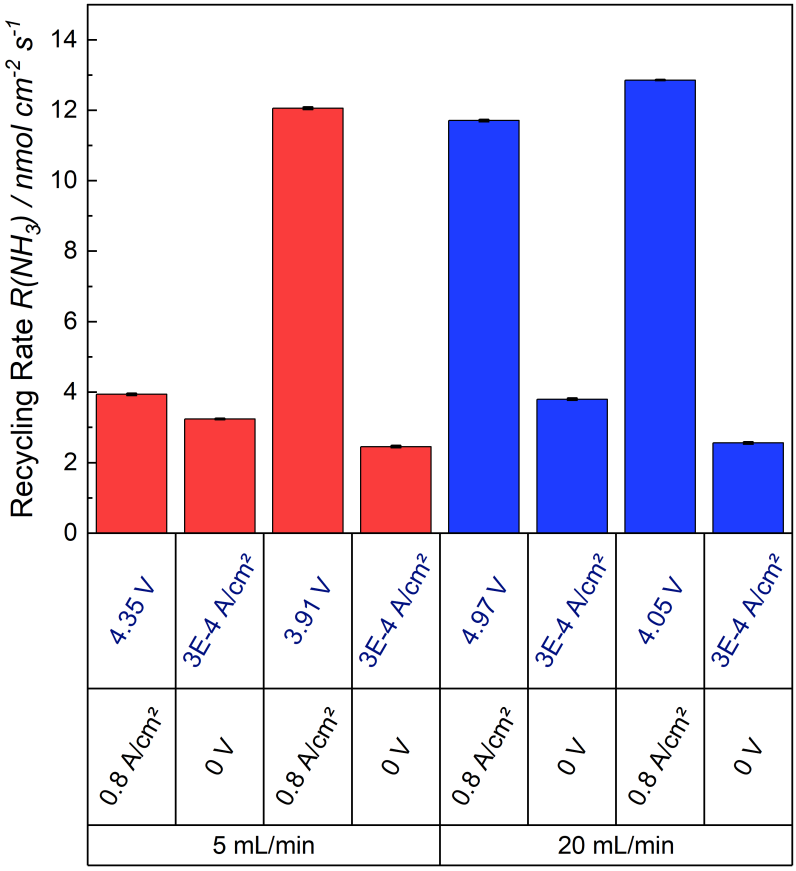


Fig. 8.5. Recycling rates of the applied solution flow rates 5 mL/min (red) and 20 mL/min (blue) in the $(NH_4)_2SO_4$ solution. In black the applied potentials and current density are written and in dark blue the corresponding measured values.

Temperature Influence

In terms of the temperature increase from RT (red bars) to 80 °C (blue bars), the recycling rate did not increase as shown in Fig. 8.6. Both experiments were executed at a flow rate of 20 mL/min and a NH_4^+ concentration of 20 mM in 0.1 L. The measured potential drops significantly from 5 V at RT to 2.4 V at 80 °C due to the better ion conductivity of Nafion at 80 °C. Leading to lower energy consumption, less stress to the electrode and thus longer life time of the cell.

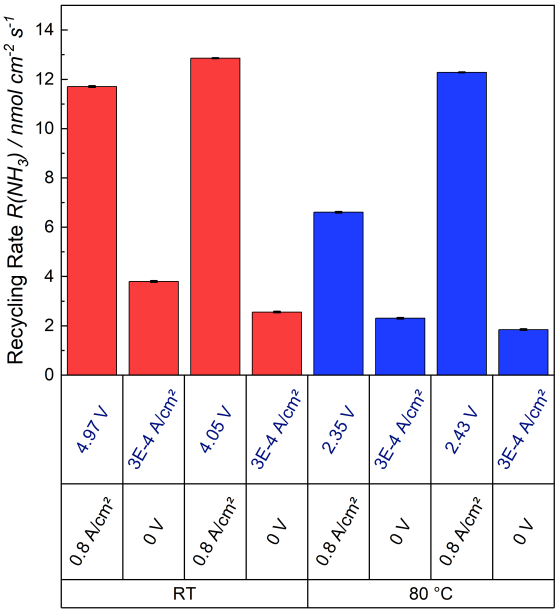
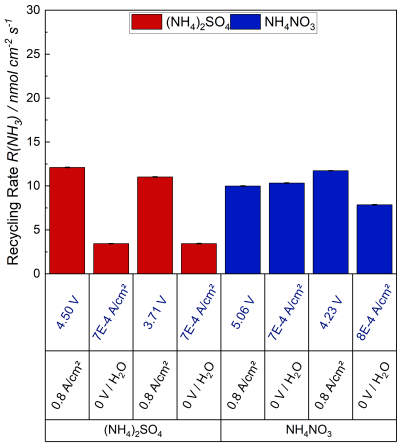


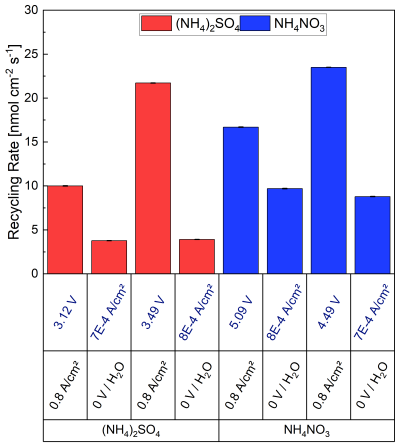
Fig. 8.6. Recycling rates at RT (red) and 80 °C (blue). In black the applied potentials and current density are written and in dark blue the corresponding measured values.

Solution Comparison - Influence of the Valence Strength

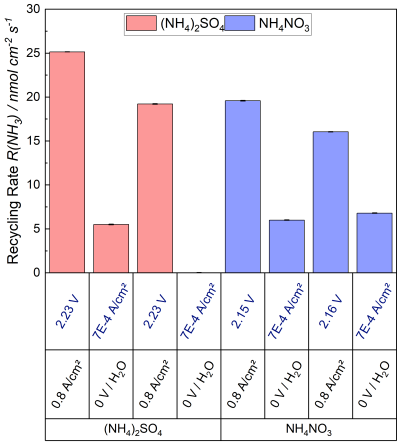
As mentioned in the introduction, NH_4NO_3 solutions were also utilized as NH_4^+ source. NH_4NO_3 is a monovalent molecule, thus 1 M of NH_4NO_3 contains 1 M NH_3 / NH_4^+. As a consequence, the following Fig. 8.7 compare the two introduced solutions in terms of their recycling rate as a function of temperature and flow rate. The graphics in Fig. 8.7 show that there is no clear trend in the recycling rate concerning a monovalent or divalent anion. Hence, the valence strength does not influence the recycling process. But, these results contradict the previously described results regarding the influence of temperature and flow rate.
In order to verify the recycling process, the reproducibility of the recycling was assessed. The exact measurement, applying $0.8\,A\,cm^{-2}$ for 30 min and 0 V for 15 min, was repeated three times with three fresh cells containing fresh MEAs, while recirculating a 0.01 M $(NH_4)_2SO_4$ solution at the conditions 20 mL/min and 80 °C. In a further step, two of these MEAs were exposed to the same measurement protocol once again. The measured recycling rates had change, in one case the rate decreased roughly about 40 % and in the other case the rate increased about 30 % as shown in the supplementary information. Consequently, this leads to the deduction that the results are not fully reliable for the process of coating the catalyst layer on the porous transport layer and subsequent hot presssing with the membrane.



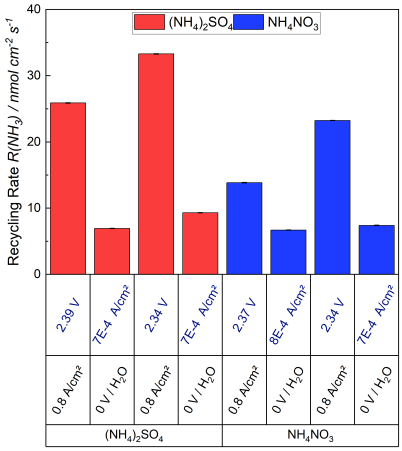
(a) Recycling Rate @ 5 mL/min, RT



(b) Recycling Rate @ 20 mL/min, RT



(c) Recycling Rate @ 5 mL/min, 80 °C



(d) Recycling Rate @ 5 mL/min, 80 °C

Fig. 8.7. Recycling comparison of the introduced solutions $(NH_4)_2SO_4$ (red) and NH_4NO_3 (blue) under different conditions of temperature and flow rate. In black the applied potentials and current density are written and in dark blue the corresponding measured values.

Non-Recirculation of the Solution / Constant Solution Concentration

The recirculation of the solution led to a depletion of the NH_4^+ concentration due to the recycled quantity of NH_4^+. Thereby the recycling rate was affected and the pH value dropped until ~2. To maintain a constant NH_4^+ concentration and stable pH,the solution was not recirculated. Fig. 8.8 displays the comparison of Δc / reciruculation (red bars) and const c / non-recirculation (blue bars) under conditions of 20 mL/min and 80 °C. Between the introduction of the solutions for constant concentration measurements, H_2O was introduced to rinse the cell during the de-energizes state measurements. Additional discharge of NH_3 due to the flow of $(NH_4)_2SO_4$ should be prevented. The maximum recycling rate at a constant concentration of NH_4^+ was almost three times as high as the rate at Δc, while the measured potentials were almost identical at $0.8\,A\,cm^{-2}$. During the de-energized states, the discharge of NH_3 was also larger. However, it cannot be concluded whether this resulted from the constant concentration concentration that led to the high recycling rate, or whether rinsing with H_2O was the crucial factor.

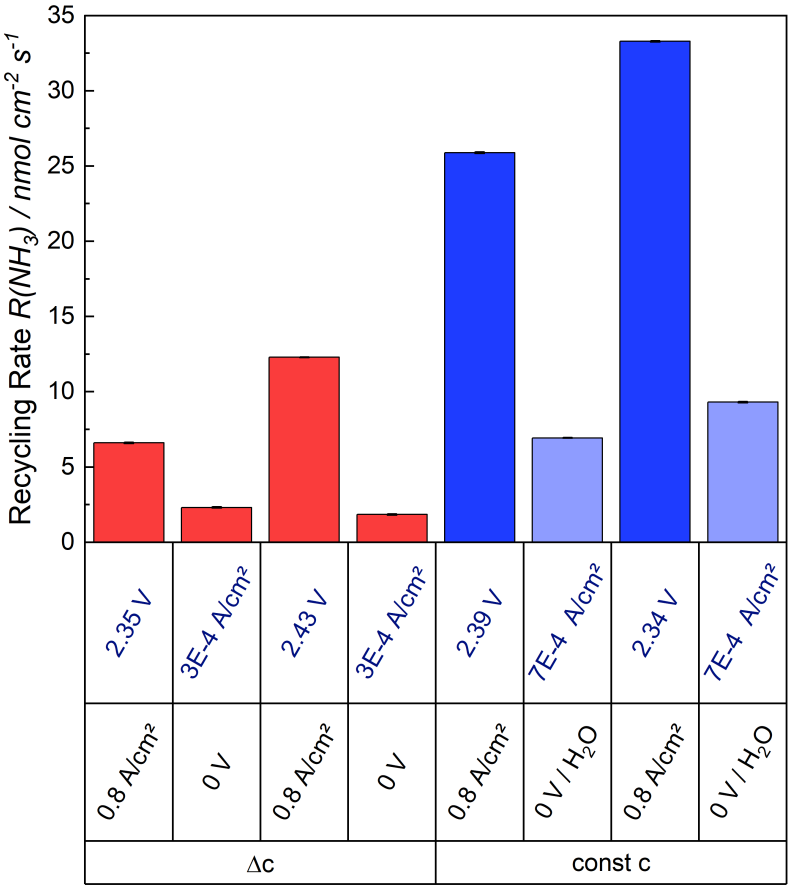


Fig. 8.8. Resulting recycling rates while the $(NH_4)_2SO_4$ solution was recirculated (red), leads to Δc and while the solution was not recirculated (blue), c was constant. In black the applied potentials and current density are written and in dark blue the corresponding measured values.

Concerning recirculation (Δc) 2000 µmol of NH_4^+ were in the 100 mL solution that resulted in a concentration of 20 mM of NH_4^+. 198 µmol were recycled (red bar Fig. 8.9) at the conditions 80 °C and 20 mL/min. The ratio of the amount of recycled NH_3 to the initial amount of NH_4^+ in the solution was approximately 10 % (black star).

Regarding non-reciculation (const. c) the required amount of substance of NH_4^+ was 18 000 µmol to obtain a constant concentration of 20 mM for the whole experiment. During this experiment 612 µmol (blue bar) were recycled, which is three time as much as while recirculation. However, the ratio was 3.4 %, that is roughly one-third of the ratio for recirculation.

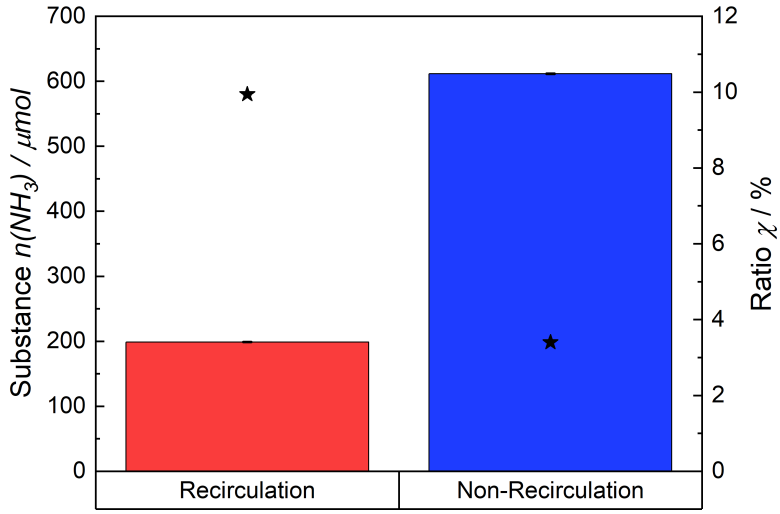


Fig. 8.9. Totaled recycled quantity of NH_3 of recirculation (red) and non-recirculation (blue) (left y-axis). The ratios of recycled quantity to the initial amount of NH_4^+ are shown as black stars (right y-axis).

The FE of these experiments are shown in Fig. 8.10 and the values are below 0.5 %. Thus, more than 99.5 % of the supplied energy / current were used for producing H_2 by water electrolysis. Hence, primarily H_2 was produced instead of NH_3 recycling at the cathode. Moreover, it needs to be mentioned that the energy consumption is much larger than the energy which is required for nitrification / denitrification.

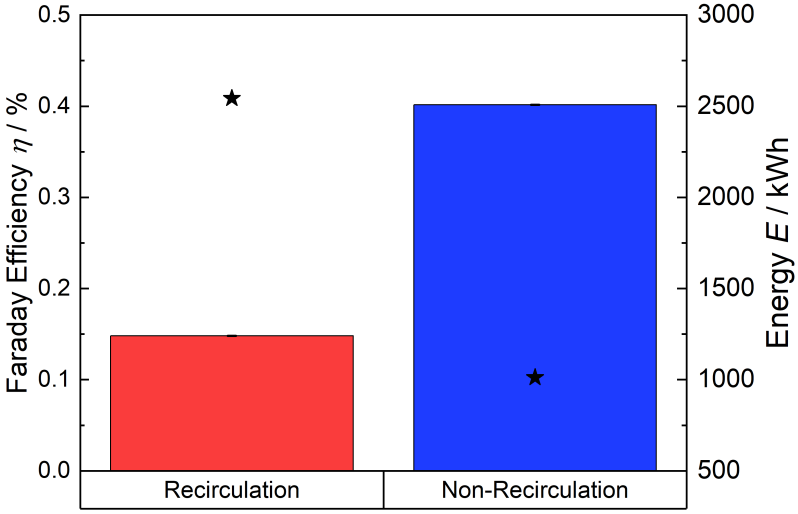


Fig. 8.10. FE of NH_3 regarding recirculation (red) and non-recirculation (blue) (left y-axis). The energy consumption for recycling 1 kg are shown as black stars (right y-axis).

8.3.2 Catalyst on Membrane

Reproducibility

Adapting the electrochemical cell by coating the catalyst directly onto the membrane led to a significant improvement in reproducibility and a considerable increase in the recycling rate. These results are presented in this section of the chapter. Fig. 8.11 illustrates the outcome of the reproducibility tests utilizing the CCM. Three fresh cells containing CCMs were utilized in the experiment. 10 mM $(NH_4)_2SO_4$ solutions at the conditions 20 mL/min and 80 °C were recirculated and current densities of 0.8 A cm^{-2} were applied for 30 min. The average recycling rates of each run, along with the corresponding scattering are shown. The initial run exhibited the highest recycling rate with an average value of 34 nmol cm^{-2} s^{-1}. The rate of the second run decreased by approximately 30 % compared to the first run. The decline in the rate from the second to the third run is minimal. The error bars indicate a discrepancy in the measured recycling rate for one cell. The third run exhibited a higher recycling rate compared to the second run. The increase of the measured potential is negligible from one run to the next.

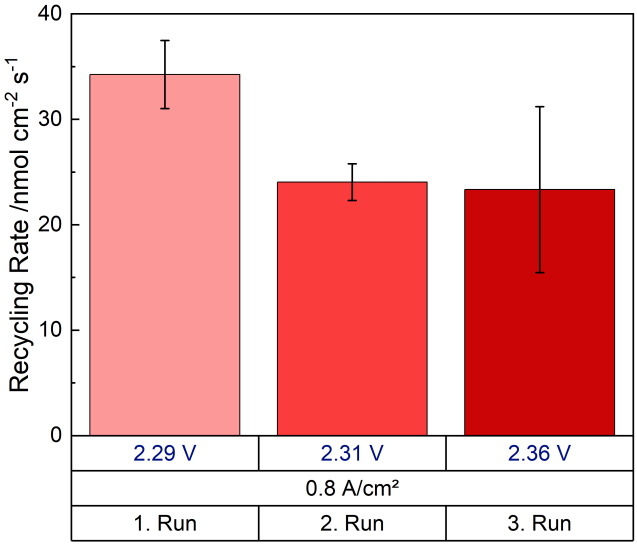


Fig. 8.11. The average NH_3 recycling rates with the respective error bars of for the three runs of the studied cells are shown in different shades of red. In black the applied current density is written and in dark blue the corresponding measured potentials.

As demonstrated in Fig. 8.12, the total amount of recycled NH_3 of each cell is represented by the red bars. The corresponding colored stars represent the ratios (χ). χ is defined as the quantity of recycled NH_3 relative to the initial amount of NH_4^+ in the solution. This results are a four- to five-fold increase in comparison to the PTL coated cell. Consequently, this constitutes a substantial enhancement in the recycling process. The green bars show the residual quantity of NH_4^+ in the solution. It was also determined by the indophenol method. The mean quantity of remaining NH_4^+ in the solution was 477.31 µmol, which is about 24 % of the initial quantity. Thus, 76 % of the ions were removed from the solution.

In the case of the first and second cells, it was assumed that the maximum quantity of NH_4^+ that the membrane could absorb was adsorbed (403 µmol), shown as the gray bars in Fig. 8.12. This resulted in the detection of 96 % of the initially introduced amount of NH_4. In the case of the third cell, the cell was disassembled at the end of the experiment. The MEA was immersed in a H_2SO_4 solution in order to drive the NH_4^+-ions out of the membrane. The expelled quantity corresponds to slightly less than 50 % of the amount assumed for complete exchange with NH_4^+ in the membrane. The distribution of the remaining quantity remains unclear.

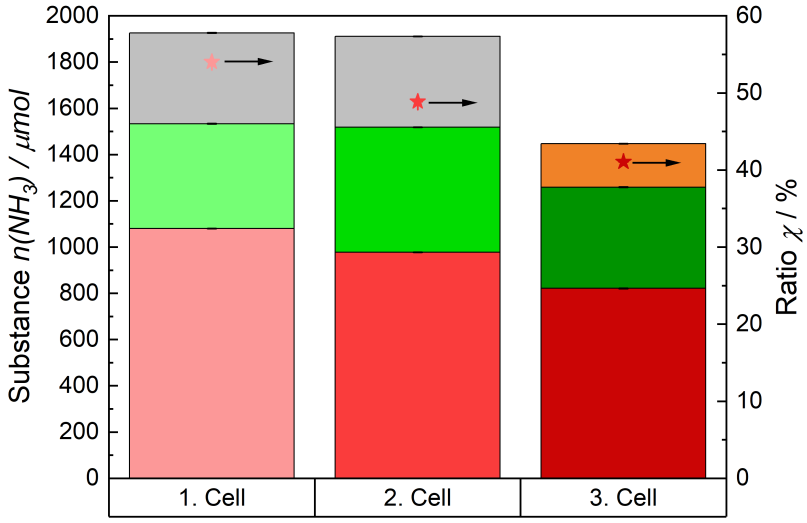


Fig. 8.12. Totaled recycled quantities of NH_3 of each cell is shown in the different red shades. In green the remaining quantity of NH_4^+ of each solution is illustrated. In grey the assumed adsorbed quantity of NH_4^+ within the membrane and in orange the detected quantity of NH_4^+ which was still in the the same membrane are shown (left y-axis). The ratios of recycled quantity to the initial amount of NH_4^+ in the solution are shown as the corresponding red stars (right y-axis).

Fig. 8.13 displays the FE and the energy consumption of the first runs of each cell (Fig. 8.12). The FE is very low, less than 0.5 %. Thus, the predominant reaction of this process is the H_2 evolution reaction. The energy consumption is roughly 60 times higher than that of the combined techniques of nitrification and denitrification. However, the electrochemical process recovers NH_3 instead of producing N_2. Furthermore, the consumption has been reduced by approximately 68 % compared to the catalyst coated on PTL, resulting in a significant improvement in energy requirement. It must be mentioned that the high energy consumption is not wasted as written, H_2 is produced as a valuable by-product. The Faraday efficiency for H_2 is the difference between 1 and the FE observed for NH_3.

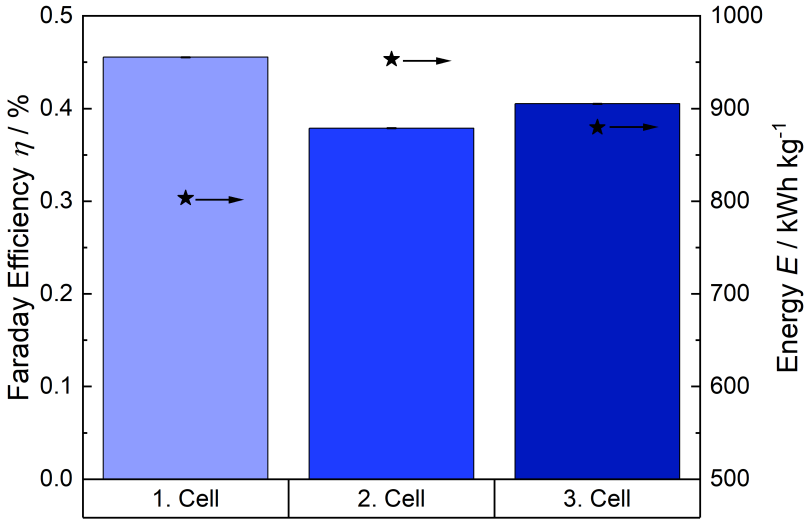


Fig. 8.13. The Faraday efficiencies of NH_3 recycling of the three cells are shown in the three shades of blue (left y-axis). The energy consumption for recycling 1 kg of NH_3 by the respective cells is shown as black stars (right y-axis).

Solution Comparison - Influence of the Valence Strength

As previously stated in the introduction, NH_4NO_3 solutions were also used as a NH_4^+ source. NH_4NO_3 is a monovalent molecule, meaning that 1 M of NH_4NO_3 contains 1 M NH_4^+. The resulting recycling rates are shown in Fig. 8.14. The experiment was conducted by applying a current density of 0.8 A cm^{-2} for three runs as well with a duration of 30 min, at a temperature of 80 °C and a flow rate of 20 mL/min. It was observed that the rate decreased over the course of the experiment due to the decrease in the amount of NH_4^+ in the solution. This trend is consistent with that depicted in Fig. 8.11. The recycling rates of the first and second runs were slightly larger for NH_4NO_3. However, considering the scattering in the rates in Fig. 8.11, a significant influence of the valence strength caused by the monovalent or divalent anion cannot be determined.

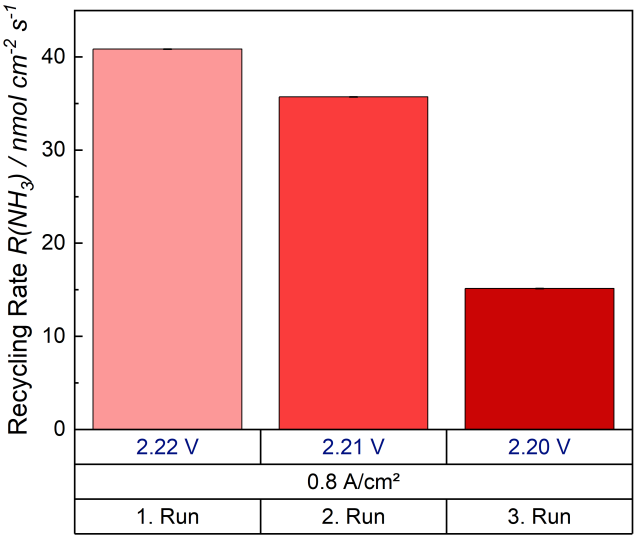


Fig. 8.14. Recycling rates of three runs of an MEA cell, while a NH_4NO_3 solution was introduced and recirculated on the anode. In black the applied current density is written and in dark blue the corresponding measured potentials.

Non-Recirculation of the Solution / Constant Solution Concentration

The recirculation of the solution led to a depletion of the NH_4^+ concentration and the quantity of NH_4^+ in the supplied solution due to the recycled quantity of NH_3. Thereby the recycling rate decreased, and the pH value decreased until ∼2. In order to ensure the maintenance of a constant NH_4^+ concentration and stable pH, the solution was not recirculated. A constant concentration of $(NH_4)_2SO_4$ (20 mM) was introduced into the cell at a temperature of 80 °C and a flow rate of 20 mL/min. This procedure was referred as "Non-recirculation". As delineated in the preceding experimental section, the solution was discharged subsequent to its passage through the cell. As demonstrated in Fig. 8.15, the measured rates are considerably higher than those observed during recirculation at the same applied current density of $0.8\,A\,cm^{-2}$. Considering a maximum recycling rate of approximately $40\,nmol\,cm^{-2}\,s^{-1}$ during recirculation, the maximum recycling rate in Fig. 8.15 is approximately $75\,nmol\,cm^{-2}\,s^{-1}$. Consequently, the maximum recycling rate at a constant concentration of aNH_4^+ supply is nearly doubled. It is noteworthy that in this case the maximum recycling rate was not achieved during the initial run of the experiment. This is most likely due to the fact that an equilibrium between NH_4^+ and H^+ must first be established in the membrane. Once the equilibrium is reached, the recycling will proceed more smoothly. Also under these circumstances, the Faraday efficiency was less than 1 %. Thus, a lower H^+ concentration does not necessarily result in enhanced NH_4^+ transport and an elevated Faraday efficiency for NH_3 recycling.

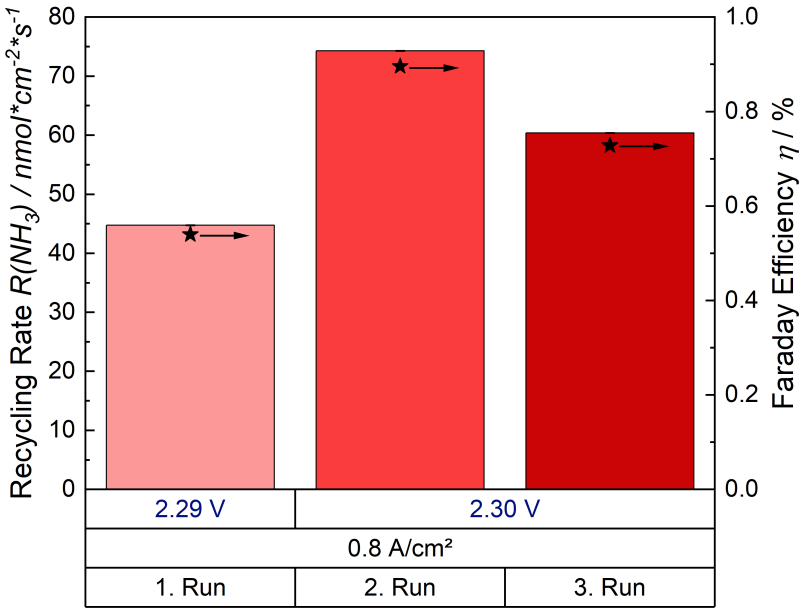


Fig. 8.15. Recorded recycling rates of NH_3 during non-recirculation / constant concentration of NH_4^+ in the introduced solution (left y-axis). The Faraday efficiency of the runs is shown as black stars (right y-axis). In black the applied current density is written and in dark blue the corresponding measured potentials.

Recovery of Ammonium and Cell Degradation

Previously, a maximum of three runs were recorded, yielding in a peak recovery ratio of 54 % while recirculating the solution. Fig. 8.16 shows the rates of an experiment in which ten runs were executed under identical conditions (0.8 A cm^{-2} for 30 min, 80 °C and 20 mL/min). As anticipated, the recycling rate of the first run was the highest with 42 nmol cm^{-2} s^{-1} and subsequently it decreased in further runs. As previously mentioned and depicted in the figures, the trend of the recycling rates fluctuates slightly from the second to the third run. Notably, the rate remains relatively stable until the sixth run, and it even exhibits a slight increase in the fifth run. The rate remained fairly constant in runs seven to ten. Nonetheless, this behavior was not the subject of further investigation because the primary focus of the experiment was on the proportion of the total NH_3 quantity that was recycled. The right y-axis shows the amount of substance (black stars) recycled per run. In total 1722 µmol of the containing NH_4^+-ions were recovered as NH_3, corresponding to 86 % of the initial solution. During these experimental runs, a slight increase in the measured potential was observed, from 2.35 to 2.4 V. Therefore, during this process of recycling (5 h) a remarkable cell degradation did not occur.

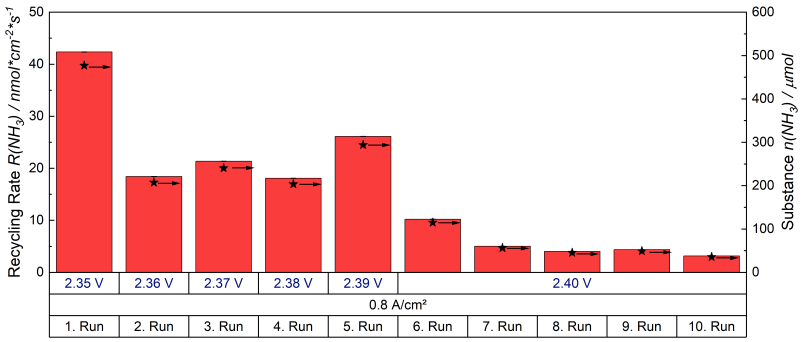


Fig. 8.16. Recorded recycling rates of each run (red bars, left y-axis). The corresponding substance of NH_3, which was recycled each run (black stars, right y-axis). In black the applied current density is written and in dark blue the corresponding measured potentials.

Influence of foreign Ions

In order to investigate the recycling of NH_3 in more realistic conditions, in which additional foreign cations are present in the solution, Na^+-ions as Na_2SO_4 were added to the solutions. Fig. 8.17 displays the recycling rates of three cells in which sodium was introduced into the recirculated solutions. The percentage values of Na^+ indicate the proportion of the Na^+-ions in relation to the $NH_4{}^+$-ions in the solution. In the first solution (red bars), 10 % Na^+ were added, corresponding to 200 µmol. In the second solution, 20 % (blue bars) and 40 % Na^+ in the third solution (green bars) were added. In each case, three runs were carried out, with an applied current of 0.8 A cm^{-2} for a duration of 30 min at the conditions 80 °C and 20 mL/min. The results of these three experiments demonstrated a similar trend. The recycling rate of the initial run of the solution containing 20 % Na^+ (blue bar) was lower than that of the initial runs of the solutions containing 10 % and 40 %. These both solutions exhibited comparable rates during the first and during the last runs. It has been demonstrated that the presence of foreign ions within this percentage range does not exert an influence on the recycling process. This observation is further substantiated due to the fact that the measured potentials were very similar. These outcomes were not anticipated as it was hypothesized that an elevated concentration of foreign ions would increase the required potential for this recycling process and leading to a decrease of the NH_3 recycling rate. Consequently, it can be concluded that the NH_3 recycling process remains unaffected within this range of foreign cations.

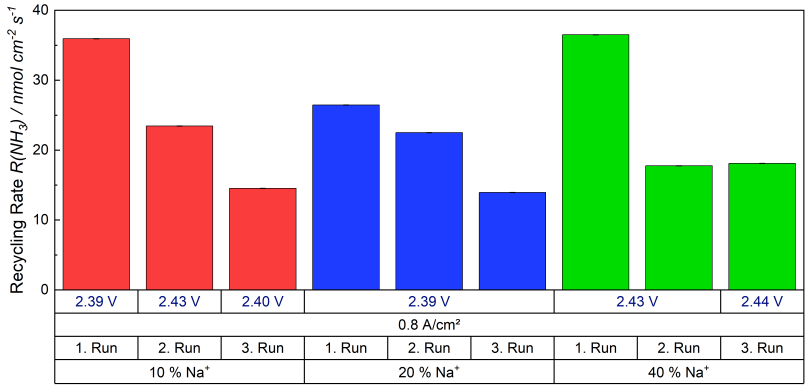


Fig. 8.17. The recycling rates in dependency of the added amount of Na^+. The solution of the red shaped production rates contained 10 %, the solution of the blue depicted rates 20 %, and the green one 40 % Na^+.

8.4 Summary and Conclusion

This chapter demonstrates the feasibility of electrochemical recycling of NH_3 utilizing a MEA cell. The process enables the recovery of ammonia from agricultural waste and wastewater, allowing for its reuse as a fertilizer or in other processes. This approach contributes to the protection of the ecosystem and conservation of resources. The selected NH_4^+ solution concentrations were based on the order of magnitude of measured concentrations in wastewater.

Various process parameters, conditions and solutions were studied. A crucial impact, resulting in a strong increase of the recycling rate and reproducibility, was the adaptation of the MEA by coating the catalyst layer on the membrane instead of the PTL. No correlation between ionic valence strength as well as the ion itself and the results were observed. In addition, in the range of the added quantity of foreign cations, the recycling process of NH_3 was not influenced by these foreign cations. The highest recycling rate was achieved while the concentration of the introduced ammonium solution was kept constant (non-recirculation). The difference in the rate is substantial compared to the results concerning an altering concentration (recirculation of the NH_4^+ solution). Yet, the ratio of the quantity of NH_3 recovered to the amount of supplied NH_4^+ is higher in the case where the solution was recirculated. Under the conditions of recirculation a maximum recovery rate of 86 % was obtained after ten runs, 5 h, with a peak rate of $75\,\mathrm{nmol\,cm^{-2}\,s^{-1}}$ / $1087\,\mathrm{g\,m^{-2}\,d^{-1}}$ being measured. In the case of the PTL coated MEA the highest measured recycling rate was approximately $33\,\mathrm{nmol\,cm^{-2}\,s^{-1}}$, equivalent to $484\,\mathrm{g\,m^{-2}\,d^{-1}}$, that is in comparison to the rates presented in the review of rates in the publication by Kuntke et al. [207] one of the highest achieved recycling rates. Though, after adapting the MEA, the measured peak rate is twice as high as in the review. Furthermore, the recovery rate / removal efficiency of 86 % achieved in this study is the second highest when compared to the values reported in the table of the Kuntke et al. publication [207]. But, the energy consumption at $0.8\,\mathrm{A\,cm^{-2}}$ with the resulting measured potential of 2.30 V was with 406 kWh significant larger for producing 1 kg of NH_3. Nevertheless, this novel recycling process offers further advantages besides a very high recycling rate of NH_3. First, NH_3 can be recovered in gaseous form. Second, H_2 is produced as a valuable by-product. Moreover, this cell system enables easy upscaling as no additional membranes or solutions are required in this MEA cell.

In comparison to the published electrochemcical ammonia production rates, the obtained recycling rates are two to three orders of magnitude greater. Concerning the anions, one possible solution to separate them would be the utilization of an anion exchange membrane.

9 Conclusion & Outlook

9.1 Summary and Conclusion

In order to ensure nutrition for the world's population, meet the rapidly growing demand for NH_3 as an energy carrier, and simultaneously reducing energy consumption and CO_2 emissions, novel, sustainable and more energy-efficient methods for NH_3 synthesis are essential. This present thesis investigages the electrochemical NH_3 synthesis in an electrochemical MEA cell and characterizes the examined catalyst for the eNRR.

Thermodynamic calculations were carried out to energetically evaluate the various NH_3 synthesis pathways. Additionally, further advantages and disadvantages of these pathways were elucidated. The direct electrochemical NH_3 synthesis is potentially the most energy-efficient. However, the reported production rates are extremely low and the reliability of the data is questionable. The evaluation of the thermodynamic stability and selectivity as shown as a Pourbaix-diagram illustrates that the potential window is very narrow.

Test benches for the synthesis of NH_3 and the enrichment of N_2 were designed and constructed. The results in chapter 5 exhibit that through the optimization of cell and process parameters, the remaining O_2 content in the air gas stream can be reduced to less than 1 % of O_2. The FE is close to 100 %. Hot pressing, a lower air flow rate, higher active cell area and an potential increase depending on the air flow rate lead to higher degrees of O_2 reduction. In comparison to the current used technologies the energy consumption, of the used electrochemical oxygen depletion cell, is slightly larger. Nevertheless, it is expected that through further optimisation the energy consumption can be reduced even further.

In chapter 6 the outcomes of the electrochemical NH_3 synthesis in aqueous electrolytes are presented. The results of the Au nanoparticles catalyst on Ni foam and the HEA on carbon felt are presented. A detailed list of the tested catalyst, their cell configurations and the respective test conditions are listed in the appendix. Various cell and process conditions were tested, but unequivocal detection of NH_3 resulting from N_2 reduction was not feasible. False-positive results occurred, which could be reduced by optimizing the measurement procedure. Nevertheless, in order to prove eNRR beyond reasonable doubt, it is necessary to exceed the combined inaccuracy

of the spectrometer, which corresponds to 206 nmol, and the inaccuracy of the gas purity, which corresponds to 192 nmol, in a reproducible manner. Nevertheless, a reliable NH_3 production exceeding the inaccuracy was not feasible and the calculated production rates from the detected quantities are far beyond commercial usage. Quantities of NH_3 were detected, whether produced from impurities or from N_2, which were observed at potentials where according to theory, no synthesis should occur.

Therefore, in chapter 7 the adsorption and desorption behavior of NH_3 in the electrochemical cell, especially in the Nafion membrane was studied. It is shown that NH_3 in form of NH_4^+ prefers to exchange with H^+ within the membrane and remains within the membrane. The equilibrium constant is larger than one. NH_4^+ can be expelled from the membrane and dissociate to NH_3 if the energy suplly is enough. The measured expelled quantities of NH_3 are reproducible as evidenced by the figures in this chapter. These measured quantities significantly exceed the margin of error resulting from the impurities in the N_2 supply and the inaccuracy of the spectrometer. Consequently, the findings are indisputable. In addition to the electrical driven force, diffusion drives the discharge as well. It is found that small amounts of NH_3 in the membrane do not effect the ohmic resistance and ion conductivity, hence if NH_3 is synthesized it can stay unnoticed within the membrane. These outcomes height the awareness of the interaction between NH_3 and Nafion and can contribute to reliable and reproducible eNRR.

Utilizing the adsoprtion and desorption properties of Nafion, the electrochemical recycling of NH_3 from ammonium salt solutions were investigated. The solutions are intended to study the recycling of NH_3 from wastewater. A novel electrochemical recycling process utilizing a MEA cell was developed. Various process parameters, conditions were studied. The highest achieved recycling rate of $75\,\mathrm{nmol\,cm^{-2}\,s^{-1}}$ is twice as high as the maximum presented in the literature and overshoot the margin of error clearly. A recovery rate / removal efficiency of 86 % was achieved. However, the Faraday efficiency regarding NH_3 synthesis is very low and the energy consumption is quite high. Nevertheless, H_2 is produced as a valuable by-product and the straightforward scalability of the process represent a notable advantage in comparison to the electrochemical recycling processes in literature.

9.2 Outlook and Future Perspectives

The thesis present that the theoretical thermodynamic efficiency of the direct electrochenical NH_3 synthesis is the most efficient one, with an energy efficiency of 89 %. The efficiency is more than twice that of the Lithium mediated electrosynthesis. But, achieving a reliable and reproducible synthesis of NH_3 could not be achieved. Production rates reported in the literature are highly questionable concerning the criteria outlined in section 2.9 and are also far from the targeted rates in mentioned in section 2.1.
For this reason, the electrified Haber-Bosch process is probably the most promising alternative for NH_3 production. Consequently, the research showed focus on the improvement of water electrolysis and electrochemical O_2 depletion. The enhancement of O_2 reduction efficiency is likely to be improved by upscaling and stack assembly, a methodology that has already been successfully implemented in water electrolysis. In addition the process of electrochemical recycling offers the possibility to recycle elements. The process of electrochemical NH_3 recycling needs to be improved energetic. Furthermore, the process of electrochemical recycling could be explored, for instance, in the recycling of Lithium.

Acknowledgement

This thesis was written as part of the "TOWARD EFFICIENT ELECTROCHEMICAL GREEN AMMONIA CYCLE (Telegram)" project, which was financially supported as part of the European Union's Horizon 2020 research and innovation program under the call H2020-LC-SC3-2020-RES-RIA.

Bibliography

[1]Zhe Xue, Xinyu Zhang, Jiaqian Qin, and Riping Liu. "High-throughput identification of high activity and selectivity transition metal single-atom catalysts for nitrogen reduction". In: *Nano Energy* 80 (2021), p. 105527. DOI: 10.1016/j.nanoen.2020.105527 (cit. on p. 1).

[2]Bryan H. R. Suryanto, Hoang-Long Du, Dabin Wang, Jun Chen, Alexandr N. Simonov, and Douglas R. MacFarlane. "Challenges and prospects in the catalysis of electroreduction of nitrogen to ammonia". In: *Nature Catalysis* 2.4 (2019), pp. 290–296. DOI: 10.1038/s41929-019-0252-4 (cit. on pp. 1, 26, 38).

[3]Schnitkey. *Fertilizer Prices Higher for 2019 Crop*. 2018. URL: https://farmdocdaily.illinois.edu/2018/09/fertilizer-prices-higher-for-2019-crop.html (visited on May 20, 2025) (cit. on p. 1).

[4]Haldrian Iriawan, Suzanne Z. Andersen, Xilun Zhang, Benjamin M. Comer, Jesús Barrio, Ping Chen, Andrew J. Medford, Ifan E. L. Stephens, Ib Chorkendorff, and Yang Shao-Horn. "Methods for nitrogen activation by reduction and oxidation". In: *Nature Reviews Methods Primers* 1.1 (2021). DOI: 10.1038/s43586-021-00053-y (cit. on pp. 1, 2, 22, 34, 35, 37, 38).

[5]K. Hasler, S. Bröring, S.W.F. Omta, and H.-W. Olfs. "Life cycle assessment (LCA) of different fertilizer product types". In: *European Journal of Agronomy* 69 (2015), pp. 41–51. DOI: 10.1016/j.eja.2015.06.001 (cit. on p. 1).

[6]Cheng Tang and Shi-Zhang Qiao. "How to explore ambient electrocatalytic nitrogen reduction reliably and insightfully". In: *Chemical Society reviews* 48.12 (2019), pp. 3166–3180. DOI: 10.1039/c9cs00280d (cit. on pp. 1, 21, 26, 32, 33, 38, 46).

[7]Vaclav Smil. "Detonator of the population explosion". In: *Nature* 400.6743 (1999), p. 415. DOI: 10.1038/22672 (cit. on pp. 1, 7).

[8]Jan Willem Erisman, Mark A. Sutton, James Galloway, Zbigniew Klimont, and Wilfried Winiwarter. "How a century of ammonia synthesis changed the world". In: *Nature Geoscience* 1.10 (2008), pp. 636–639. DOI: 10.1038/ngeo325 (cit. on pp. 1, 7, 9).

[9]Cornelis J. M. van der Ham, Marc T. M. Koper, and Dennis G. H. Hetterscheid. "Challenges in reduction of dinitrogen by proton and electron transfer". In: *Chemical Society reviews* 43.15 (2014), pp. 5183–5191. DOI: 10.1039/c4cs00085d (cit. on pp. 1, 23, 64).

[10]Katja Li, Suzanne Z. Andersen, Michael J. Statt, Mattia Saccoccio, Vanessa J. Bukas, Kevin Krempl, Rokas Sažinas, Jakob B. Pedersen, Vahid Shadravan, Yuanyuan Zhou, Debasish Chakraborty, Jakob Kibsgaard, Peter C. K. Vesborg, Jens K. Nørskov, and Ib Chorkendorff. "Enhancement of lithium-mediated ammonia synthesis by addition of oxygen". In: *Science (New York, N.Y.)* 374.6575 (2021), pp. 1593–1597. DOI: 10.1126/science.abl4300 (cit. on pp. 1, 14, 15, 64).

[11]Huidong Shen, Changhyeok Choi, Justus Masa, Xin Li, Jieshan Qiu, Yousung Jung, and Zhenyu Sun. "Electrochemical ammonia synthesis: Mechanistic understanding and catalyst design". In: *Chem* 7.7 (2021), pp. 1708–1754. DOI: 10.1016/j.chempr.2021.01.009 (cit. on pp. 1, 10, 22, 23, 29, 30, 38, 64, 75).

[12]Tingting Wu, Wenjun Fan, Yang Zhang, and Fuxiang Zhang. "Electrochemical synthesis of ammonia: Progress and challenges". In: *Materials Today Physics* 16 (2021), p. 100310. DOI: 10.1016/j.mtphys.2020.100310 (cit. on pp. 1, 23, 64).

[13]Islam Rafiqul, Christoph Weber, Bianca Lehmann, and Alfred Voss. "Energy efficiency improvements in ammonia production—perspectives and uncertainties". In: *Energy* 30.13 (2005), pp. 2487–2504. DOI: 10.1016/j.energy.2004.12.004 (cit. on p. 1).

[14]A. Valera-Medina, H. Xiao, M. Owen-Jones, W.I.F. David, and P. J. Bowen. "Ammonia for power". In: *Progress in Energy and Combustion Science* 69 (2018), pp. 63–102. DOI: 10.1016/j.pecs.2018.07.001 (cit. on p. 2).

[15]Lin Hu, Asim Khaniya, Jun Wang, Gang Chen, William E. Kaden, and Xiaofeng Feng. "Ambient Electrochemical Ammonia Synthesis with High Selectivity on Fe/Fe Oxide Catalyst". In: *ACS Catalysis* 8.10 (2018), pp. 9312–9319. DOI: 10.1021/acscatal.8b02585 (cit. on p. 2).

[16]Debabrata Chanda, Ruimin Xing, Tong Xu, Qian Liu, Yonglan Luo, Shanhu Liu, Ramatu Ashu Tufa, Tarekegn Heliso Dolla, Tiziano Montini, and Xuping Sun. "Electrochemical nitrogen reduction: recent progress and prospects". In: *Chemical communications (Cambridge, England)* 57.60 (2021), pp. 7335–7349. DOI: 10.1039/d1cc01451j (cit. on pp. 2, 22, 26).

[17]The Royal Society. *Ammonia: zero-carbon fertiliser, fuel and energy store*. URL: https://royalsociety.org/-/media/policy/projects/green-ammonia/green-ammonia-policy-briefing.pdf (visited on Mar. 23, 2024) (cit. on pp. 3, 4).

[18]Ann Raleigh. *OPPORTUNITIES FOR AUSTRALIA FROM HYDROGEN EXPORTS*. 2018. URL: https://arena.gov.au/assets/2018/08/opportunities-for-australia-from-hydrogen-exports.pdf (visited on May 20, 2025) (cit. on p. 4).

[19]A. Hermann. "Haber und Bosch: Brot aus Luft - Die Ammoniaksynthese". In: *Physik Journal* 21.4 (1965), pp. 168–171. DOI: 10.1002/phbl.19650210403 (cit. on p. 7).

[20]E. Leibnitz, H. Koch, and A. Götze. "Über die drucklose Aufbereitung von Braunkohlenkokereigas auf Starkgas nach dem Girbotol–Verfahren". In: *Journal für Praktische Chemie* 13.3-4 (1961), pp. 215–236. DOI: 10.1002/prac.19610130315 (cit. on p. 8).

[21]Detlev Forst, Maximilian Kolb, and Helmut Roßwag. *Chemie für Ingenieure*. Springer eBook Collection Computer Science and Engineering. Berlin, Heidelberg and s.l.: Springer Berlin Heidelberg, 1993. DOI: 10.1007/978-3-662-00654-2 (cit. on pp. 8, 9).

[22]Fritz Haber and Robert Le Rossignol. "Über die technische Darstellung von Ammoniak aus den Elementen". In: *Zeitschrift für Elektrochemie und angewandte physikalische Chemie* 19.2 (1913), pp. 53–72. DOI: 10.1002/bbpc.19130190201 (cit. on p. 9).

[23]Frank Neese. "The Yandulov/Schrock cycle and the nitrogenase reaction: pathways of nitrogen fixation studied by density functional theory". In: *Angewandte Chemie (International ed. in English)* 45.2 (2005), pp. 196–199. DOI: 10.1002/anie.200502667. URL: https://onlinelibrary.wiley.com/doi/full/10.1002/anie.200502667 (cit. on p. 10).

[24]*Prokaryotic nitrogen fixation: A model system for the analysis of a biological process*. Wymondham: Horizon Scientific Press, 2000. URL: https://www.cabidigitallibrary.org/doi/full/10.5555/20001907313 (cit. on p. 10).

[25]Tianchang Liu, Michael R. Gau, and Neil C. Tomson. "Mimicking the Constrained Geometry of a Nitrogen-Fixation Intermediate". In: *Journal of the American Chemical Society* 142.18 (2020), pp. 8142–8146. DOI: 10.1021/jacs.0c01861 (cit. on p. 10).

[26]Barbara K. Burgess and David J. Lowe. "Mechanism of Molybdenum Nitrogenase". In: *Chemical reviews* 96.7 (1996), pp. 2983–3012. DOI: 10.1021/cr950055x (cit. on p. 10).

[27]Marcia A. Murry, Patrick C. Hallenbeck, Diane Esteva, and John R. Benemann. "Nitrogenase inactivation by oxygen and enzyme turnover in Anabaena cylindrica". In: *Canadian Journal of Microbiology* 29.10 (1983), pp. 1286–1294. DOI: 10.1139/m83-201 (cit. on p. 10).

[28]Martyn Poliakoff, J. Michael Fitzpatrick, Trevor R. Farren, and Paul T. Anastas. "Green chemistry: science and politics of change". In: *Science (New York, N.Y.)* 297.5582 (2002), pp. 807–810. DOI: 10.1126/science.297.5582.807 (cit. on p. 10).

[29]Xiaolan Xue, Renpeng Chen, Changzeng Yan, Peiyang Zhao, Yi Hu, Wenjun Zhang, Songyuan Yang, and Zhong Jin. "Review on photocatalytic and electrocatalytic artificial nitrogen fixation for ammonia synthesis at mild conditions: Advances, challenges and perspectives". In: *Nano Research* 12.6 (2019), pp. 1229–1249. DOI: 10.1007/s12274-018-2268-5 (cit. on pp. 11, 12).

[30]Chengcheng Li, Tuo Wang, and Jinlong Gong. "Alternative Strategies Toward Sustainable Ammonia Synthesis". In: *Transactions of Tianjin University* 26.2 (2020), pp. 67–91. DOI: 10.1007/s12209-020-00243-x (cit. on p. 11).

[31]Sheng Chu, Wei Li, Yanfa Yan, Thomas Hamann, Ishiang Shih, Dunwei Wang, and Zetian Mi. "Roadmap on solar water splitting: current status and future prospects". In: *Nano Futures* 1.2 (2017), p. 022001. DOI: 10.1088/2399-1984/aa88a1 (cit. on p. 11).

[32]Di Zhu, Linghong Zhang, Rose E. Ruther, and Robert J. Hamers. "Photo-illuminated diamond as a solid-state source of solvated electrons in water for nitrogen reduction". In: *Nature materials* 12.9 (2013), pp. 836–841. DOI: 10.1038/nmat3696 (cit. on p. 11).

[33]N. N. Rao, Sangeeta Dube, Manjubala, and P. Natarajan. “Photocatalytic reduction of nitrogen over (Fe, Ru or Os) /TiO2 catalysts”. In: *Applied Catalysis B: Environmental* 5.1-2 (1994), pp. 33–42. DOI: 10.1016/0926-3373(94)00042-5 (cit. on p. 11).

[34]Weirong Zhao, Jing Zhang, Xi Zhu, Meng Zhang, Jing Tang, Min Tan, and Yan Wang. “Enhanced nitrogen photofixation on Fe-doped TiO2 with highly exposed (101) facets in the presence of ethanol as scavenger”. In: *Applied Catalysis B: Environmental* 144 (2014), pp. 468–477. DOI: 10.1016/j.apcatb.2013.07.047 (cit. on p. 11).

[35]Jianhua Yang, Yanzhen Guo, Ruibin Jiang, Feng Qin, Han Zhang, Wenzheng Lu, Jianfang Wang, and Jimmy C. Yu. “High-Efficiency "Working-in-Tandem" Nitrogen Photofixation Achieved by Assembling Plasmonic Gold Nanocrystals on Ultrathin Titania Nanosheets”. In: *Journal of the American Chemical Society* 140.27 (2018), pp. 8497–8508. DOI: 10.1021/jacs.8b03537 (cit. on p. 11).

[36]Tong Xu, Jie Liang, Shaoxiong Li, Zhaoquan Xu, Luchao Yue, Tingshuai Li, Yonglan Luo, Qian Liu, Xifeng Shi, Abdullah M. Asiri, Chun Yang, and Xuping Sun. “Recent Advances in Nonprecious Metal Oxide Electrocatalysts and Photocatalysts for N 2 Reduction Reaction under Ambient Condition”. In: *Small Science* 1.5 (2021), p. 2000069. DOI: 10.1002/smsc.202000069 (cit. on p. 12).

[37]Shelby L. Foster, Sergio I. Perez Bakovic, Royce D. Duda, Sharad Maheshwari, Ross D. Milton, Shelley D. Minteer, Michael J. Janik, Julie N. Renner, and Lauren F. Greenlee. “Catalysts for nitrogen reduction to ammonia”. In: *Nature Catalysis* 1.7 (2018), pp. 490–500. DOI: 10.1038/s41929-018-0092-7 (cit. on p. 12).

[38]Shanshan Lin, Xinghua Zhang, Lungang Chen, Qi Zhang, Longlong Ma, and Jianguo Liu. “A review on catalysts for electrocatalytic and photocatalytic reduction of N 2 to ammonia”. In: *Green Chemistry* 24.23 (2022), pp. 9003–9026. DOI: 10.1039/D2GC03174D (cit. on p. 12).

[39]Suzanne Z. Andersen, Michael J. Statt, Vanessa J. Bukas, Sarah G. Shapel, Jakob B. Pedersen, Kevin Krempl, Mattia Saccoccio, Debasish Chakraborty, Jakob Kibsgaard, Peter C. K. Vesborg, Jens Nørskov, and Ib Chorkendorff. “Increasing stability, efficiency, and fundamental understanding of lithium-mediated electrochemical nitrogen reduction”. In: *Energy & Environmental Science* 13.11 (2020), pp. 4291–4300. DOI: 10.1039/D0EE02246B (cit. on pp. 13, 22).

[40]S. Giddey, S.P.S. Badwal, and A. Kulkarni. “Review of electrochemical ammonia production technologies and materials”. In: *International Journal of Hydrogen Energy* 38.34 (2013), pp. 14576–14594. DOI: 10.1016/j.ijhydene.2013.09.054 (cit. on pp. 13, 16, 17, 21).

[41]Fengling Zhou, Luis Miguel Azofra, Muataz Ali, Mega Kar, Alexandr N. Simonov, Ciaran McDonnell-Worth, Chenghua Sun, Xinyi Zhang, and Douglas R. MacFarlane. “Electro-synthesis of ammonia from nitrogen at ambient temperature and pressure in ionic liquids”. In: *Energy & Environmental Science* 10.12 (2017), pp. 2516–2520. DOI: 10.1039/C7EE02716H (cit. on pp. 14, 22).

[42]Xinghua Guo, Yunpei Zhu, and Tianyi Ma. “Lowering reaction temperature: Electrochemical ammonia synthesis by coupling various electrolytes and catalysts”. In: *Journal of Energy Chemistry* 26.6 (2017), pp. 1107–1116. DOI: 10.1016/j.jechem.2017.09.012 (cit. on p. 14).

[43]Douglas R. MacFarlane, Maria Forsyth, Patrick C. Howlett, Mega Kar, Stefano Passerini, Jennifer M. Pringle, Hiroyuki Ohno, Masayoshi Watanabe, Feng Yan, Wenjun Zheng, Shiguo Zhang, and Jie Zhang. “Ionic liquids and their solid-state analogues as materials for energy generation and storage”. In: *Nature Reviews Materials* 1.2 (2016). DOI: 10.1038/natrevmats.2015.5 (cit. on p. 14).

[44]S. Stevanovic and M. F. Costa Gomes. “Solubility of carbon dioxide, nitrous oxide, ethane, and nitrogen in 1-butyl-1-methylpyrrolidinium and trihexyl(tetradecyl)phosphonium tris(pentafluoroethyl)trifluorophosphate (eFAP) ionic liquids”. In: *The Journal of Chemical Thermodynamics* 59 (2013), pp. 65–71. DOI: 10.1016/j.jct.2012.11.010 (cit. on p. 14).

[45]Kwiyong Kim, Nara Lee, Chung-Yul Yoo, Jong-Nam Kim, Hyung Chul Yoon, and Jong-In Han. “Communication—Electrochemical Reduction of Nitrogen to Ammonia in 2-Propanol under Ambient Temperature and Pressure”. In: *Journal of The Electrochemical Society* 163.7 (2016), F610–F612. DOI: 10.1149/2.0231607jes (cit. on p. 14).

[46]Joshua M. McEnaney, Aayush R. Singh, Jay A. Schwalbe, Jakob Kibsgaard, John C. Lin, Matteo Cargnello, Thomas F. Jaramillo, and Jens K. Nørskov. “Ammonia synthesis from N 2 and H 2 O using a lithium cycling electrification strategy at atmospheric pressure”. In: *Energy & Environmental Science* 10.7 (2017), pp. 1621–1630. DOI: 10.1039/C7EE01126A (cit. on p. 14).

[47]Bryan H. R. Suryanto, Karolina Matuszek, Jaecheol Choi, Rebecca Y. Hodgetts, Hoang-Long Du, Jacinta M. Bakker, Colin S. M. Kang, Pavel V. Cherepanov, Alexandr N. Simonov, and Douglas R. MacFarlane. “Nitrogen reduction to ammonia at high efficiency and rates based on a phosphonium proton shuttle”. In: *Science (New York, N.Y.)* 372.6547 (2021), pp. 1187–1191. DOI: 10.1126/science.abg2371 (cit. on pp. 14, 15).

[48]Shaofeng Li, Yuanyuan Zhou, Katja Li, Mattia Saccoccio, Rokas Sažinas, Suzanne Z. Andersen, Jakob B. Pedersen, Xianbiao Fu, Vahid Shadravan, Debasish Chakraborty, Jakob Kibsgaard, Peter C. K. Vesborg, Jens K. Nørskov, and Ib Chorkendorff. “Electrosynthesis of ammonia with high selectivity and high rates via engineering of the solid-electrolyte interphase”. In: *Joule* 6.9 (2022), pp. 2083–2101. DOI: 10.1016/j.joule.2022.07.009 (cit. on p. 14).

[49]Nikifar Lazouski, Minju Chung, Kindle Williams, Michal L. Gala, and Karthish Manthiram. “Non-aqueous gas diffusion electrodes for rapid ammonia synthesis from nitrogen and water-splitting-derived hydrogen”. In: *Nature Catalysis* 3.5 (2020), pp. 463–469. DOI: 10.1038/s41929-020-0455-8 (cit. on p. 14).

[50]Akira Tsuneto, Akihiko Kudo, and Tadayoshi Sakata. “Lithium-mediated electrochemical reduction of high pressure N2 to NH3”. In: *Journal of Electroanalytical Chemistry* 367.1-2 (1994), pp. 183–188. DOI: 10.1016/0022-0728(93)03025-K (cit. on p. 14).

[51]Aayush R. Singh, Brian A. Rohr, Michael J. Statt, Jay A. Schwalbe, Matteo Cargnello, and Jens K. Nørskov. "Strategies toward Selective Electrochemical Ammonia Synthesis". In: *ACS Catalysis* 9.9 (2019), pp. 8316–8324. DOI: 10.1021/acscatal.9b02245 (cit. on p. 14).

[52]F. Gibanel, M. C. Lpez, F. M. Royo, J. Santaf, and J. S. Urieta. "Solubility of nonpolar gases in tetrahydrofuran at 0 to 30C and 101.33 kPa partial pressure of gas". In: *Journal of Solution Chemistry* 22.3 (1993), pp. 211–217. DOI: 10.1007/BF00649244 (cit. on p. 14).

[53]Michael A. Shipman and Mark D. Symes. "Recent progress towards the electrosynthesis of ammonia from sustainable resources". In: *Catalysis Today* 286 (2017), pp. 57–68. DOI: 10.1016/j.cattod.2016.05.008 (cit. on p. 14).

[54]Douglas R. MacFarlane, Pavel V. Cherepanov, Jaecheol Choi, Bryan H.R. Suryanto, Rebecca Y. Hodgetts, Jacinta M. Bakker, Federico M. Ferrero Vallana, and Alexandr N. Simonov. "A Roadmap to the Ammonia Economy". In: *Joule* 4.6 (2020), pp. 1186–1205. DOI: 10.1016/j.joule.2020.04.004 (cit. on p. 15).

[55]Akira Tsuneto, Akihiko Kudo, and Tadayoshi Sakata. "Efficient Electrochemical Reduction of N 2 to NH 3 Catalyzed by Lithium". In: *Chemistry Letters* 22.5 (1993), pp. 851–854. DOI: 10.1246/cl.1993.851 (cit. on p. 15).

[56]Tsuyoshi Murakami, Tokujiro Nishikiori, Toshiyuki Nohira, and Yasuhiko Ito. "Electrolytic synthesis of ammonia in molten salts under atmospheric pressure". In: *Journal of the American Chemical Society* 125.2 (2003), pp. 334–335. DOI: 10.1021/ja028891t (cit. on p. 16).

[57]Jaecheol Choi, Bryan H. R. Suryanto, Dabin Wang, Hoang-Long Du, Rebecca Y. Hodgetts, Federico M. Ferrero Vallana, Douglas R. MacFarlane, and Alexandr N. Simonov. "Identification and elimination of false positives in electrochemical nitrogen reduction studies". In: *Nature communications* 11.1 (2020), p. 5546. DOI: 10.1038/s41467-020-19130-z (cit. on pp. 16, 21, 34, 38, 109).

[58]Xuan Yang, Jared Nash, Jacob Anibal, Marco Dunwell, Shyam Kattel, Eli Stavitski, Klaus Attenkofer, Jingguang G. Chen, Yushan Yan, and Bingjun Xu. "Mechanistic Insights into Electrochemical Nitrogen Reduction Reaction on Vanadium Nitride Nanoparticles". In: *Journal of the American Chemical Society* 140.41 (2018), pp. 13387–13391. DOI: 10.1021/jacs.8b08379 (cit. on pp. 16, 25, 29, 135).

[59]Ben Hui Wang, Ji de Wang, RuiQuan Liu, Ya Hong Xie, and Zhi Jie Li. "Synthesis of ammonia from natural gas at atmospheric pressure with doped ceria–Ca3(PO4)2–K3PO4 composite electrolyte and its proton conductivity at intermediate temperature". In: *Journal of Solid State Electrochemistry* 11.1 (2007), pp. 27–31. DOI: 10.1007/s10008-005-0042-6 (cit. on p. 16).

[60]Ibrahim A. Amar, Christophe T.G. Petit, Lei Zhang, Rong Lan, Peter J. Skabara, and Shanwen Tao. "Electrochemical synthesis of ammonia based on doped-ceria-carbonate composite electrolyte and perovskite cathode". In: *Solid State Ionics* 201.1 (2011), pp. 94–100. DOI: 10.1016/j.ssi.2011.08.003 (cit. on p. 16).

[61]V. Kordali, G. Kyriacou, and Ch. Lambrou. “Electrochemical synthesis of ammonia at atmospheric pressure and low temperature in a solid polymer electrolyte cell”. In: *Chemical Communications* 17 (2000), pp. 1673–1674. DOI: 10.1039/b004885m (cit. on pp. 17, 31, 135).

[62]Ted H. Yu, Yao Sha, Wei-Guang Liu, Boris V. Merinov, Pezhman Shirvanian, and William A. Goddard. “Mechanism for degradation of Nafion in PEM fuel cells from quantum mechanics calculations”. In: *Journal of the American Chemical Society* 133.49 (2011), pp. 19857–19863. DOI: 10.1021/ja2074642 (cit. on p. 18).

[63]Marnellos and Stoukides. “Ammonia synthesis at atmospheric pressure”. In: *Science (New York, N.Y.)* 282.5386 (1998), pp. 98–100. DOI: 10.1126/science.282.5386.98 (cit. on p. 19).

[64]V. Kyriakou, I. Garagounis, E. Vasileiou, A. Vourros, and M. Stoukides. “Progress in the Electrochemical Synthesis of Ammonia”. In: *Catalysis Today* 286 (2017), pp. 2–13. DOI: 10.1016/j.cattod.2016.06.014 (cit. on p. 19).

[65]Ibrahim A. Amar, Rong Lan, Christophe T. G. Petit, and Shanwen Tao. “Solid-state electrochemical synthesis of ammonia: a review”. In: *Journal of Solid State Electrochemistry* 15.9 (2011), pp. 1845–1860. DOI: 10.1007/s10008-011-1376-x (cit. on p. 19).

[66]Rui-Quan Liu, Ya-Hong Xie, Ji-De Wang, Zhi-Jie Li, and Ben-Hui Wang. “Synthesis of ammonia at atmospheric pressure”. In: *Solid State Ionics* 177.1 (2006), pp. 73–76. DOI: 10.1016/j.ssi.2005.07.018 (cit. on p. 19).

[67]Egill Skúlason, Thomas Bligaard, Sigrídur Gudmundsdóttir, Felix Studt, Jan Rossmeisl, Frank Abild-Pedersen, Tejs Vegge, Hannes Jónsson, and Jens K. Nørskov. “A theoretical evaluation of possible transition metal electro-catalysts for N2 reduction”. In: *Physical chemistry chemical physics : PCCP* 14.3 (2012), pp. 1235–1245. DOI: 10.1039/c1cp22271f (cit. on pp. 21, 27, 28).

[68]T. L. Cottrell. *The Strengths of Chemical Bonds*. Academic Press, 1954. URL: https://books.google.de/books?id=7J09AAAAIAAJ (cit. on p. 22).

[69]Petra Moritz. *Chemie auf Schritt und Tritt: Wie? Warum? Weshalb?* 2. Aufl. Eisenstadt: Weber, 2006. URL: https://permalink.obvsg.at/AC03818221 (cit. on p. 22).

[70]Geletu Qing, Reza Ghazfar, Shane T. Jackowski, Faezeh Habibzadeh, Mona Maleka Ashtiani, Chuan-Pin Chen, Milton R. Smith, and Thomas W. Hamann. “Recent Advances and Challenges of Electrocatalytic N2 Reduction to Ammonia”. In: *Chemical reviews* 120.12 (2020), pp. 5437–5516. DOI: 10.1021/acs.chemrev.9b00659 (cit. on pp. 22, 30).

[71]Yao Yao, Shangqian Zhu, Haijiang Wang, Hui Li, and Minhua Shao. “A Spectroscopic Study on the Nitrogen Electrochemical Reduction Reaction on Gold and Platinum Surfaces”. In: *Journal of the American Chemical Society* 140.4 (2018), pp. 1496–1501. DOI: 10.1021/jacs.7b12101 (cit. on pp. 22, 28).

[72]Rubin Battino, Timothy R. Rettich, and Toshihiro Tominaga. “The Solubility of Nitrogen and Air in Liquids”. In: *Journal of Physical and Chemical Reference Data* 13.2 (1984), pp. 563–600. DOI: 10.1063/1.555713 (cit. on p. 22).

[73]Nishithan C. Kani, Aditya Prajapati, Brianna A. Collins, Jason D. Goodpaster, and Meenesh R. Singh. “Competing Effects of pH, Cation Identity, H 2 O Saturation, and N 2 Concentration on the Activity and Selectivity of Electrochemical Reduction of N 2 to NH 3 on Electrodeposited Cu at Ambient Conditions”. In: *ACS Catalysis* 10.24 (2020), pp. 14592–14603. DOI: 10.1021/acscatal.0c04864 (cit. on pp. 22, 27, 74).

[74]Aayush R. Singh, Brian A. Rohr, Jay A. Schwalbe, Matteo Cargnello, Karen Chan, Thomas F. Jaramillo, Ib Chorkendorff, and Jens K. Nørskov. “Electrochemical Ammonia Synthesis—The Selectivity Challenge”. In: *ACS Catalysis* 7.1 (2017), pp. 706–709. DOI: 10.1021/acscatal.6b03035 (cit. on pp. 22, 33).

[75]Suzanne Z. Andersen, Viktor Čolić, Sungeun Yang, Jay A. Schwalbe, Adam C. Nielander, Joshua M. McEnaney, Kasper Enemark-Rasmussen, Jon G. Baker, Aayush R. Singh, Brian A. Rohr, Michael J. Statt, Sarah J. Blair, Stefano Mezzavilla, Jakob Kibsgaard, Peter C. K. Vesborg, Matteo Cargnello, Stacey F. Bent, Thomas F. Jaramillo, Ifan E. L. Stephens, Jens K. Nørskov, and Ib Chorkendorff. “A rigorous electrochemical ammonia synthesis protocol with quantitative isotope measurements”. In: *Nature* 570.7762 (2019), pp. 504–508. DOI: 10.1038/s41586-019-1260-x (cit. on pp. 22, 34–36, 38, 110, 135).

[76]Dong Liu, Mingpeng Chen, Xinyu Du, Haoqiang Ai, Kin Ho Lo, Shuangpeng Wang, Shi Chen, Guichuan Xing, Xuesen Wang, and Hui Pan. “Development of Electrocatalysts for Efficient Nitrogen Reduction Reaction under Ambient Condition”. In: *Advanced Functional Materials* 31.11 (2021), p. 2008983. DOI: 10.1002/adfm.202008983 (cit. on pp. 22, 26–30, 35, 38, 135).

[77]Yongwen Ren, Chang Yu, Xinyi Tan, Xiaotong Han, Hongling Huang, Huawei Huang, and Jieshan Qiu. “Is It Appropriate to Use the Nafion Membrane in Electrocatalytic N 2 Reduction?” In: *Small Methods* 3.12 (2019), p. 1900474. DOI: 10.1002/smtd.201900474 (cit. on pp. 22, 36, 110, 135).

[78]Xiaoyang Cui, Cheng Tang, and Qiang Zhang. “A Review of Electrocatalytic Reduction of Dinitrogen to Ammonia under Ambient Conditions”. In: *Advanced Energy Materials* 8.22 (2018), p. 1800369. DOI: 10.1002/aenm.201800369 (cit. on pp. 23, 31, 32).

[79]Zhonghao Wang, Xun Hu, Zhenzhen Liu, Guojun Zou, Guannan Wang, and Kan Zhang. “Recent Developments in Polymeric Carbon Nitride-Derived Photocatalysts and Electrocatalysts for Nitrogen Fixation”. In: *ACS Catalysis* 9.11 (2019), pp. 10260–10278. DOI: 10.1021/acscatal.9b03015 (cit. on pp. 23, 24, 29).

[80]Xiao-Fei Li, Qin-Kun Li, Jin Cheng, Lingling Liu, Qing Yan, Yingchao Wu, Xiang-Hua Zhang, Zhi-Yong Wang, Qi Qiu, and Yi Luo. “Conversion of Dinitrogen to Ammonia by FeN3-Embedded Graphene”. In: *Journal of the American Chemical Society* 138.28 (2016), pp. 8706–8709. DOI: 10.1021/jacs.6b04778 (cit. on p. 23).

[81]Younes Abghoui, Anna L. Garden, Valtýr Freyr Hlynsson, Snædís Björgvinsdóttir, Hrefna Ólafsdóttir, and Egill Skúlason. “Enabling electrochemical reduction of nitrogen to ammonia at ambient conditions through rational catalyst design”. In: *Physical chemistry chemical physics : PCCP* 17.7 (2015), pp. 4909–4918. DOI: 10.1039/c4cp04838e (cit. on pp. 25, 29).

[82]Jinxian Feng and Hui Pan. “Electronic state optimization for electrochemical N 2 reduction reaction in aqueous solution”. In: *Journal of Materials Chemistry A* 8.28 (2020), pp. 13896–13915. DOI: 10.1039/D0TA04709K (cit. on pp. 26, 27).

[83]Yuchi Wan, Jichu Xu, and Ruitao Lv. “Heterogeneous electrocatalysts design for nitrogen reduction reaction under ambient conditions”. In: *Materials Today* 27 (2019), pp. 69–90. DOI: 10.1016/j.mattod.2019.03.002 (cit. on p. 26).

[84]Hongjie Yu, Ziqiang Wang, Shuli Yin, Chunjie Li, You Xu, Xiaonian Li, Liang Wang, and Hongjing Wang. “Mesoporous Au3Pd Film on Ni Foam: A Self-Supported Electrocatalyst for Efficient Synthesis of Ammonia”. In: *ACS applied materials & interfaces* 12.1 (2020), pp. 436–442. DOI: 10.1021/acsami.9b14187 (cit. on p. 27).

[85]Yu-Chen Hao, Yu Guo, Li-Wei Chen, Miao Shu, Xin-Yu Wang, Tong-An Bu, Wen-Yan Gao, Nan Zhang, Xin Su, Xiao Feng, Jun-Wen Zhou, Bo Wang, Chang-Wen Hu, An-Xiang Yin, Rui Si, Ya-Wen Zhang, and Chun-Hua Yan. “Promoting nitrogen electroreduction to ammonia with bismuth nanocrystals and potassium cations in water”. In: *Nature Catalysis* 2.5 (2019), pp. 448–456. DOI: 10.1038/s41929-019-0241-7 (cit. on pp. 27, 33).

[86]Mohammadreza Nazemi, Sajanlal R. Panikkanvalappil, and Mostafa A. El-Sayed. “Enhancing the rate of electrochemical nitrogen reduction reaction for ammonia synthesis under ambient conditions using hollow gold nanocages”. In: *Nano Energy* 49 (2018), pp. 316–323. DOI: 10.1016/j.nanoen.2018.04.039 (cit. on p. 28).

[87]Si-Jia Li, Di Bao, Miao-Miao Shi, Ba-Ri Wulan, Jun-Min Yan, and Qing Jiang. “Amorphizing of Au Nanoparticles by CeOx -RGO Hybrid Support towards Highly Efficient Electrocatalyst for N2 Reduction under Ambient Conditions”. In: *Advanced Materials* 29.33 (2017). DOI: 10.1002/adma.201700001 (cit. on p. 28).

[88]Robert Schlögl. “Catalytic synthesis of ammonia-a "never-ending story"?” In: *Angewandte Chemie (International ed. in English)* 42.18 (2003), pp. 2004–2008. DOI: 10.1002/anie.200301553 (cit. on p. 28).

[89]Canyu Hu, Xing Chen, Jianbo Jin, Yong Han, Shuangming Chen, Huanxin Ju, Jun Cai, Yunrui Qiu, Chao Gao, Chengming Wang, Zeming Qi, Ran Long, Li Song, Zhi Liu, and Yujie Xiong. “Surface Plasmon Enabling Nitrogen Fixation in Pure Water through a Dissociative Mechanism under Mild Conditions”. In: *Journal of the American Chemical Society* 141.19 (2019), pp. 7807–7814. DOI: 10.1021/jacs.9b01375 (cit. on p. 29).

[90]Wu Tong, Bolong Huang, Pengtang Wang, Leigang Li, Qi Shao, and Xiaoqing Huang. “Crystal-Phase-Engineered PdCu Electrocatalyst for Enhanced Ammonia Synthesis”. In: *Angewandte Chemie International Edition* 59.7 (2020), pp. 2649–2653. DOI: 10.1002/anie.201913122 (cit. on p. 29).

[91]Jaime A. Pool, Emil Lobkovsky, and Paul J. Chirik. “Hydrogenation and cleavage of dinitrogen to ammonia with a zirconium complex”. In: *Nature* 427.6974 (2004), pp. 527–530. DOI: 10.1038/nature02274 (cit. on p. 29).

[92]Runbo Zhao, Hongtao Xie, Le Chang, Xiaoxue Zhang, Xiaojuan Zhu, Xin Tong, Ting Wang, Yonglan Luo, Peipei Wei, Zhiming Wang, and Xuping Sun. "Recent progress in the electrochemical ammonia synthesis under ambient conditions". In: *EnergyChem* 1.2 (2019), p. 100011. DOI: 10.1016/j.enchem.2019.100011 (cit. on p. 29).

[93]Changhyeok Choi, Seoin Back, Na-Young Kim, Juhyung Lim, Yong-Hyun Kim, and Yousung Jung. "Suppression of Hydrogen Evolution Reaction in Electrochemical N 2 Reduction Using Single-Atom Catalysts: A Computational Guideline". In: *ACS Catalysis* 8.8 (2018), pp. 7517–7525. DOI: 10.1021/acscatal.8b00905 (cit. on p. 29).

[94]Dan Zhang, Huan Zhao, Xueke Wu, Ying Deng, Zuochao Wang, Yi Han, Hongdong Li, Yue Shi, Xilei Chen, Shaoxiang Li, Jianping Lai, Bolong Huang, and Lei Wang. "Multi–Site Electrocatalysts Boost pH–Universal Nitrogen Reduction by High–Entropy Alloys". In: *Advanced Functional Materials* 31.9 (2021), p. 2006939. DOI: 10.1002/adfm.202006939 (cit. on pp. 29, 30).

[95]Rafael B. Araujo, Ilknur Bayrak Pehlivan, and Tomas Edvinsson. "High-entropy alloy catalysts: Fundamental aspects, promises towards electrochemical NH3 production, and lessons to learn from deep neural networks". In: *Nano Energy* 105 (2023), p. 108027. DOI: 10.1016/j.nanoen.2022.108027 (cit. on p. 30).

[96]Jia Wang, Silong Chen, Zijian Li, Guangkai Li, and Xien Liu. "Recent Advances in Electrochemical Synthesis of Ammonia through Nitrogen Reduction under Ambient Conditions". In: *ChemElectroChem* 7.5 (2020), pp. 1067–1079. DOI: 10.1002/celc.201901967 (cit. on pp. 30, 31).

[97]Rui Quan Liu and Gao Chao Xu. "Comparison of Electrochemical Synthesis of Ammonia by Using Sulfonated Polysulfone and Nafion Membrane with Sm 1.5 Sr 0.5 NiO 4". In: *Chinese Journal of Chemistry* 28.2 (2010), pp. 139–142. DOI: 10.1002/cjoc.201090044 (cit. on p. 31).

[98]Rong Lan, John T. S. Irvine, and Shanwen Tao. "Synthesis of ammonia directly from air and water at ambient temperature and pressure". In: *Scientific reports* 3 (2013), p. 1145. DOI: 10.1038/srep01145 (cit. on pp. 31, 135).

[99]Hui-Min Liu, Shu-He Han, Yue Zhao, Ying-Ying Zhu, Xin-Long Tian, Jing-Hui Zeng, Jia-Xing Jiang, Bao Yu Xia, and Yu Chen. "Surfactant-free atomically ultrathin rhodium nanosheet nanoassemblies for efficient nitrogen electroreduction". In: *Journal of Materials Chemistry A* 6.7 (2018), pp. 3211–3217. DOI: 10.1039/C7TA10866D (cit. on p. 31).

[100]Kurt Kugler, Mareike Luhn, Jean André Schramm, Khosrow Rahimi, and Matthias Wessling. "Galvanic deposition of Rh and Ru on randomly structured Ti felts for the electrochemical NH3 synthesis". In: *Physical chemistry chemical physics : PCCP* 17.5 (2015), pp. 3768–3782. DOI: 10.1039/c4cp05501b (cit. on p. 31).

[101]Gao–Feng Chen, Shiyu Ren, Lili Zhang, Hui Cheng, Yaru Luo, Kehan Zhu, Liang–Xin Ding, and Haihui Wang. "Advances in Electrocatalytic N 2 Reduction—Strategies to Tackle the Selectivity Challenge". In: *Small Methods* 3.6 (2019), p. 1800337. DOI: 10.1002/smtd.201800337 (cit. on pp. 33, 35, 38, 109).

[102]Shreya Mukherjee, David A. Cullen, Stavros Karakalos, Kexi Liu, Hao Zhang, Shuai Zhao, Hui Xu, Karren L. More, Guofeng Wang, and Gang Wu. "Metal-organic framework-derived nitrogen-doped highly disordered carbon for electrochemical ammonia synthesis using N2 and H2O in alkaline electrolytes". In: *Nano Energy* 48 (2018), pp. 217–226. DOI: 10.1016/j.nanoen.2018.03.059 (cit. on p. 33).

[103]Marco Dunwell, Wesley Luc, Yushan Yan, Feng Jiao, and Bingjun Xu. "Understanding Surface-Mediated Electrochemical Reactions: CO 2 Reduction and Beyond". In: *ACS Catalysis* 8.9 (2018), pp. 8121–8129. DOI: 10.1021/acscatal.8b02181 (cit. on p. 33).

[104]Yang Song, Daniel Johnson, Rui Peng, Dale K. Hensley, Peter V. Bonnesen, Liangbo Liang, Jingsong Huang, Fengchang Yang, Fei Zhang, Rui Qiao, Arthur P. Baddorf, Timothy J. Tschaplinski, Nancy L. Engle, Marta C. Hatzell, Zili Wu, David A. Cullen, Harry M. Meyer, Bobby G. Sumpter, and Adam J. Rondinone. "A physical catalyst for the electrolysis of nitrogen to ammonia". In: *Science advances* 4.4 (2018), e1700336. DOI: 10.1126/sciadv.1700336 (cit. on p. 33).

[105]Hiroshi Ito, Tetsuhiko Maeda, Akihiro Nakano, and Hiroyasu Takenaka. "Properties of Nafion membranes under PEM water electrolysis conditions". In: *International Journal of Hydrogen Energy* 36.17 (2011), pp. 10527–10540. DOI: 10.1016/j.ijhydene.2011.05.127 (cit. on pp. 33, 80).

[106]Yunxuan Zhao, Fan Wu, Yingxuan Miao, Chao Zhou, Ning Xu, Run Shi, Li-Zhu Wu, Junwang Tang, and Tierui Zhang. "Revealing Ammonia Quantification Minefield in Photo/Electrocatalysis". In: *Angewandte Chemie (International ed. in English)* 60.40 (2021), pp. 21728–21731. DOI: 10.1002/anie.202108769 (cit. on pp. 34, 46, 47).

[107]Daoliang Li, Xianbao Xu, Zhen Li, Tan Wang, and Cong Wang. "Detection methods of ammonia nitrogen in water: A review". In: *TrAC Trends in Analytical Chemistry* 127 (2020), p. 115890. DOI: 10.1016/j.trac.2020.115890 (cit. on p. 34).

[108]WilliamH. Schlesinger and AnneE. Hartley. "A global budget for atmospheric NH3". In: *Biogeochemistry* 15.3 (1992), pp. 191–211. DOI: 10.1007/BF00002936 (cit. on pp. 35, 37).

[109]Claire Turner, Patrik Spanel, and David Smith. "A longitudinal study of ammonia, acetone and propanol in the exhaled breath of 30 subjects using selected ion flow tube mass spectrometry, SIFT-MS". In: *Physiological measurement* 27.4 (2006), pp. 321–337. DOI: 10.1088/0967-3334/27/4/001 (cit. on p. 35).

[110]Richard Dabundo, Moritz F. Lehmann, Lija Treibergs, Craig R. Tobias, Mark A. Altabet, Pia H. Moisander, and Julie Granger. "The contamination of commercial 15N2 gas stocks with 15N-labeled nitrate and ammonium and consequences for nitrogen fixation measurements". In: *PloS one* 9.10 (2014), e110335. DOI: 10.1371/journal.pone.0110335 (cit. on p. 35).

[111]Jaecheol Choi, Hoang-Long Du, Cuong Ky Nguyen, Bryan H. R. Suryanto, Alexandr N. Simonov, and Douglas R. MacFarlane. "Electroreduction of Nitrates, Nitrites, and Gaseous Nitrogen Oxides: A Potential Source of Ammonia in Dinitrogen Reduction Studies". In: *ACS Energy Letters* 5.6 (2020), pp. 2095–2097. DOI: 10.1021/acsenergylett.0c00924 (cit. on p. 35).

[112]Hoang-Long Du, Thomas R. Gengenbach, Rebecca Hodgetts, Douglas R. MacFarlane, and Alexandr N. Simonov. "Critical Assessment of the Electrocatalytic Activity of Vanadium and Niobium Nitrides toward Dinitrogen Reduction to Ammonia". In: *ACS Sustainable Chemistry & Engineering* 7.7 (2019), pp. 6839–6850. DOI: 10.1021/acssuschemeng.8b06163 (cit. on p. 36).

[113]Yifu Chen, Hengzhou Liu, Nguon Ha, Stuart Licht, Shuang Gu, and Wenzhen Li. "Revealing nitrogen-containing species in commercial catalysts used for ammonia electrosynthesis". In: *Nature Catalysis* 3.12 (2020), pp. 1055–1061. DOI: 10.1038/s41929-020-00527-4 (cit. on p. 36).

[114]Huimin Liu, Néstor Guijarro, and Jingshan Luo. "The pitfalls in electrocatalytic nitrogen reduction for ammonia synthesis". In: *Journal of Energy Chemistry* 61 (2021), pp. 149–154. DOI: 10.1016/j.jechem.2021.01.039 (cit. on pp. 36, 110, 135).

[115]Laiquan Li, Cheng Tang, Dazhi Yao, Yao Zheng, and Shi-Zhang Qiao. "Electrochemical Nitrogen Reduction: Identification and Elimination of Contamination in Electrolyte". In: *ACS Energy Letters* 4.9 (2019), pp. 2111–2116. DOI: 10.1021/acsenergylett.9b01573 (cit. on p. 36).

[116]Fatemeh Hanifpour, Arnar Sveinbjörnsson, Camila Pía Canales, Egill Skúlason, and Helga Dögg Flosadóttir. "Preparation of Nafion Membranes for Reproducible Ammonia Quantification in Nitrogen Reduction Reaction Experiments". In: *Angewandte Chemie (International ed. in English)* 59.51 (2020), pp. 22938–22942. DOI: 10.1002/anie.202007998 (cit. on pp. 36, 110, 135).

[117]Xiyang Cai, Haldrian Iriawan, Fan Yang, Liuxuan Luo, Shuiyun Shen, Yang Shao-Horn, and Junliang Zhang. "Interaction of Ammonia with Nafion and Electrolyte in Electrocatalytic Nitrogen Reduction Study". In: *The Journal of Physical Chemistry Letters* 12.29 (2021), pp. 6861–6866. DOI: 10.1021/acs.jpclett.1c01714 (cit. on pp. 36, 110, 135).

[118]Huimin Liu, Yidan Zhang, and Jingshan Luo. "The removal of inevitable NO species in catalysts and the selection of appropriate membrane for measuring electrocatalytic ammonia synthesis accurately". In: *Journal of Energy Chemistry* 49 (2020), pp. 51–58. DOI: 10.1016/j.jechem.2020.01.029 (cit. on p. 37).

[119]Helmut Günzler and Hans-Ulrich Gremlich. *IR-Spektroskopie: Eine Einführung*. 4. vollst. überarb. u. aktualis. Auflage. Weinheim: Wiley-VCH, 2012. URL: http://site.ebrary.com/lib/alltitles/Doc?id=10565114 (cit. on p. 45).

[120]Fabian Scheepers. *Quantitative Analyse der Trocknungsverläufe von Katalysatordispersionen: = Quantitative analysis of the drying process of catalyst dispersions*. Vol. Band/volume 452. Schriften des Forschungszentrums Jülich. Reihe Energie & Umwelt. Jülich: Forschungszentrum Jülich GmbH, Zentralbibliothek, Verlag, 2019 (cit. on p. 45).

[121]Peter R. Griffiths and James A. de Haseth. *Fourier transform infrared spectrometry*. 2. ed. Vol. 171. Chemical analysis. Hoboken, NJ: Wiley-Interscience, 2007. DOI: 10.1002/047010631X (cit. on p. 45).

[122]D. B. Horn and C. R. Squire. “The estimation of ammonia using the indophenol blue reaction”. In: *Clinica Chimica Acta* 14.2 (1966), pp. 185–194. DOI: 10.1016/0009-8981(66)90085-4 (cit. on p. 46).

[123]Laiquan Li, Cheng Tang, Bingquan Xia, Huanyu Jin, Yao Zheng, and Shi-Zhang Qiao. “Two-Dimensional Mosaic Bismuth Nanosheets for Highly Selective Ambient Electrocatalytic Nitrogen Reduction”. In: *ACS Catalysis* 9.4 (2019), pp. 2902–2908. DOI: 10.1021/acscatal.9b00366 (cit. on p. 46).

[124]Dong Kim Loan, Tran Hong Con, Tran Thi Hong, and Luong Thi Mai Ly. “Quick determination of ammonia ions in water environment based on thymol color creating reaction”. In: *Environmental Sciences* 1 (2013), pp. 83–92. DOI: 10.12988/es.2013.31010 (cit. on p. 46).

[125]M. S. Wilson and S. Gottesfeld. “Thin-film catalyst layers for polymer electrolyte fuel cell electrodes”. In: *Journal of Applied Electrochemistry* 22.1 (1992), pp. 1–7. DOI: 10.1007/BF01093004 (cit. on p. 52).

[126]Rachela G. Milazzo, Stefania M.S. Privitera, Silvia Scalese, Salvatore Mirabella, Corrado Bongiorno, Salvatore A. Lombardo, and Emanuele Rimini. “New insight into Pt nucleation mechanism on Si surface during galvanic displacement deposition”. In: *Journal of Physics and Chemistry of Solids* 148 (2021), p. 109722. DOI: 10.1016/j.jpcs.2020.109722 (cit. on p. 53).

[127]Rachela G. Milazzo, Stefania M.S. Privitera, Silvia Scalese, Francesca Monforte, Corrado Bongiorno, Guglielmo G. Condorelli, and Salvatore A. Lombardo. “Ultralow loading electroless deposition of IrOx on nickel foam for efficient and stable water oxidation catalysis”. In: *International Journal of Hydrogen Energy* 45.51 (2020), pp. 26583–26594. DOI: 10.1016/j.ijhydene.2020.07.049 (cit. on p. 53).

[128]Abhishek Lahiri, Giridhar Pulletikurthi, and Frank Endres. “A Review on the Electroless Deposition of Functional Materials in Ionic Liquids for Batteries and Catalysis”. In: *Frontiers in chemistry* 7 (2019), p. 85. DOI: 10.3389/fchem.2019.00085 (cit. on p. 53).

[129]Peter Kurzweil. *Angewandte Elektrochemie*. Wiesbaden: Springer Fachmedien Wiesbaden, 2020. DOI: 10.1007/978-3-658-32421-6 (cit. on pp. 55, 63).

[130]Ernesto Amores, Jesús Rodríguez, José Oviedo, and Antonio de Lucas-Consuegra. “Development of an operation strategy for hydrogen production using solar PV energy based on fluid dynamic aspects”. In: *Open Engineering* 7.1 (2017), pp. 141–152. DOI: 10.1515/eng-2017-0020 (cit. on p. 56).

[131]Carl H. Hamann. *Elektrochemie*. 4., vollst. überarb. und aktualisierte Aufl. Weinheim: Wiley-VCH, 2005 (cit. on p. 56).

[132]Bo Han, Stuart M. Steen, Jingke Mo, and Feng-Yuan Zhang. “Electrochemical performance modeling of a proton exchange membrane electrolyzer cell for hydrogen energy”. In: *International Journal of Hydrogen Energy* 40.22 (2015), pp. 7006–7016. DOI: 10.1016/j.ijhydene.2015.03.164 (cit. on p. 56).

[133]J. Eigeldinger and H. Vogt. “The bubble coverage of gas-evolving electrodes in a flowing electrolyte”. In: *Electrochimica Acta* 45.27 (2000), pp. 4449–4456. DOI: 10.1016/S0013-4686(00)00513-2 (cit. on p. 57).

[134]*Ullmann’s Encyclopedia of Industrial Chemistry*. Wiley, 2000. DOI: 10.1002/14356007 (cit. on p. 57).

[135]L.J.J. Janssen, C.W.M.P. Sillen, E. Barendrecht, and S.J.D. van Stralen. “Bubble behaviour during oxygen and hydrogen evolution at transparent electrodes in KOH solution”. In: *Electrochimica Acta* 29.5 (1984), pp. 633–642. DOI: 10.1016/0013-4686(84)87122-4 (cit. on p. 57).

[136]Xiao-Zi Yuan. *Electrochemical Impedance Spectroscopy in PEM Fuel Cells: Fundamentals and Applications*. SpringerLink Bücher. London: Springer London, 2010. DOI: 10.1007/978-1-84882-846-9 (cit. on p. 58).

[137]Dietmar Ende and Klaus–Michael Mangold. “Impedanzspektroskopie”. In: *Chemie in unserer Zeit* 27.3 (1993), pp. 134–140. DOI: 10.1002/ciuz.19930270305 (cit. on p. 58).

[138]Christoph Rakousky. “Langzeitstabilität der Polymerelektrolyt-Wasserelektrolyse bei reduziertem Iridiumgehalt”. Dissertation. Jülich: RWTH Aachen University, 2016. URL: https://publications.rwth-aachen.de/record/667188 (cit. on p. 58).

[139]Vadim F. Lvovich. *Impedance spectroscopy: Applications to electrochemical and dielectric phenomena*. Hoboken, N.J: Wiley, 2012. DOI: 10.1002/9781118164075 (cit. on p. 59).

[140]H. Nyquist. “Regeneration Theory”. In: *Bell System Technical Journal* 11.1 (1932), pp. 126–147. DOI: 10.1002/j.1538-7305.1932.tb02344.x (cit. on p. 59).

[141]H. W. Bode. “Relations Between Attenuation and Phase in Feedback Amplifier Design”. In: *Bell System Technical Journal* 19.3 (1940), pp. 421–454. DOI: 10.1002/j.1538-7305.1940.tb00839.x (cit. on p. 59).

[142]Choi Woosung,Shin Heon-Cheol,Kim Ji Man,Choi Jae-Young,Yoon Won-Sub. “Modeling and Applications of Electrochemical Impedance Spectroscopy (EIS) for Lithium-ion Batteries”. In: *J. Electrochem. Sci. Technol* 11.1 (2020), pp. 1–13. DOI: 10.33961/jecst.2019.00528 (cit. on p. 59).

[143]*Tabellensammlung Chemie/ Enthalpie und Bindungsenergie – Wikibooks, Sammlung freier Lehr-, Sach- und Fachbücher*. 2023. URL: https://de.wikibooks.org/wiki/Tabellensammlung_Chemie/_Enthalpie_und_Bindungsenergie (visited on Nov. 17, 2023) (cit. on p. 62).

[144]Collin Smith, Alfred K. Hill, and Laura Torrente-Murciano. “Current and future role of Haber–Bosch ammonia in a carbon-free energy landscape”. In: *Energy & Environmental Science* 13.2 (2020), pp. 331–344. DOI: 10.1039/C9EE02873K (cit. on pp. 64, 69, 70).

[145]Peter W. Atkins, Julio de Paula, and James J. Keeler. *Atkins’ physical chemistry*. Twelfth edition. Oxford: Oxford University Press, 2023 (cit. on p. 66).

[146]Detlef Stolten and Bernd Emonts, eds. *Hydrogen science and engineering: Materials, processes, systems and technology*. Weinheim: Wiley-VCH Verlag GmbH & Co. KGaA, 2016 (cit. on pp. 69, 70).

[147]T. Katan and A. B. Campa. “Vapor Pressure of Ammonia in Aqueous Potassium Hydroxide Solutions”. In: *Journal of Chemical & Engineering Data* 8.4 (1963), pp. 574–575. DOI: 10.1021/je60019a031 (cit. on p. 74).

[148]Marcelo Carmo, David L. Fritz, Jürgen Mergel, and Detlef Stolten. “A comprehensive review on PEM water electrolysis”. In: *International Journal of Hydrogen Energy* 38.12 (2013), pp. 4901–4934. DOI: 10.1016/j.ijhydene.2013.01.151 (cit. on pp. 79–81, 147).

[149]Dominik Sachse. “Hydrogen-Crossover of Ion-Conducting Membranes for Water Electrolysis”. In: (2021) (cit. on p. 80).

[150]Kenneth A. Mauritz and Robert B. Moore. “State of understanding of nafion”. In: *Chemical reviews* 104.10 (2004), pp. 4535–4585. DOI: 10.1021/cr0207123 (cit. on p. 80).

[151]Pyoungho Choi, Nikhil H. Jalani, and Ravindra Datta. “Thermodynamics and Proton Transport in Nafion”. In: *Journal of The Electrochemical Society* 152.3 (2005), E123. DOI: 10.1149/1.1859814 (cit. on p. 80).

[152]Thomas A. Zawodzinski, Charles Derouin, Susan Radzinski, Ruth J. Sherman, T. van Smith, Thomas E. Springer, and Shimshon Gottesfeld. “Water Uptake by and Transport Through Nafion® 117 Membranes”. In: *Journal of The Electrochemical Society* 140.4 (1993), pp. 1041–1047. DOI: 10.1149/1.2056194 (cit. on p. 80).

[153]E. Slavcheva, I. Radev, S. Bliznakov, G. Topalov, P. Andreev, and E. Budevski. “Sputtered iridium oxide films as electrocatalysts for water splitting via PEM electrolysis”. In: *Electrochimica Acta* 52.12 (2007), pp. 3889–3894. DOI: 10.1016/j.electacta.2006.11.005 (cit. on pp. 80, 88, 90).

[154]Apichai Therdthianwong, Phochan Manomayidthikarn, and Supaporn Therdthianwong. “Investigation of membrane electrode assembly (MEA) hot-pressing parameters for proton exchange membrane fuel cell”. In: *Energy* 32.12 (2007), pp. 2401–2411. DOI: 10.1016/j.energy.2007.07.005 (cit. on pp. 80, 88, 90, 91).

[155]Géraldine Merle, Matthias Wessling, and Kitty Nijmeijer. “Anion exchange membranes for alkaline fuel cells: A review”. In: *Journal of Membrane Science* 377.1-2 (2011), pp. 1–35. DOI: 10.1016/j.memsci.2011.04.043 (cit. on p. 81).

[156]Kimberly F. L. Hagesteijn, Shanxue Jiang, and Bradley P. Ladewig. “A review of the synthesis and characterization of anion exchange membranes”. In: *Journal of Materials Science* 53.16 (2018), pp. 11131–11150. DOI: 10.1007/s10853-018-2409-y (cit. on pp. 81, 82).

[157]S. Siracusano, N. van Dijk, E. Payne-Johnson, V. Baglio, and A. S. Aricò. “Nano-sized IrOx and IrRuOx electrocatalysts for the O2 evolution reaction in PEM water electrolysers”. In: *Applied Catalysis B: Environmental* 164 (2015), pp. 488–495. DOI: 10.1016/j.apcatb.2014.09.005 (cit. on p. 81).

[158]Dirk Henkensmeier, Malikah Najibah, Corinna Harms, and Žitka, Jan and Hnát, Jaromír and Bouzek, Karel. “Overview: State-of-the Art Commercial Membranes for Anion Exchange Membrane Water Electrolysis”. In: *Journal of Electrochemical Energy Conversion and Storage* 18.2 (2021). DOI: 10.1115/1.4047963 (cit. on p. 82).

[159]Shuang Gu, Rui Cai, Ting Luo, Kurt Jensen, Christian Contreras, and Yushan Yan. "Quaternary phosphonium-based polymers as hydroxide exchange membranes". In: *ChemSusChem* 3.5 (2010), pp. 555–558. DOI: 10.1002/cssc.201000074 (cit. on p. 82).

[160]S. Giddey, F. T. Ciacchi, and S.P.S. Badwal. "High purity oxygen production with a polymer electrolyte membrane electrolyser". In: *Journal of Membrane Science* 346.1 (2010), pp. 227–232. DOI: 10.1016/j.memsci.2009.09.042 (cit. on pp. 83, 88).

[161]Energy.gov. *Fuel Cells*. 2023. URL: https://www.energy.gov/eere/fuelcells/fuel-cells (visited on Sept. 3, 2023) (cit. on p. 83).

[162]Chen Zhang, Shuzhuang Sun, Su He, and Chunfei Wu. "Direct air capture of CO2 by KOH-activated bamboo biochar". In: *Journal of the Energy Institute* 105 (2022), pp. 399–405. DOI: 10.1016/j.joei.2022.10.017 (cit. on p. 83).

[163]A.R Smith and J. Klosek. "A review of air separation technologies and their integration with energy conversion processes". In: *Fuel Processing Technology* 70.2 (2001), pp. 115–134. DOI: 10.1016/s0378-3820(01)00131-x (cit. on p. 83).

[164]*Air-separation-plants-history-and-technological-progress-2019_tcm19-457349*. URL: https://www.linde-engineering.com/en/images/Air-separation-plants-history-and-technological-progress-2019_tcm19-457349.pdf (visited on Mar. 26, 2024) (cit. on p. 83).

[165]J. Rizk, M. Nemer, and D. Clodic. "A real column design exergy optimization of a cryogenic air separation unit". In: *Energy* 37.1 (2012), pp. 417–429. DOI: 10.1016/j.energy.2011.11.012 (cit. on p. 83).

[166]A. Schulte-Schulze-Berndt and K. Krabiell. "Nitrogen generation by pressure swing adsorption based on carbon molecular sieves". In: *Gas Separation & Purification* 7.4 (1993), pp. 253–257. DOI: 10.1016/0950-4214(93)80026-S (cit. on pp. 83, 84).

[167]Onsite Gas. *Pressure Swing Adsorption Technology| On Site Gas*. 2016. URL: https://www.onsitegas.com/blog/pressure-swing-adsorption-technology/ (visited on Sept. 25, 2023) (cit. on p. 84).

[168]Rafael Kuwertz, Carina Kirstein, Thomas Turek, and Ulrich Kunz. "Influence of acid pretreatment on ionic conductivity of Nafion® membranes". In: *Journal of Membrane Science* 500 (2016), pp. 225–235. DOI: 10.1016/j.memsci.2015.11.022 (cit. on p. 85).

[169]V. Schröder, B. Emonts, H. Janßen, and H.-P. Schulze. "Explosion Limits of Hydrogen/Oxygen Mixtures at Initial Pressures up to 200 bar". In: *Chemical Engineering & Technology* 27.8 (2004), pp. 847–851. DOI: 10.1002/ceat.200403174 (cit. on p. 87).

[170]Brenda Johnston, Michael C. Mayo, and Anshuman Khare. "Hydrogen: the energy source for the 21st century". In: *Technovation* 25.6 (2005), pp. 569–585. DOI: 10.1016/j.technovation.2003.11.005 (cit. on p. 87).

[171]K. C. Sandeep, Rupsha Bhattacharyya, Chandrashekhar Warghat, Kalyan Bhanja, and Sadhana Mohan. "Experimental investigation on the kinetics of catalytic recombination of hydrogen with oxygen in air". In: *International Journal of Hydrogen Energy* 39.31 (2014), pp. 17906–17912. DOI: 10.1016/j.ijhydene.2014.08.148 (cit. on p. 87).

[172] *Milliarden für überflüssigen Solarstrom – Neue Forderung: Wer einspeist, muss zahlen.* 2024. URL: https://www.fr.de/wirtschaft/milliarden-fuer-ueberfluessigen-solarstrom-neue-forderung-wer-einspeist-muss-zahlen-zr-93256838.html (visited on Nov. 20, 2024) (cit. on p. 87).

[173] S. Shiva Kumar and V. Himabindu. "Hydrogen production by PEM water electrolysis – A review". In: *Materials Science for Energy Technologies* 2.3 (2019), pp. 442–454. DOI: 10.1016/j.mset.2019.03.002 (cit. on p. 88).

[174] S. Litster and G. McLean. "PEM fuel cell electrodes". In: *Journal of Power Sources* 130.1-2 (2004), pp. 61–76. DOI: 10.1016/j.jpowsour.2003.12.055 (cit. on p. 88).

[175] Elizabeth Kay Berner and Robert A. Berner. *Global Environment: Water, Air, and Geochemical Cycles - Second Edition.* 2nd ed. Princeton, NJ: Princeton University Press, 2012. DOI: 10.1515/9781400842766?locatt=mode:legacy (cit. on p. 89).

[176] David R. Lide, ed. *CRC handbook of chemistry and physics: A ready-reference book of chemical and physical data.* 85. ed. Boca Raton: CRC Press, 2004 (cit. on p. 89).

[177] Q. Meyer, N. Mansor, F. Iacoviello, P. L. Cullen, R. Jervis, D. Finegan, C. Tan, J. Bailey, P. R. Shearing, and D.J.L. Brett. "Investigation of Hot Pressed Polymer Electrolyte Fuel Cell Assemblies via X-ray Computed Tomography". In: *Electrochimica Acta* 242 (2017), pp. 125–136. DOI: 10.1016/j.electacta.2017.05.028 (cit. on p. 90).

[178] Hui Li, Yanghua Tang, Zhenwei Wang, Zheng Shi, Shaohong Wu, Datong Song, Jianlu Zhang, Khalid Fatih, Jiujun Zhang, Haijiang Wang, Zhongsheng Liu, Rami Abouatallah, and Antonio Mazza. "A review of water flooding issues in the proton exchange membrane fuel cell". In: *Journal of Power Sources* 178.1 (2008), pp. 103–117. DOI: 10.1016/j.jpowsour.2007.12.068 (cit. on p. 94).

[179] Mikaela Görlin, Petko Chernev, Jorge Ferreira de Araújo, Tobias Reier, Sören Dresp, Benjamin Paul, Ralph Krähnert, Holger Dau, and Peter Strasser. "Oxygen Evolution Reaction Dynamics, Faradaic Charge Efficiency, and the Active Metal Redox States of Ni-Fe Oxide Water Splitting Electrocatalysts". In: *Journal of the American Chemical Society* 138.17 (2016), pp. 5603–5614. DOI: 10.1021/jacs.6b00332 (cit. on p. 105).

[180] Rafael B. Araujo and Tomas Edvinsson. "Supervised AI and Deep Neural Networks to Evaluate High-Entropy Alloys as Reduction Catalysts in Aqueous Environments". In: *ACS Catalysis* (2024), pp. 3742–3755. DOI: 10.1021/acscatal.3c05017 (cit. on pp. 126, 161).

[181] Sudesh Kumari, Sahar Pishgar, Marcus E. Schwarting, William F. Paxton, and Joshua M. Spurgeon. "Synergistic plasma-assisted electrochemical reduction of nitrogen to ammonia". In: *Chemical communications (Cambridge, England)* 54.95 (2018), pp. 13347–13350. DOI: 10.1039/c8cc07869f (cit. on p. 135).

[182] Shiming Chen, Siglinda Perathoner, Claudio Ampelli, Chalachew Mebrahtu, Dangsheng Su, and Gabriele Centi. "Electrocatalytic Synthesis of Ammonia at Room Temperature and Atmospheric Pressure from Water and Nitrogen on a Carbon-Nanotube-Based Electrocatalyst". In: *Angewandte Chemie (International ed. in English)* 56.10 (2017), pp. 2699–2703. DOI: 10.1002/anie.201609533 (cit. on p. 135).

[183]Kitiya Hongsirikarn, James G. Goodwin, Scott Greenway, and Stephen Creager. "Influence of ammonia on the conductivity of Nafion membranes". In: *Journal of Power Sources* 195.1 (2010), pp. 30–38. DOI: 10.1016/j.jpowsour.2009.07.013 (cit. on p. 135).

[184]Nikhil H. Jalani and Ravindra Datta. "The effect of equivalent weight, temperature, cationic forms, sorbates, and nanoinorganic additives on the sorption behavior of Nafion®". In: *Journal of Membrane Science* 264.1-2 (2005), pp. 167–175. DOI: 10.1016/j.memsci.2005.04.047 (cit. on p. 136).

[185]Rune Halseid, Preben J. S. Vie, and Reidar Tunold. "Influence of Ammonium on Conductivity and Water Content of Nafion 117 Membranes". In: *Journal of The Electrochemical Society* 151.3 (2004), A381. DOI: 10.1149/1.1641035 (cit. on p. 139).

[186]David R. Morris and Xiaodong Sun. "Water–sorption and transport properties of Nafion 117 H". In: *Journal of Applied Polymer Science* 50.8 (1993), pp. 1445–1452. DOI: 10.1002/app.1993.070500816 (cit. on p. 139).

[187]Umweltbundesamt. *Review of internationally proposed critical levels for ammonia.* 2024. URL: https://www.umweltbundesamt.de/en/publikationen/review-of-internationally-proposed-critical-levels (visited on Mar. 26, 2024) (cit. on p. 163).

[188]Jianyin Huang, Nadeeka Rathnayake Kankanamge, Christopher Chow, David T. Welsh, Tianling Li, and Peter R. Teasdale. "Removing ammonium from water and wastewater using cost-effective adsorbents: A review". In: *Journal of environmental sciences (China)* 63 (2018), pp. 174–197. DOI: 10.1016/j.jes.2017.09.009 (cit. on pp. 163, 164).

[189]Tom Augspurger, Anne E. Keller, Marsha C. Black, W. Gregory Cope, and F. James Dwyer. "Water quality guidance for protection of freshwater mussels (Unionidae) from ammonia exposure". In: *Environmental toxicology and chemistry* 22.11 (2003), pp. 2569–2575. DOI: 10.1897/02-339 (cit. on p. 163).

[190]M. A. Sutton, C.E.R. Pitcairn, and D. Fowler. "The Exchange of Ammonia Between the Atmosphere and Plant Communities". In: *Advances in Ecological Research*. Ed. by M. Begon and A. H. Fitter. Vol. 24. Academic Press, 1993, pp. 301–393. DOI: 10.1016/S0065-2504(08)60045-8 (cit. on p. 163).

[191]A. Fangmeier, A. Hadwiger-Fangmeier, L. van der Eerden, and H. J. Jäger. "Effects of atmospheric ammonia on vegetation–a review". In: *Environmental pollution (Barking, Essex : 1987)* 86.1 (1994), pp. 43–82. DOI: 10.1016/0269-7491(94)90008-6 (cit. on p. 163).

[192]Amit Bhatnagar and Mika Sillanpää. "A review of emerging adsorbents for nitrate removal from water". In: *Chemical Engineering Journal* 168.2 (2011), pp. 493–504. DOI: 10.1016/j.cej.2011.01.103 (cit. on p. 163).

[193]V.H. Smith, G.D. Tilman, and J.C. Nekola. "Eutrophication: impacts of excess nutrient inputs on freshwater, marine, and terrestrial ecosystems". In: *Environmental pollution (Barking, Essex : 1987)* 100.1 (1999), pp. 179–196. DOI: 10.1016/S0269-7491(99)00091-3 (cit. on p. 163).

[194]Abwasser Analysezentrum. *Ammonium-Stickstoff*. 2024. URL: https://www.abwasser-analysezentrum.de/parameteruebersicht/ammonium-stickstoff (visited on Mar. 12, 2024) (cit. on p. 163).

[195]M. Maurer, P. Schwegler, and T. A. Larsen. "Nutrients in urine: energetic aspects of removal and recovery". In: *Water Science and Technology* 48.1 (2003), pp. 37–46. DOI: 10.2166/wst.2003.0011 (cit. on p. 163).

[196]Perry L. McCarty, Jaeho Bae, and Jeonghwan Kim. "Domestic wastewater treatment as a net energy producer–can this be achieved?" In: *Environmental science & technology* 45.17 (2011), pp. 7100–7106. DOI: 10.1021/es2014264 (cit. on p. 163).

[197]G. Tchobanoglous, H. Stensel, R. Tsuchihashi, and F. Burton. *Wastewater engineering: Treatment and resource recovery*. Fifth Edition. McGraw-Hill Education, 2014. URL: https://ebookcentral.proquest.com/lib/kxp/detail.action?docID=5662641 (cit. on p. 163).

[198]Dianxun Hou, Arpita Iddya, Xi Chen, Mengyuan Wang, Wenli Zhang, Yifu Ding, David Jassby, and Zhiyong Jason Ren. "Nickel-Based Membrane Electrodes Enable High-Rate Electrochemical Ammonia Recovery". In: *Environmental science & technology* 52.15 (2018), pp. 8930–8938. DOI: 10.1021/acs.est.8b01349 (cit. on pp. 163, 164).

[199]Mustafa Turan. "Application of Nanoporous Zeolites for the Removal of Ammonium from Wastewaters: A Review". In: *Low-Dimensional and Nanostructured Materials and Devices*. Ed. by Hilmi Ünlü, Norman J. M. Horing, and Jaroslaw Dabowski. NanoScience and Technology Ser. Cham: Springer International Publishing, 2015, pp. 477–504. DOI: 10.1007/978-3-319-25340-4 (cit. on p. 164).

[200]Wouter Pronk, Martin Biebow, and Markus Boller. "Electrodialysis for recovering salts from a urine solution containing micropollutants". In: *Environmental science & technology* 40.7 (2006), pp. 2414–2420. DOI: 10.1021/es051921i (cit. on p. 164).

[201]S. Georg, A. T. Puari, M.P.G. Hanantyo, T. Sleutels, P. Kuntke, A. ter Heijne, and C.J.N. Buisman. "Low-energy ammonium recovery by a combined bio-electrochemical and electrochemical system". In: *Chemical Engineering Journal* 454 (2023), p. 140196. DOI: 10.1016/j.cej.2022.140196 (cit. on p. 164).

[202]Stephan Wasielewski. *Ammoniumrückgewinnung aus Schlammwasser mittels Ionenaustausch an Klinoptilolith*. URL: https://elib.uni-stuttgart.de/bitstream/11682/11481/3/Wasielewski_Ammoniumr%c3%bcckgewinnung%20aus%20Schlammwasser.pdf (visited on Mar. 12, 2024) (cit. on p. 164).

[203]Mehmet Uğurlu and M. Hamdi Karaoğlu. "Adsorption of ammonium from an aqueous solution by fly ash and sepiolite: Isotherm, kinetic and thermodynamic analysis". In: *Microporous and Mesoporous Materials* 139.1 (2011), pp. 173–178. DOI: 10.1016/j.micromeso.2010.10.039 (cit. on p. 164).

[204]Philipp Kuntke, Mariana Rodrigues, Tom Sleutels, Michel Saakes, Hubertus V. M. Hamelers, and Cees J. N. Buisman. "Energy-Efficient Ammonia Recovery in an Up-Scaled Hydrogen Gas Recycling Electrochemical System". In: *ACS sustainable chemistry & engineering* 6.6 (2018), pp. 7638–7644. DOI: 10.1021/acssuschemeng.8b00457 (cit. on p. 164).

[205]Chang Liu, Klaus Wippermann, Marcin Rasinski, Yanpeng Suo, Meital Shviro, Marcelo Carmo, and Werner Lehnert. "Constructing a Multifunctional Interface between Membrane and Porous Transport Layer for Water Electrolyzers". In: *ACS applied materials & interfaces* 13.14 (2021), pp. 16182–16196. DOI: 10.1021/acsami.0c20690 (cit. on p. 164).

[206]Bundesamt für Verbraucherschutz. *Abwasserverordnung*. URL: https://www.gesetze-im-internet.de/abwv/AbwV.pdf (visited on Mar. 12, 2024) (cit. on p. 164).

[207]P. Kuntke, T. H. J. A. Sleutels, M. Rodríguez Arredondo, S. Georg, S. G. Barbosa, A. ter Heijne, Hubertus V. M. Hamelers, and C. J. N. Buisman. "(Bio)electrochemical ammonia recovery: progress and perspectives". In: *Applied microbiology and biotechnology* 102.9 (2018), pp. 3865–3878. DOI: 10.1007/s00253-018-8888-6 (cit. on pp. 164, 190).

[208]William A. Tarpeh, James M. Barazesh, Tzahi Y. Cath, and Kara L. Nelson. "Electrochemical Stripping to Recover Nitrogen from Source-Separated Urine". In: *Environmental science & technology* 52.3 (2018), pp. 1453–1460. DOI: 10.1021/acs.est.7b05488 (cit. on p. 164).

[209]Landwirtschaftskammer Nordrhein-Westfalen. *Stickstoffdüngemittel*. URL: https://www.landwirtschaftskammer.de/landwirtschaft/ackerbau/pdf/n-duengemittel-pdf.pdf (visited on Feb. 29, 2024) (cit. on p. 167).

List of Figures

1.1 Schematic illustration of nitrogen compounds synthesized from NH_3 and their respective field of application involving, fertilizers, rocket fuel, dyes and synthetic materials. 2

1.2 Schematic illustration of the conventional and new NH_3 field of application. 3

1.3 Transportation cost of the energy carriers NH_3, liquid H_2, and compressed H_2 for a distance of 1 km and a weight of 1 t. The different transportation possibilities cargo ships, railway, road trailers are compared. Adapted and based on [18]. Found in [17]. 4

1.4 Illustration of the process steps of the Haber-Bosch process, the industrial synthetic NH_3 production. Starting with the production of the synthesis mixture until the production of NH_3 in the blue reactor. . . 8

1.5 Illustration of photo-driven ammonia production systems, (a) the photochemical system is based on semiconductor nanoparticle catalysts dispersed in aqueous solution, (b) different types of photoelectrochemical nitrogen fixation systems. Adapted with permission from [29], Springer Nature. 12

1.6 Different electrochemical NH_3 synthesis systems with respect to different electrolytes and temperature ranges. Adapted with permission from [40], Elsevier. 13

1.7 Illustration of the necessary steps of the Li mediated eNRR. Li^+ are dissociated in the electrolyte. Under an electrical potential Li is deposited. Li dissociates N_2 to produce Li_3N. Under supply of a H^+-source and e^--transport NH_3 is formed. Own illustration based on the illustration of [47]. 15

1.8 Nafion structural formula. Nafion consist of a non-polar and polar part. The sulphit ion is incorporated into the chemical structure of Nafion. The attached H^+ ensure charge neutrality in the membrane. Adapted with permission from [62], American Chemical Society. 18

1.9 Schematic illustration of the microstructure of Nafion. The sulphit ions (SO_4^{2-}) are bound to $[CF_2]_n$, resulting in SO_3^-. SO_3^- is firmly bound within the membrane. The protons (white circles) are mobile and can be exchanged with other cations within the membrane. 18

2.1 The different reaction mechanisms on heterogeneous catalysts of the NH_3 synthesis. (a) Dissociative mechanism, where the triple bond of nitrogen is broken before hydrogenation. (b) Alternating mechanism, the N atoms of N_2 are alternately hydrogenated. (c) Distal pathway, the N atom removed from the adsorption site is first sequentially hydrogenated. (d) Enzymatic pathway, the adsorption of N_2 onto the surface of the catalyst results in a side-on mode instead of the end-on mode. Adapted with permission from [79], American Chemical Society. 24

2.2 Illustration of the activation and deactivation of the catalytic reaction pathway for the NRR via Mars-van Krevelen mechanism. Adapted with permission from [58], American Chemical Society. 25

2.3 The number of publications based on ambient eNRR during 2016 and 2019. Adapted with permission from [6], Royal Society of Chemistry. . 26

2.4 Volcano diagrams evaluating the onset potential (U) on metal surfaces for the reduction of N_2. The solid lines illustrates the dissociative mechanisms, and the dashed lines the associative. A catalyst reaction on a flat surface area is indicated in blue and a stepped surface area in red. An overlap of the red and blue lines is indicated by the black line. The surfaces of catalysts, which are likely covered by adsorbed nitrogen are in the green shaded area and the ones covered by hydrogen are in the white area [67, 76]. Adapted with permission from [76], John Wiley and Sons. 28

2.5 Schematic illustration of a HEA catalyst that consists at least out of five metals. In this case, the catalyst consist of Ni, Cr, Co, Mn, Fe. . . 29

2.6 Schematic illustration of the different reactor configuration for electrochemical NRR, (a) back-to-back cell, (b) PEM-type cell, (c) H-type cell, and (d) single chamber cell. Adapted with permission from [78], John Wiley and Sons. 32

3.1 Illustration of the test bench utilizing H_2 as reactant. H_2 is supplied via a mass flow controller on the anode side. The gas is humidified with a humidifier cell. Due to the chemical reaction O_2 is produced at the anode. On the cathode side either N_2 or Ar are supplied via mass flow controllers. The gases are also humidified. The humidification is needed for the membrane. The gas streams through a cleaning trap before entering the cell. The synthesized NH_3 is determined with the indophenol method or with an IR-spectrometer. H_2 is determined with a hydrogen sensor. 40
3.2 Illustration of the test bench utilizing H_2O as reactant. H_2O is introduced on the anode side via a circulation pump. Due to the supply of H_2O humidifier cells are not required. At the anode O_2 is as well produced. On the cathode side either N_2 or Ar are supplied via mass flow controllers. The gas streams through a cleaning trap before entering the cell. The synthesized NH_3 is determined with the indophenol method or with an IR-spectrometer. H_2 is determined with a hydrogen sensor. 41
3.3 The end plate, which are made of stainless steel enables the electrical contact of the cell components and applies mechanical compression to the cell. The flow fields in the bipolar plates channels the reactants into the cell and exports the products out of the cell. The anode bipolar plate is coated in platinium and the cathode one in gold. The flat sheet sealing is PTFE, which is adapted to the thickness of the porous transport layers of the MEA. In the center of the cell is the MEA, which consist of PTLs on anode and cathode side, catalyst layers and the membrane. The catalyst layers can be coated on either the PTLs or the membrane. 44
3.4 The reaction of monochloramine with phenol. 46
3.5 The reaction to indophenol blue. 47
3.6 Indophenol blue absorbance spectrum of the calibration samples from 0.2 to 6 $\mathrm{mg\,L^{-1}}$. 48
3.7 Color change of samples. The higher the intensity of the blue color, the more NH_3 the sample contains. 48
3.8 Calibration line of the NH_3 samples of the known concentration in range from 0 to 6 $\mathrm{mg\,L^{-1}}$. The red dots are the measured absorbance of the calibration samples. 50
3.9 Schematic illustration of the spontaneous galvanic displacement deposition process. Nickel is displaced with gold particles. 54

3.10 Polarisation curves of H_2O electrolysis at 25 (red line) and 80 °C (green line). The resulting overpotentials actionvation, ohmic, and concentration are marked. The reversible cell potential of both temperatures are drawn as dashed lines with the respective color [130]. 56
3.11 Randle circuit for describing electrochemical systems. The randle cell consist of an ohmic resistance (R_Ω), which is in serial connection with a capacitor, which is connected in parallel with a resistor. The capacitor (C_{DL}) describes the electrochemical double layer and the resistance (R_{CT}) the charge transfer resistance. 59
3.12 The Nquist plot is shown on the left side and the Bode plot on the right side. They can be converted into each other [142]. 59

4.1 Simplified illustration of the Haber-Bosch process. Fossil fuels and water are used to generate H_2 in the the steam reformer. N_2 from air is enriched with PSA. The reactants, H_2 and N_2 are then introduced into the Haber-Bosch reactor. NH_3 is synthesized in the Haber-Bosch reactor. NH_3 is condensed and the reactant gases that do not react are fed back into teh reactor. Own illustration based on the illustration of [144]. 64
4.2 Gibbs energy (red line, left y-axis) and voltage (blue line, right y-axis) considering constant enthalpy and entropy in dependency of temperature. The temperature ranges in which the electrochemical NH_3 synthesis (green area) and the Haber-Bosch process (orange area) operate are highlighted. The dashed grey line indicates the change from an exothermic to an endothermic process. 65
4.3 The equilibrium constant K_x at 1 bar (red line) and 200 bar (blue line) depends on the temperature. The small graphic in this figure shows the trend of the K_x in the temperature region from 440 to 500 °C. In case of a constant pressure at 1 bar, K_x falls below 1, thus the Haber-Bosch process shifts to the reactant side The temperature ranges in which the electrochemical NH_3 synthesis (green area) and the Haber-Bosch process (orange area) operate are highlighted. 68
4.4 Schematic illustration of the electrified Haber-Bosch process. A water electrolyzer is utilized to produce H_2 from H_2O. The further part of the process is the same as the process of the Haber-Bosch process. Own illustration based on the illustration of [144]. 69

4.5 Schematic illustration of the direct electrochemical NH_3 synthesis and the movement of molecules and ions in an alkaline cell. H_2O is introduced into the PTL of the anode, where it diffuses through the membrane. N_2, which is supplied at the cathode, reacts with H_2O and the electrons to NH_3 and OH^- in the catalyst layer. This process is facilitated by the applied electrical energy. The resulting NH_3 exits the cell on the cathode side. Concurrently. OH^- diffuses through the membrane and oxidizes to O_2 and H_2O. The produced O_2 exits the cell on the anode side. The coloring of the atoms is done according to the CPK color model. 73
4.6 Pourbaix diagram for N_2 and H_2O. The red solid line represents the NRR to NH_4^+ or NH_3. The blue solid line represents the N_2 oxidation to NO_3^-. The black dotted lines denote the H_2O reduction and oxidation. 75
4.7 Graphical illustration of the energy losses that occur during the electrochemical conversion of electrical energy into NH_3 and the thermodynamic efficiency of the three NH_3 synthesis pathways. 77

5.1 Water electrolysis cells in acid and alkaline environment [149]. 80
5.2 Illustration of the pressure swing adsorption method, which is based on physical adsorption. The carbon molecular sieves adsorb O_2 at high pressure, leading to the separation of O_2 and N_2. At the same time, in the other tower vessel the previous captured O_2 desorbs by reducing the pressure to ambient pressure. The figure is taken from [167]. . . . 84
5.3 Illustration of the oxygen depletion cell with the incoming H_2O and air. Resulting in O_2 production on anode side and N_2 accumulation and O_2 depletion on cathode side. 85
5.4 The Nernst potential is plotted as a function of the O_2 concentration of the gas mixture at the cathode. 86
5.5 Illustration of the O_2 depletion test set-up. H_2O is introduced with a circulation pump on the anode side. Due to the applied electrical potential O_2 is produced and H^+ are generated. At the cathode the H^+ reacts with the incoming O_2 from air to H_2O. The produced H_2O is condensed with a water cooler and the remaining O_2 in the gas stream is measured with the O_2 sensor. Additionally, if H_2 is generated, it can be determined with the H_2 sensor. 89
5.6 Sketch of the hot pressing process. An applied pressure presses the catalyst layer onto the membrane, leading to a reduction of ohmic resistance, thus better ion conductivity. 90

5.7 (a) Remaining O_2 content (as line with dots) at the cathode outlet and current density results (as dashed line), without hot pressing the MEA, (b) remaining oxygen content and current density, with hot pressing the MEA. 91
5.8 (a) Comparison of the oxygen content of different membrane thicknesses (127 µm, red and 51 µm, blue). (b) The respective voltage-current characteristic showing that there is no clear trend. 92
5.9 (a) Comparison of the O_2 content of different active cell areas with respect to different air flow rates. (b) The respective voltage-current characteristic. The violet characteristic curves are the results of the green characteristic curves in relation to an active cell area of 6.25 cm^2, to enable an area-related comparison of both cells. 93
5.10 (a) Measured O_2 content of all trials at room temperature, (b) measured O_2 content for all trials at 80 °C, (c) measured H_2 content for all trials at room temperature, and (d) measured H_2 content for all trials at 80 °C. 96
5.11 Polarisation curves showing the effect of temperature increase and the resulting influence of degradation while applying an air flow rate of 50 mL/min at RT (blue lines) and 80 °C (orange lines). 97
5.12 FE of O_2 depletion (solid line) and H_2 evolution (dashed line) for all measurements while applying an air flow rate of 50 mL/min. 98
5.13 Polarisation curves of the MEA at different air flow rates. 99
5.14 EIS and fits, 10 mL/min 101
5.15 Electrochemical impedance spectra (dotted lines) and their respective fits (solid lines) for both air flow rates. 101
5.16 Equivalent circuits for the O_2 depletion process. Both circuits contain artefacts, which are represented through inductance. Ohmic resistances are present due to electrolyte resistance and the eletrochemical double layer in the circuits are described with the charge transfer resistance parallel to the constant phase element. Constant phase element are chosen as the semicircles are depressed. In addition, a resistor connected in parallel with a constant phase element are added to describe the incomplete low frequency semicircle. In (b) a diffusion resistance is added, because the current of the flow rates 50 and 100 mL/min is also controlled by diffusion. 102
5.17 Remaining O_2 content (line) and the resulting error (colored area) of each air flow rate. 104
5.18 Faraday efficiency of O_2 (lines with dotes) and respective error (colored area) of each air flow rate. 105

5.19 Parameters that lead to a relative O_2 depletion and N_2 enrichment on the cathode side are marked in green, those that have no influence on the O_2 content are marked in yellow and the parameter that leads to a relative increase in the O_2 content on the cathode side is marked in red in the table. The illustration of the cell shows, that the O_2 content of an air gas stream can be reduced to less than 1 % of remaining O_2, while achieving a high FE close to 100 %. 108

6.1 Schematic illustration of the different sources of contaminations. These sources of impurities are (1) impurities from the environment, (2) impurities in the anode supply, (3) impurities in the cathode supply, (4) impurities in the anode components, (5) impurities in the cathode components, and (6) impurities in the membrane. The produced NH_3 from these contaminations overlap the signal of NH_3 synthesized by NRR from N_2 (NH_3 molecule, blue line). 111

6.2 Schematic illustration of the direct electrochemical NH_3 synthesis and the movemnet of molecules and ions in an acid and neutral cell. H_2O is introduced into the GDL of the anode. In the catalyst layer it oxidizes to O_2 and H^+. The produced O_2 exits the cell on the anode side and the H^+ diffuses through the membrane. N_2 is reduced at cathode and reacts with the incoming H^+ to NH_3 in the catalyst layer. This process is facilitated by the electrical energy. The resulting NH_3 exits the cell on the cathode side. The coloring of the atoms is done according to the CPK color model. 112

6.3 SEM images of the Au particles. (a) Magnification of 1000, (b) magnification of 10.000 and (c) magnification of 100.000. 113

6.4 Illustration of the ion exchanged Nafion membrane. The H^+, which are bounded to SO_3^- are exchanged with Na^+ during the immersion of the Nafion membrane into a NaOH solution. Nafio is transferred into its Na^+-form. 114

6.5 Detected NH_3 (solid lines) and H_2O (dashed lines) in their corresponding concentration with the FTIR spectrometer. The black lines are measured during the Ar supply and the colored ones during N_2 supply. 116

6.6 Absorbance spectra of the VIS spectrometer for the different applied potentials while introducing H_2 at the anode. 117

6.7 (a) CV results of the experiments. In red and blue the results during N_2 supply and in black during Ar supply. (b) The corresponding detected NH_3 and the error bars of the first MEA cell employing KOH as electrolyte. 119

6.8 (a) CV results of the experiments. In red and blue the results during N_2 supply and in black during Ar supply. (b) The corresponding detected NH_3 and the error bars of the second MEA cell employing KOH as electrolyte. 120
6.9 Calculated rates of NH_3 production and the corresponding error bars that are determined while Ar is supplied at the specific conditions. . . 121
6.10 Calculated rates of NH_3 production and the corresponding error bars that are determined while N_2 was supplied at the specific conditions. . 122
6.11 Polarisation curves of the three samples, which were used for electrochemical NH_3 production. These three samples, three MEA cells, had identical materials and were operated under equivalent conditions. . . 124
6.12 CV results and the corresponding detected NH_3 of the trials employing Na_2SO_4 as electrolyte. In red and blue the results during N_2 supply and in black and grey during Ar supply. 125
6.13 Calculated rates of NH_3 production and the corresponding error bars that are determined while N_2 was supplied at the specific conditions. . 126
6.14 Calculated production rates of NH_3 production and the corresponding error bars that are determined while N_2 was supplied at tje specific conditions in the H-cell. 127
6.15 SEM images of the sputtered HEA on carbon felt. (a) Magnification of 16000 using an "InLens" detector, (b) magnification of 500 using an "InLens" detector and (c) magnification of 500 using an "AsB" detector. 128
6.16 CV results and the corresponding detected NH_3 employing KOH as electrolyte. In red are the results during N_2 supply and in black and grey during Ar supply. 130
6.17 Calculated rates of NH_3 production and the corresponding error bars that were determined while N_2 was supplied at the specific conditions. 131
6.18 CV results and the corresponding detected NH_3 employing Na_2SO_4 as electrolyte. In red the results during N_2 supply and in black and grey during Ar supply. 132
6.19 Calculated rates of NH_3 production and the corresponding error barsthat were determined while N_2 was supplied at the specific conditions. . . . 132

7.1 Illustration of the ion exchanged Nafion membrane. H^+, which are bounded to SO_3^- are exchanged with NH_4^+ during the immersion of the Nafion membrane into a $(NH_4)_2SO_4$ solution. Nafion is transferred into its NH_4^+-form. 137

7.2 Deviation of the ion exchange for two different ratios of NH_4^+ vs. H^+ (bright colors). The y-axis displays the quantity of NH_4^+ remaining in the solution. The average of both ratios is indicated by the red and blue bar. 139
7.3 Equilibrium constants of the different ratios of NH_4^+ vs. H^+ (red squares) and their corresponding error bars. The average value of K_{eq} is shown as the blue line. The colored area is the error of the average value. The value of the ratio 2:1 is not considered for the average value. 141
7.4 The detected and measured quantities of NH_3 are presented. In red the quantity of NH_4^+ that remained in the solution is represented and in green the initial quantity of NH_4^+ that was exchanged into the membrane. The blue bar presents the sum NH_3 that was driven out from the membrane. In total the membrane was placed three times in a fresh $(NH_4)_2SO_4$ solution, because an equilibrium of NH_3 is established between membrane and solution, thereby preventing further desorption of NH_3. These quantities are referred as first to third drag-out, depicted as the bright blue bars. 143
7.5 Schematic illustration of the exchange and desorption process of NH_4^+ within the membrane. H_2O is introduced into the PTL of the anode. In the catalyst layer it oxidizes to O_2 and H^+. The produced O_2 exits the cell on the anode side. The generated H^+ interacts with NH_4^+ within the membrane. NH_4^+ is displaced with H^+. NH_4^+ desorbs from the membrane. At the cathode, NH_4^+ deprotonates, producing NH_3. The dissociated H^+ is reduced to H_2 with the supplied e^- from the cathode. N_2 is used as carrier gas to remove NH_3 and H_2 from the cell. The coloring of the atoms is done according to the CPK color model. . 145
7.6 Schematic illustration of the test bench. H_2O is supplied and O_2 is produced at the anode. NH_3 is expelled from the membrane and H_2 is produced at the cathode. 146
7.7 Expelled amount of NH_3 of the 2:1 ratio, a logarithmic scale is used. The red color represents the measurement protocol of the first run and the blue of the second run. The applied potentials / current densities are written in black, while the measured potentials / current densities are written in blue. 148
7.8 Expelled amount of NH_3 of the 1:1 ratio, a logarithmic scale is used. The red color represents the measurement protocol of the first run, the blue the second, and the green the third run. The applied potentials / current densities are written in black, while the measured potentials / current densities are writtem in blue. 149

7.9 Comparison and ratio of the expelled amount of NH_3 compared to the initial amount of NH_3 in the membrane. Green dots refer to the ratio of the expelled amount to the initial amount in the entire membrane. The blue dots refer to the ratio of the expelled amount to the initial amount in the active area of the membrane only. 150
7.10 Galvanostatic experiments for both ratios at RT. The first trials are depicted as the solid lines and the second trials as the dotted lines. The measured potentials for the first runs are shown in red, that for the second run in blue and that for the third run in green. 151
7.11 Polarisation curves for both trials at RT. The first trials are depicted as the solid lines with square dots and the second trials as dashed lines with circular dots. The measured current densities for the first runs are shown in red, that for the second run in blue. 152
7.12 Recorded impedance spectra at 1.5 V and RT. The specta of the first trials are depicted as the solid lines and the second trials as dashed lines. The spectra of the first runs are shown in red, that for the second run in blue and that for the third run in green. 153
7.13 (a) Impedance spectra of T2 of the ratio 2:1 NH_4^+ vs. H^+ with their corresponding fits at 1.5 V and (b) the Randles equivalent circuit used for fitting. 154
7.14 Measured desorption of NH_3 while applying an electric current (red and blue bar) and the desorption of NH_3 during the dead-voltage state (bright bars). 155
7.15 Detected amount of NH_3 in the cell components, a logarithmic scale is chosen to show small amounts present in some components. The frame area of the membrane and the active area of the membrane were re-inserted into a fresh solution, because not all of the NH_4^+-ions within these areas were expelled in the first solution. 157
7.16 NH_3 expelled electrochemically (red) and the detected amounts of NH_3 expelled from the cell components. A logarithmic scale is chosen to show small amounts present in some components. The frame area of the membrane and the active area of the membrane were re-inserted into a fresh solution, because not all of the NH_4^+-ions within these areas were expelled in the first solution. 158
7.17 NH_3 expelled electrochemical (red and blue bar) and the total amount of NH_3 that was found, electrochemical plus the quantity which were expelled afterwards in the H_2SO_4 solutions from the cell components (dark red and blue). 160

8.1 Schmatic illustration of the NH_3 recycling process through the membrane. H_2O, which contains dissolved NH_4^+ and SO_4^{2-} is introduced into the PTL of the anode. The NH_4^+-ions can diffuse through the membrane, because Nafion is cation conductive. The SO_4^{2-} can not diffuse through the membrane, the remain on the anode side. In the catalyst layer H_2O is oxidized to O_2 and H^+. The produced O_2 exits the cell at the anode outlet. The generated H^+ either remain on the anode side, diffuses through the membrane and is reduced to H_2 or it interacts with the NH_4^+-ions, which were introduced into the membrane, within the membrane. The diffused NH_4^+-ions deprotonate at the cathode. NH_3 is produced and the resulting H^+ are reduced to H_2 with the supplied e^- from the cathode. N_2 is used as carrier gas to remove NH_3 and H_2 from the cell. The coloring of the atoms is done according to the CPK color model. 166
8.2 Schematic illustration of the test setup. 168
8.3 Discharge of NH_3 during the supply of H_2O (red and green bars) and $(NH_4)_2SO_4$ solution (blue bars). Two trials were carried out, ensuring reproducibility. In black the applied potentials and current density are written and in dark blue the corresponding measured values. 171
8.4 Recycling rates of the NH_4^+ concentration of 0.02 M (red) and 0.04 M (blue) in the $(NH_4)_2SO_4$ solution. In black the applied potentials and current density are written and in dark blue the corresponding measured values. 173
8.5 Recycling rates of the applied solution flow rates 5 mL/min (red) and 20 mL/min (blue) in the $(NH_4)_2SO_4$ solution. In black the applied potentials and current density are written and in dark blue the corresponding measured values. 174
8.6 Recycling rates at RT (red) and 80 °C (blue). In black the applied potentials and current density are written and in dark blue the corresponding measured values. 175
8.7 Recycling comparison of the introduced solutions $(NH_4)_2SO_4$ (red) and NH_4NO_3 (blue) under different conditions of temperature and flow rate. In black the applied potentials and current density are written and in dark blue the corresponding measured values. 177
8.8 Resulting recycling rates while the $(NH_4)_2SO_4$ solution was recirculated (red), leads to Δc and while the solution was not recirculated (blue), c was constant. In black the applied potentials and current density are written and in dark blue the corresponding measured values. 179

8.9 Totaled recycled quantity of NH_3 of recirculation (red) and non-recirculation (blue) (left y-axis). The ratios of recycled quantity to the initial amount of NH_4^+ are shown as black stars (right y-axis). 180
8.10 FE of NH_3 regarding recirculation (red) and non-recirculation (blue) (left y-axis). The energy consumption for recycling 1 kg are shown as black stars (right y-axis). 181
8.11 The average NH_3 recycling rates with the respective error bars of for the three runs of the studied cells are shown in different shades of red. In black the applied current density is written and in dark blue the corresponding measured potentials. 182
8.12 Totaled recycled quantities of NH_3 of each cell is shown in the different red shades. In green the remaining quantity of NH_4^+ of each solution is illustrated. In grey the assumed adsorbed quantity of NH_4^+ within the membrane and in orange the detected quantity of NH_4^+ which was still in the the same membrane are shown (left y-axis). The ratios of recycled quantity to the initial amount of NH_4^+ in the solution are shown as the corresponding red stars (right y-axis). 183
8.13 The Faraday efficiencies of NH_3 recycling of the three cells are shown in the three shades of blue (left y-axis). The energy consumption for recycling 1 kg of NH_3 by the respective cells is shown as black stars (right y-axis). 184
8.14 Recycling rates of three runs of an MEA cell, while a NH_4NO_3 solution was introduced and recirculated on the anode. In black the applied current density is written and in dark blue the corresponding measured potentials. 185
8.15 Recorded recycling rates of NH_3 during non-recirculation / constant concentration of NH_4^+ in the introduced solution (left y-axis). The Faraday efficiency of the runs is shown as black stars (right y-axis). In black the applied current density is written and in dark blue the corresponding measured potentials. 187
8.16 Recorded recycling rates of each run (red bars, left y-axis). The corresponding substance of NH_3, which was recycled each run (black stars, right y-axis). In black the applied current density is written and in dark blue the corresponding measured potentials. 188
8.17 The recycling rates in dependency of the added amount of Na^+. The solution of the red shaped production rates contained 10 %, the solution of the blue depicted rates 20 %, and the green one 40 % Na^+. 189

List of Tables

2.1 Criteria for reliable NH_3 detection. The three criteria are a sufficient NH_3 production rate, the quantitative analysis of NH_3 via isotope determination and the control of oxidised forms of N_2. 38

3.1 Impedance elements for EIS and their physical meaning. 58

4.1 Thermodynamic energy efficiency of the three synthesis pathways and their specific advantage. 76

5.1 Oxygen depletion, values of the elements of the equivalent circuits. . . 103

6.1 Average mole fraction the sputtered metals on the carbon felt of the images (a) and (b). 129

7.1 The different studied rates, the corresponding quantity and concentration of $NH_4{}^+$ are listed. Additionally the mass of $(NH_4)_2SO_4$, which is required for preparing the rates. 138

7.2 Elements of the impedance spectra of T2 of the ratio 2:1. 154

7.3 Σn_{tot} is the sum of the quantity of NH_3, that was expelled during the runs in the dead-voltage states. V1 was the first 10 min time interval of 0 V, V2 the second, and V3 the third. χ is defined as the percentage of NH_3 removed without applying a potential, relative to the amount removed at a current density of $0.8\,A\,cm^{-2}$ for n_{tot}. Additionally, it represents the percentage of NH_3 removed without applying a potential for the various time intervals, in relation to the total amount of NH_3 removed without the application of a potential. 156

8.1 Limits of $NH_4{}^+$ in wastewater for different sections of industry [206]. . 164

8.2 The different concentrations of $NH_4{}^+$, the corresponding quantity and concentration of $(NH_4)_2SO_4$ and NH_4NO_3 are listed. Additionally, the ratio, the amount of $NH_4{}^+$ within the solution in comparison to the amount of H^+ within the membrane is listed. 169

Glossary

AEL	Alkaline Electrolysis
AEM	Anion Exchange Membrane
CE	Counter Electrode
CMS	Carbon Molecular Sieves
CV	Cyclic Voltammetry
DFT	Density Functional Theory
eNRR	electrochemical Nitrogen Reduction Reaction
FE	Faraday Efficiency
FTIR	Fourier Transformation Infrared Spectroscopy
HEA	High Entropy Alloys
HER	Hydrogen Evolution Reaction
HHV	Higher Heating Value
IR	Infrared Spectroscopy
LHV	Lower Heating Value
MEA	Membrane Electrode Assembly
MvK	Mars-van-Krevelen
NMR	Nuclear Magentic Resonance Spectroscopy
NP	Nano Particle
NRR	Nitrogen Reduction Reaction
PEM	Proton Exchange Membrane
PSA	Pressure Swing Adsorption
PTFE	Polytetrafluorethylen
PTL	Porous Transport Layer
RE	Referene Electrode
SAC	Single Atom Catalyst
SEI	Solid Electrolyte Interface
SHE	Standard Hydrogen Electrode
SOEC	High-Temperature Electrolysis
WE	Working Electrode

Symbols

Symbol	Description	Unit
A	Area	$[\mathrm{m}^2]$
A_0	Absorbance	[–]
C_{Ox}	Concentration anode	$[\mathrm{mol\,L}^{-1}]$
C_{Re}	Concentration cathode	$[\mathrm{mol\,L}^{-1}]$
D	Diffusion coefficient	$[\mathrm{m}^2\,\mathrm{s}^{-1}]$
E	Energy	[J]
F	Faraday constant	$[\mathrm{C\,mol}^{-1}]$
I	Intensity	[–]
I_0	Initial intensity	[–]
J	Diffusion flux	$[\mathrm{mol\,m}^{-2}\,\mathrm{s}^{-1}]$
K	Equilibrium constant	[–]
K_x	Equilibrium constant mole fraction	[–]
L	Diffusion length	[m]
M	Molar mass	$[\mathrm{g\,mol}^{-1}]$
Q	Charge	[C]
Q_{tot}	Charge total	$[\mathrm{g\,mol}^{-1}]$
R	Production rate	$[\mathrm{mol\,cm}^{-2}\,\mathrm{s}^{-1}]$
T	Temperature	[K]
U	Potential	[V]
U^0	Equilibrium potential	[V]
V	Volume	$[\mathrm{m}^3]$
c	Concentration	$[\mathrm{mol\,L}^{-1}]$
l	Path length	[m]
m	Mass	[kg]
n	Amount of substance	[mol]
p	Pressure	[Pa]
p_x	Partial pressure	[Pa]
p^{Θ}	Standard pressure	[Pa]
t	Time	[s]
x	Mole fraction	[–]
z	Number of electrons	[–]

Symbol	Description	Unit
ΔG	Gibbs energy	[J/mol]
ΔH_R	Reaction enthalpy	$[\mathrm{J\,mol^{-1}}]$
ΔS_R	Reaction enntropy	$[\mathrm{J\,mol^{-1}\,K^{-1}}]$
β	Mass concentration	$[\mathrm{kg\,L^{-1}}]$
ϵ	Absorbance coefficient	[–]
η	Faraday efficiency	[%]
$\eta_{An/Ca}$	Charge transfer overpotential	[V]
η_{Diff}	Diffusion overpotential	[V]
η_{Ω}	Ohmic overpotential	[V]
ρ	Density	$[\mathrm{kg\,m^{-3}}]$
ν	Stoichiometric coefficient	[–]
χM	Molar mass fraction	[–]

/

List of Publication

Publications published

1. Dominik Sachse, Basil Noha Chelachottil, Andreas Glüsen, Martin Müller, Uwe Rau, Ralf Peters, *Generation of nitrogen by means of electrochemical oxygen depletion*, Reaction Chemistry & Engineering, Royal Society of Chemistry (2024)
2. Dominik Sachse, Andreas Glüsen, Klaus Wippermann, Martin Müller, Uwe Rau, Ralf Peters, *The Ammonia Adsorption and Desorption Behavior of Nafion*, Membranes, MDPI (2025)

Publications in revision

1. Dominik Sachse, Marquise Akame Mboutou, Andreas Glüsen, Martin Müller, Uwe Rau, Ralf Peters, *Electrochemical Ammonia Recovery from Wastewater utilizing a MEA cell*, Advanced Energy and Sustainability Research, Wiley (2025)

Patent application

The process of electrochemical ammonia recycling utilizing a MEA cell was submitted as an patent application to the German Patent Office. The title of this submission is "Ammoniakrecycling und Wasserstoffgewinnung aus ammoniumhaltigen Lösungen / Abwasser". The official reference number is: 102024212071.5

Curriculum Vitae

Personal Information

Name	Dominik Sachse
Date of Birth	11.01.1995
Place of Birth	Bocholt
Citizenship	German

Education

2021 - 2025	PhD thesis at the Forschungszentrum Jülich GmbH IET-4 Electrochemical Process Engineering
March 2023	Research Internship - National research concil Catania, Italy
2018 - 2021	Master of Science in Material Science at the RWTH Aachen University
11.2017 - 02.2018	Research Internship - NAIST, Japan
2014 - 2017	Bachelor of Science in Material Science at the RWTH Aachen University
2011 - 2014	Abitur, Technology Gymnasium Borken

A

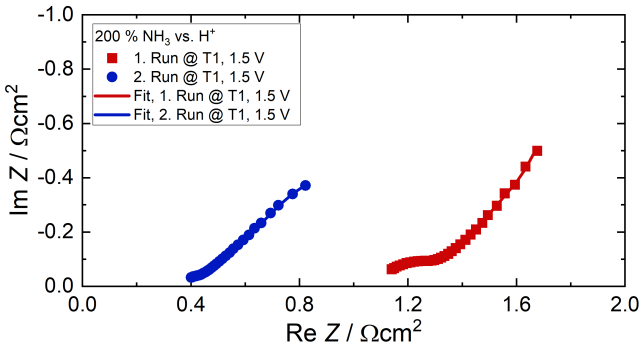
Tested Catalyst

Catalyst	Membrane	Reactants	Detection Method	Temperature
An: Pt/C Ca: MoV_2Ni	Nafion 115 H^+-form	N_2: 50, 100 mL/min H_2: 30, 60 mL/min	IR	RT, 40 80 °C
An: Pt/C Ca: MoV_2Ni	Nafion 115 H^+-form + 15 *wt*% Nafion sol	N_2: 10, 20, 50 100 mL/min H_2: 30, 60 mL/min	IR	RT, 80 °C
An: Pt/C Ca: MoV_2Ni	Nafion 115 H^+-form + 15 *wt*% Nafion sol	N_2: 100, 200 mL/min H_2 50 mL/min	IR	RT, 80 °C
An: Pt/C Ca: MoV_2Ni	Nafion 212 H^+-form	N_2: 50, 100 mL/min H_2O: 30 mL/min	IR	RT, 40, 60 80 °C
An: Pt/C Ca: Au/C	Nafion 115 H^+-form	N_2: 50, 100 mL/min H_2: 30, 60 mL/min	IR	RT, 40, 60 80 °C
An: Pt/C Ca: AuNi	Nafion 115 H^+-form	N_2: 50, 100 mL/min H_2: 30, 60 mL/min	IR	RT
An: Pt/C Ca: AuNi	Nafion 115 H^+-form + 15 *wt*% Nafion sol	N_2: 25, 50 mL/min H_2: 20, 30 mL/min	IR	RT, 40 80 °C
An: Pt/C Ca: AuNi	Nafion 115 Na^+-form	N_2: 25, 50 mL/min H_2: 20, 30 mL/min	IR	RT, 40 80 °C
An: IrOx Ca: Pt/C	Nafion 212 H^+-formt	N_2: 50, 100 mL/min H_2O: 30, 50 mL/min	IR	RT, 40, 60 80 °C
An: IrOx Ca: Ti	Nafion 115 H^+-form	N_2: 25, 50 mL/min H_2O: 10 mL/min	IR	RT 50 °C
An: Pt/C Ca: Ti	Nafion 115 H^+-form + 15 *wt*% Nafion sol	N_2: 50, 100 mL/min H_2: 30 mL/min	IR	RT, 60 80 °C
An: Pt/C Ca: Ti	Nafion 115 Na^+-form	N_2: 50, 100 mL/min H_2: 30 mL/min	IR	RT, 60 80 °C
An: Pt/C Ca: AuMo	Nafion 115 H^+-form + 15 *wt*% Nafion so	N_2: 50 mL/min H_2: 20, 30 mL/min	IR, Indophenol	RT, 50 °C
An: Pt/C Ca: AuMo	Nafion 115 Na^+-form	N_2: 50 mL/min H_2: 20, 30 mL/min	IR, Indophenol	RT, 50 °C
An: Pt/C Ca: AuMo	Zirfon	N_2: 50 mL/min KOH: 0.1, 1 M	Indophenol	RT
An: Pt/C Ca: AuMo	Zirfon	N_2: 50 mL/min Na_2SO_4: 0.1 M	Indophenol	RT
An: Pt/C Ca: Pt/C	Nafion 115 H^+-form + 15 *wt*% Nafion sol	N_2: 50 mL/min H_2: 20 mL/min	IR, Indophenol	RT
An: Pt/C Ca: Pt/C	Nafion 115 Na^+-form	N_2: 50 mL/min H_2: 20 mL/min	IR, Indophenol	RT
An: Pt/C Ca: FeOx	Nafion 115 Na^+-form	N_2: 50 mL/min H_2: 20 mL/min	IR, Indophenol	RT
An: Pt/C Ca: Ru/C	Nafion 115 H^+-form	N_2: 50 mL/min H_2: 20 mL/min	Indophenol	RT
An: Pt/C Ca: Ru/C	Zirfon	N_2: 10 mL/min Na_2SO_4: 0.1 M	Indophenol	RT
An: Pt/C Ca: CoCrFeMnNi	Nafion 115 Na^+-form	N_2: 10 mL/min H_2: 20 mL/min	Indophenol	RT
An: Pt/C Ca: CoCrFeMnNi	Zirfon	N_2: 10 mL/min KOH: 0.1, 1 M	Indophenol	RT
An: Pt/C Ca: AuCuNi	Zirfon	N_2: 10 mL/min KOH: 0.1 M	Indophenol	RT

Tested catalyst and their corresponding process parameters.

B

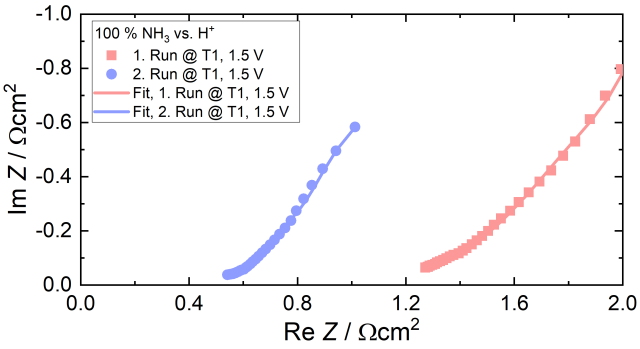
Impedance Spectra and Fits



Fit of T1 2:1

$\mathbf{R}_\Omega$ [Ω]	$\mathbf{R}_{CT}$ [Ω]	$\mathbf{W}_R$ [Ω]	$\mathbf{W}_T$ [F]	$\mathbf{W}_P$	$\mathbf{CPE}_T$ [Ω^{-1} $\mathbf{s}^{-1}$]	$\mathbf{CPE}_P$
0.172 ± 0.001	0.044 ± 0.002	0.35 ± 0.01	1.28 ± 0.05	0.580 ± 0.006	0.17 ± 0.03	0.67 ± 0.02
0.049 ± 0.009	0.02 ± 0.01	0.197 ± 0.003	0.93 ± 0.04	0.469 ± 0.003	0.10 ± 0.07	0.6 ± 0.2

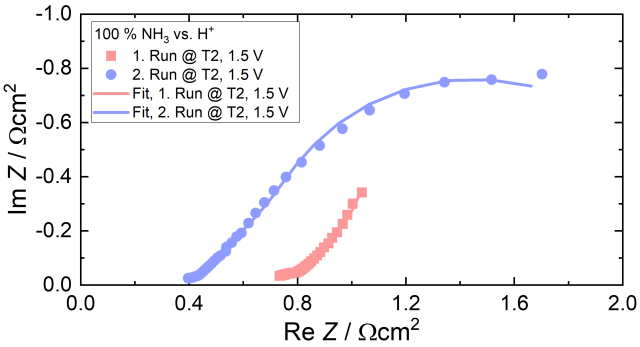
T1 2:1



Fit of T1 1:1

$\mathbf{R}_{\Omega}$ [Ω]	$\mathbf{R}_{CT}$ [Ω]	$\mathbf{W}_{R}$ [Ω]	$\mathbf{W}_{T}$ [F]	$\mathbf{W}_{P}$	$\mathbf{CPE}_{T}$ [Ω^{-1} $\mathbf{s}^{-1}$]	$\mathbf{CPE}_{P}$
0.192 ± 0.002	0.08 ± 0.03	0.8 ± 0.2	0.9 ± 0.2	0.61 ± 0.04	0.7 ± 0.4	0.51 ± 0.07
0.076 ± 0.004	0.023 ± 0.008	0.29 ± 0.03	0.70 ± 0.06	0.57 ± 0.02	0.412 ± 0.05	0.6 ± 0.2

T1 1:1



Fit of T2 1:1

$\mathbf{R}_{\Omega}$ [Ω]	$\mathbf{R}_{CT}$ [Ω]	$\mathbf{W}_{R}$ [Ω]	$\mathbf{W}_{T}$ [F]	$\mathbf{W}_{P}$	$\mathbf{CPE}_{T}$ [Ω^{-1} $\mathbf{s}^{-1}$]	$\mathbf{CPE}_{P}$
0.108 ± 0.002	0.027 ± 0.005	0.22 ± 0.02	0.94 ± 0.06	0.59 ± 0.02	0.8 ± 0.4	0.51 ± 0.08
0.059 ± 0.001	0.014 ± 0.002	0.34 ± 0.03	2.1 ± 0.1	0.54 ± 0.01	1.5 ± 0.4	0.51 ± 0.05

T2 1:1

Band / Volume 694
Entwicklung von Korrosionsschutzschichten für Protonen-Austausch-Membran-Wasserelektrolyseure
T. Sievert (2026), 201 pp
ISBN: 978-3-95806-888-9

Band / Volume 695
Hierarchical Modeling of Electrocatalytic Reactions from a Local Perspective
X. Zhu (2026), ix, 121 pp
ISBN: 978-3-95806-889-6

Band / Volume 696
Nanocrystalline Silicon Carbide in Transparent Passivating Contact Solar Cells
A. Eberst (2026), xiii, 225 pp
ISBN: 978-3-95806-891-9

Band / Volume 697
Theory of Electronic and Ionic Perturbations at Supported Electrocatalyst Nanoparticles
Y. Zhang (2026), XI, 131 pp
ISBN: 978-3-95806-896-4

Band / Volume 698
Aufbau und Einsatz eines on-board Messsystems zur Untersuchung der Abgaszusammensetzung von Fahrzeugen betrieben mit konventionellen und alternativen Kraftstoffen
V. Polinowski (2026), VIII, 269 pp
ISBN: 978-3-95806-897-1

Band / Volume 699
Ab Initio-based large-scale Atomistic Simulations of Cathode Materials for Secondary Batteries: From Computational Methodologies to Applications towards improved Structural and Chemical Stability
K. Köster (2026), x, 204, x pp
ISBN: 978-3-95806-898-8

Band / Volume 700
Materials Design, Processing and Application of Proton-Conducting Oxides for Electrochemical Energy Conversion
Y. Zeng (2026), vii, 117 pp
ISBN: 978-3-95806-899-5

Band / Volume 701
Accelerating the discovery of alkaline-stable anion exchange membrane materials via computational exploration
F. P. Tipp (2026), xii, 135 pp
ISBN: 978-3-95806-900-8

Band / Volume 702
Methods for Investigating the Structure-Performance Correlation in Membrane Electrode Assemblies
N. Utsch (2026), XIII, 138, LXVII pp
ISBN: 978-3-95806-901-5

Band / Volume 703
Hot-Spot Formation in Cu(In,Ga)Se_2 Thin Film Solar Cells
S. Nofal (2026), xvii, 131 pp
ISBN: 978-3-95806-903-9

Band / Volume 704
Machine Learning Guidance of Manufacturing Process of Solid Oxide Cells
T. LE DINH (2026), xxi, 122 pp
ISBN: 978-3-95806-904-6

Band / Volume 705
Drivers of spatiotemporal variability of European terrestrial ecosystem processes
C. Poppe Téran (2026), 254 pp
ISBN: 978-3-95806-905-3

Band / Volume 706
Characterization of Nitrogen Reduction Reaction Catalysts for the electrochemical Ammonia Synthesis
D. Sachse (2026), xi, 235, 6 pp
ISBN: 978-3-95806-907-7

Weitere ***Schriften des Verlags im Forschungszentrum Jülich*** unter
http://wwwzb1.fz-juelich.de/verlagextern1/index.asp

Energie & Umwelt / Energy & Environment
Band / Volume 706
ISBN 978-3-95806-907-7

Mitglied der Helmholtz-Gemeinschaft

JÜLICH
Forschungszentrum